

**Geochronology, Petrogenesis, and Tectonic
Significance of the Laiyuan Magmatic Complex
in the Central North China Craton**

July 2021

FEI XUE

**Geochronology, Petrogenesis, and Tectonic
Significance of the Laiyuan Magmatic Complex
in the Central North China Craton**

A Dissertation Submitted to
the Graduate School of Life and Environmental Sciences,
the University of Tsukuba
in Partial Fulfillment of the Requirements
for the Degree of Doctor of Philosophy in Science
(Doctoral Program in Earth Evolution Sciences)

FEI XUE

Contents

Contents	i
Abstract.....	v
List of Figures.....	ix
List of Tables	xix
Chapter 1 Introduction.....	1
1.1 Research background and controversies.....	1
1.2 Research progress	3
1.2.1 The NCC destruction	3
1.2.2 Heterogeneity in the magmatic complex	8
1.2.3 Research progress and remaining questions in the study area.....	9
1.3 Objectives of this study	10
Chapter 2 Regional geology	13
2.1 North China Craton	13
2.2 Northern Taihang Mountains.....	14
2.2.1 Regional strata	14
2.2.2 Regional structures	15
2.2.3 Magmatism	16
2.3 Laiyuan magmatic complex.....	17
Chapter 3 Field observation and petrographic characteristics.....	19
3.1 Volcanic rocks.....	20
3.2 Granitoids	23
3.2.1 Syenogranite	24
3.2.2 Monzogranite.....	26
3.2.3 Quartz monzonite	26
3.2.4 Monzonite.....	28
3.3 Dyke suites	28
3.3.1 Lamprophyre	29

3.3.2 Dolerite and dolerite porphyry	30
3.3.3 Felsic dykes	31
3.4 Ultramafic-mafic rocks.....	31
3.5 Spatial links between diverse magmatic suites.....	33
Chapter 4 Analytical methods.....	34
4.1 EPMA	34
4.2 Whole rock geochemistry	34
4.3 Zircon U-Pb dating	34
4.4 Zircon in-situ Lu-Hf isotopes	35
Chapter 5 Geochronology of the Laiyuan complex.....	37
5.1 Zircon age data on magmatic suites in the Laiyuan complex.....	37
5.1.1 Volcanic rocks.....	37
5.1.2 Granitoids	38
5.1.3 Dyke suites	41
5.2 Temporal links between diverse magmatic suites	51
Chapter 6 Zircon Hf isotopic compositions of the Laiyuan complex.....	57
6.1 Zircon in-situ Lu-Hf isotopic results	57
6.1.1 Volcanic rocks.....	57
6.1.2 Granitoids	57
6.1.3 Dyke suites	58
6.2 Source variations between diverse magmatic suites.....	59
Chapter 7 Petrogenesis of volcanic rocks.....	64
7.1 Introduction	64
7.2 Petrography.....	66
7.3 Geochemistry.....	66
7.4 Petrogenesis	67
7.4.1 Crustal contamination.....	67
7.4.2 Fractional crystallization	68
7.4.3 Nature of magma source.....	70

7.4.4 Origin of high Ba-Sr and adakitic signatures	73
7.5 Summary.....	78
Chapter 8 Petrogenesis of granitoids	80
8.1 Introduction	80
8.2 Petrography.....	81
8.3 Geochemistry.....	82
8.4 Petrogenesis.....	84
8.4.1 Genetic types	84
8.4.2 Fractional crystallization	86
8.4.3 Two types of magmatic evolution.....	89
8.4.4 Crust-mantle interaction	99
8.5 Summary.....	101
Chapter 9 Petrogenesis of dyke suites	102
9.1 Introduction	102
9.2 Petrography and mineral chemistry	103
9.2.1 Pyroxenes.....	103
9.2.2 Feldspars.....	104
9.2.3 Amphibole	105
9.2.4 Biotite	105
9.3 Geochemistry.....	106
9.4 Petrogenesis.....	109
9.4.1 Effects of crustal contamination and fractional crystallization	109
9.4.2 Implication of U-Pb ages.....	113
9.4.3 Petrogenesis of felsic dykes.....	115
9.4.4 Magma source of mafic dykes.....	117
9.4.5 Lithosphere-asthenosphere interaction	120
9.5 Summary.....	123
Chapter 10 Tectonic implications	124
10.1 Tectonic regime transition from compression to extension.....	124

10.2 Geodynamic trigger for the NCC destruction.....	127
10.3 Different lithospheric evolution beneath the eastern and central NCC	130
10.4 Destruction mechanism in the central NCC	134
10.5 An integrated petrogenetic model for the Laiyuan complex	136
Chapter 11 Summary and conclusions	139
Acknowledgements	142
References	144
Appendix I: Analytical data.....	170
Appendix II: Curriculum Vitae.....	222

Abstract

The igneous complex incorporating variable magmatic suites is the perfect object for investigating magma differentiation, tectonic setting, crustal structure, and lithospheric evolution. In the North China Craton (NCC), during the late Mesozoic, extensive magmatism occurred and generated plenty of magmatic complexes with complicated compositional variations offering the opportunity to study the NCC destruction. The focus of this study is the craton destruction and lithospheric evolution in the central NCC compared with the eastern NCC by reconstructing the Laiyuan magmatic complex. Here, new petrological, mineral chemical, geochemical, geochronological, and isotopic data have been presented to reveal the spatial, temporal, petrogenetic, and tectonic linkages between different magmatic suites, to establish an integrated petrogenetic model for the Laiyuan complex, and to assess the craton destruction mechanism and lithospheric evolution in the central NCC.

Various magmatic units with different compositions constitute the Laiyuan complex, including the volcanic rocks (andesite-dacite), intermediate-felsic granitoids (syenogranite, monzogranite, quartz monzonite, and monzonite), mafic-ultramafic intrusions, and some dyke suites (felsic dykes, dolerites, and lamprophyres). The volcanic rocks, granitoids, felsic dykes, dolerites, and lamprophyres were formed at 131-127 Ma, 137-128 Ma, 131-127 Ma, 125-117 Ma, and 115-110 Ma, with zircon $\epsilon_{\text{Hf}}(t)$ values ranging from -23.5 to -19.4, -21.8 to -16.8, -22.3 to -17.2, -23.3 to -14.2, and -17.2 to -3.7, respectively.

The studied Early Cretaceous volcanic suite represented by rocks of andesitic-dacitic composition shows enrichment in light rare earth elements (LREEs) and large ion lithophile elements (LILEs) and depletion in high field strength elements (HFSEs) with no obvious Eu anomalies. They also show typical adakitic features such as high Sr/Y and La/Yb ratios and high Ba-Sr concentrations. The geochemical and isotopic data show that the enriched lithospheric mantle source

experienced fluid-related subduction metasomatism. The distinct geochemical features of these identified in this study, including high Ba-Sr concentrations and adakitic affinities, were not only inherited from their magma source but are also a result of fractional crystallization during magma evolution including amphibole-dominated fractional crystallization at depth and limited plagioclase removal.

The granitoids display variable compositions and can be classified into two groups. The parental mafic magma for the Group I rocks (monzonite, quartz monzonite, and mafic microgranular enclaves [MMEs]) were derived from the enriched lithospheric mantle and subsequently experienced the hornblende-dominated fractional crystallization to form the monzonitic/dioritic magmas, then the magma mixing and mingling with the crustal melts/magmas generated the hybrid magmas to form the MMEs and variable intermediate suites. Group II rocks are classified as high-K calc-alkaline I-type suites including monzogranites and syenogranites. These granitic rocks were most likely generated by partial melting of the thickened mafic lower crust at high pressure, with some addition of the mafic magma from an enriched mantle, and followed by intense plagioclase-dominated fractional crystallization to form the highly-fractionated syenogranites. The compositional heterogeneities of the igneous complex resulted from the intense crust-mantle interaction which involved multiple mantle and crustal sources, chaotic mixing and mingling, and complicated fractional crystallization.

The mafic dyke samples exhibit enrichment in LILEs and no obvious Eu anomalies, and the dolerites show strong depletion in HFSEs, whereas the Th-U and Ta-Nb depletions in lamprophyres are not obviously similar to OIB-type. The newly presented geochemical data suggest that the mafic dykes experienced limited crustal contamination and were dominated by olivine and clinopyroxene fractional crystallization. The mafic dykes were derived through partial melting of mantle previously enriched by subduction-related fluids within amphibole- and garnet-stability field (80-100 km) with increasing input of asthenospheric material

through time. The felsic dykes show adakitic features sharing similar petrogenesis with the granitoids, which were formed through crust-mantle interaction. Subsequently, the enriched mantle-derived magmas migrated through lithospheric faults and were emplaced as dolerite dykes at 125-117 Ma. The asthenosphere upwelling contributed to the thermo-mechanical erosion along weak zones, and the limited lithosphere-asthenosphere interaction generated the lamprophyres with transitional geochemical features during ~115-110 Ma.

The intense magmatism to form the Laiyuan complex was under the extension tectonic setting triggered by the subduction of the Paleo-Pacific Plate. The subduction, retreat, roll back, and stagnation of the Paleo-Pacific slab result in the heterogeneous lithosphere and various evolutionary processes in depth beneath the NCC. The slow and gradual thermal-mechanical erosion occurred at the central NCC, whereas the rapid and intense lithospheric delamination occurred at the eastern NCC, contributing to different lithospheric evolution. Both of the two mechanisms combined with the Paleo-Pacific slab played a significant role in the NCC destruction process to form variable magmatic rocks.

An integrated formation model has been proposed to describe the formation mechanism of the Laiyuan magmatic complex. During Early Jurassic (~200-150 Ma), the subduction of the Paleo-Pacific Plate has reached the position beneath the central NCC. During this period, the central NCC was under compression which thickened the lithosphere. The Late Jurassic volcanic rocks (~146 Ma) were formed during this period whose petrogenesis could be attributed to the partial melting of the thickened lower crust and the deep hornblende-dominated fractional crystallization process. During 145-140 Ma, fast slab rollback occurred, leading to hot asthenosphere upwelling and extensional setting in the central NCC. Induced by the upwelling of hot asthenosphere, the extensive crust-mantle interaction occurred, accounting for the petrogenesis for the formation of granitoids (137-126 Ma), MMEs (129-126 Ma), volcanic rocks (131-127 Ma), and felsic dykes (131-127 Ma). Over time, the lithosphere became substantially thin that lithospheric mantle-derived magmas could

migrate through the lithospheric faults and intruded the plutons or country rocks leading to the formation of dolerite dykes at 125-117 Ma. The continuous lithospheric thinning eventually resulted in the upwelling asthenosphere reached the depth where it could melt (80 km). The partial melting of the asthenospheric mantle and its interaction with the eroded lithospheric mantle material produced the lamprophyre from ~115 to 110 Ma representing the end of Early Cretaceous magmatism in the central NCC.

Keywords: Mesozoic magmatism, Lithospheric evolution, North China Craton destruction, Geochemical modeling, Laiyuan magmatic complex

List of Figures

- Fig. 1-1 Distribution of Precambrian cratons on the Earth (modified after Zhu et al., 2011)..... 2
- Fig. 1-2 The distribution of lithospheric thickness beneath the North China Craton (after Zhu et al., 2011). Abbreviation: TNCO-Trans-North China Orogen; CAOB-Central Asian Orogenic Belt. 6
- Fig. 2-1 (a) Major tectonic units of China. (b) Tectonic subdivision of the North China Craton (modified after Zhao et al., 2005). Abbreviations of metamorphic complexes: CD, Chengde; NH, Northern Hebei; XH, Xuanhua; HA, Huai'an; HS, Hengshan; WT, Wutai; FP, Fuping; LL, Lüliang; ZH, Zhanhuang; ZT, Zhongtiao; DF, Dengfeng; TH, Taihua..... 14
- Fig. 2-2 (a) Major tectonic units of China. (b) Tectonic map of the NCC showing the distributions of Early Cretaceous magmatic rocks (modified after Zhang et al., 2014; Zhao et al., 2005)..... 15
- Fig. 2-3 (a) Sketch geological map of the Taihang Mountains (after Li et al., 2013b). (b) Simplified geological map showing the distributions of Mesozoic intrusions in the NTM. 17
- Fig. 3-1 Geological map of the Laiyuan magmatic complex after the mineral and geological map in Laishui-Yixian areas (1979) and this fieldwork showing the sample locations of dyke suites and volcanic rocks, and the zircon U-Pb dating results yielded in this study..... 19
- Fig. 3-2 Representative photographs and photomicrographs of the Laiyuan volcanic rocks. (a), (b), (c) and (d) Greenish to brownish exposures of andesites-dacites with porphyritic textures. (e) Dacite composed of quartz, biotite and hornblende phenocrysts. (f) Andesite containing abundant amphibole and clinopyroxene phenocrysts and plagioclase groundmass. (g) Directional arrangement of plagioclase microcrystal in andesite. (h) Hornblende with dark-colored edge and alterations in andesite. (i) Phenocrysts of plagioclase and clinopyroxene and dark groundmass composed of glass and plagioclase microcrystals in trachyandesite.

(j) Amphibole minerals with dark-colored edges in trachyandesite. (k) Subhedral plagioclase phenocrysts surrounded by iron oxides and oriented textures in groundmass in trachyandesite. (l) Groundmass exhibiting typical trachytic texture in trachydacite. Mineral abbreviation: Amp-amphibole; Bt-biotite; Cpx-clinopyroxene; Hbl-hornblende; Kfs-K-feldspar; Mag-magnetite; Pl-plagioclase; Qtz-quartz. 23

Fig. 3-3 Geological map of the Sigezhuang pluton showing the sample locations of granitoids, and the zircon U-Pb dating results yielded in this study..... 24

Fig. 3-4 Field photographs of the Laiyuan granitoids. (a) Rapakivi monzogranite with zoning K-feldspar (LYN-1/3). (b) Monzogranite containing MME (LY-19/1). (c) Monzonite containing mafic xenolith and TTG fragment from basement rocks (LY-20/1). (d) Diorite containing mafic xenolith cut by later felsic dyke. (e) The contact zone between rapakivi quartz monzonite (LY-21/1) and porphyritic monzogranite (LY-21/2). (f) Rapakivi quartz monzonite (LY-21/1) containing rounded MME. (g) Monzonite porphyry (LY-22/1) containing MME (LY-22/4-2). (h) Syenogranite (LY-33/1) containing MME. (i) Syenogranite (LY-37/1-1) containing MME (LY-37/1-2). 25

Fig. 3-5 Representative photomicrographs of the Laiyuan dykes under cross-polarized light. (a) Syenogranite (LY-33/1). (b) and (c) Biotite syenogranite (LY-36/1). (d) Biotite syenogranite (LY-37/1-1). (e) Biotite monzogranite (LY-21/2). (f), (g) and (h) Rapakivi biotite monzogranite (Fig. 22/4-1). (i) Quartz monzonite showing zoning K-feldspar and plagioclase (LY-21/1). (j) Quartz monzonite showing textural disequilibrium in plagioclase (LY-21/1). (k) Quartz monzonite (LY-22/4-2, MME). (l) Quartz monzonite (LY-37/1-2, MME). (m) Monzonite (LY-42/1). (n) Monzonite exhibiting textural disequilibrium (LY-20/1). (o) Monzonite (LY-20/1). (p) Monzonite porphyry displaying anhedral quartz grains surrounded by dark rim (LY-22/1). Mineral abbreviations: Amp-amphibole; Bt-biotite; Hbl-hornblende; Kfs-K-feldspar; Mag-magnetite; Pl-plagioclase; Qtz-quartz; Sph-sphene; Zrn-Zircon. 27

Fig. 3-6 Field photographs of the Laiyuan dykes. (a) Dolerite sills cut by later vertical lamprophyre dyke. (b) Greyish green colored lamprophyre with abundant mafic phenocrysts. (c) Dolerite sill showing compositional variations from bottom to top with granite fragments. (d) Fine-grained and dark gray colored lamprophyre dyke intruding host granite. (e) Dark diorite porphyry dyke with feldspar phenocrysts. (f) Multiple dykes intruding pink syenogranite..... 29

Fig. 3-7 Representative photomicrographs of the Laiyuan dykes under cross-polarized light (left) and plane-polarized light (right). (a) Vogesite (LY-16/1): clinopyroxene phenocrysts and amphibole crystallites in the matrix. (b) Vogesite (LY-16/1): olivine pseudomorph. (c) Vogesite (LY-16/1): clinopyroxene and orthopyroxene minerals of zoning texture and strip amphibole minerals. (d) Camptonite (LY-8/1): paired hornblende phenocrysts. (e) Camptonite (LY-8/1): acicular apatite in matrix. (f) Minette (LYN-1/1): leucocratic ocelli with a round edge rimmed by melanocratic minerals of biotite and amphibole. (g) Minette (LYN-2/1): biotite phenocrysts and altered carbonate minerals. (h) Dolerite (LY-18/1): calcite intergrown with euhedral K-feldspar. (i) Dolerite (LYN-4/1): ophitic texture with clinopyroxene and hornblende minerals. (j) Diorite porphyry (LY-34/1): biotite phenocrysts and abundant hornblende crystallites in matrix. (k) Diorite porphyry (LY-34/1): magnetite aggregation. (l) Granodiorite: paired hornblende and granophyric texture in the matrix. Mineral abbreviations: Amp-amphibole; Ap-apatite; Bt-biotite; Cpx-clinopyroxene; Cal-calcite; Hbl-hornblende; Kfs-K-feldspar; Mag-magnetite; Ol-olivine; Pl-plagioclase; Qtz-quartz. 32

Fig. 5-1 Representative CL images of zircon grains showing ages and $\epsilon_{\text{Hf}}(t)$ values and U–Pb concordia plots and age data histograms with probability curves. In CL images, the larger circles represent locations of Hf isotopic analyses, whereas the smaller circles indicate spots of U–Pb dating..... 38

Fig. 5-2 Representative CL images of zircon grains from granitoids showing ages and $\epsilon_{\text{Hf}}(t)$ values. 39

Fig. 5-3 U–Pb concordia plots and combined age data histogram with probability curves.....	41
Fig. 5-4 Representative CL images of zircon grains from lamprophyres showing ages and $\varepsilon_{\text{Hf}}(t)$ values. The larger circles represent locations of Hf isotopic analyses, whereas the smaller circles indicate spots of U–Pb dating.....	42
Fig. 5-5 U–Pb concordia plots and age data histograms with probability curves for samples LY-8/1 and LY-16/1 (lamprophyre dykes).	43
Fig. 5-6 U–Pb concordia plots and age data histograms with probability curves for samples LYN-1/1 and LYN-2/1 (lamprophyre dykes).....	45
Fig. 5-7 Representative CL images of zircon grains from dolerites or diabase porphyries showing ages and $\varepsilon_{\text{Hf}}(t)$ values.	46
Fig. 5-8 U–Pb concordia plots and age data histograms with probability curves for samples LY-15/1 and LY-16/2 (dolerite dykes).....	47
Fig. 5-9 U–Pb concordia plots and age data histograms with probability curves for samples LY-18/1, LY-26/1 and LYN-4/1 (dolerite dykes).	48
Fig. 5-10 Representative CL images of zircon grains from felsic dykes showing ages and $\varepsilon_{\text{Hf}}(t)$ values.....	49
Fig. 5-11 U–Pb concordia plots and age data histograms with probability curves for samples LYN-1/4 and LY-34/1 (felsic dykes).	50
Fig. 5-12 Compilation of age data on magmatic rocks including data from literatures and this study. The data are listed in Table 5-4.....	51
Fig. 5-13 Stratigraphic columns for the late Mesozoic volcanic-sedimentary rocks across the NCC (after Wu et al., 2019). Three episodes of volcanic rocks are the Nandaling (intraplate basalt), Tiaojishan, and Zhangjiakou/Yixian Formations.	53
Fig. 6-1 Zircon $\varepsilon_{\text{Hf}}(t)$ values vs. age diagram for the Laiyuan Mesozoic magmatic rocks compiled from previous studies and this study. Data sources: Basemen rocks of the Fuping Complex (Tang et al., 2015; Tang et al., 2016); Granitoids from the Laiyuan complex (this study; Shen et al., 2015a; Yang et al., 2019a); Late Jurassic volcanic rocks (Duan et al., 2016); Sub-volcanic rocks (Qu, 2012;	

Shen et al., 2015b); Early Cretaceous volcanic rocks (this study); Dyke suites from the Laiyuan complex (this study) and Shandong Peninsula (Ma et al., 2014a; Ma et al., 2016)..... 60

Fig. 6-2 Sr-Nd isotope diagram for magmatic rocks from the Laiyuan complex. The fields of EMI and EMII are after DePaolo (1981). The metasomatized sub-continental lithospheric mantle (SCLM) field is modified after Zhang et al. (2008a). Lower and upper crust of the NCC, and lower crust of the Yangtze Craton are after Jahn et al. (1999), Fan et al. (2001), and Gao et al. (2004), respectively. Isotopic data of Dabie mafic dykes (Jahn et al., 1999), Fangcheng basalt (Zhang et al., 2002), and Xu-Huai eclogites xenoliths (Gao et al., 2004) are given for comparison. Data source for the magmatic rocks in the Laiyuan complex: Gao et al., 2012; Gao et al., 2013; Hou et al., 2015; Liu et al., 2010; Zhang et al., 2016; Zhang et al., 2003b. 63

Fig. 7-1 (a) TAS diagram for classification (Middlemost, 1994). (b) K₂O vs. SiO₂ diagram (Peccerillo and Taylor, 1975). (c) Chondrite-normalized REE distribution diagrams. (d) Primitive mantle-normalized trace element diagrams. Normalized values: chondrite (McDonough and Sun, 1995), primitive mantle (Sun and McDonough, 1989). 67

Fig. 7-2 Major elemental variation diagrams for the Laiyuan volcanic, mafic and ultramafic rocks compiled from previous studies and this study. Data sources: volcanic suites (Gao et al., 2012; Hou et al., 2015); mafic suites (Hou et al., 2015; Liu et al., 2010); ultramafic suites (Gao et al., 2012; Hou et al., 2015; Liu et al., 2010)..... 69

Fig. 7-3 Trace elemental variation diagrams. Symbols and data sources are same as in Fig. 7-2..... 70

Fig. 7-4 (a) Th/Yb vs. Nb/Yb diagram (after Pearce, 2008). (b) (Hf/Sm)_N vs. (Ta/La)_N diagram (La Flèche et al., 1998). (c) Rb/Sr vs. Ba/Rb diagram. (d) Dy/Yb vs. La/Yb diagram (after Jung et al., 2006). Symbols and data sources are same as in Fig. 7-2. Abbreviation: MORB, mid-ocean-ridge basalt; E-MORB, enriched

mid-ocean-ridge basalt; OIB, oceanic-island basalt; SZE, subduction zone enrichment; CC, crustal contamination; WPE, within-plate enrichment; FC, fractional crystallization. 72

Fig. 7-5 Variation diagrams for the Laiyuan volcanic and sub-volcanic rocks compiled from this study and previous literature. (a) Rb/Nb vs. SiO₂ and (b) Nb/Zr vs. Nb/La, showing calculated curves corresponding to magmatic evolution by simple mixing. Ticks on these curves represent 10% increments. (c) Sr/Y vs. Y (after Defant and Drummond, 1990) and (d) La/Yb vs. Yb (after Castillo, 2012) diagrams exhibiting the calculated curves of Rayleigh fractional crystallization modeling. The detailed parameters and start compositions in the modeling are listed in Table 7-2. Data sources: volcanic suites (Gao et al., 2012; Hou et al., 2015); sub-volcanic porphyries (Gao et al., 2013). Abbreviation: ADR-normal arc andesite-dacite-rhyolite; Amp-amphibole; Pl-plagioclase; Zrn-zircon. 76

Fig. 7-6 Cartoon of the five genetic models for the formation of adakites or adakitic rocks (modified after Zhang et al., 2019). Adakitic signature may be produced under different tectonic settings. HSA: high-SiO₂ adakites, HMA: high-Mg[#] adakitic rocks, C-type: C-type adakitic rocks..... 77

Fig. 8-1 (a) TAS diagram for classification of the Laiyuan dykes (Middlemost, 1994). (b) R1 vs. R2 classification diagram (De La Roche et al., 1980). (c) K₂O vs. SiO₂ classification diagram (Peccerillo and Taylor, 1975). (d) A/NK vs. A/CNK classification diagram (Rickwood, 1989)..... 83

Fig. 8-2 (a), (c) Chondrite-normalized REE distribution diagrams, and (b), (d) Primitive mantle-normalized trace element diagrams for granite and monzonite series, respectively. Normalized values: chondrite (McDonough and Sun, 1995), primitive mantle (Sun and McDonough, 1989)..... 85

Fig. 8-3 Genetic type discrimination diagrams for the Laiyuan granitoids (modified after Whalen et al., 1987). Abbreviation: A-type, A-type granite; FG, fractionated felsic granite; OGT, unfractionated M-, I-, and S-type granite. 87

Fig. 8-4 Major elemental variation diagrams for the Laiyuan magmatic rocks from

previous studies and this study. Data sources: gabbroic rocks (Hou et al., 2015; Liu et al., 2010); MME (Chen et al., 2009b; Zhang et al., 2016); granitoids (Zhang et al., 2016)..... 89

Fig. 8-5 Trace elemental variation diagrams for the Laiyuan magmatic rocks from previous studies and this study. Date sources and legend are as same as in Fig. 8-4..... 91

Fig. 8-6 Mg[#] vs. SiO₂ (wt. %) diagram. AFC curve is modified after (Stern and Kilian, 1996). Fields of metabasaltic and eclogite experimental melts hybridized with peridotite are after (Rapp et al., 1999). Field of metabasaltic and eclogitic melts (1-4 GPa) is after (Wang et al., 2006) and (Rapp and Watson, 1995). Fields of delaminated and thick lower crust-derived adakitic rocks are after (Wang et al., 2006). Date sources and legend are as same as in Fig. 8-4. 93

Fig. 8-7 Elemental ratio-ratio diagrams showing the magma mixing process in the Laiyuan magmatic rock. (a) SiO₂/MgO vs. Al₂O₃/MgO. (b) SiO₂/MgO vs. MgO/Al₂O₃. (c) Na₂O/CaO vs. Al₂O₃/CaO. (d) Sc/Ga vs. Sr/Sc displaying the calculated curves corresponding to magmatic evolution by simple mixing. The gabbro sample LY-12/1 (unpublished data, Sr=299.30 ppm, Sc=32.22 ppm, Ga=8.84 ppm) represents mafic end-member, and the monzogranite sample LY-21/2 (this study, Sr=608.40 ppm, Sc=2.08 ppm, Ga=18.85 ppm) represents the felsic end-member. Ticks on these curves represent 10% increments..... 95

Fig. 8-8 Variation diagrams for the Laiyuan magmatic rocks compiled from this study and previous literature. (a) Rb vs. Sr and (b) Ba vs. Sr diagrams showing modeling of fractional crystallization for the Laiyuan granitoids. (c), (d) Sr/Y vs. Y diagrams exhibiting the calculated curves of Rayleigh fractional crystallization modeling, and calculated curves of batch partial melting of the mafic lower crust of the NCC (Y=16.5 ppm and Sr/Y=21) with different restites after Ma et al. (2015), respectively. The detailed parameters and start compositions in the modeling are listed in Table 7-2. Fields of adakites and classical island andesite–dacite–rhyolite rocks are modified from Defant and Drummond (1990).

Abbreviation: ADR-normal arc andesite-dacite-rhyolite; Amp-amphibole; Bt-biotite; Cpx-clinopyroxene; Kfs-K-feldspar; Pl-plagioclase; Zrn-zircon. Data sources and legend are as same as in Fig. 8-4. 97

Fig. 9-1 Classification diagrams for minerals. (a) Enstatite-Ferrosilite-Wollastonite ternary diagram for pyroxene (Lindsley and Andersen, 1983). (b) Anorthite-Orthoclase-Albite ternary classification diagram for feldspar (Smith and Brown, 1974). (c) Mg/(Mg+Fe) vs. Si classification diagram for amphibole (Leake et al., 1997). (d) Mg/(Mg+Fe) vs. Σ Al classification plot for biotite (Barbarin, 1999)..... 104

Fig. 9-2 (a) TAS diagram for classification of the Laiyuan dykes (Middlemost, 1994). (b) K₂O vs. SiO₂ classification diagram (Peccerillo and Taylor, 1975). The fields of alkali lamprophyres and calc-alkali lamprophyres are modified after Rock (1987). (c) K₂O vs. Na₂O classification diagram. (d) Sr/Y-Y classification diagram for adakite (Defant and Drummond, 1990). Data sources: Wanganzhen pluton (Zhang et al., 2016); Taihang host granite and mafic enclaves (Chen et al., 2009b); Mapeng pluton (Li et al., 2015a); Wanganzhen volcanic rocks (Gao et al., 2012); Mujicun porphyries (Gao et al., 2013)..... 106

Fig. 9-3 Elemental variation diagrams for the Laiyuan dykes showing possible fractionating phases during magma evolution (Guo et al., 2004). 108

Fig. 9-4 Chondrite-normalized rare earth element (REE) distribution diagrams (a, c, e) and primitive mantle-normalized multi-element variation diagrams (b, d, f). Normalized values: chondrite (McDonough and Sun, 1995), primitive mantle (Sun and McDonough, 1989) and N-MORB and OIB (Sun and McDonough, 1989)..... 110

Fig. 9-5 Nb/U vs. Nb diagram for mafic dykes from the NCC. Data sources: dolerites and lamprophyres from western Shandong (Li et al., 2017); Low-Ti and high-Ti lamprophyres (Ma et al., 2014a), dolerites (Ma et al., 2016), other lamprophyres (Ma et al., 2014b) from Jiaodong area; MORB and OIB (Hofmann et al., 1986); Lower and upper crust (Rudnick and Gao, 2003). 113

Fig. 9-6 (a) Histogram and probability curves of age data from Early Cretaceous mafic dykes compiled from previous studies and this study in the NCC. (b) Histograms and probability curves of compiled $\varepsilon_{\text{Hf}}(t)$ data from Early Cretaceous mafic dykes compiled from previous studies and this study in the NCC, as well, histograms and probability curves of compiled $\varepsilon_{\text{Hf}}(t)$ data from Early Cretaceous eruptive and intrusive intermediate-felsic rocks compiled from previous studies in north Taihang Mountain. Data sources: Wanganzhen pluton (Zhang et al., 2016); Mapeng pluton (Li et al., 2015a); Laiyuan volcanic rocks (Gao et al., 2012); Chiwawu pluton (He and Santosh, 2014); Luxi mafic dykes (Li et al., 2017; Liu et al., 2008); Hebei mafic dykes (Liu et al., 2018); Taihang-Da Hinggan mafic dykes (Liu et al., 2017b); Jiaodong mafic dykes (Deng et al., 2017b; Guo et al., 2004; Liu et al., 2009b; Ma et al., 2014a; Ma et al., 2016; Tan et al., 2008; Yang et al., 2004)..... 115

Fig. 9-7 (a) Th/Yb vs. Nb/Yb (after Pearce, 2008), (b) (Hf/Sm)_N vs. (Ta/La)_N (La Flèche et al., 1998), (c) Rb/Sr vs. Ba/Rb, and (d) K/Yb vs. Dy/Yb diagrams for mafic dykes in the NCC. Melting curves for garnet lherzolite, spinel lherzolite, garnet-facies phlogopite lherzolite, garnet-facies amphibole lherzolite and spinel-facies amphibole lherzolite are after Duggen et al. (2005) and reference therein. Data sources are same with Fig. 9-5..... 118

Fig. 9-8 (a) Nb/La vs. La/Yb (Smith et al., 1999) and (b) TiO₂ vs. TFe₂O₃ diagrams for mafic dykes in the NCC. Data sources are same with Fig. 7-4. Fertile peridotite melts and refractory peridotite melts are defined by the study of experimental melts (after Falloon et al., 1988)..... 121

Fig. 10-1 (a) Tectonic map of the North China Craton and surrounding regions showing the metamorphic core complex (modified after Zhu et al., 2015a) and Early Cretaceous and Late Jurassic magmatic rocks (Zhang et al., 2014; Zhao et al., 2005). (b) Histogram of zircon U-Pb ages of Late Mesozoic igneous rocks in the NCC. (c) Projection of zircon U-Pb ages along the section A-B (in Fig. 10-1a) cross the NCC. The combinations of the zircon U-Pb ages are modified after Wu

et al. (2019) and reference therein. Metamorphic core complex: KQ-Kalaqing metamorphic core complex; WZ-Waziyu metamorphic core complex; LN-Liaonan metamorphic core complex; WF-Wanfu metamorphic core complex; YM-Yunmengshan metamorphic core complex; FS-Fangshan metamorphic core complex; HH-Hohhot metamorphic core complex. 125

Fig. 10-2 Tectonic discriminative diagrams for magmatic rocks from the Laiyuan complex. (a) Rb vs. Yb+Ta diagram (Pearce, 1984). (b) Th vs. Ta diagram (Pearce and Peate, 1995). (c) Th/Ta vs. Yb diagram (Pearce and Peate, 1995). (d) Nb/Zr vs. Zr diagram (Tarney and Jones, 1994). (e) Ti/100-Zr-Sr/2 ternary diagram (Pearce and Cann, 1973). Field abbreviations: syn-COLG, syn-collisional granitoids; VAG, volcanic arc granitoids; post-COLG, post-collisional granitoids; WPG, within plate granitoids; ORG, orogenic granitoids; VAB, volcanic arc basalt; WPB, within-plate basalt; MORB, mid-ocean ridge basalt; CAB, calc-alkali basalt; LKT, low-potassium tholeiite; OFB, ocean-floor basalt. Data sources are same as in Fig. 8-4 and Fig. 7-2. ... 128

Fig. 10-3 The North China Craton and its adjacent plates in the Paleozoic to Mesozoic (modified after Windley et al., 2010). 130

Fig. 10-4 (a) Tomographic images to show the velocity structures of the present mantle transition zone of the NCC (modified after Huang and Zhao, 2006). (b) The schematic lithospheric structure of the current NCC from the eastern Jiaodong Peninsula through the central Taihang Mountain (not to scale) to the western Ordos Basin revealing the lithosphere heterogeneity beneath the NCC (modified after Liu et al., 2019). 132

Fig. 10-5 Schematic plate tectonic model to explain the lithospheric destruction of the North China Craton during Early Cretaceous through thermal-mechanical erosion and lithospheric delamination. Detailed discussions are in the text. AMDR, asthenospheric mantle-derived rocks; CC, continental crust; ELM, enriched lithospheric mantle; HMA, high-Mg adakites; LM, lithospheric mantle; LMDR, lithospheric mantle-derived rocks; TLC, thickened lower crust. 135

List of Tables

Table 1-1 Details of completed research works of this study	11
Table 3-1 Summary of locations, rock types and mineralogy of samples analyzed in this study. Mineral abbreviations are same as in Fig. 3-5.....	20
Table 5-1 LA-MC-ICPMS zircon U-Pb data of the Laiyuan volcanic rocks analyzed in this study.....	169
Table 5-2 LA-MC-ICPMS zircon U-Pb data of the Laiyuan granitoids analyzed in this study.....	174
Table 5-3 LA-MC-ICPMS zircon U-Pb data of the Laiyuan dyke suites analyzed in this study.....	181
Table 5-4 Compilation of age data of the Laiyuan magmatic rocks.....	55
Table 6-1 Zircon in-situ Lu-Hf isotopic analytical results of the Laiyuan magmatic rocks in this study.	194
Table 7-1 Major and trace elemental data of the Laiyuan volcanic rocks analyzed in this study.....	202
Table 7-2 Starting compositions and partition coefficients used in the geochemical modeling. Mineral abbreviation: Amp-amphibole; Cpx-clinopyroxene; Ol-olivine; Pl-plagioclase; Sph-Sphene; Zrn-zircon.....	74
Table 9-1 EPMA data of clinopyroxene.....	209
Table 9-2 EPMA data of feldspar.....	212
Table 9-3 EPMA data of amphibole.....	215
Table 9-4 EPMA data of biotite.....	217
Table 9-5 Major and trace elemental data of the Laiyuan dyke suites analyzed in this study.....	218

Chapter 1 Introduction

1.1 Research background and controversies

The processes associated with magmatism play important roles in the material differentiation of the Earth and the lithosphere (Rudnick, 1995). The course of magma from its source to ascent and emplacement usually involves several petrogenetic processes such as partial melting of the source, assimilation and fractional crystallization, and magma mixing and mingling, which eventually contribute to the formation of an igneous complex with compositional diversities (Annen et al., 2006; Spera and Bohron, 2001). Igneous complexes or batholiths with variable rock types have attracted significant attention, providing critical petrological implications for petrogenesis, tectonic setting, crustal structure, and lithospheric evolution. In the North China Craton (NCC), during Mesozoic, extensive magmatism occurred and formed lots of magmatic complexes offering the window to investigate the NCC destruction phenomenon.

The term “craton” is generally defined as a stable tectonic domain which formed through long geological time (Fig. 1-1), and examples include Siberia (Boyd et al., 1997) and Indian cratons (Pearson et al., 1995). Based on modern research on deep mantle xenoliths, the typical thickness of a cratonic lithosphere is estimated as ~200 km with a heat flow of ~40 mW/m² (Lee et al., 2011). In other words, the cratonic roots are so rigid, cold, and buoyant that could enable the overlying crust to resist extensive magmatism and crustal deformation except for minor eruptions of anorogenic and deep mantle-derived carbonatite, kimberlite, and related igneous rocks (Hawkesworth et al., 2017; Lee et al., 2011). This common fate of the cratonic lithosphere has been reviewed by many researchers (Arndt et al., 2009; Hawkesworth et al., 2017; Lee et al., 2011; Pearson et al., 1995; Scott et al., 2019). However, the NCC shows distinct features of destruction after its formation. The NCC is one of the oldest cratons globally with a long evolutionary history during the Precambrian (Zhai

and Santosh, 2011). Following its final cratonization during the late Paleoproterozoic, like other cratons, the NCC remained quiescent for a long time until Mesozoic, when voluminous magmatism (Zhang et al., 2014), associated metallogeny generating some of the world-class deposits (Cai et al., 2018; Groves and Santosh, 2016; Li and Santosh, 2017), and basin sedimentation (Li et al., 2012) in the eastern and central occurred referred to as craton destruction or decratonization (Zhu et al., 2011). Detailed geological and geophysical researches have proved that more than 100 km of the ancient refractory lithospheric mantle has been eroded and replaced by young and fertile mantle materials beneath the eastern portion of the NCC since Mesozoic (Gao et al., 2002; Liu et al., 2019; Liu et al., 2017a; Wu et al., 2019).

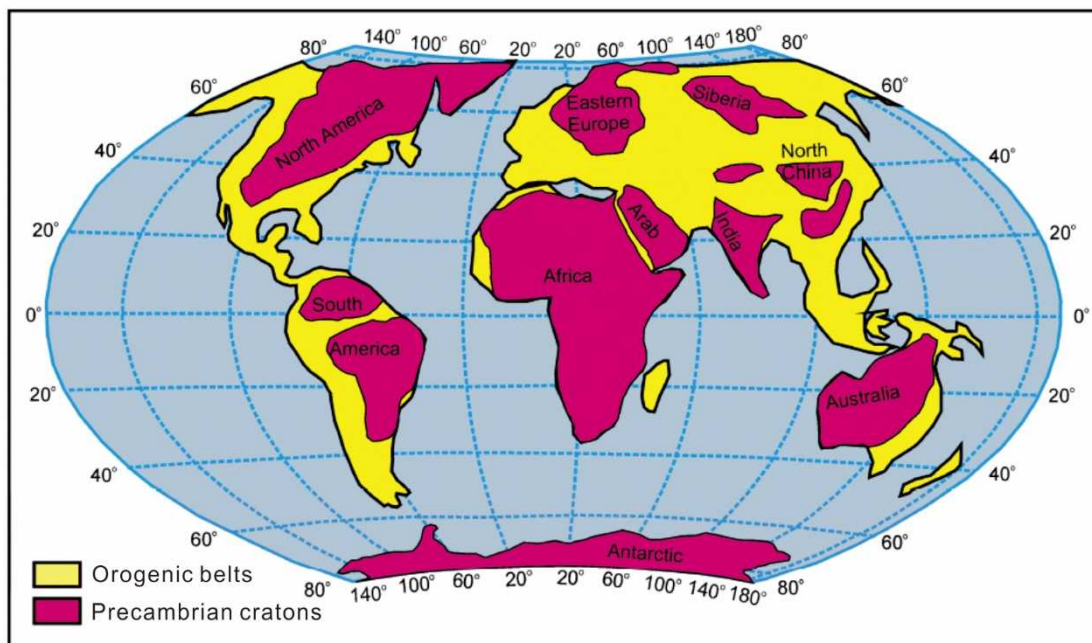


Fig. 1-1 Distribution of Precambrian cratons on the Earth (modified after Zhu et al., 2011).

Several mechanisms have been proposed to interpret how the lithospheric root was replaced, and two most popular models are continental delamination (Gao et al., 2004) and chemical-mechanical erosion (Xu, 2001). These two models have been used to interpret the intense magmatism and mineralization in the eastern NCC and its northern margins. However, the central NCC (craton interior) also witnessed extensive magmatism, especially in the Taihang Mountains (TM) forming diverse

plutons or igneous complexes. Whether these magmatic suites were products of the craton destruction process and whether the lithosphere beneath the TM had a similar evolutionary process with the lithosphere in the eastern NCC are still debated. As indicated by the geophysical data (Fig. 1-2) the thickness of the lithosphere in the Jiaodong Peninsula is 60-100 km, whereas it is thicker (100-150 km thick) in the TM (Liu et al., 2019; Zhu et al., 2011). All these features suggest that the lithosphere beneath the central NCC has different lithospheric structures and lithospheric evolution from those of the eastern NCC. The northern Taihang Mountains (NTM) area is precisely also the border between the eastern and central NCC, marking the transitional zone of the two domains with different lithospheric evolutionary processes and destruction mechanisms. Thus, by studying a magmatic complex from the NTM in the spatial-temporal-petrogenetic-tectonic aspects, the craton destruction and lithospheric evolution throughout the NCC could be well understood. Furthermore, because the Laiyuan magmatic complex is composed of various magmatic rocks including mafic-ultramafic intrusive suites, intermediate-felsic intrusions, volcanic rocks, and dyke suites acting as the perfect object to study the relationship between the magmatic evolution and compositional heterogeneity, it was selected to investigate the Mesozoic magmatism, lithospheric evolution, and lithospheric destruction in the NCC.

1.2 Research progress

1.2.1 The NCC destruction

Although the craton destruction and thinning of the NCC has been identified in several previous studies (Fan, 1992; Gao et al., 2002; Griffin et al., 1998; Liu et al., 2019; Menzies et al., 2007; Wu et al., 2005; Wu et al., 2008; Wu et al., 2019; Xu, 2001; Zhang et al., 2014; Zheng et al., 2001; Zhu et al., 2011), temporal-spatial distribution, mechanism, and geodynamic trigger of these processes are still debated. A brief introduction to the research progress of the NCC destruction is summarized below.

1.2.1.1 Lithospheric modification, lithospheric thinning and craton destruction

The lithospheric thinning and craton destruction are the most common terms when discussing craton destruction, and the relationship between these is also of key significance (Wu et al., 2014). Therefore, it is necessary to clarify the concepts of lithospheric thinning and craton destruction.

Lithospheric thinning describes only the change in the lithosphere thickness of a geological unit, which does not imply any mechanism involved. Previous studies have shown that lithospheric thinning occurred in most areas of the Earth in geological history and, in particular, is more common in orogenic belts (Krystopowicz and Currie, 2013). Most cratons existing on the Earth (e.g., Siberia, North America, South America, and Australia) have been subjected to significant lithospheric thinning, especially the Dharwar Craton in which the lithosphere has been thinned from ~200 km at 1.1 Ga to less than 100 km at present (Griffin et al., 2009; Karmalkar et al., 2009). The lithospheric thinning has been recognized in the NCC for a long time, starting from the studies on mantle xenoliths and mineral inclusion in diamond trapped by the Paleozoic kimberlite in Mengying and Fuxian areas (Fan, 1992; Griffin et al., 1998). It is estimated that the lithosphere of the NCC had a thickness of more than 200 km during the Precambrian. Constraints from mantle xenoliths entrained in the Cenozoic basalts, however, reveal that the Cenozoic lithosphere of the NCC has a thickness less than 80 km, which is also consistent with the geophysical data (Chen et al., 2006). Thus, the above discussions indicate that lithospheric thinning is not unique for the NCC but common for all cratons globally.

In general, craton destruction is referred to as the phenomenon by which a craton loses its stability (Wu et al., 2008), which could also be termed decratonization or destabilization (Yang et al., 2009). As implied by its definition, a destroyed or destructed craton does not share any characteristics of stable cratons unless it has been reocratonized later. The geologic indicator of craton stabilization is that its sedimentary cover preserves its original horizontal status (Wu et al., 2019). During the Mesozoic, the NCC experienced intensive thrust and extensional deformation accompanied by

the exhumation of deep crust, volcanic eruptions, basin filling, granitic intrusions, and related gold mineralization, hence lost its stability (Cai et al., 2018; Li and Santosh, 2017; Wang and Mo, 1995; Wu et al., 2019). From this perspective, craton destruction is like mantle replacement (Zheng, 1999), lithospheric transformation, and metacratonization (Liégeois et al., 2013). As can be seen from these definitions, craton destruction is not equal to lithosphere thinning, and there is no relationship between each other. A detailed investigation on global cratons of India, Siberia, and Brazil indicates (Wu et al., 2014; Wu et al., 2019) that lithospheric thinning is very common during the evolution of craton rather than occurred uniquely in the NCC. Unlike the NCC, lithosphere thinning in these cratons was not accompanied by craton destruction. Specifically, craton destruction can be accompanied by lithospheric thinning, whereas the occurrence of lithosphere thinning does not certainly cause craton destruction.

In addition to the destruction, lithospheric modification is another important factor in mantle petrology/geochemistry related to craton destruction (Wu et al., 2019). Some degree of modification is ubiquitous for every craton, including lateral subduction and vertical upwelling of anomalously hot plume magmas and fluids from the deep (Ernst and Buchan, 2003). Such processes result in various kinds/extents of mantle metasomatism, hydration, and fertilization. Lithospheric modification can accelerate or act as the prerequisite condition for lithospheric thinning and even craton destruction by modifying the rheological characteristics of the lithosphere. The lithospheric modification is common throughout the whole NCC including the eastern, central, and western portions (Wang et al., 2020; Xia et al., 2017).

1.2.1.2 The temporal-spatial distribution of the NCC destruction

The timing of the NCC destruction is the first step to understand the processes and mechanisms involved in the destruction of a stable craton and also has an important bearing on the evolution of continents (Zhu et al., 2012). However, the timing of destruction remains debated, i.e., Late Triassic (Yang et al., 2010), Late Jurassic (Gao et al., 2004), Early Cretaceous (Liu et al., 2019; Wu et al., 2019; Xue et

al., 2019a; Xue et al., 2018), and long term from Late Carboniferous to Early Cenozoic (Windley et al., 2010; Xu et al., 2009a). Based on the detailed summary of the studies of mantle xenoliths, mantle metasomatism, mantle-derived melts, intermediate-felsic igneous rocks, and geophysical data from the NCC, Liu et al. (2019) connected the destruction to the slab roll-back of the Paleo-Pacific Plate and thus constrained the timing of the destruction to Early Cretaceous which is consistent with the time when asthenospheric mantle-derived high-Ti lamprophyres and lithospheric mantle-derived low-Ti were intruded simultaneously at ca. 121 Ma (Ma et al., 2014a). Another important point of view assumes that the NCC destruction lasted for a long-term, initiating from Late Carboniferous, peaking at Early Cretaceous, and terminating at Cenozoic (Xu et al., 2009a). Even though the initiation and termination times are still debated, most researchers have reached a consensus that the NCC destruction reached its peak at Early Cretaceous with the explosive formation of voluminous magmatic rocks and metallic mineral deposits.

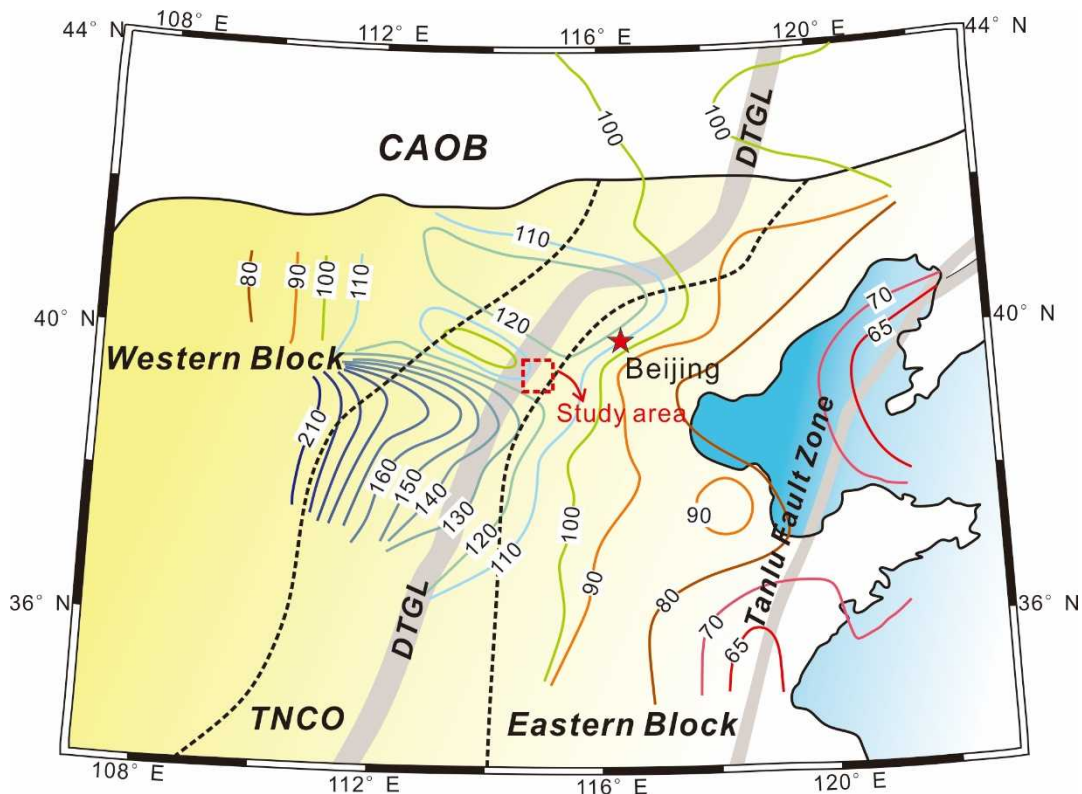


Fig. 1-2 The distribution of lithospheric thickness beneath the North China Craton (after Zhu et al., 2011). Abbreviation: TNCO- Trans-North China Orogen; CAOB- Central Asian Orogenic Belt.

Detailed knowledge on the geographical scope of the NCC destruction is crucial for a better understanding of the deep dynamics and mechanism of this process (Zhu et al., 2011). Such knowledge mainly comes from studies of the Paleozoic kimberlites and Mesozoic-Cenozoic basalts and their mantle xenoliths throughout the NCC. However, the rare exposures of mantle xenoliths and igneous rocks limited the studies of the lithosphere, especially for basins and vegetation-covered areas in the craton interior. In recent years, the rapid expansion of large-scale temporary seismic arrays and the consequent data renaissance in the NCC enabled the detailed study of the crustal and lithospheric structure (Chen et al., 2009a). A combination of petrological and geophysical clues shows that the craton destruction mostly happened in the eastern NCC, resulting in the root removal and intact replacement of the ancient lithospheric mantle beneath the eastern NCC (Chen et al., 2009a; Liu et al., 2019; Liu et al., 2017a; Wu et al., 2014; Wu et al., 2019). In addition, it is particularly worth noting that near the boundary between the eastern and central NCC, a rapid thickness variation of both crust and lithosphere occurs, indicating the distinct lithospheric structure and evolution beneath the central NCC (Taihang Mountains) from the eastern NCC (Zhu et al., 2011). The next focus of the NCC destruction should be the variation of the destruction extent by comparing the eastern, central, and western NCC.

1.2.1.3 Mechanism of the NCC destruction

Current discussions about the mechanism for destruction of the NCC are focused on how the lithospheric root was lost and on the tectonic triggers for this destruction (Wu et al., 2019). To interpret how the craton destruction happened, diverse models have been presented, including continental delamination (Gao et al., 2002; Gao et al., 2004; Wu et al., 2019), thermal-mechanical-chemical erosion (Menzies et al., 2007; Xu, 2001), peridotite-melt interaction (Zhang et al., 2003a), and lithospheric mantle hydration (Niu, 2005). Among these models, the prolonged thermal-chemical-mechanical erosion of lithosphere lasting at least 100 Ma, and rapid lithospheric delamination over a short period of ~10 Ma, has received much attention.

The thermal-chemical-mechanical erosion model highlights the critical role of upwelling of hot asthenosphere's weakening, softening, and eroding the bottom of the lithospheric mantle, which was supported by the long-term Mesozoic mantle-derived magmatism (Xu et al., 2009a). On the other hand, the delamination model assumed that the thickened mafic lower crust transformed to eclogites with high density and then foundered into the asthenosphere with the underlying lithospheric mantle causing the interaction among lower crust, lithospheric mantle, and asthenosphere (Gao et al., 2004). The petrogenesis of high-Mg adakites in Liaoxi (Gao et al., 2004) and Sulu-Dabie areas (Xu et al., 2008) could be well interpreted using this delamination hypothesis. Although the various theories attempt to explain the significant changes in the structure and composition of the mantle beneath the NCC, several controversies remain unresolved, such as the dominant mechanism controlling the craton destruction in the central NCC.

1.2.1.4 Dynamic trigger for the NCC destruction

The India-Eurasian collision (Menzies et al., 2007), Yangtze-NCC collision (Xu et al., 2008), plume activity (Wilde et al., 2003), and subduction of Paleo-Pacific Plate (Zheng et al., 2007a) are some possible tectonic triggers for the NCC destruction. Recently, more and more studies strengthen the significant role of the subduction of the Paleo-Pacific Plate in the NCC destruction (Liu et al., 2019; Wang et al., 2020; Wu et al., 2019; Xue et al., 2020). Zhu et al. (2012) reviewed the tectonothermal events (especially magmatism and tectonism) of the NCC since Ordovician, and summarized that the southward subduction and subsequent closure of the Paleo-Asian ocean, together with the assembly of the NCC and Yangtze cratons, just modified the NCC in limited areas from Late Carboniferous to Jurassic, whereas the Paleo-Pacific Plate subduction triggered the NCC destruction related to lithospheric removal or replacement during Early Cretaceous.

1.2.2 Heterogeneity in the magmatic complex

The giant igneous complexes comprising various types of magmatic rocks are important targets to investigate the magmatic differentiation contributing to the

compositional variations from mafic to felsic. To interpret the heterogeneity in the magmatic complex, several mechanisms have been proposed, such as aggregation of multiple pulses of magmas from partial melting, fractional crystallization of magma, magma mixing and mingling, assimilation and contamination of surrounding rocks, and liquid immiscibility (Zhu et al., 2012). Magma mixing, assimilation and contamination, and liquid immiscibility may be possible to generate stock-scale to enclave-scale intrusions but could not have the power to cause a pluton-scale intrusion with compositional variations (Wu et al., 2017). In contrast, partial melting and crystal fractionation are the main mechanisms to devote to the differentiation of granite (Gao et al., 2016). Partial melting means that the different portions of various types in the granitoid complex were directly crystallized from incremental batches of the magma (Glazner et al., 2004; Walker Jr et al., 2007; Žák and Paterson, 2005). Crystal fractionation means that different types of rocks were sourced from the same batch of magma by crystal separation and were crystallized in the magma chamber at different periods (Bateman and Chappell, 1979; Pitcher, 1997; Wilson, 1993). Therefore, the compositional characteristics of rocks generated by fractional crystallization do not necessarily equate to the source features, but it could reveal much physicochemical condition of the magma and its variation during crystallization (Xu et al., 2019). In the case of the Tuolumne magmatic complex in Sierra Nevada, the origin of the composition variations of the variable magmatic suites has transformed from traditional point of in-situ fractional crystallization (Bateman and Chappell, 1979) to prolonged partial melting of the sources at different periods (Coleman et al., 2004).

1.2.3 Research progress and remaining questions in the study area

The TM is located at the boundary between the eastern and central NCC, and mark the westernmost region of the Mesozoic magmatism with a length of ~700 km from the north to the south and a width of 50-100 km from the east to the west, connecting the southern Qinling-Dabie orogenic belt and northern Yanshan fold and thrust belt. The TM could be divided into two domains, the southern Taihang

Mountains (STM) and the NTM. There are voluminous magmatic suites distributed in this magmatic belt which could provide abundant clues on the petrogenesis for magmatism in the central NCC. Although there were many studies concentrated on the magmatism and related mineralization in the STM (Chen et al., 2004; Chen et al., 2008; Li et al., 2019a; Zhang et al., 2011; Zhang et al., 2015) and NTM (Chen et al., 2009b; Li et al., 2013a; Xue et al., 2019b), the petrogenesis and tectonic setting of magmatic rocks in this area during Mesozoic are still debated. Some researchers favored the concept that the granitoids with adakitic affinity were formed by partial melting of the thickened mafic lower crust (Cai et al., 2003; He and Santosh, 2014; Zhang et al., 2016), whereas others highlighted the dominant role of fractional crystallization of magmas sourced from partial melting of the ancient enriched lithospheric mantle on the formation of variable magmatic suites (Gao et al., 2012; Hou et al., 2015; Li et al., 2019a). In addition, magma mixing and mingling process between mantle-derived basaltic magmas and siliceous crustal melts was also thought to be the possible petrogenesis for granitoids with adakitic feature (Chen et al., 2013). Another remaining question is the relationship between the Mesozoic magmatism in the TM and the subduction of Paleo-Pacific Plate: the direct impact (Chen et al., 2005) or the far-field effect (Yang et al., 2020) exerted by the slab subduction.

It is thus essential to study the magmatic complex on the whole, to conduct the precise petrological studies on variable magmatic suites, and to reconstruct the evolutionary process of the magmas according to the temporal series or lithologic sequence. Previous studies on the Laiyuan complex just focus on the single magmatic units and lack the concentrations on the genetic relationships between different magmatic units leading to the unilateral recognition of the magmatic evolution, petrogenesis, and tectonic setting. It should be noted that the formation of a voluminous complex with compositional variations cannot be generated by a single genesis, and it must involve multiple interactions among crust, lithospheric mantle, and/or asthenospheric mantle and various sources involved in the magmas' evolution.

1.3 Objectives of this study

In this study, in order to address the existing controversies and debates in the central NCC, the Laiyuan complex was chosen as the research area. It is a typical volcano-intrusive complex in the NTM with the largest exposure areas, and it comprises various rock types. Multidisciplinary investigations were carried out including field studies, petrology, mineral chemistry, whole-rock geochemistry, zircon U-Pb geochronology, zircon Hf isotopes, and geochemical modeling on different rock types from the Laiyuan complex, with several research objectives as summarized below:

(1) Detailed field and petrographic studies: to clarify the rock types, mineral compositions, paragenetic order, and field relationship between various magmatic suites.

(2) Systematic geochronology studies: based on zircon dating results with available data from related literatures, to constrain the geochronological framework of magmatism; to investigate the geochronological implications on the NCC destruction.

(3) Systematic petrogenetic interpretations: based on mineral chemistry, whole-rock geochemistry, geochemical modeling, and zircon Lu-Hf isotopes with available data from related literatures, to investigate the multiple sources and genesis of the dyke suites, volcanic rocks, and granitoid rocks; to establish an integrated petrogenetic model for the Laiyuan complex.

(4) Tectonic implications: based on mineral chemistry, whole-rock chemistry, zircon U-Pb geochronology, and Lu-Hf isotopes with available data from related literatures, to discuss the tectonic setting in the study area during Mesozoic; to investigate the lithospheric evolution in the central NCC during Mesozoic; to explore the mechanism and dynamic trigger for the NCC destruction.

Based on the above research objectives, detailed field investigations and systematic analytical works were carried out, and the completed research works are shown in [Table 1-1](#).

Table 1-1 Details of completed research works of this study.

No.	Research details	Contents	Participants
1	Field investigation	15 days	Fei Xue, M. Santosh, Fan Yang
2	Sample collection	50	Fei Xue, M. Santosh, Fan Yang
3	Field photographs	Over 300	Fei Xue, M. Santosh, Fan Yang
4	Thin sections	60	Fei Xue, Peking University
5	Photomicrographs	Over 400	Fei Xue
6	Zircon separate, U-Pb dating	19	Fei Xue, Shan-Shan Li, Yue-Sheng Han,
7	Zircon Lu-Hf isotopes	15	Fei Xue, Shan-Shan Li, Yue-Sheng Han,
8	EMPA	150	Fei Xue, Toshiaki Tsunogae, Sam Uthmp
9	Whole rock geochemistry	41	Fei Xue
10	Literature reading	Over 400	Fei Xue

Chapter 2 Regional geology

2.1 North China Craton

The NCC is one of the oldest cratons in the world (Zhai and Santosh, 2011) and the main component of Chinese continental collage (Fig. 2-1a) containing Eoarchean rocks as old as 3.8 Ga (Liu et al., 1992). With an area of ~1.5 million km², the NCC is bound by the Central Asian Orogenic Belt to the north, Su-Lu Orogen to the east, Qilianshan Orogen to the west, and Triassic Qinling-Dabie Orogenic Belt to the south (Fig. 2-1a). The NCC has been divided into three major tectonic units (Zhao et al., 2005): the Western Block, the Eastern Block, and the Trans-North China Orogen (TNCO) (Fig. 2-1b) that marks the collisional belt between the Western and Eastern Blocks which amalgamated during late Paleoproterozoic at ~1.85 Ga (Kröner et al., 2005; Tang and Santosh, 2018; Zhao et al., 2006). The Western Block is considered to have formed by a prolonged subduction-accretion-collision history of the Yinshan Block and the Ordos Block, eventually leading to the formation of the Inner Mongolia Suture Zone during Paleoproterozoic (Santosh, 2010). A ‘double-sided’ subduction model has been proposed between the Yinshan and Ordos Blocks to form the unified Western Block, and its assembly with the Eastern Block during the final phase of cratonization of the NCC and its incorporation of the craton within the Paleoproterozoic Columbia supercontinent (Santosh, 2010).

The TNCO is a nearly north-south-trending orogen across the central part of the NCC. As shown in Fig. 2-1b, this Paleoproterozoic collisional orogen incorporates several fragments of basement terranes which include the Chengde, Northern Hebei, Xuanhua, Huai’an, Hengshan, Wutai, Fuping, Lüliang, Zanhuang, Zhongtiao, Dengfeng, and Taihua Complexes from the north to the south (Wei et al., 2014). The basement rocks comprise Neoproterozoic to Paleoproterozoic tonalite-trondhjemite-granodiorite (TTG) gneisses, meta-supracrustal rocks, syn- to post-tectonic granitoids, mafic dykes, and ultramafic to mafic rocks. A detailed

overview of the geological and tectonic history of the TNCO has been presented by [Tang and Santosh \(2018\)](#). The present study area is located in the Fuping area in the NTM, along the eastern part of the TNCO ([Fig. 2-2](#)).

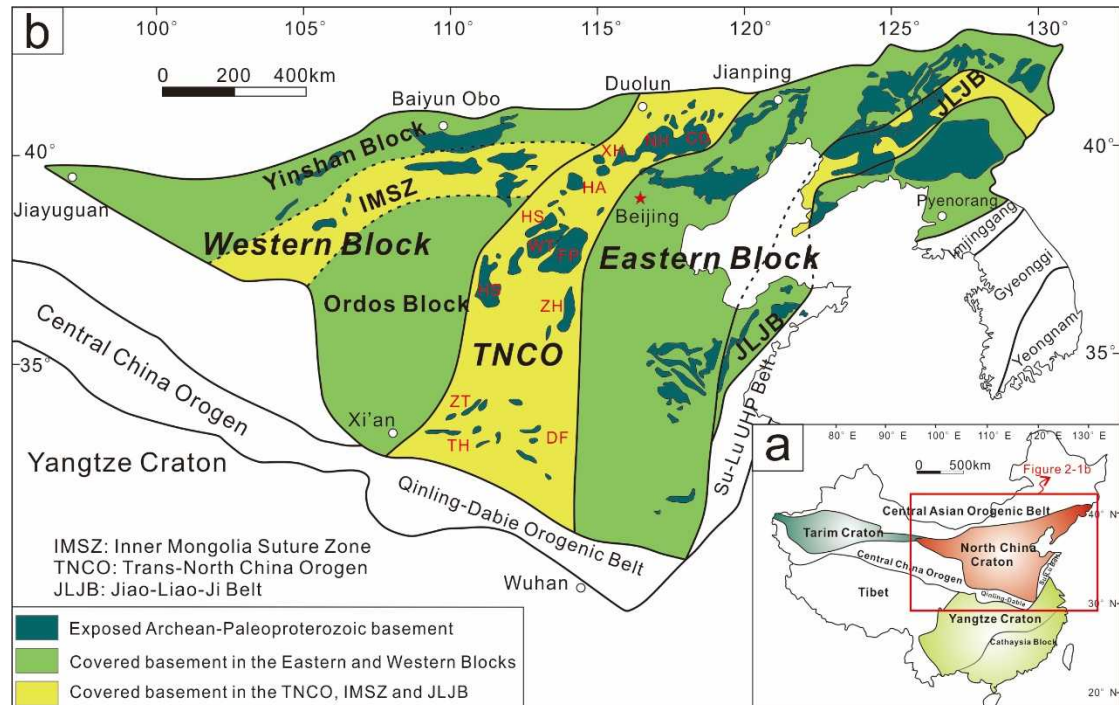


Fig. 2-1 (a) Major tectonic units of China. (b) Tectonic subdivision of the North China Craton (modified after [Zhao et al., 2005](#)). Abbreviations of metamorphic complexes: CD, Chengde; NH, Northern Hebei; XH, Xuanhua; HA, Huai'an; HS, Hengshan; WT, Wutai; FP, Fuping; LL, Lüliang; ZH, Zanhuang; ZT, Zhongtiao; DF, Dengfeng; TH, Taihua.

2.2 Northern Taihang Mountains

2.2.1 Regional strata

The major exposed strata in the area belong to the Archean basement metamorphic rocks, Proterozoic sedimentary sequences, Paleozoic sedimentary cover rocks, Mesozoic volcanic and volcanoclastic rocks, and Cenozoic sediments ([Fig. 2-3a](#)).

The Archean basement rocks are dominantly the Fuping Group represented by high-grade metamorphic rocks including TTG gneisses, amphibolite, marble, and magnetite-quartzite with metamorphic ages in the range of 2.5–2.7 Ga ([Liu et al.,](#)

1984). These basement rocks are unconformably covered by Proterozoic sedimentary sequences including a thick succession of ca. 1400 Ma dolomite (the Gaoyuzhuan Formation), streaky chert dolomite (including the Hongshuizhuan Formation, Tieling Formation and Wumishan Formation), sandy mudstone, shale, and quartz sandstone (including the Xiamaling Formation, Longshan Formation and Jingeryu Formation). Unconformably covering the Paleoproterozoic sequences, the overlying Cambrian-Ordovician strata are dominantly composed of marine limestone, bioclastic limestone, and oolitic limestone (Dong et al., 2013). The Mesozoic strata are represented by a sequence of volcano-sedimentary rocks of andesite and andesitic breccia belonging to the Tiaojishan Formation, rhyolite, and rhyolitic breccia and tuff which have been dated as Jurassic to Cretaceous (Duan et al., 2016; Gao et al., 2012) unconformably underlying the Paleozoic sedimentary rocks. The above successions were intruded by extensive Mesozoic batholiths and stocks (Fig. 2-3a).

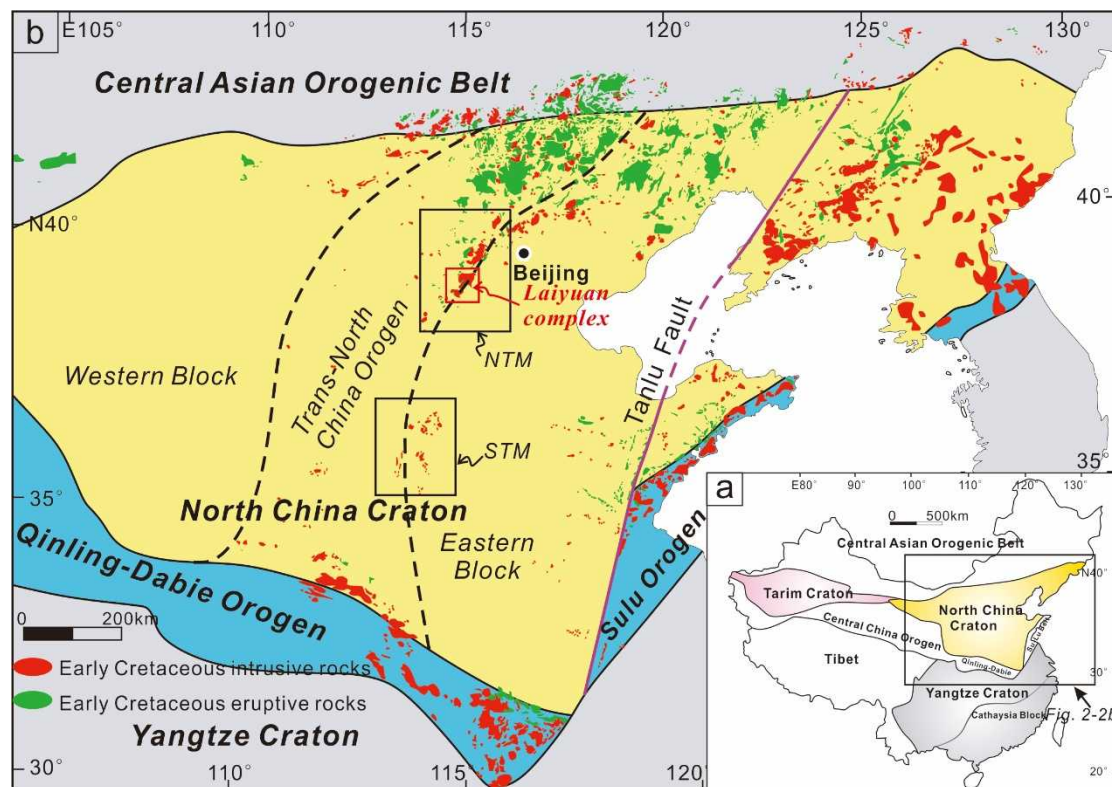


Fig. 2-2 (a) Major tectonic units of China. (b) Tectonic map of the NCC showing the distributions of Early Cretaceous magmatic rocks (modified after Zhang et al., 2014; Zhao et al., 2005).

2.2.2 Regional structures

The NTM has experienced multiple tectonic activities including Archean EW trending folds, and Mesozoic NNE trending regional faults and folds. The EW axial trending Fuping anticlinorium was developed in the Archean basement rocks with the metamorphic rocks of the Fuping Group in the core and Proterozoic to Paleozoic sedimentary rocks in the limbs. Furthermore, the Mesozoic folds show characteristics of NE-NEE axial trending and wide-shaped superimposed on the earlier Fuping folds. The major controlling structures in the NTM are the Mesozoic Zijingguan and Wulonggou faults (Fig. 2-3b). These NNE-trending regional faults cut across the Precambrian basement and Paleozoic strata, and form part of the NE–SW-trending Daxin'anling–Taihangshan gravity lineament, considered as the lithospheric boundary between the TNCO and the Eastern Block (Niu, 2005). The NEE-trending framework controls the distribution of large plutons and extrusive rocks in this area (Fig. 2-3b).

2.2.3 Magmatism

As discussed above, the TM witnessed extensive magmatism occurred since late Mesozoic, generating voluminous eruption of intermediate-felsic volcanic rocks, and large granitoid batholiths and plutons which are distributed in the NTM and the STM (Fig. 2-2). The NTM hosts plutons and stocks including the Yunwushan, Dahaituo, Sihai, Dahenan, Wanganzhen and Sigezhuang (Laiyuan magmatic complex), Chiwawu, and Mapeng plutons (Fig. 2-3b). Meanwhile, the Kuangshan, Cishan, Fushan, Hongshan, Huanglongnao and Wu'an plutons/stocks were distributed in the STM (Fig. 2-3a). The intrusive rocks in the NTM are characterized by intermediate-felsic granitic rocks represented by monzogranite, syenogranite, quartz monzonite, and monzonite (He and Santosh, 2014; Li et al., 2013a; Zhang et al., 2016), whereas the intrusive rocks in the STM are dominantly mafic-intermediate rocks including gabbroic diorite, diorite, diorite porphyry, monzodiorite, monzonite, and syenite (Chen et al., 2008; Zhang et al., 2015). In the NTM, the Laiyuan magmatic complex comprising the Wanganzhen and Sigezhuang plutons (Fig. 2-3b) is the most representative intrusion which incorporates several magmatic suites consisting of voluminous granitoid plutons, sporadic extrusive volcanic lava, small

ultramafic-mafic intrusive bodies, and mafic-felsic dykes. The detailed discussion about the petrology of this complex and geochronological framework of the magmatic rocks in the NTM will be discussed in the following sections.

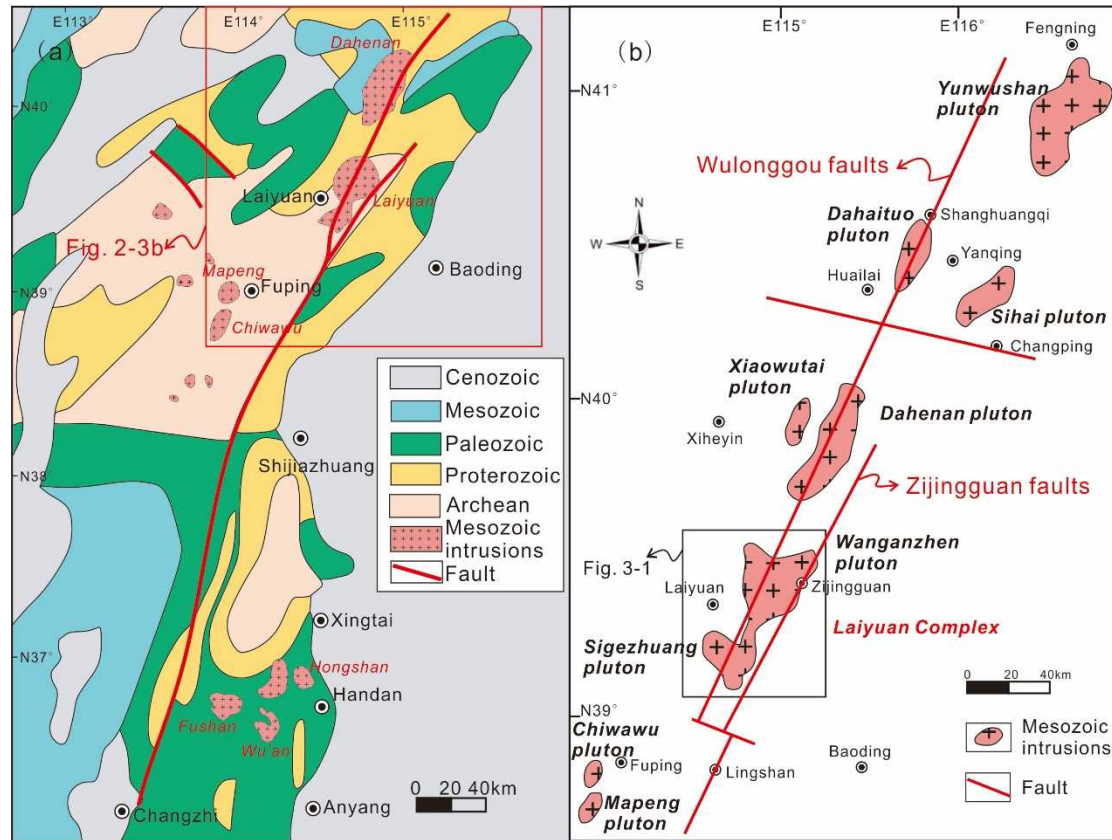


Fig. 2-3 (a) Sketch geological map of the Taihang Mountains (after Li et al., 2013b). (b) Simplified geological map showing the distributions of Mesozoic intrusions in the NTM.

2.3 Laiyuan magmatic complex

The Laiyuan complex is the largest volcano-plutonic complex in the NTM with a NEE-trending dumbbell shape and a total outcrop area of over 1000 km². The complex has been divided into two domains: the northern Wanganzhen pluton and the southern Sigezhuang pluton with a multi-stage magmatic history of at least three distinct phases (Cai et al., 2003) leading to a multiple ringed structure from the periphery to the core (Fig. 3-1).

The earliest intrusive magmatism contributed to the formation of small ultramafic-mafic intrusions along the margin of the complex, as represented by the

intrusions of Yaogou and Longmengou. [Hou et al. \(2015\)](#) reported a ^{40}Ar - ^{39}Ar age of 154.2 ± 4.5 Ma from the Yaogou hornblendite. The sporadically distributed extrusive rocks in the Wanganzhen pluton belonging to the Tiaojishan Formation represent the next phase, and are mainly composed of andesites which were dated at Late Jurassic ([Duan et al., 2016](#); [Gao et al., 2012](#)). The next phase of intermediate-felsic intrusive rocks occupied most of the Laiyuan complex comprising variable rock types ([Fig. 2-4](#)). Several sub-units have also been proposed with variations in lithology and composition from core to rim ([Dong et al., 2013](#)). Previous geochronological studies on the Wanganzhen pluton reported ages from quartz diorite (128.3 ± 1.9 Ma; [Zhang et al., 2016](#)), granodiorite (135.7 ± 1.3 Ma; [Shen et al., 2015a](#)), monzogranite (133.7 ± 1.1 Ma; [Shen et al., 2015a](#)), and porphyritic granite (132.1 ± 0.6 Ma; [Shen et al., 2015a](#)). The latest magmatic pulse of the Wanganzhen pluton occurred between 126 to 135 Ma during the Early Cretaceous. Furthermore, several dyke suites of various compositions intruded the different host rocks. These previous studies of the Laiyuan complex only concentrated on the Wanganzhen pluton lacking detailed geochronological and petrological researches on the Sigezhuang pluton. In this study, combining available data from literatures, systematic sampling and studying have been conducted in the Laiyuan magmatic complex especially focusing on the diverse magmatic rocks from the Sigezhuang pluton.

Chapter 3 Field observation and petrographic characteristics

Integrated fieldwork was conducted in the Laiyuan complex with collection of representative samples from different magmatic suites. The salient petrological features are listed in Table 3-1. According to their field and petrographical characteristics, these rocks could be classified as three major types: volcanic rocks, granitoids, and dyke suites.

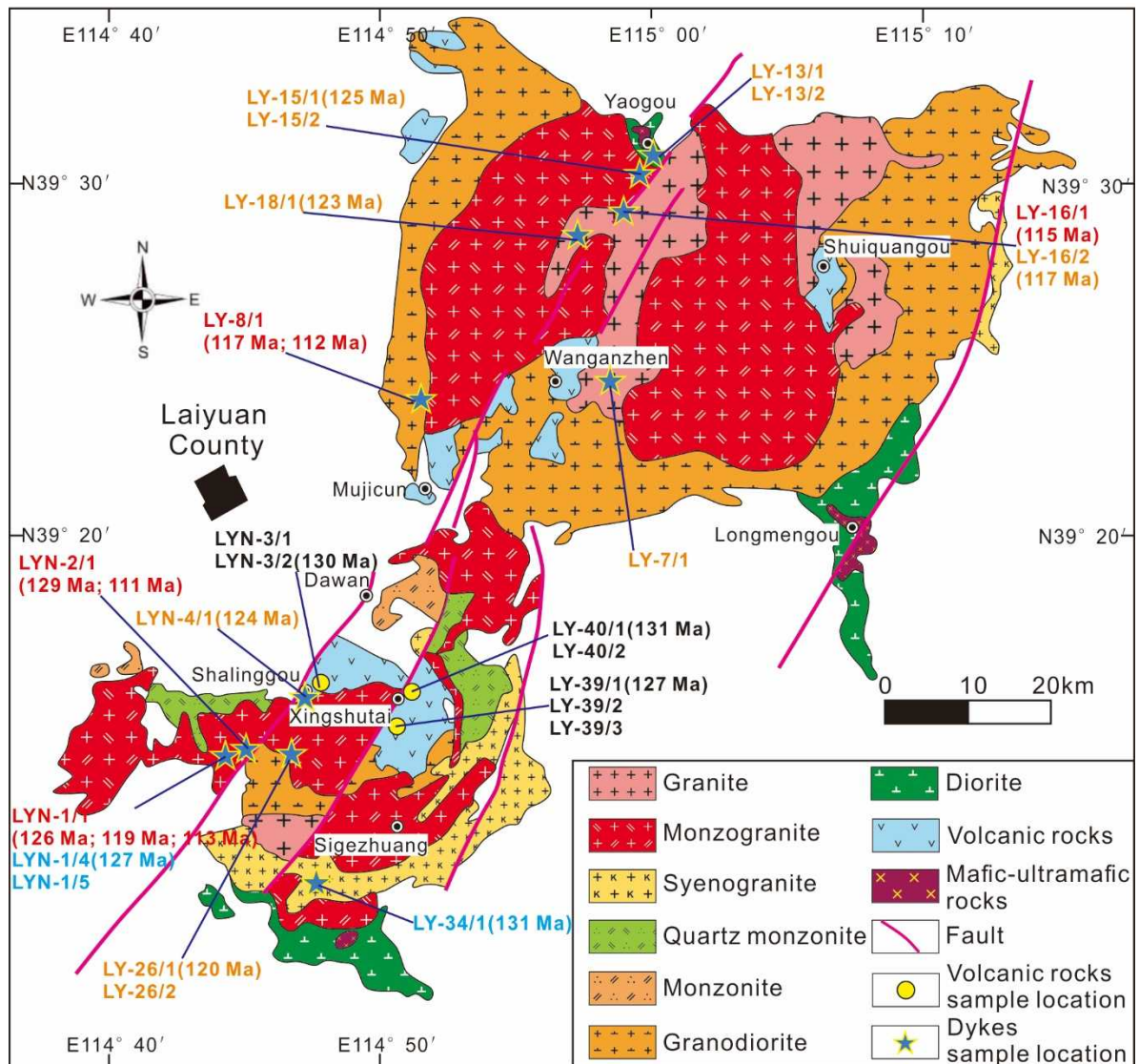


Fig. 3-1 Geological map of the Laiyuan magmatic complex after the mineral and geological map in Laishui-Yixian areas (1979) and this fieldwork showing the sample locations of dyke suites and volcanic rocks, and the zircon U-Pb dating results yielded in this study.

3.1 Volcanic rocks

The studied volcanic rocks were collected from the northern domain of the Sigezhuang pluton (Fig. 3-1). The volcanic rocks cover Paleozoic Cambrian-Ordovician strata. They show grey or dark purple colors massive structure and porphyritic texture. Based on petrological features, they belong to the andesite-dacite series. The detailed petrological descriptions are given below.

Table 3-1 Summary of locations, rock types and mineralogy of samples analyzed in this study.

Mineral abbreviations are same as in Fig. 3-5.

Serial No.	Sample No.	Rock Type	Coordinates	Mineralogy
1	LY-39/1	Dacite	N 39°14'26.51" E 114°50'24.59"	Pl+Bt+Amp+Kfs+Qtz
2	LY-39/2	Andesite	N 39°14'26.51" E 114°50'24.59"	Pl+Amp+Cpx+Qtz
3	LY-39/3	Andesite	N 39°14'26.51" E 114°50'24.59"	Pl+Hbl+Cpx
4	LY-40/1	Trachyandesite	N 39°15'32.66" E 114°50'45.00"	Pl+Cpx+Hbl
5	LY-40/2	Trachyandesite	N 39°15'32.66" E 114°50'45.00"	Pl+Cpx+Amp
6	LYN-3/1	Trachyandesite	N 39°15'34.58" E 114°47'26.89"	Pl+Kfs+Amp+Bt
7	LYN-3/2	Trachydacite	N 39°15'34.58" E 114°47'26.89"	Pl+Kfs+Qtz+Hbl+Bt
8	LY-33/1	Syenogranite	N 39°09'43.51" E 114°47'46.33"	Mc(50%)+Qtz(30%)+Pl(15%)+Bt(5%)
9	LY-36/1	Syenogranite	N 39°11'17.93" E 114°51'22.93"	Kfs(50%)+Qtz(30%)+Pl(15%)+Bt(5%)
10	LY-37/1-1	Syenogranite	N 39°13'37.71" E 114°55'02.85"	Kfs(45%)+Qtz(30%)+Pl(20%)+Bt(5%)
11	LY-19/1	Monzogranite	N 39°15'35.86" E 114°40'50.78"	Kfs(30%)+Pl(30%)+Qtz(25%)+Bt(10%)+Hbl(5%)
12	LY-21/2	Monzogranite	N 39°15'54.53" E 114°41'57.93"	Qtz(35%)+Kfs(30%)+Pl(25%)+Bt(7%)+Hbl(3%)
13	LY-22/3	Monzogranite	N 39°14'37.52" E 114°43'13.79"	Kfs(30%)+Pl(30%)+Qtz(30%)+Bt(7%)+Hbl(3%)
14	LY-22/4-1	Monzogranite	N 39°14'37.52"	Kfs(35%)+Qtz(25%)+Pl(25%)+Bt(10%)+Hbl(5%)

			E 114°43'13.79"	
15	LYN-1/3	Monzogranite	N 39°13'49.62" E 114°44'51.98"	Kfs(35%)+Qtz(25%)+Pl(20%)+Bt(15%)+Hbl(5%)
16	LY-21/1	Quartz Monzonite	N 39°15'54.53" E 114°41'57.93"	Pl(30%)+Kfs(30%)+Qtz(20%)+Hbl(10%)+Bt(10%)
17	LY-22/4-2	Quartz Monzonite	N 39°14'37.52" E 114°43'13.79"	Kfs(35%)+Pl(25%)+Qtz(20%)+Bt(20%)
18	LY-37/1-2	Quartz Monzonite	N 39°13'37.71" E 114°55'02.85"	Pl(35%)+Kfs(30%)+Qtz(15%)+Hbl(20%)
19	LYN-1/2	Quartz Monzonite	N 39°13'49.62" E 114°44'51.98"	Pl(35%)+Kfs(30%)+Qtz(15%)+Bt(20%)
20	LY-20/1	Monzonite	N 39°15'49.29" E 114°40'39.24"	Pl(40%)+Kfs(30%)+Hbl(20%)+Bt(10%)
21	LY-22/1	Monzonite	N 39°14'37.52" E 114°43'13.79"	Pl(40%)+Kfs(30%)+Hbl(25%)+Bt(5%)
22	LY-22/2	Monzonite	N 39°14'37.52" E 114°43'13.79"	Pl(35%)+Kfs(35%)+Hbl(25%)+Bt(5%)
23	LY-42/1	Monzonite	N 39°19'03.80" E 114°52'01.41"	Pl(35%)+Kfs(35%)+Bt(20%)+Hbl(5%)+Qtz(5%)
24	LY-42/2	Monzonite	N 39°19'03.80" E 114°52'01.41"	Pl(35%)+Kfs(35%)+Bt(20%)+Hbl(10%)
25	LY-8/1	Lamprophyre	N 39°23'51.45" E 114°51'29.44"	Hbl+Kfs+Cpx+Pl+Opx
26	LY-16/1	Lamprophyre	N 39°29'14.34" E 114°58'30.57"	Cpx+Hbl+Ol+Pl+Kfs
27	LYN-1/1	Lamprophyre	N 39°13'49.62" E 114°44'51.98"	Bt+Kfs+Hbl
28	LYN-2/1	Lamprophyre	N 39°13'49.50" E 114°45'02.72"	Bt+Kfs+Hbl
29	LY-7/1	Dolerite	N 39°24'23.08" E 114°58'26.95"	Pl+ Cpx+Hbl+Kfs
30	LY-13/1	Dolerite	N 39°31'36.84" E 114°59'50.14"	Pl+Cpx+Hbl
31	LY-13/2	Dolerite	N 39°31'36.84" E 114°59'50.14"	Pl+Cpx+Hbl
32	LY-15/1	Dolerite porphyry	N 39°30'35.35" E 114°59'44.54"	Pl+Cpx+Ep
33	LY-15/2	Dolerite porphyry	N 39°30'35.35" E 114°59'44.55"	Pl+Cpx+Ep
34	LY-16/2	Dolerite porphyry	N 39°29'14.34" E 114°58'30.57"	Pl+Cpx+Qtz
35	LY-18/1	Dolerite	N 39°28'45.43" E 114°57'05.32"	Pl+Cpx+Hbl+Kfs+Cal

36	LY-26/1	Dolerite	N 39°13'44.08" E 114°46'47.89"	Pl+Cpx
37	LY-26/2	Dolerite	N 39°13'44.08" E 114°46'47.89"	Pl+Cpx
38	LYN-4/1	Dolerite	N 39°15'30.40" E 114°47'13.87"	Pl+Hbl+Cpx
39	LY-34/1	Diorite porphyry	N 39°09'42.78" E 114°47'52.62"	Hbl+Bt+Pl+Kfs
40	LYN-1/4	Granodiorite	N 39°13'49.62" E 114°44'51.98"	Kfs+Pl+Hbl+Qtz+Bt
41	LYN-1/5	Granodiorite	N 39°13'49.50" E 114°45'02.72"	Kfs+Pl+Hbl+Qtz+Bt

The andesites (sample LY-39/2 and LY-39/3) are dark purple colored and display massive structure (Fig. 3-2b). They are characterized by porphyritic texture with plagioclase, amphibole, and pyroxene occurring as phenocrysts accounting for ~40% (Fig. 3-2f, g, h). The plagioclase phenocrysts exhibit zoned texture with common sericitization and carbonatation (Fig. 3-2g, h). The amphibole phenocrysts commonly experienced epidotization and are partly pseudomorphed by granular aggregates of epidote (Fig. 3-2f, g, h). The matrix is characterized by typical pilotaxitic texture with oriented plagioclase microcrystals accounting for ~60% (Fig. 3-2g). The trachyandesites including samples LY-40/1, LY-40/2, and LYN-3/1 are dark grey and greenish colored with massive structure (Fig. 3-2c, d). The plagioclase, K-feldspar, clinopyroxene, and amphibole occur as phenocrysts accounting for ~35%. Plagioclase phenocrysts are subhedral to xenomorphic surrounded by iron oxide minerals and ranging from ~0.5 to 1 mm in length (Fig. 3-2i, k). The granulous clinopyroxene phenocrysts contain opaque mineral inclusions and amphibole (Fig. 3-2i, j). The oriented plagioclase microcrystals are surrounded by anhedral K-feldspar which accounts for most of the groundmass (Fig. 3-2i, j, k). The dacite (sample LY-39/1) is characterized by grey greenish color and is composed of quartz, plagioclase, biotite, and amphibole phenocrysts (Fig. 3-2a, e). The quartz phenocrysts are granulous and anhedral with grain size ranging from 0.5-1.5 mm (Fig. 3-2e). The hornblende phenocrysts are partly altered to epidote and chlorite (Fig. 3-2e). Plagioclase,

K-feldspar, and quartz constitute the matrix with magnetite, apatite, and zircon as the accessory minerals (Fig. 3-2e). The trachydacite (sample LYN-3/2) shows porphyritic texture with a mineral assemblage of plagioclase, K-feldspar, hornblende, and quartz as phenocrysts (Fig. 3-2l). The groundmass shows typical trachytic texture composed of K-feldspar, plagioclase, and quartz minerals (Fig. 3-2i).

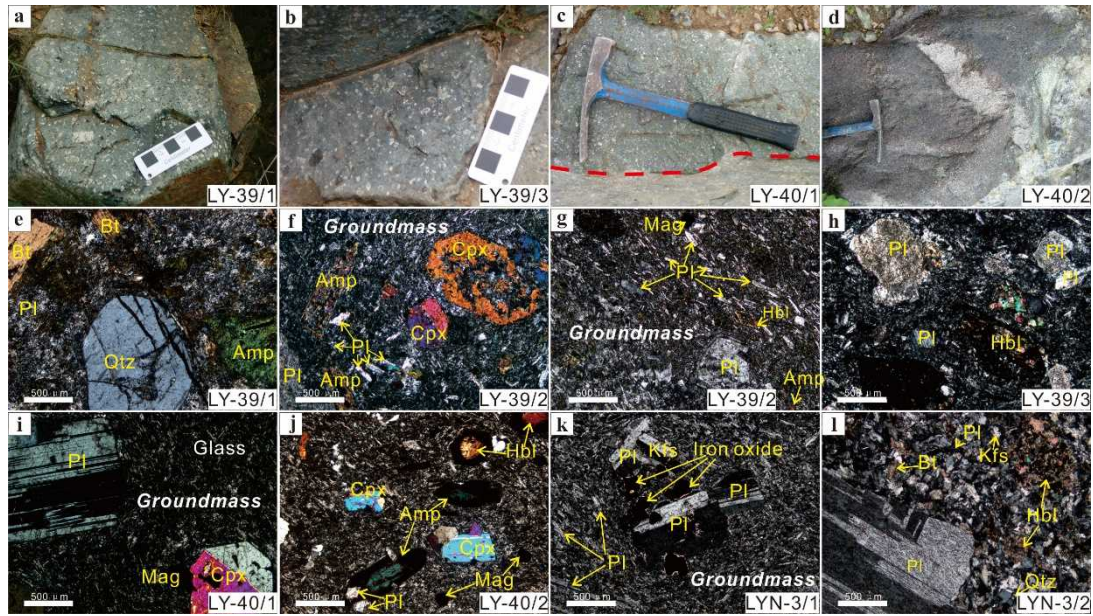


Fig. 3-2 Representative photographs and photomicrographs of the Laiyuan volcanic rocks. (a), (b), (c), and (d) Greenish to brownish exposures of andesites-dacites with porphyritic textures. (e) Dacite composed of quartz, biotite and hornblende phenocrysts. (f) Andesite containing abundant amphibole and clinopyroxene phenocrysts and plagioclase groundmass. (g) Directional arrangement of plagioclase microcrystal in andesite. (h) Hornblende with dark-colored edge and alterations in andesite. (i) Phenocrysts of plagioclase and clinopyroxene and dark groundmass composed of glass and plagioclase microcrystals in trachyandesite. (j) Amphibole minerals with dark-colored edges in trachyandesite. (k) Subhedral plagioclase phenocrysts surrounded by iron oxides and oriented textures in groundmass in trachyandesite. (l) Groundmass exhibiting typical trachytic texture in trachydacite. Mineral abbreviation: Amp-amphibole; Bt-biotite; Cpx-clinopyroxene; Hbl-hornblende; Kfs-K-feldspar; Mag-magnetite; Pl-plagioclase; Qtz-quartz.

3.2 Granitoids

The granitoids account for the major domain of the Laiyuan complex

incorporating variable lithologies. In this study, several samples were collected from the Sigezhuang pluton (Fig. 3-3). In the field, the contact between different magmatic units is sometimes clear indicating they emplaced in multiple magmatic events, not crystallized from single magmatism (Fig. 3-4e). A particular feature of the Laiyuan magmatic complex is that abundant xenoliths are founded in this huge granitic batholith. Precambrian felsic gneisses fragments still exhibit their original bedding features, are found as xenoliths in the pluton (Fig. 3-4c). Additionally, gabbroic xenoliths are also contained by the granitoids showing angular shape (Fig. 3-4c, d). The felsic and mafic dykes intruded the granitoids in some regions of the complex exhibiting clear contact relationship with the host granitoids (Fig. 3-4d and Fig. 3-6). The Sigezhuang pluton is composed of syenogranite, monzogranite (porphyritic monzogranite), quartz monzonite, and monzonite (Fig. 3-4). The detailed petrological descriptions are given below and their salient details are listed in Table 3-1.

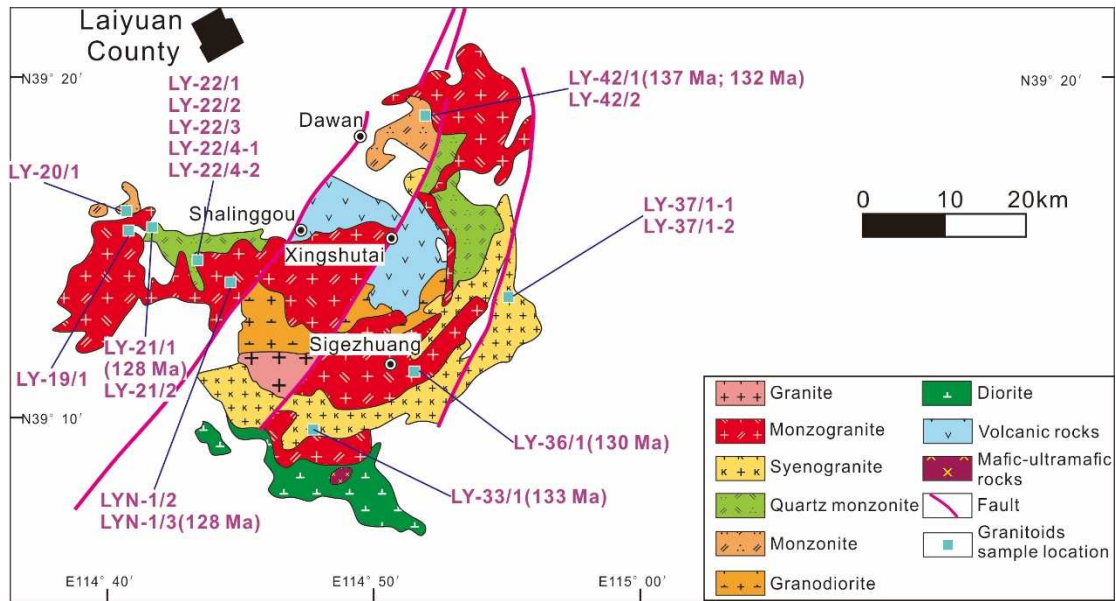


Fig. 3-3 Geological map of Sigezhuang pluton showing the sample locations of granitoids, and the zircon U-Pb dating results yielded in this study.

3.2.1 Syenogranite

The syenogranites are exposed along the rim of the pluton and exhibit massive structure and flesh red color (Fig. 3-4h). They are coarse to medium grained and show

typical granitic texture with abundant K-feldspar minerals (Fig. 3-5a, c). They are composed of microcline (~50%) or K-feldspar (~45-50%), quartz (~30%), plagioclase (15-20%), and biotite (~5%). The microcline crystals are subhedral to anhedral with minor alteration (Fig. 3-5a) whereas the plagioclase minerals are mainly subhedral to euhedral (Fig. 3-5b, d). The quartz grains are anhedral and filled in the space between the feldspar grains (Fig. 3-5a, c). The mafic minerals in the syenogranites are of small amount, and are mainly biotites which are sometimes chloritized (Fig. 3-5a, d). The rhombus-shaped sphene minerals occur as the accessory minerals in the syenogranite rocks (Fig. 3-5c).

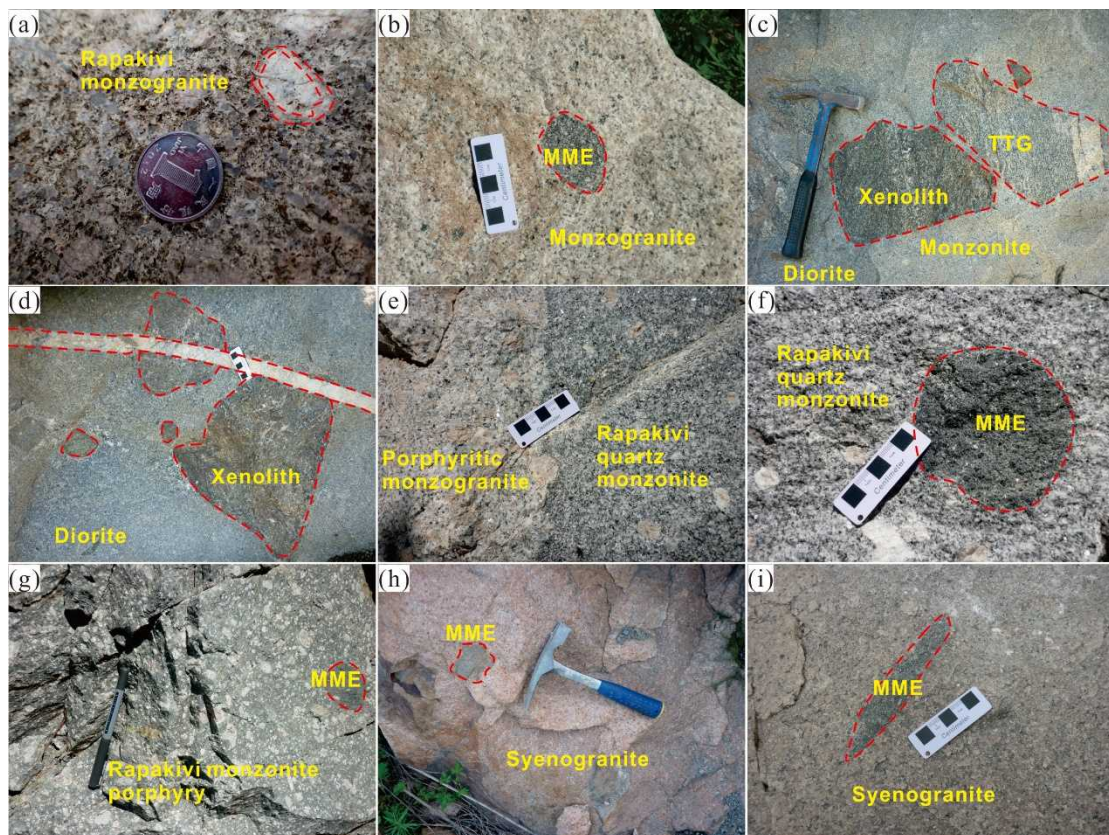


Fig. 3-4 Field photographs of the Laiyuan granitoids. (a) Rapakivi monzogranite with zoning K-feldspar (LYN-1/3). (b) Monzogranite containing MME (LY-19/1). (c) Monzonite containing mafic xenolith and TTG fragment from basement rocks (LY-20/1). (d) Diorite containing mafic xenolith cut by later felsic dyke. (e) Contact zone between rapakivi quartz monzonite (LY-21/1) and porphyritic monzogranite (LY-21/2). (f) Rapakivi quartz monzonite (LY-21/1) containing rounded MME. (g) Monzonite porphyry (LY-22/1) containing MME (LY-22/4-2). (h) Syenogranite (LY-33/1) containing MME. (i) Syenogranite (LY-37/1-1) containing MME (LY-37/1-2).

3.2.2 Monzogranite

The monzogranite occupies major domains and are exposed in the core of the intrusive complex (Fig. 3-3). They display granitic texture and massive structure, and are coarse to medium grained in hand specimen with dark white color. Rapakivi texture (Fig. 3-4a) and porphyritic texture (Fig. 3-4e) also occurred in the monzogranite rocks containing abundant mafic microgranular enclaves (MMEs). The monzogranites majorly comprise K-feldspar (~30-35%), plagioclase (~25-30%), quartz (~25-35%), biotite (~5-10%), hornblende (~3-5%), and some accessory minerals including magnetite, sphene, and zircon (Fig. 3-5e, h). The K-feldspar crystals are primarily subhedral-euhedral and coarse grained with a size of 1-4 mm. Some coarse K-feldspar grains are oscillatory-zoned containing hornblende, quartz, and plagioclase as inclusions (Fig. 3-5h). Medium- to coarse-grained plagioclase grains (0.5-2.0 mm) often exhibit zoned texture and surround the K-feldspar grains (Fig. 3-5g). Quartz grains are anhedral with variable grain sizes ranging from 0.1 to 2.0 mm, and fill in the space between plagioclase and K-feldspar (Fig. 3-5e, f). The previously formed hornblende phase was replaced by alteration minerals such as biotite, and enclosed in quartz or plagioclase grains (Fig. 3-5f). According to the mineral constituent, the monzogranites are specifically classified as hornblende-containing biotite monzogranites.

3.2.3 Quartz monzonite

The quartz monzonites are grey white or grey colored, medium grained, and display massive structure and monzonitic texture (Fig. 3-4e, f). MMEs sampled from the granitoids in this study are also quartz monzonites (Fig. 3-5k, l). Euhedral to subhedral plagioclase (~25-35%), euhedral K-feldspar (~30-35%), anhedral quartz (~15-20%), euhedral biotite (~10-20%), and euhedral to subhedral hornblende (~10-20%) account for the mineral phases of the quartz monzonites. The zoning texture is common in plagioclase (0.6-2.0 mm) and K-feldspar (0.5-3.0 mm) crystals (Fig. 3-5i). Additionally, the textural disequilibrium was found in some plagioclase

xenocrysts (Fig. 3-5j) indicating the existence of magma mixing of basaltic and felsic melts (Chen et al., 2013). The quartz phase (0.4-1.2 mm) is present between the plagioclase and K-feldspar grains (Fig. 3-5k). The biotite (0.2-1.0 mm) and hornblende are the major mafic mineral phases in the quartz monzonite filling in the interstice between minerals (Fig. 3-5i, l).

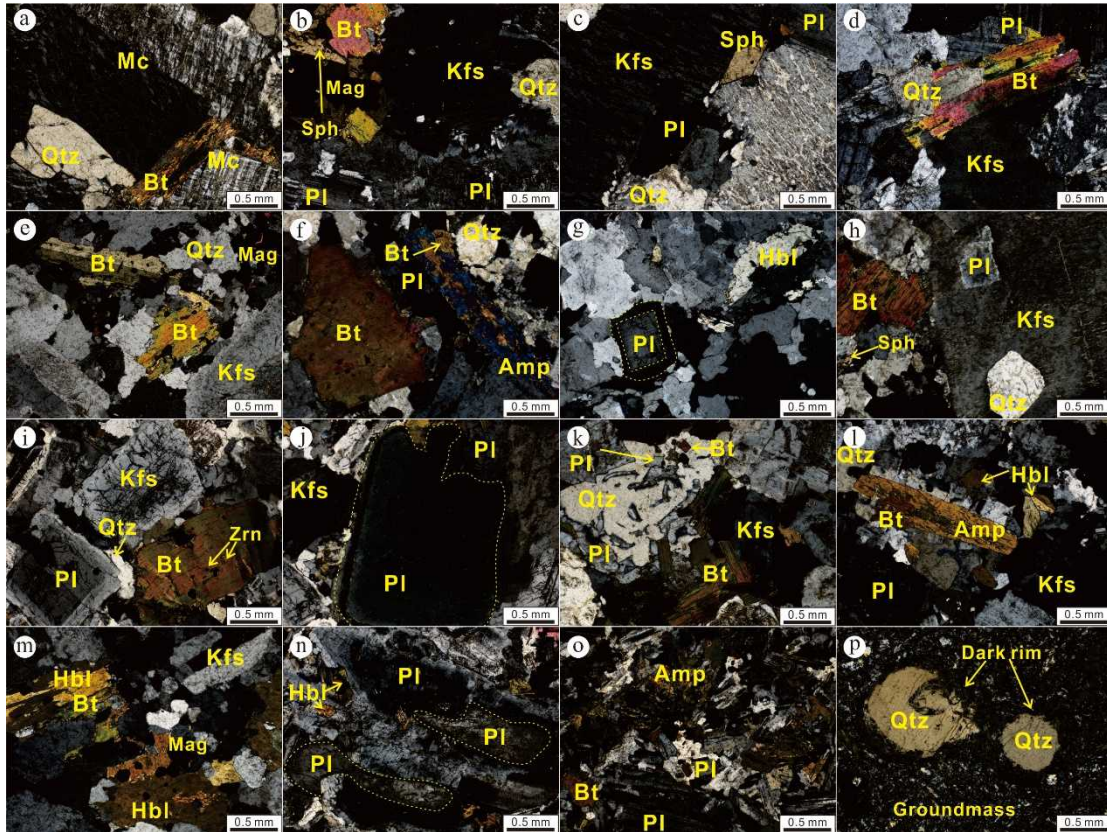


Fig. 3-5 Representative photomicrographs of the Laiyuan dykes under cross-polarized light. (a) Syenogranite (LY-33/1). (b) and (c) Biotite syenogranite (LY-36/1). (d) Biotite syenogranite (LY-37/1-1). (e) Biotite monzogranite (LY-21/2). (f), (g) and (h) Rapakivi biotite monzogranite (Fig. 22/4-1). (i) Quartz monzonite showing zoning K-feldspar and plagioclase (LY-21/1). (j) Quartz monzonite showing textural disequilibrium in plagioclase (LY-21/1). (k) Quartz monzonite (LY-22/4-2, MME). (l) Quartz monzonite (LY-37/1-2, MME). (m) Monzonite (LY-42/1). (n) Monzonite exhibiting textural disequilibrium (LY-20/1). (o) Monzonite (LY-20/1). (p) Monzonite porphyry displaying anhedral quartz grains surrounded by dark rim (LY-22/1). Mineral abbreviations: Amp-amphibole; Bt-biotite; Hbl-hornblende; Kfs-K-feldspar; Mag-magnetite; PI-plagioclase; Qtz-quartz; Sph-sphene; Zrn-Zircon.

3.2.4 Monzonite

The monzonite and monzonite porphyry were sampled from the northern and western rim of the pluton exhibiting grey or grey white colors (Fig. 3-4). The monzonitic and porphyritic textures are the common textures in these rocks. The monzonites are composed of plagioclase (~35-40%), K-feldspar (~30-35%), hornblende (~5-15%), biotite (~5-20%), and quartz (~5%). The zoning texture is identified in euhedral plagioclase grains, with a size of 0.1-2.0 mm, which were sometimes included in K-feldspar grains (Fig. 3-5m, n). The mafic minerals are mainly hornblende and biotite, but a small amount of pyroxene crystals as well (Fig. 3-5m, n, o). The phenocryst phases (~20%) for monzonite porphyry are dominantly composed of euhedral plagioclase grains (~10%) which are at some places altered to carbonate, and rounded anhedral quartz crystals (~10%) surrounded by dark mineral assemblage rim which are majorly hornblende which experienced intense alteration (Fig. 3-5p). The matrix (~80%) is composed of hornblende and plagioclase crystallites (Fig. 3-5p). Accessory minerals set in the groundmass include magnetite, apatite, sphene, and zircon (Fig. 3-5p).

3.3 Dyke suites

Seventeen dyke samples, including lamprophyres, dolerite (porphyry), and felsic dykes were collected from different locations in the Laiyuan complex covering the Wanganzhen pluton and the Sigezhuang pluton. The samples locations are shown in Fig. 3-1 and salient petrological features are listed in Table 3-1.

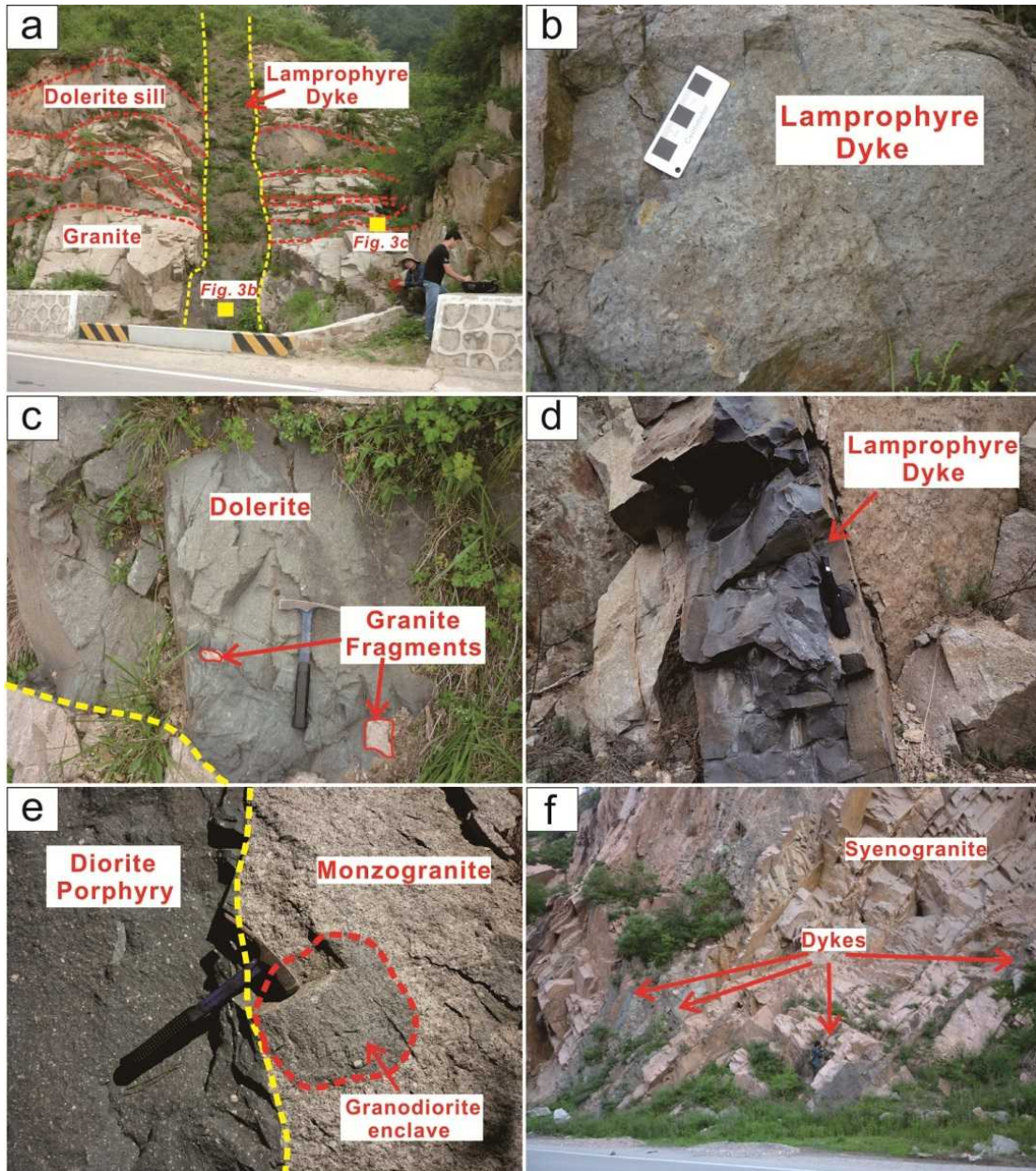


Fig. 3-6 Field photographs of the Laiyuan dykes. (a) Dolerite sills cut by later vertical lamprophyre dyke. (b) Greyish green colored lamprophyre with abundant mafic phenocrysts. (c) Dolerite sill showing compositional variations from bottom to top with granite fragments. (d) Fine-grained and dark gray colored lamprophyre dyke intruding host granite. (e) Dark diorite porphyry dyke with feldspar phenocrysts. (f) Multiple dykes intruding pink syenogranite.

3.3.1 Lamprophyre

Abundant mafic dykes were identified in Laiyuan area intruding the granitoids, Archean gneisses, and Paleozoic dolomites. Samples LYN-1/1, LYN-2/1, LY-8/1, and

LY-16/1 were collected from fresh exposures of dykes with W–E trending controlled by the regional faults. They are greenish colored with width ranging from 0.5 to 3 m (Fig. 3-6b, d). The dykes intrude host granitoids and show sharp contact with the surrounding rocks suggesting rapid ascent of magma and fast solidification (Fig. 3-6d). The lamprophyres are generally fine grained with typical lamprophyric texture of abundant mafic minerals occurring as phenocrysts (Rock, 1977). The phenocryst phases are dominantly composed of euhedral to subhedral mafic minerals of amphibole, clinopyroxene, biotite (phlogopite), and minor olivine dominantly (40-50%; by volume) which are at some places altered to carbonate, chlorite, and sericite (Fig. 3-7a, b, c, d). The matrix is composed of pyroxene, hornblende, and plagioclase crystallites (Fig. 3-7c). Accessory minerals set in the groundmass include magnetite, apatite, and zircon. Leucocratic ocelli (LYN-1/1) with a rounded edge rimmed by melanocratic minerals of biotite and amphibole (Fig. 3-7f) are also seen. Based on mineralogy, these rocks can be classified as minette (LYN-1/1, LYN-2/1), camptonite (LY-8/1), and vogesite (LY-16/1) following the classification scheme of Wooley et al. (1996).

3.3.2 Dolerite and dolerite porphyry

Similar to the lamprophyres, several dolerite dykes also occur in the study area. Samples of dolerite or dolerite porphyry are gray to light green and display massive structure (Fig. 3-6a, c). Under microscope, some of the samples show typical ophitic texture (Fig. 3-7h, i). The dolerites are composed of euhedral to subhedral plagioclase (~50%), subhedral altered pyroxene (~35%), stumpy biotite crystallite (~10%), and altered mineral of calcite (~10%) with accessory mineral of zircon. Magnetite and acicular apatite also occur as accessory minerals. In dolerite porphyry, euhedral to subhedral clinopyroxene (~15%), euhedral plagioclase (~10%), and rare olivine phenocrysts (~5%) occur as the phenocryst phases. The groundmass contains plagioclase (~35%), clinopyroxene (~25%), amphibole (~5%), and biotite (~5%). Two textural types of calcite can be recognized in the dolerite and diorite porphyry. One is xenomorphic and minor occurring as an alteration phase filling the other mineral

grains, and another is intergrown with euhedral K-feldspar (Fig. 3-7h), indicating magmatic origin. Chloritization, carbonation, and epidotization are common alteration types in the mafic dykes.

3.3.3 Felsic dykes

Besides mafic dykes, felsic dykes are also widespread in the Laiyuan complex. Samples LY-34/1, LYN-1/4, and LYN-1/5 of felsic dyke samples are classified as diorite porphyry and granodiorite. The diorite porphyries are grayish and range in width from 1 to 2 m exhibiting porphyritic texture (Fig. 3-6e). Sample LY-34/1 is a representative diorite porphyry with matrix and phenocryst occupying 80% and 20%, respectively (Fig. 3-7j, k). The phenocrysts consist of euhedral-subhedral hornblende (~10%), xenomorphic plagioclase with corrosion border (~5%), xenomorphic and tabular biotite (~5%), and quartz (~2%). The matrix contains abundant rhombic hornblende microlites ranging from 20 to 300 μ m (35%), very fine-grained feldspar (~25%), and some other cryptocrystalline minerals (~15%). Magnetites intergrowth with mafic minerals and apatite occur as accessory minerals. Granodiorites (LYN-1/4 and LYN-1/5) are brown colored with fine-grained matrix of feldspar and phenocryst of feldspar and amphibole (Fig. 3-7l). The phenocrysts are composed of abundant rhombic hornblende. Around the rapakivi-textured K-feldspar phenocrysts, coniform and granophyric textures can be observed. The feldspars are sometimes altered to sericite (Fig. 3-7l).

3.4 Ultramafic-mafic rocks

Except the collected volcanic rocks, granitoids, and dyke suites, the ultramafic-mafic rocks were outcropped in some places of the complex, such as Yaogou and Longmengou which have been studied by several researches (Gao et al., 2012; Hou et al., 2015; Liu et al., 2010; Liu et al., 2009a; Zhai et al., 2014; Zhang et al., 2017). At Longmengou (Fig. 3-1), the ultramafic-mafic rocks consist mainly of three rock units: hornblende pyroxenite, hornblende gabbro, and gabbroic diorite (Liu et al., 2010). The pyroxenite unit shows typical cumulate textures. The Yaogou

ultramafic-mafic rocks are dominated by pyroxene hornblendite and gabbronorite, and occur as isolated bodies in the rim of the Wanganzhen pluton (Fig. 3-1). The hornblendite bodies at Yaogou occur as variously sized enclaves or rock blocks scattered in the gabbronorite intrusion (Hou et al., 2015). These ultramafic-mafic rocks are commonly hosted in granitoids including diorite and quartz diorite (Fig. 3-1).

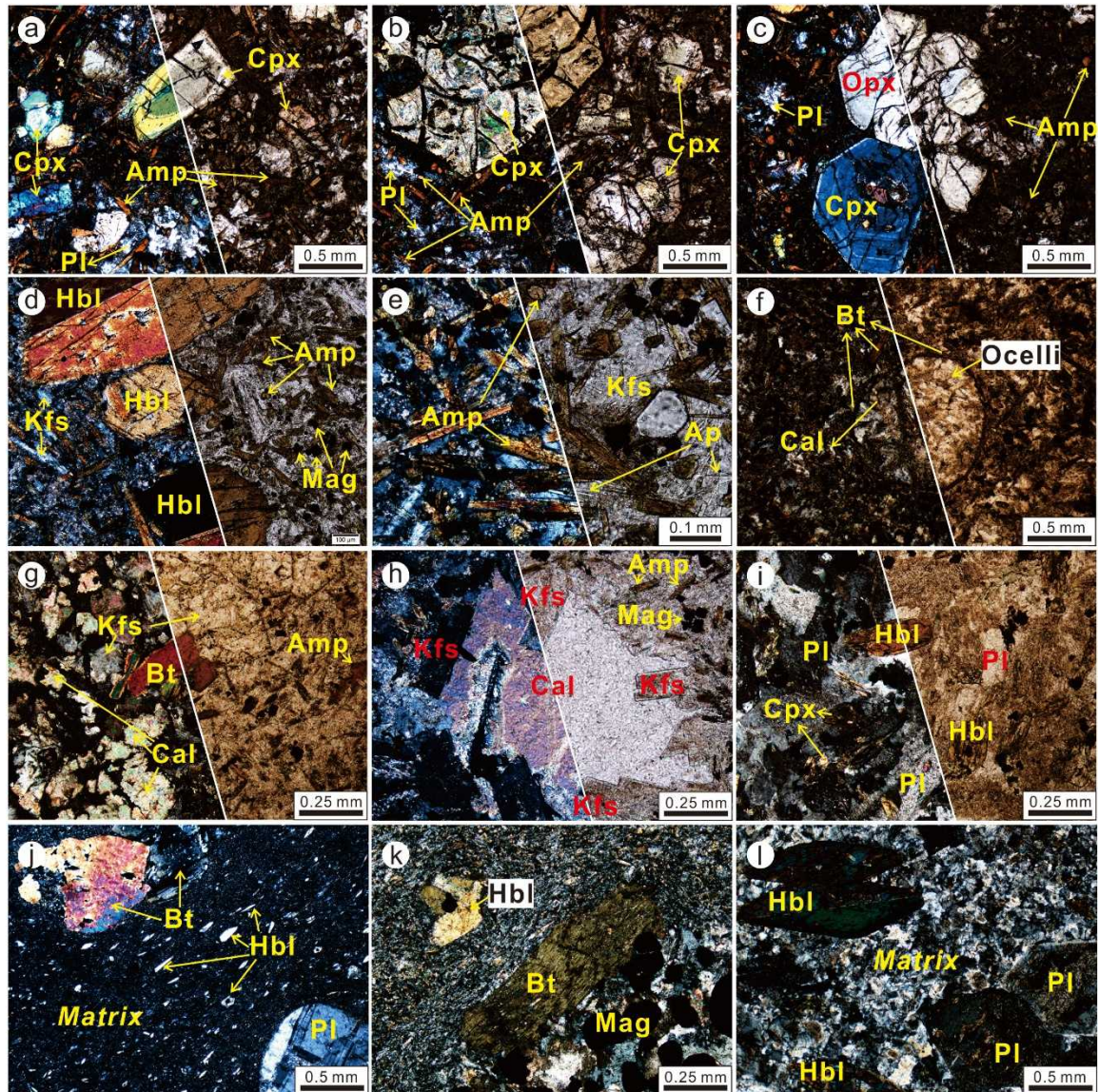


Fig. 3-7 Representative photomicrographs of the Laiyuan dykes under cross-polarized light (left) and plane-polarized light (right). (a) Vogesite (LY-16/1): clinopyroxene phenocrysts and amphibole crystallites in matrix. (b) Vogesite (LY-16/1): olivine pseudomorph. (c) Vogesite (LY-16/1): clinopyroxene and orthopyroxene minerals of zoning texture and strip amphibole

minerals. (d) Camptonite (LY-8/1): paired hornblende phenocrysts. (e) Camptonite (LY-8/1): acicular apatite in matrix. (f) Minette (LYN-1/1): leucocratic ocelli with a round edge rimed by melanocratic minerals of biotite and amphibole. (g) Minette (LYN-2/1): biotite phenocrysts and altered carbonate minerals. (h) Dolerite (LY-18/1): calcite intergrown with euhedral K-feldspar. (i) Dolerite (LYN-4/1): ophitic texture with clinopyroxene and hornblende minerals. (j) Diorite porphyry (LY-34/1): biotite phenocrysts and abundant hornblende crystallites in matrix. (k) Diorite porphyry (LY-34/1): magnetite aggregation. (l) Granodiorite: paired hornblende and granophyric texture in matrix. Mineral abbreviations: Amp-amphibole; Ap-apatite; Bt-biotite; Cpx-clinopyroxene; Cal-calcite; Hbl-hornblende; Kfs-K-feldspar; Mag-magnetite; Ol-olivine; Pl-plagioclase; Qtz-quartz.

3.5 Spatial links between diverse magmatic suites

The volcanic series of andesites and dacites are exposed in horizontal integration of contact relationships (Fig. 3-2c) indicating they were formed by same volcanism. In terms of volume, the granitoids occupy the most of the Laiyuan complex and occur as the host rocks for ultramafic-mafic suites in the borders of the complex. The mafic rocks were hosted by the granitoids in forms of small enclaves or large stocks indicating the emplacement of granitoids was slightly later than or simultaneous with the mafic intrusions. The concentrically-zoned granitoids comprise diverse magmatic units (Fig. 3-1). Contact boundaries between these various intrusive suites are legible and clear (Fig. 3-4e) which are called as pulsating contact relationship indicating they were formed simultaneously. As well, the containing MMEs in the granitoids have clear contact boundaries suggesting their similar formation ages (Fig. 3-4). Furthermore, the felsic dykes intruded the granitoids and cut the MMEs (Fig. 3-4d), and diverse mafic dykes were identified in the granitoids throughout the complex (Fig. 3-6). The dolerite sills were cut by the vertical lamprophyre dykes exhibiting the lamprophyre dyking event was the latest magmatism in the Laiyuan complex.

Chapter 4 Analytical methods

4.1 EPMA

The analyses were performed on polished thin sections by using Electron Probe Micro Analyzer (Model: JEOL JXA8530F Hyperprobe) under the conditions of 15 kV accelerating voltage and 10 mA sample current at the Chemical Analysis Division of the Research Facility Center for Science and Technology, the University of Tsukuba. The data were regressed using oxide-ZAF correction method. Synthetic and natural minerals were used as standards. Counting times were 10s on peak and 10s on background for all elements and detection limits are typically 0.01-0.004 wt. % (details in [Tang et al., 2016](#)).

4.2 Whole rock geochemistry

The fresh and homogeneous domains of rock samples were crushed and powdered to a grain size less than 200 mesh to perform geochemical analyses. The whole rock geochemical analyses were conducted at National Research Center for Geoanalysis, Beijing. Trace elements, including rare earth elements (REEs) were measured using an Agilent 7500ce inductively coupled plasma mass spectrometry (ICP-MS) with analytical uncertainties of 10% for elements whose abundances <10 ppm and 5% for those >10 ppm. The major elements were determined by X-ray fluorescence (XRF model PW 4400) with analytical uncertainty ranging from 1% to 3%.

4.3 Zircon U-Pb dating

Zircon grains were separated using gravimetric and magnetic separation techniques, and handpicked under a binocular microscope at Yu'neng Geological and Mineral Separation Survey Centre of Langfang, Hebei Province, China. Then about 150 grains of each sample were mounted into an epoxy resin disc. All grains were taken pictures under transmitted and reflected, and also examined using the cathode

luminescence (CL) image technique at Beijing Geoanalysis Co., Ltd.

Some selected zircons from volcanic rocks and dyke suites were analyzed for U-Pb at the Tianjin Center, China Geological Survey, using the LA-ICP-MS instrument. The laser-ablation system was a Geo Las 200 M equipped with a 193 nm laser whose ablation pit was 35 μm in diameter and average power output was approximately 4 W. Zircon 91,500 and glass NIST610 were used as external standards for U-Pb dating and trace element calibration, respectively. Zircon standards GJ-1 and Plešovice were used as unknown samples to monitor the stability and accuracy of acquired U-Pb data. Common Pb correction was made by using the program Com Pb Corr#3-17 (Andersen, 2002). The U-Pb isotopic ratios were calculated using the Glitter 4.0 program and U-Pb age calculation was done with the Isoplot program (Ludwig, 2003).

Selected zircon grains from granitoid samples were analyzed for their U-Pb ages at Korea Basic Science Institute (KBSI), Korea using a NWR193UC laser ablation system (Elemental Scientific Lasers LLC) coupled to a Nu Plasma II multicollector-inductively coupled plasma-mass spectrometer (MC-ICP-MS) (Nu Instruments). The Nu Plasma II mass spectrometer includes fixed collectors of sixteen Faraday detectors and five ion-counting electron multipliers. The standard zircons are 91500 (1062 ± 0.4 Ma, Wiedenbeck et al., 1995) and Plešovice (337.1 ± 0.4 Ma, Sláma et al., 2008), used as the primary and secondary zircon reference material respectively. Iolite 2.5 software (Paton et al., 2011) was used for data normalized and uncertainty propagated offline, and Isoplot 3.71 software (Ludwig, 2003) for calculating age data with 2 sigma uncertainty.

4.4 Zircon in-situ Lu-Hf isotopes

Zircon Lu-Hf isotopic analyses were conducted on the same or adjacent domains of the grains from where the U-Pb dating was done using a Neptune MC-ICP-MS equipped with a 193 nm Geolas Q Plus Ar F exciplex laser ablation and a spot size of 50 μm and a laser repetition rate of 10 Hz at 100 Mj at Tianjin Center, China Geological Survey. GJ-1 was used for in-situ zircon Hf isotopic analyses with

$^{176}\text{Hf}/^{177}\text{Hf}$ ratio of 0.282000 ± 0.000030 (2σ , $n = 200$) (Elhlou et al., 2006) and another external standard (Mud Tank) were also analyzed for in situ zircon Hf isotopic analyses with $^{176}\text{Hf}/^{177}\text{Hf}$ ratio of 0.282500 ± 0.000030 (2σ , $n = 200$) (Woodhead and Hergt, 2005). For correcting the isobaric interference ^{176}Lu and ^{176}Yb on ^{176}Hf , the method proposed by Chu et al. (2002) was taken. The $^{176}\text{Lu}/^{175}\text{Lu}$ ratio of 0.02669 and the $^{176}\text{Yb}/^{172}\text{Yb}$ ratio of 0.5886 were recommended to calculate $^{176}\text{Lu}/^{177}\text{Hf}$ ratios and mean β_{Yb} value from ^{172}Yb and ^{173}Yb , respectively. The detailed descriptions of the experimental methods are given in Geng et al. (2011).

Chapter 5 Geochronology of the Laiyuan complex

5.1 Zircon age data on magmatic suites in the Laiyuan complex

A total of nineteen rocks samples were dated in this research by using zircon U-Pb dating, including three volcanic rock samples, eleven dyke samples, and five granitoid samples.

5.1.1 Volcanic rocks

Three samples were selected for geochronology (samples LYN-3/2, LY-39/1, and LY-40/1), and their zircon U-Pb data are listed in [Table 5-1](#). The CL images of typical zircon grains and the age results are plotted in [Fig. 5-1](#). The zircon grains are euhedral to subhedral, light gray colored, and transparent, and range from 80 to 150 μm in length and from 40 to 100 μm in width with aspect ratios of 2:1 to 1:1 ([Fig. 5-1](#)). Almost all grains possess thick oscillatory-zoned texture from core to rim without resorbed cores implying their magmatic origin ([Corfu, 2003](#)).

The weighted-mean ages obtained for zircon standard GJ-1 are 600.2 ± 4.3 Ma ($n=8$), 600.5 ± 4.4 Ma ($n=7$), and 600.3 ± 4.5 Ma ($n=7$) for the analyses of samples LY-39/1, LY-40/1, and LYN-3/2, respectively, which match well the recommended values (600 Ma; [Jackson et al., 2004](#)). A total of 19 spots from dacite (sample LY-39/1) and 37 spots from trachyandesite (LY-40/1) show weighted mean $^{206}\text{Pb}/^{238}\text{U}$ ages of 127.1 ± 1.3 Ma (MSWD=1.0) and 131.4 ± 0.9 Ma (MSWD=2.8) with ages ranging from 131.2 to 121.7 Ma and from 137.7 to 126.3 Ma, respectively. Similarly, 37 zircon grains from trachydacite (sample LYN-3/2) yielded a weighted mean $^{206}\text{Pb}/^{238}\text{U}$ age of 130.3 ± 0.8 (MSWD=2.8) with ages ranging from 135.5 to 126.1 Ma. Separately, the Th/U ratios of zircons from samples LYN-3/2, LY-39/1, and LY-40/1 show ranges of 0.44-1.19, 0.73-1.91, and 0.67-1.23, showing typical features of magmatic zircons.

Thus, the Early Cretaceous ages of 131.4 ± 0.9 Ma, 130.3 ± 0.8 Ma, and 127.1 ± 1.3 Ma can be regarded as the crystallization ages of the Laiyuan volcanic rocks.

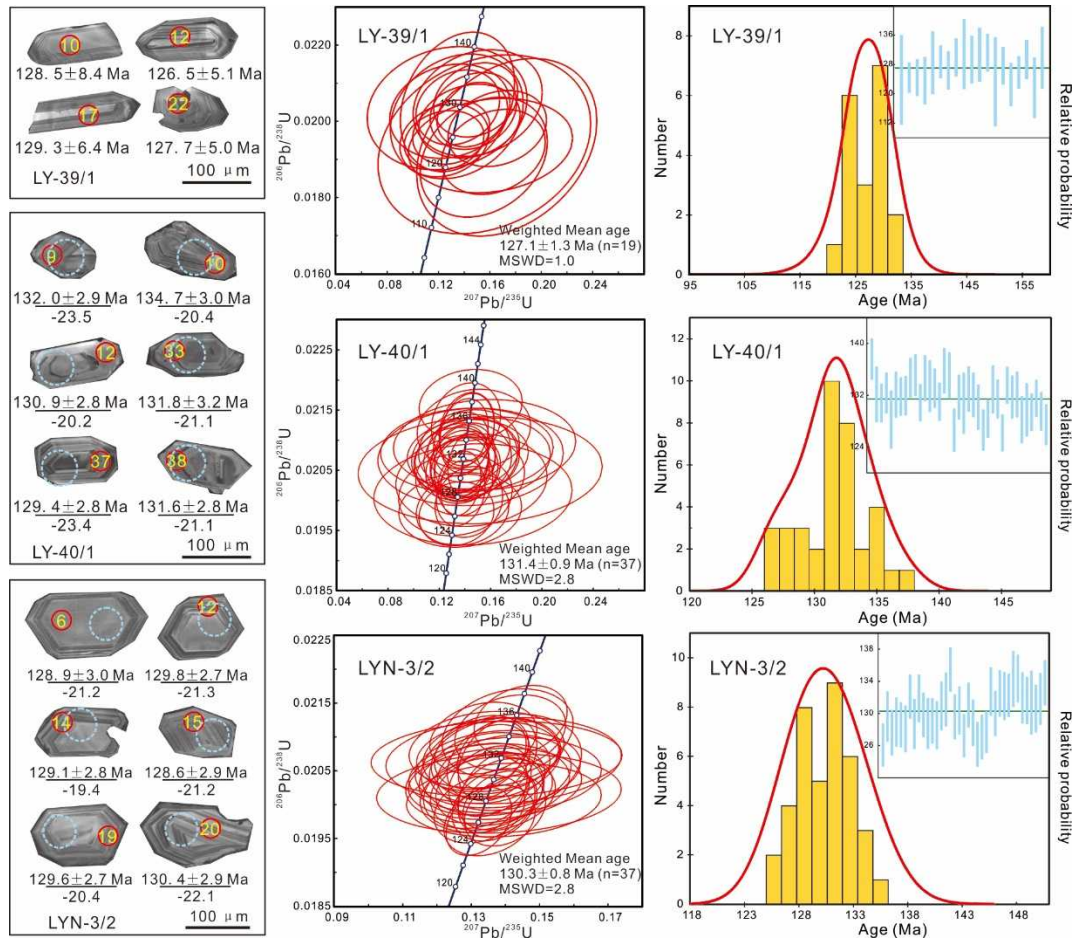


Fig. 5-1 Representative CL images of zircon grains showing ages and $\epsilon_{\text{Hf}}(t)$ values and U–Pb concordia plots and age data histograms with probability curves. In CL images, the larger circles represent locations of Hf isotopic analyses, whereas the smaller circles indicate spots of U–Pb dating.

5.1.2 Granitoids

Five samples were selected for geochronology (samples LY-21/1, LY-33/1, LY-36/1, LY-42/1, and LYN-1/3), and their zircon U-Pb data are listed in Table 5-2. The CL images of typical zircon grains and the age results are plotted in Fig. 5-2. The zircon grains are euhedral to subhedral, light gray colored, and transparent, and their size ranges are 80–200 μm in length and 40–100 μm in width with aspect ratios of 2:1

to 1:1 (Fig. 5-2). Almost all grains possess thick oscillatory-zoned texture from core to rim without resorbed cores implying their magmatic origin (Corfu, 2003).



Fig. 5-2 Representative CL images of zircon grains from granitoids showing ages and $\epsilon_{\text{Hf}}(t)$ values.

A total of 29 spots from sample LY-21/1 (quartz monzonite) yielded a weighted mean $^{206}\text{Pb}/^{238}\text{U}$ age of 127.9 ± 0.6 Ma (MSWD=2.1) with ages ranging from 133.1 to 125.6 Ma (Fig. 5-3a). Besides, there is one single zircon grain yielded a $^{206}\text{Pb}/^{238}\text{U}$ age of 140.4 ± 2.4 Ma which may be an antecryst zircon from earlier magmatism. The zircon grains show autocryst texture (Miller et al., 2007), thus this weighted-mean age (128 Ma) could be interpreted as the crystallization age of the quartz monzonite from the Laiyuan complex. A total of 30 spots from sample LY-33/1 (syenogranite) yielded a weighted mean $^{206}\text{Pb}/^{238}\text{U}$ age of 133.1 ± 0.5 Ma (MSWD=1.5) with ages ranging from 135.3 to 130.6 Ma (Fig. 5-3b). This Early Cretaceous age (133 Ma) is taken to represent the crystallization age of the syenogranite. Zircon grains from sample LY-36/1 (syenogranite) show a large range of $^{206}\text{Pb}/^{238}\text{U}$ ages from 137.5 to 125.3 Ma, therefore cannot yield a weighted mean age (Fig. 5-3c). It is suggested that a

long-lived granitic magmatism existed and the Early Cretaceous age of ~125 Ma could be regarded as the emplacement age of the granitic magma. A total of 35 zircon spots were analyzed for U-Pb dating for sample LY-42/1 and the data show two clusters of ages. The younger group of 13 concordant spots yielded a weighted-mean $^{206}\text{Pb}/^{238}\text{U}$ age of 131.9 ± 0.9 Ma (MSWD=2.6) whereas the older population of 22 concordant spots yielded a weighted-mean $^{206}\text{Pb}/^{238}\text{U}$ age of 137.2 ± 0.6 Ma (MSWD=2.2) (Fig. 5-3d). The younger age (132 Ma) is interpreted as the crystallization age of monzonite, and the older age (137 Ma) represents an earlier magmatic event. The monzogranite sample (LYN-1/3) yield a weighted-mean $^{206}\text{Pb}/^{238}\text{U}$ age of 128.2 ± 0.7 Ma (MSWD=2.2) with ages ranging from 133.2 to 123.8 Ma based on the analysis of 36 zircon spots (Fig. 5-3e). This dating result (128 Ma) also represents the crystallization age of the monzogranite.

In summary, these results suggest intense felsic magmatism during 137-128 Ma in the Laiyuan complex, generating diverse felsic magmas which crystallized and were emplaced as a wide variety of granitoids.

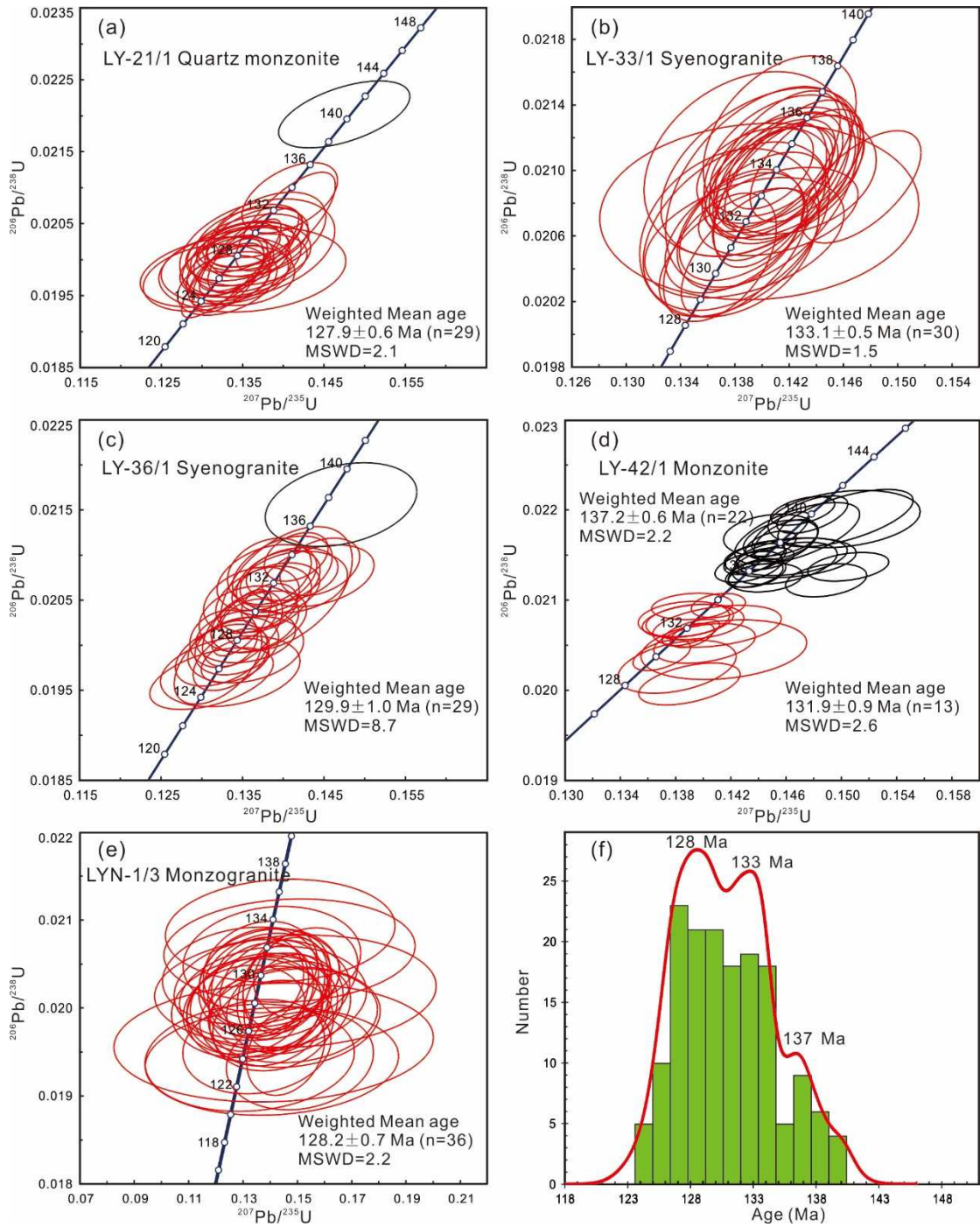


Fig. 5-3 U–Pb concordia plots and combined age data histogram with probability curves.

5.1.3 Dyke suites

Eleven samples of different dykes were selected for zircon geochronology and the zircon U-Pb data are listed in [Table 5-3](#). CL images of typical zircon grains and age data are plotted in [Fig. 5-4](#) to [Fig. 5-11](#).

5.1.3.1 Lamprophyre

The size of zircon grains in the lamprophyre sample LY-8/1 ranges from 50 to 120 μm in length and from 25 to 60 μm in width, with an aspect ratio of 4:1 to 2:1. They display subhedral to xenomorphic morphology (Fig. 5-4). The grains are prismatic, colorless, and transparent, and a few grains display oval shape. Based on zoning texture, the zircons grains can be divided into two groups. Some grains show faint and board zoning whereas others display typical magmatic growth zoning. Core-rim texture is uncommon in these zircons. Most of the zircon grains are autocrysts but zircon of spot 25 (116 ± 2 Ma) shows a typical antecryst texture indicating that it came from earlier magmatic pluses (Miller et al., 2007). A total of 28 zircon spots were analyzed for U-Pb dating and the data show two groups of ages. The younger group of 7 concordant spots yielded a weighted-mean $^{206}\text{Pb}/^{238}\text{U}$ age of 112.2 ± 0.9 Ma (MSWD=0.2) with Th/U ratios ranging from 0.21 to 1.71 (Fig. 5-5), whereas the older population of 13 concordant spots yielded a weighted-mean $^{206}\text{Pb}/^{238}\text{U}$ age of 117.3 ± 1.1 Ma (MSWD=2.0) with Th/U ratios ranging from 0.10 to 1.84. The younger age is interpreted as the emplacement age of lamprophyre whereas the older age represents an earlier magmatic event.

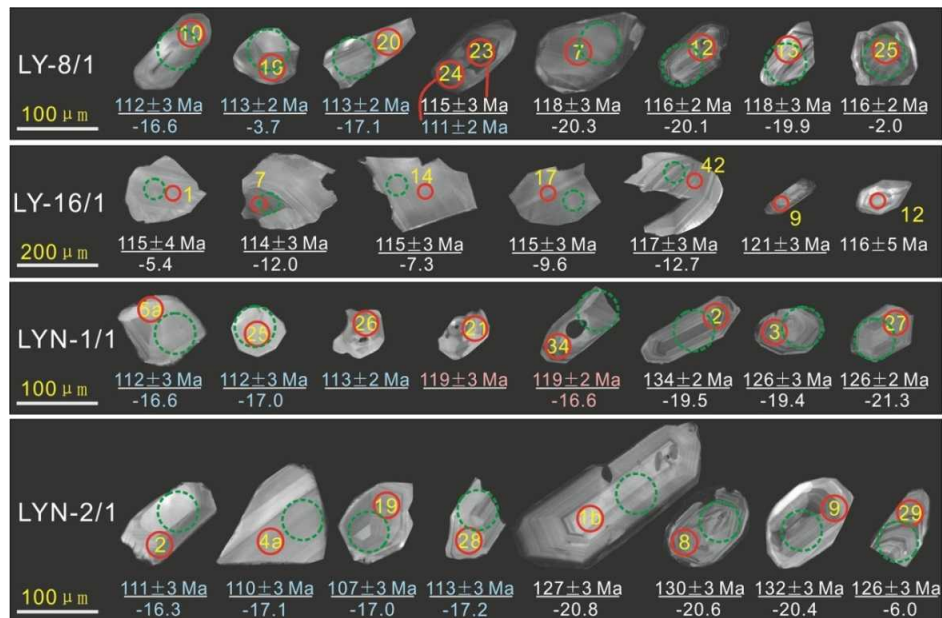


Fig. 5-4 Representative CL images of zircon grains from lamprophyres showing ages and $\epsilon_{\text{Hf}}(t)$ values. The larger circles represent locations of Hf isotopic analyses, whereas the smaller circles indicate spots of U-Pb dating.

Zircon grains from sample LY-16/1 (lamprophyre) occur as xenomorphic, colorless, and transparent crystals with faint and board zoning texture. The size of the zircon grains ranges from 150 to 200 μm in length and from 150 to 250 μm in width, with an aspect ratio of 1:1 to 1.5:1 (Fig. 5-4). Most of the zircon grains are autocrysts but zircon grains of spots 9 and 12 are antecrysts from earlier magmatic pluses. A total of 40 spots yielded a weighted-mean $^{206}\text{Pb}/^{238}\text{U}$ age of 114.5 ± 1.0 Ma (MSWD=3.0) with Th/U ratios ranging from 0.34 to 1.92 which is consistent with other ages of lamprophyres (Fig. 5-5). The Early Cretaceous is taken to represent the emplacement age of the lamprophyre.

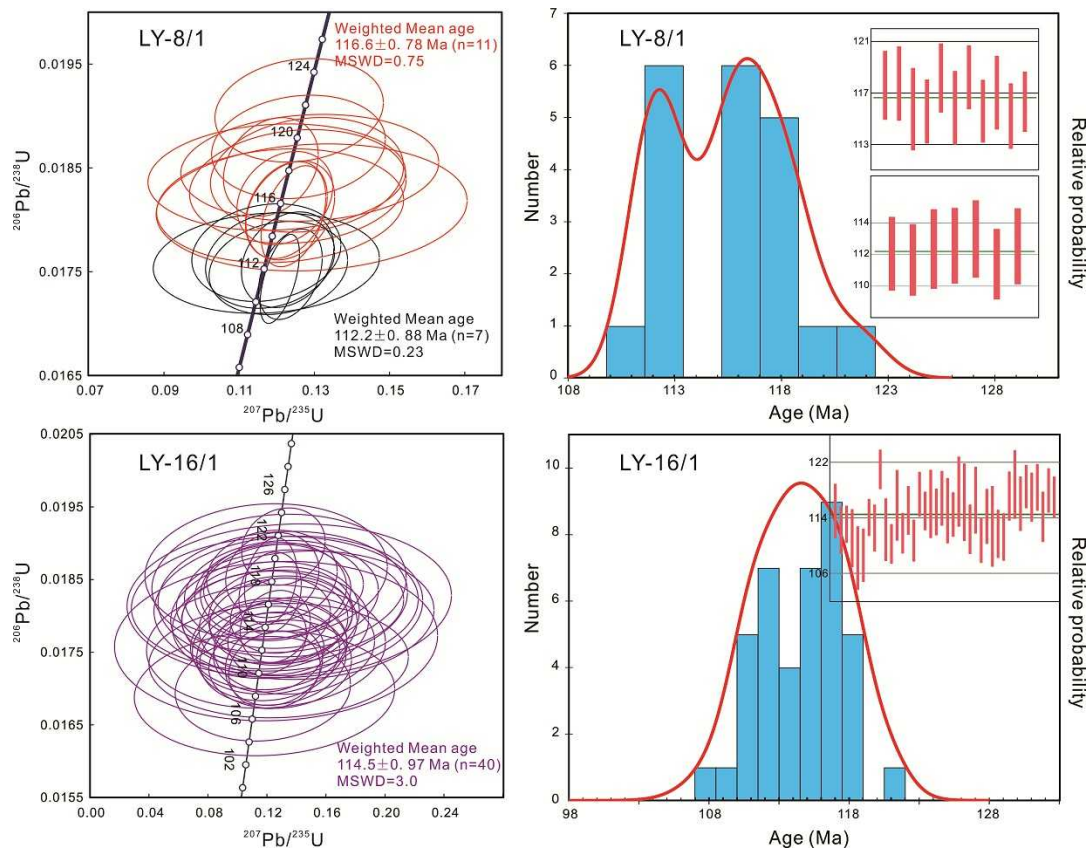


Fig. 5-5 U–Pb concordia plots and age data histograms with probability curves for samples LY-8/1 and LY-16/1 (lamprophyre dykes).

Zircon grains from sample LYN-1/1 show complex textures in CL images. Some grains show typical growth zoning texture surrounded by bright domains of rims (Spot 2). They are prismatic, euhedral to subhedral, off-white colored and translucent

with length ranging from 50 to 100 μm and width from 20 to 50 μm , with an aspect ratio of 3:1 to 1.5:1 (Fig. 5-4). The spot ages of this type of zircons range from 122 to 134 Ma yielding a weighted-mean $^{206}\text{Pb}/^{238}\text{U}$ age of 126.4 ± 1.1 Ma (MSWD=2.0, $n=15$, Fig. 5-6) and Th/U ratios varies from 0.31 to 1.38 indicating magmatic origin (Corfu, 2003). They are zircon antecrysts which were formed in an earlier magmatic event. In contrast, some grains exhibit different features of light gray color, faint zoning texture, and subhedral shape. The size of these zircon grains ranges from 50 to 70 μm in length and 20 to 40 μm in width, with an aspect ratio of 3:1 to 1:1. Their spot ages range from 117 to 119 Ma with a weighted-mean $^{206}\text{Pb}/^{238}\text{U}$ age of 118.5 ± 1.2 Ma (MSWD=0.51, $n=5$) with Th/U ratios in the range of 0.68 to 1.23 (Fig. 5-6). This age can be interpreted as another magmatic pulse. Another group of zircons can be identified. They are colorless and transparent, with faint zoning and xenomorphic appearance with a size range of 50-70 $\mu\text{m} \times$ 40-50 μm and aspect ratios of about 1:1. They yield a weighted-mean $^{206}\text{Pb}/^{238}\text{U}$ age of 112.8 ± 1.3 Ma (MSWD=0.38, $n=4$) with Th/U ratios varying from 0.82 to 1.59 (Fig. 5-6). Since these grains define the youngest magmatic group in this rock, the ca. 112 Ma age is interpreted as the emplacement age of the lamprophyre.

Based on the different zoning textures, zircon grains from sample LYN-2/1 can be divided into two distinct populations. One group possesses a typical and well-developed magmatic oscillatory zoning texture with a size range of 50-150 $\mu\text{m} \times$ 30-60 μm and aspect ratios of 3:1 to 1.5:1 (Fig. 5-4). They are subhedral to euhedral, prismatic, transparent, and colorless, and do not show any core-rim texture. Fourteen zircon grains belonging to this group yield a weighted-mean $^{206}\text{Pb}/^{238}\text{U}$ age of 128.6 ± 1.3 Ma (MSWD=2.9) and spot ages ranging from 132 to 125 Ma (Fig. 5-6). Their Th/U ratios range from 0.29 to 1.23 indicating their same magmatic origin. In contrast, the other group of zircon grains shows weak magmatic oscillatory zoning and the grains are bright and colorless, transparent, and xenomorphic. They range in size from 30 to 150 μm in length and from 30 to 60 μm in width with aspect ratios of 2:1 to 1:1. Th/U ratios of this group range from 0.33 to 1.52. The $^{206}\text{Pb}/^{238}\text{U}$ ages for

this group are younger than those of the other group yielding a weighted-mean age of 111.0 ± 1.2 Ma (MSWD=3, n=13, Fig. 5-6). Among these two groups, the older zircon grains are regarded as antecrysts or xenocrysts of an earlier magmatic event, whereas the younger zircon grains are autocrysts of the lamprophyre magma. It is also noted in particular that there are no older inherited zircon grains from the Precambrian basement. The Early Cretaceous age of 110 Ma is interpreted as the age of emplacement of lamprophyre.

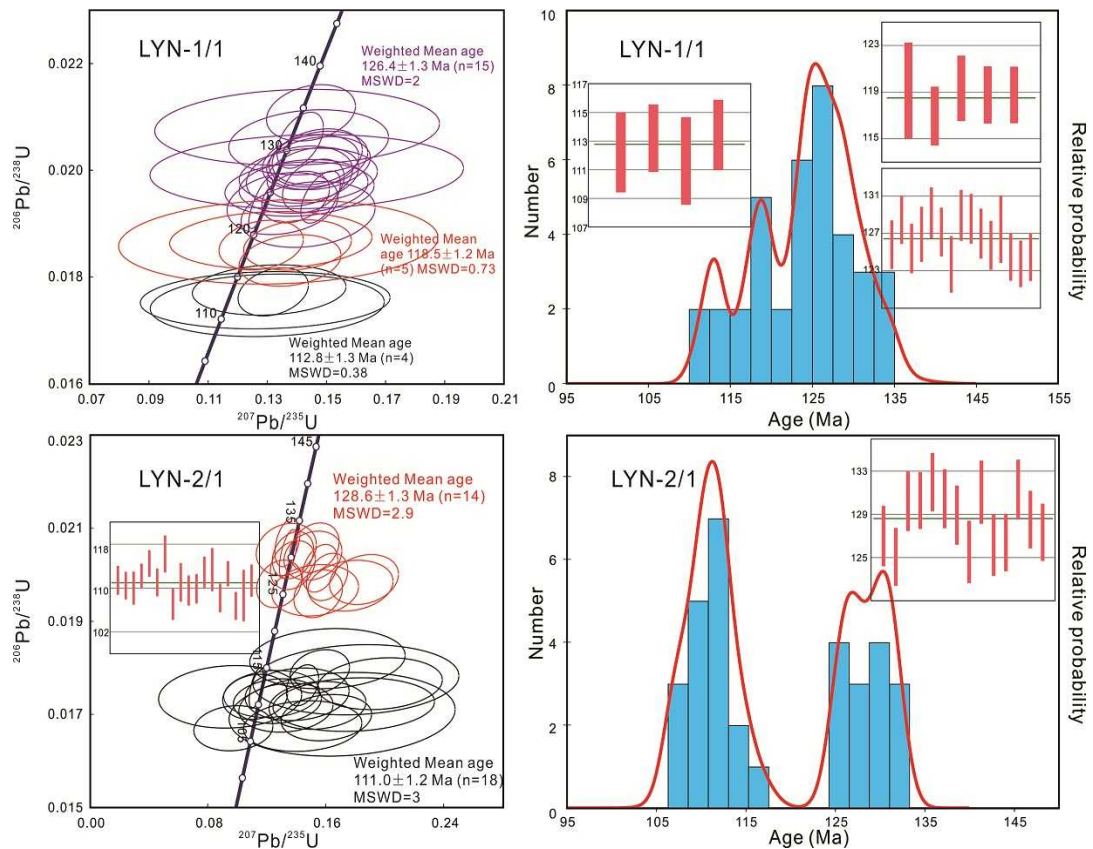


Fig. 5-6 U–Pb concordia plots and age data histograms with probability curves for samples LYN-1/1 and LYN-2/1 (lamprophyre dykes).

5.1.3.2 Dolerite and dolerite porphyry

Zircons grains from LY-15/1 (dolerite porphyry) are generally euhedral, prismatic, and transparent to translucent, and range in size from 50 to 150 μm with length to width ratios of about 3:1 to 1:1 (Fig. 5-7). In CL images, magmatic oscillatory zoning is clearly seen without any dark residual zircon cores. The zircon grains show large

ranges of Th (67-744 ppm) and U (68-1275 ppm) contents, with Th/U ratios varying from 0.54 to 2.02, suggesting a magmatic origin. Based on 27 concordant spots, a weighted-mean $^{206}\text{Pb}/^{238}\text{U}$ age of 125.2 ± 1.0 Ma (MSWD=3.8, Fig. 5-8) is obtained. The Early Cretaceous age can be interpreted as the emplacement age of the dolerite. The rock also contains older xenocryst grain with an age of 2560 ± 38 Ma ($^{207}\text{Pb}/^{206}\text{Pb}$ age) derived from the Precambrian basement of the NCC.

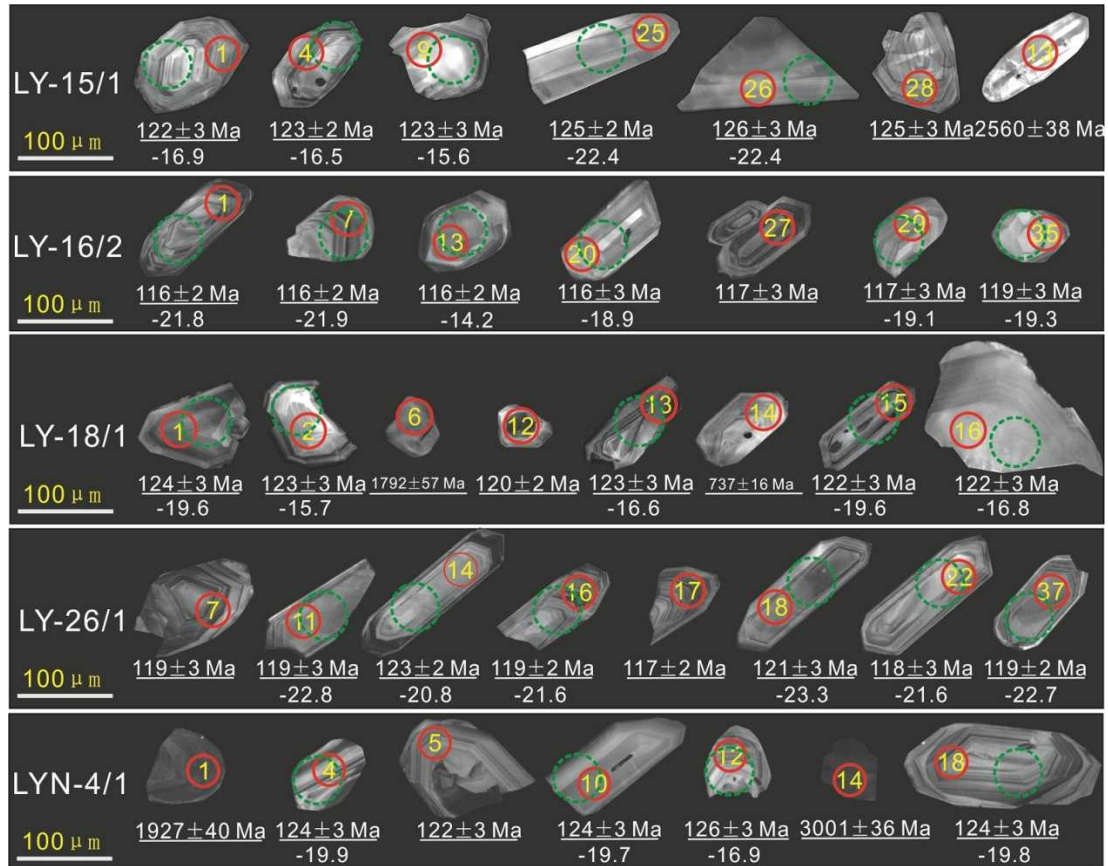


Fig. 5-7 Representative CL images of zircon grains from dolerites or diabase porphyries showing ages and $\epsilon_{\text{Hf}}(t)$ values.

Zircon grains from LY-16/2 (dolerite porphyry) are light gray, long-prismatic, euhedral to subhedral, and transparent to translucent. They show size ranges of 50-150 μm in length and 20-50 μm in width with aspect ratios of 4:1 to 2:1 (Fig. 5-7). Magmatic oscillatory zoning can be noted in almost all grains. A total of 36 grains were analyzed, which yield a weighted-mean $^{206}\text{Pb}/^{238}\text{U}$ age of 116.6 ± 0.7 Ma (MSWD=2.5, Fig. 5-8) with wide ranges of Th (47-923 ppm) and U (50-1465 ppm)

contents and Th/U ratios of 0.32 to 1.72 (only 3 spots among 34 spots show values over 1.0). There are no older inherited zircon grains in this sample, and the age of 116.6 Ma from the autocrusts is considered to represent the emplacement age of the magma.

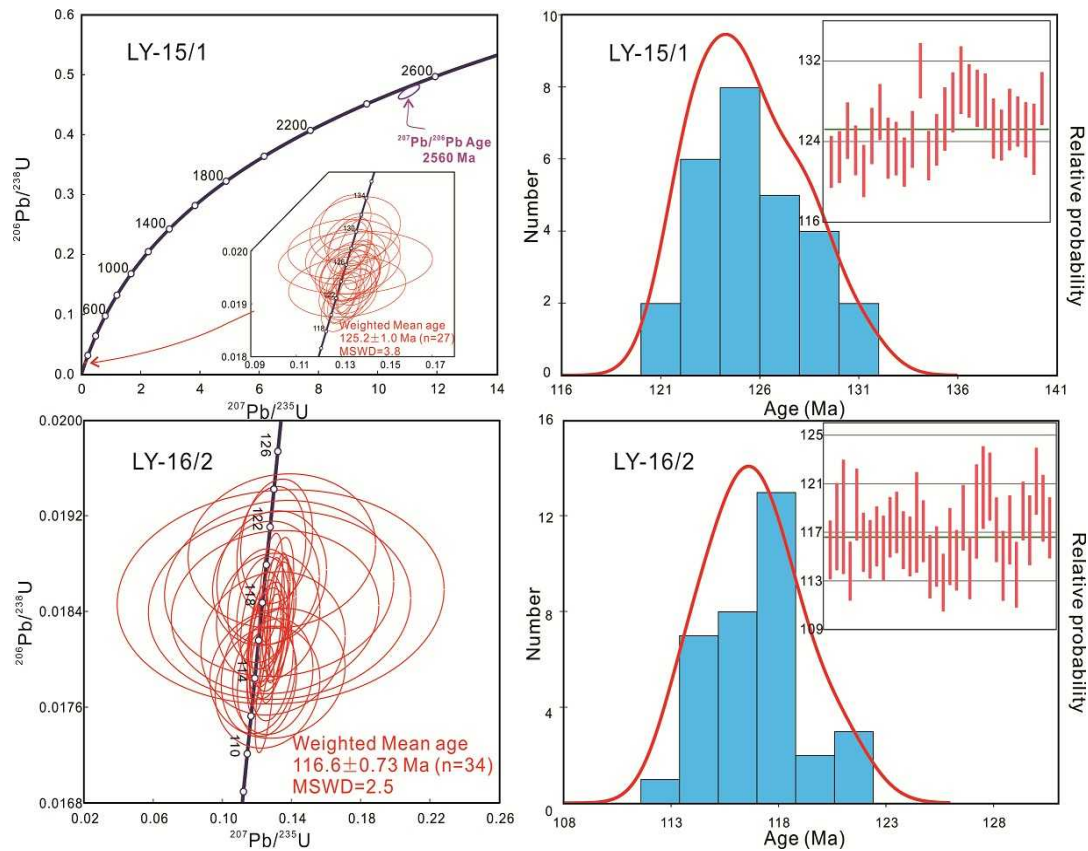


Fig. 5-8 U-Pb concordia plots and age data histograms with probability curves for samples LY-15/1 and LY-16/2 (dolerite dykes).

Zircon grains in sample LY-18/1 (dolerite) are about 50-150 μm long and 20-80 μm wide with aspect ratios of 2.5:1 to 1:1. Most of them are prismatic to sub-rounded, generally euhedral to subhedral, light gray colored, and transparent with light oscillatory zoning (Fig. 5-7). The Th/U ratios of zircon grains range from 0.69 to 1.26 with U and Th contents varying between 28 to 972 ppm and 61 to 1060 ppm, respectively. Twenty-four zircon grains were analyzed among which only 12 spots show concordant values. Two grains yielded a $^{207}\text{Pb}/^{206}\text{Pb}$ age of 1792 ± 52 Ma (spot 6) and a $^{206}\text{Pb}/^{238}\text{U}$ age of 737 ± 16 Ma (spot 14). Based on their CL images, they are

regarded as residual grains from other rocks possibly trapped in the magma. Therefore, spot 6 and spot 14 might correspond to metamorphic and magmatic zircons, respectively. Ten concordant data points form a tight cluster with a weighted-mean $^{206}\text{Pb}/^{238}\text{U}$ age of 122.5 ± 1.2 Ma (MSWD=1.4, Fig. 5-9). These zircon grains do not possess any inherited cores indicating they are autocrysts of mafic magma emplacement (Miller et al., 2007).

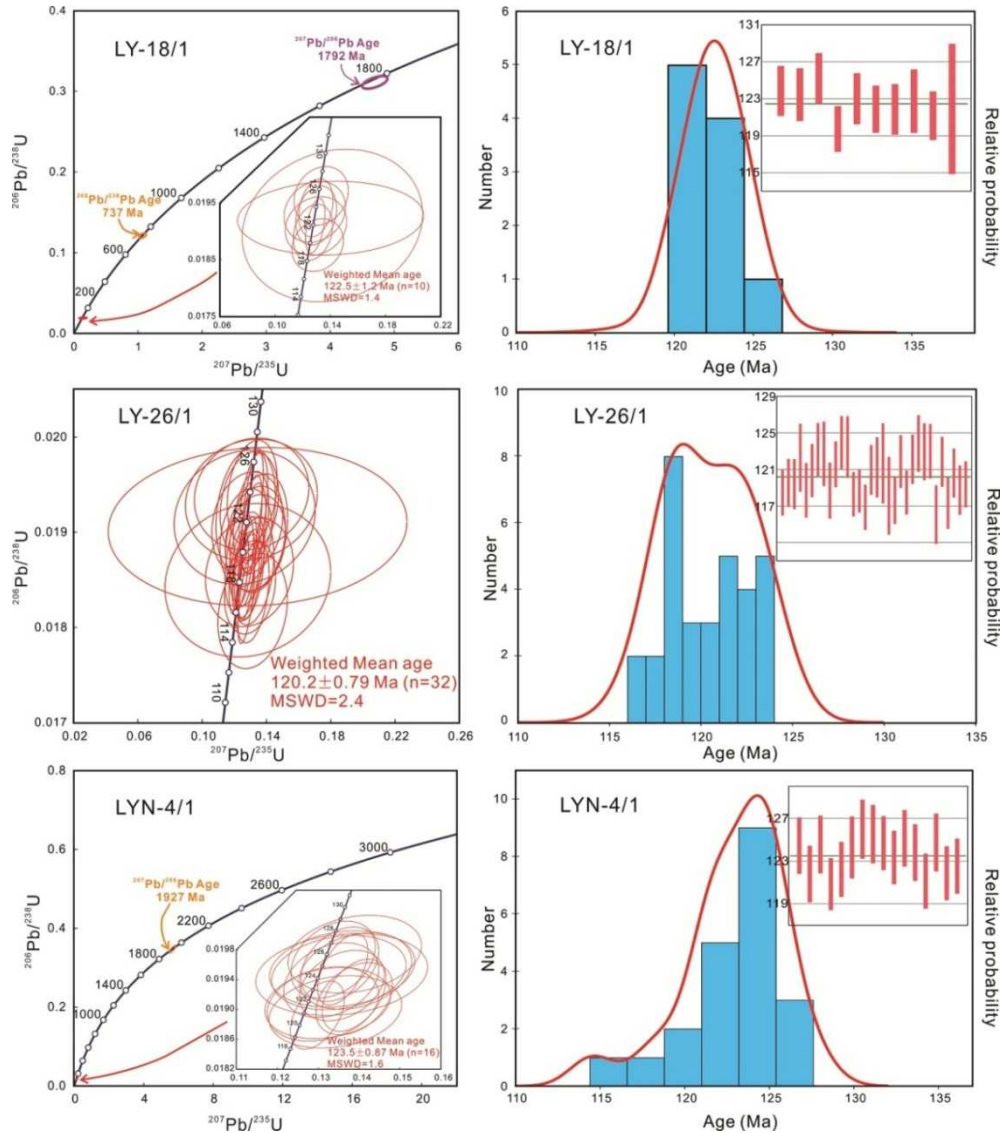


Fig. 5-9 U-Pb concordia plots and age data histograms with probability curves for samples LY-18/1, LY-26/1 and LYN-4/1 (dolerite dykes).

Zircons from dolerite (sample LY-26/1) exhibit similar morphology, mostly

ehedral, prismatic, coreless, transparent, and up to 100 μm in length with aspect ratios of 4:1 to 2:1. They show parallel growth zones from core to rim containing few resorbed zircon cores (Fig. 5-7). Thirty-four analyses on 32 zircon grains exhibit wide ranges in U (33 to 896 ppm) and Th (44 to 1476 ppm) concentration, and Th/U ratios of 0.31 to 2.07. The spot ages range from 124 to 116 Ma with a weighted-mean $^{206}\text{Pb}/^{238}\text{U}$ age of 120.2 ± 0.8 Ma (MSWD=2.4) (Fig. 5-9). The 120 Ma age is taken to represent the timing of formation of the rock.

Zircon crystals from diabase (sample LYN-4/1) show euhedral morphology, light gray color, and length up to 150 μm with length:width ratios of 3:1 to 1:1. In CL images, the grains show typical uniform oscillatory zoning, indicating magmatic origin (Fig. 5-7). Twenty-four spots were analyzed on 24 zircon grains among which 18 analyses yielded concordant ages. One xenocryst yielded a $^{207}\text{Pb}/^{206}\text{Pb}$ age of 1927 ± 40 Ma (spot 1) which is considered to be inherited from the Paleoproterozoic basement rocks of the NCC. Sixteen analyses gave a weighted mean $^{206}\text{Pb}/^{238}\text{U}$ age of 123.5 ± 0.9 Ma (MSWD=1.6) and the spot ages range from 121 to 126 Ma with Th/U ratios of 0.51 to 1.12 (Fig. 5-9). And this Early Cretaceous age of 124 Ma can be considered as the emplacement age of the mafic magma.

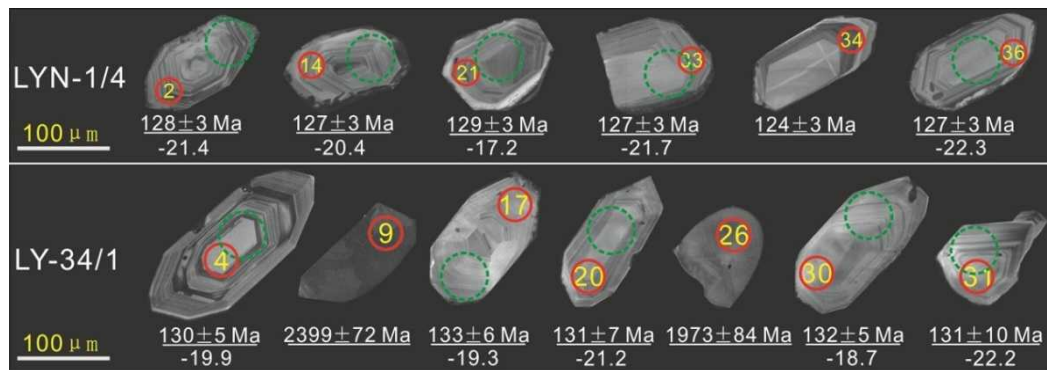


Fig. 5-10 Representative CL images of zircon grains from felsic dykes showing ages and $\epsilon_{\text{Hf}}(t)$ values.

5.1.3.3 Felsic dykes

Most of the zircon grains from the felsic dykes (samples LY-34/1 and LYN-1/4) are euhedral to subhedral, light gray colored, and transparent, and range in length from 50 to 120 μm and from 40 to 100 μm in width with aspect ratios of 2:1 to 1:1.

Almost all grains possess thick oscillatory zoning from core to rim without resorbed cores (Fig. 5-10). They are homogeneous suggesting crystallization from a single magmatic event. A total of 33 analyses were conducted on zircon grains in sample LY-34/1, among which two spots were excluded because of their high discordance. Also, two xenocrysts in sample LY-34/1 without zoning texture and indicating metamorphic origin show $^{207}\text{Pb}/^{206}\text{Pb}$ ages of 2399 ± 72 Ma (spot 9) and 1973 ± 84 Ma (spot 26). Other 29 spots in sample LY-34/1 yielded a weighted-mean $^{206}\text{Pb}/^{238}\text{U}$ age of 130.6 ± 1.0 Ma (MSWD=1.1, Fig. 5-11) with spot ages ranging from 135 to 123 Ma and tight Th/U ratios of 0.64 to 1.46. A total of 40 spots from 40 zircon grains were analyzed in sample LYN-1/4 and 5 spots were excluded due to high discordance. The remaining 35 spots show spot ages ranging from 131 to 122 Ma and a weighted mean $^{206}\text{Pb}/^{238}\text{U}$ age of 126.9 ± 0.8 Ma (MSWD=2.8). The data show Th/U ratios in the range of 0.65 to 1.62 (Fig. 5-11). The Cretaceous ages of 127 Ma and 131 Ma may mark the emplacement ages of samples LYN-4/1 and LY-34/1.

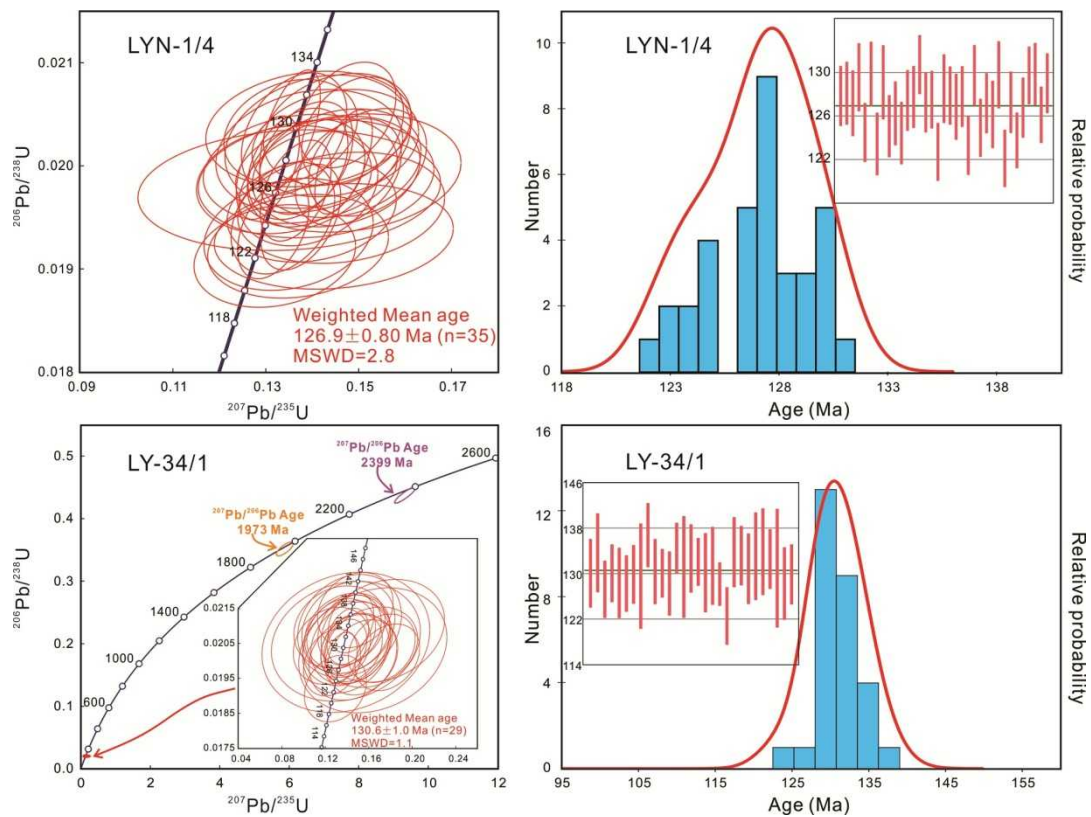


Fig. 5-11 U-Pb concordia plots and age data histograms with probability curves for samples LYN-1/4 and LY-34/1 (felsic dykes).

5.2 Temporal links between diverse magmatic suites

Several geochronological studies have been conducted in the Laiyuan complex focusing on the ultramafic-mafic rocks (Chen et al., 2005; Hou et al., 2015; Zhang, 2014), intermediate-felsic granitoids (Chen et al., 2009b; Chen et al., 2005; Chen et al., 2007a; Qu, 2012; Zhang et al., 2016; Zhang, 2014), volcanic and sub-volcanic rocks (Dong et al., 2013; Duan et al., 2016; Gao et al., 2012; Gao et al., 2013; Gao et al., 2011; Huang, 2014; Song et al., 2014), and mafic-felsic dyke suites. By combining available dating results yielded from this study and literatures (Table 5-4), the temporal connection between diverse magmatic suites could be established (Fig. 5-12).

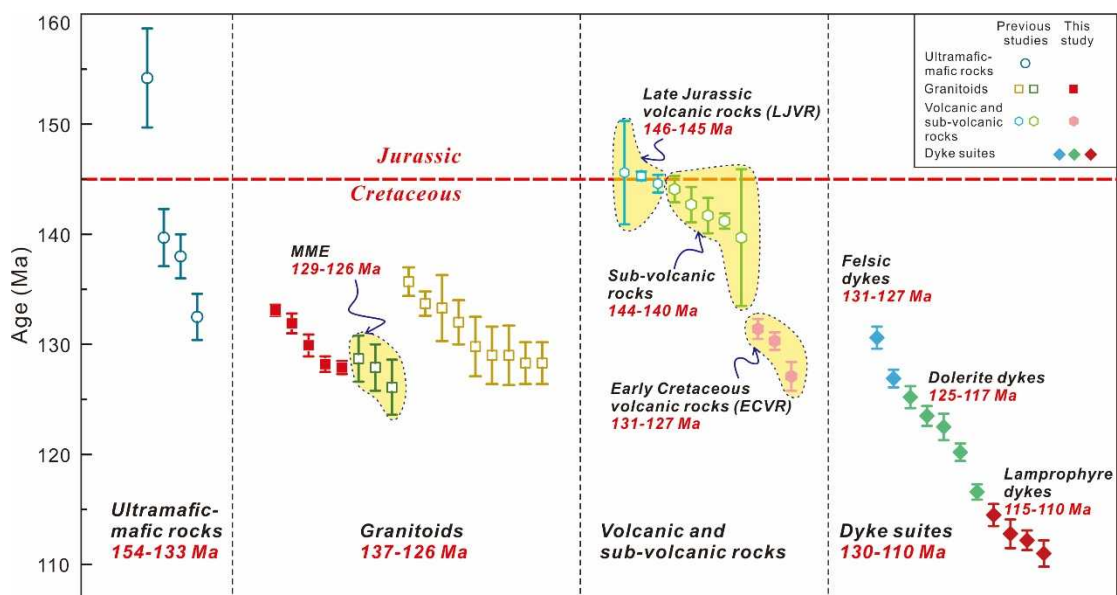


Fig. 5-12 Compilation of age data on magmatic rocks including data from literatures and this study.

The data are listed in Table 5-4.

The ultramafic-mafic rocks are majorly exposed in Longmengou and Yaogou areas with lithology dominated by hornblendite, pyroxenite, gabbro, and gabbroic diorite occurring as isolated bodies around the complex (Liu et al., 2010; Liu et al., 2009a; Zhai et al., 2014; Zhang et al., 2017). Hou et al. (2015) yielded hornblende ^{40}Ar - ^{39}Ar ages of 154 and 133 Ma from the Yaogou hornblendite, and Chen et al. (2005) and Zhang (2014) dated the Longmengou gabbro and gabbroic diorite at 138

Ma and 140 Ma, respectively. At Yaogou area, the hornblendite intrusions occurred as variously sized enclaves or rock bodies scattered in the mafic intrusions which were intruded by ~132 Ma granitoids (Hou et al., 2015). Similarly, the Longmengou pyroxenites were entrained by mafic intrusions that intruded the Proterozoic metamorphic basement and surrounding diorites (Fig. 3-1). The field and petrographical investigations indicate that these ultramafic-mafic bodies resulted from independent magmatic events, rather than xenoliths captured by the surrounding granitoids (Zhai et al., 2014; Zhang et al., 2017). As indicated by the spatial and temporal relationships, the ultramafic-mafic rocks act as the earliest intrusive phases of the magmatic evolutionary series in the Laiyuan complex ranging from Late Jurassic to Early Cretaceous (154-133 Ma).

The earliest intrusive phases were followed by Late Jurassic volcanic episode (146-145 Ma, Fig. 5-12) in some places within the complex. This volcanic episode was characterized by andesitic-dacitic-rhyolitic lava eruption accounting for the typical Mujicun caldera which is composed of welded breccias, ignimbrite sheets, and lava flows (Gao et al., 2012). The lava flows erupted from cinder cones and domes within the caldera and on the external flanks of the collapsed caldera. Within the volcanic edifice, a half ring of small sub-volcanic stocks and plugs associated with porphyry Cu-Mo deposits is found around the collapsed caldera. The emplacement of sub-volcanic suites including quartz diorite porphyry, diorite porphyry, and rhyolite porphyry took place at ~144-140 Ma following the eruption of andesitic-dacitic magmas. In the NCC, the volcanism was intense at Late Jurassic contributing to the widespread exposures of volcanic strata referred to as Tiaojishan Formation (Dong et al., 2018; Duan et al., 2016; Gao et al., 2012; Wu et al., 2019) (Fig. 5-13). Lithostratigraphic and geochronological correlations indicate that the Late Jurassic volcanic rocks (LJVR) in the Laiyuan complex are equivalent to the Tiaojishan Formation (Fig. 5-13).

This study also identified another volcanic episode which was dated at Early Cretaceous (131-127 Ma) showing a ~15 Myrs. temporal gap with earlier eruptions

(Fig. 5-12). They were outcropped at the northern domain of the Sigezhuang pluton (Fig. 3-1). Apparently, the Early Cretaceous volcanic rocks (ECVR) are illogical to belong to the Tiaojiashan Formation whereas their lithological and geochronological features are consistent with the Zhangjiakou Formation which was majorly distributed in the central and northern margins of the NCC (Fig. 5-13).

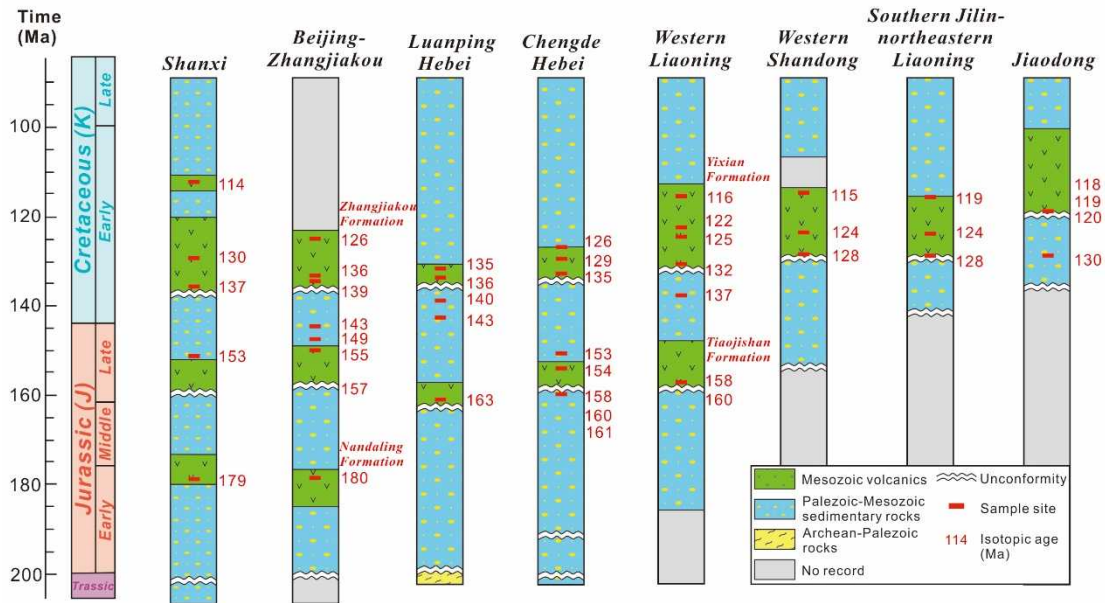


Fig. 5-13 Stratigraphic columns for the late Mesozoic volcanic-sedimentary rocks across the NCC (after Wu et al., 2019). Three episodes of volcanic rocks are the Nandaling (intraplate basalt), Tiaojiashan, and Zhangjiakou/Yixian Formations.

In addition to the volcanism, the Early Cretaceous witnessed the magmatic peak in the Laiyuan complex as well (Fig. 5-12). After the Late Jurassic volcanism and related sub-volcanic emplacement, the Early Cretaceous (~137-126 Ma) intermediate-felsic magmatic event dominated the formation of the Laiyuan complex occurring as concentrically-zoned granitoids that constitute the most of the plutonic-volcanic complex (Fig. 3-1). Contact boundaries between these synchronous various intrusive suites are legible and clear (Fig. 3-4e) which are called pulsating contact relationship indicating the compositional diversities of granitoids stem from multiple magmatic rather than simple crystallization differentiation of single magma. The MMEs contained in the granitoids were dominated by diorite and quartz

monzonite and simultaneous with the host rocks. It is noteworthy that the MMEs, ECVR, and felsic dykes which all display andesitic-dacitic lithology, were formed at the same time (~131-126 Ma). Geochronological, petrological, and spatial connections imply their concordance in the petrogenesis. They are of different forms (enclaves, dykes, and lavas) but sharing similar magma source and petrogenesis.

Mafic dyking events were developed after the major parts of the complex established occurring as dolerite and lamprophyre dykes. Obtained data suggest a long-lived mafic magmatic event in the Laiyuan complex from 125 to 117 Ma generating the dolerite dyke suite (Fig. 5-12). In contrast to the dolerites, the lamprophyres are characterized by a limited and younger range of ages from 115 to 110 Ma (Fig. 5-12). Compared with the mafic intrusions, granitoids, and volcanic suites, these tiny dykes only account for insignificant proportions of the complex, however these widespread mafic dyking events throughout the complex and even intruding the country rocks (Fig. 3-1) suggest a common and continuous mafic dyking magmatism from 125 to 110 Ma in the NTM (Yang, 1989; Yang, 1991; Zhang et al., 2003b). In terms of geochronological aspect, this younger mafic magmatic event is distinct from the earlier mafic magmatism reducing the possibility of direct petrogenetic link between these two mafic magmatic events.

The compiled and new radiometric age data, combined with field observations, define a complicated history of magmatism for the Laiyuan complex, beginning with hornblendite and pyroxenite formation at ~154 Ma, then the first proceeding to eruption of andesitic-dacitic-rhyolitic lavas at ~146 Ma and emplacement of ore-related sub-volcanic rocks at ~144 Ma, reaching the peak with the intrusion of large, concentrically-zoned granitoids from ~137 to 126 Ma, following the second episode of volcanism at ~130 Ma, and concluding with the tiny but widespread mafic dyking events from ~125 to 110 Ma. To illuminate the spatio-temporal links between diverse magmatic suites is the postulate to investigate the petrogenetic relationships, and the indepth tectonic universality.

Table 5-4 Compilation of age data of the Laiyuan magmatic rocks.

No.	Locations	Rock types	Ages	2 σ	Methods	References
1	Longmengou	Hornblendite	154.2	4.5	Hbl Ar-Ar	(Hou et al., 2015)
2	Longmengou	Hornblende gabbro	139.7	2.6	LA-ICP-MS Zircon U-Pb	(Zhang, 2014)
3	Longmengou	Gabbro	138.0	2.0	SHRIMP Zircon U-Pb	(Chen et al., 2005)
4	Longmengou	Hornblendite	132.5	2.1	Hbl Ar-Ar	(Hou et al., 2015)
5	Sigezhuang pluton	Syenogranite	133.1	0.5	LA-ICP-MS Zircon U-Pb	This study
6	Sigezhuang pluton	Monzonite	131.9	0.9	LA-ICP-MS Zircon U-Pb	This study
7	Sigezhuang pluton	Syenogranite	129.9	1.0	LA-ICP-MS Zircon U-Pb	This study
8	Sigezhuang pluton	Monzogranite	128.2	0.7	LA-ICP-MS Zircon U-Pb	This study
9	Sigezhuang pluton	Quartz monzonite	127.9	0.6	LA-ICP-MS Zircon U-Pb	This study
10	Sigezhuang pluton	MME	128.7	2.1	SHRIMP Zircon U-Pb	(Chen et al., 2009b)
11	Sigezhuang pluton	MME	127.9	2.1	SHRIMP Zircon U-Pb	(Chen et al., 2009b)
12	Sigezhuang pluton	MME	126.1	2.5	SHRIMP Zircon U-Pb	(Chen et al., 2007b)
13	Wanganzhen pluton	Granodiorite	135.7	1.3	SHRIMP Zircon U-Pb	(Shen et al., 2015a)
14	Wanganzhen pluton	Monzogranite	133.7	1.1	SHRIMP Zircon U-Pb	(Shen et al., 2015a)
15	Wanganzhen pluton	Monzonite	133.3	3.0	LA-ICP-MS Zircon U-Pb	(Qu, 2012)
16	Sigezhuang pluton	Quartz monzonite	132.0	2.0	SHRIMP Zircon U-Pb	(Chen et al., 2005)
17	Wanganzhen pluton	Monzogranite	129.8	2.7	LA-ICP-MS Zircon U-Pb	(Zhang, 2014)
18	Wanganzhen pluton	Monzonite	129.0	2.6	SHRIMP Zircon U-Pb	(Chen et al., 2005)
19	Wanganzhen pluton	Granodiorite	129.0	2.7	LA-ICP-MS Zircon U-Pb	(Zhang et al., 2016)
20	Wanganzhen pluton	Quartz diorite	128.3	1.9	LA-ICP-MS Zircon U-Pb	(Zhang et al., 2016)
21	Wanganzhen pluton	Granodiorite	128.3	1.9	LA-ICP-MS Zircon U-Pb	(Zhang, 2014)
22	Wanganzhen pluton	Andesite	145.6	4.7	LA-ICP-MS Zircon U-Pb	(Gao et al., 2012)
23	Wanganzhen pluton	Andesite	145.3	0.4	LA-ICP-MS Zircon U-Pb	(Duan et al., 2016)
24	Wanganzhen pluton	Andesite	144.6	0.8	LA-ICP-MS Zircon U-Pb	(Duan et al., 2016)
25	Mujicun	Diorite porphyry	144.1	1.2	LA-ICP-MS Zircon U-Pb	(Dong et al., 2013)
26	Mujicun	Diorite porphyry	142.7	1.6	LA-ICP-MS Zircon U-Pb	(Gao et al., 2013)
27	Mujicun	Diorite porphyry	141.7	1.6	LA-ICP-MS Zircon U-Pb	(Gao et al., 2011)
28	Dawan	Rhyolite porphyry	141.2	0.7	LA-ICP-MS Zircon U-Pb	(Song et al., 2014)
29	Dawan	Rhyolite porphyry	139.7	6.2	Whole-rock Rb-Sr	(Huang, 2014)
30	Sigezhuang pluton	Andesite-dacite	131.4	0.9	LA-ICP-MS Zircon U-Pb	This study
31	Sigezhuang pluton	Andesite-dacite	130.3	0.8	LA-ICP-MS Zircon U-Pb	This study
32	Sigezhuang pluton	Andesite-dacite	127.1	1.3	LA-ICP-MS Zircon U-Pb	This study
33	Laiyuan complex	Felsic dyke	130.6	1.0	LA-ICP-MS Zircon U-Pb	This study
34	Laiyuan complex	Felsic dyke	126.9	0.8	LA-ICP-MS Zircon U-Pb	This study
35	Laiyuan complex	Dolerite	125.2	1.0	LA-ICP-MS Zircon U-Pb	This study
36	Laiyuan complex	Dolerite	123.5	0.9	LA-ICP-MS Zircon U-Pb	This study

37	Laiyuan complex	Dolerite	122.5	1.2	LA-ICP-MS Zircon U-Pb	This study
38	Laiyuan complex	Dolerite	120.2	0.8	LA-ICP-MS Zircon U-Pb	This study
39	Laiyuan complex	Dolerite	116.6	0.7	LA-ICP-MS Zircon U-Pb	This study
40	Laiyuan complex	Lamprophyre	114.5	1.0	LA-ICP-MS Zircon U-Pb	This study
41	Laiyuan complex	Lamprophyre	112.8	1.3	LA-ICP-MS Zircon U-Pb	This study
42	Laiyuan complex	Lamprophyre	112.2	0.9	LA-ICP-MS Zircon U-Pb	This study
43	Laiyuan complex	Lamprophyre	111.0	1.2	LA-ICP-MS Zircon U-Pb	This study

Chapter 6 Zircon Hf isotopic compositions of the Laiyuan complex

6.1 Zircon in-situ Lu-Hf isotopic results

In-situ zircon Lu-Hf isotope data for the volcanic rocks, dykes, and granitoids from the Laiyuan complex are listed in [Table 6-1](#). The Lu-Hf isotopes were analyzed in the same domains or adjacent domains of the zircon grains where U–Pb age data were obtained as shown in Chapter 5.

6.1.1 Volcanic rocks

Zircon Lu-Hf isotopic data are plotted in the $\epsilon_{\text{Hf}}(t)$ vs. age diagram ([Fig. 6-1](#)). Twelve zircon grains were selected for isotopic analysis including 6 spots from sample LYN-3/2 and 6 spots from sample LY-40/1 ([Fig. 5-1](#)). The initial $^{176}\text{Hf}/^{177}\text{Hf}$ ratios of samples LYN-3/2 and LY-40/1 vary from 0.282067 to 0.282144 and 0.282026 to 0.282121, respectively. The Hf crustal model ages (T_{DM}^{C}) range from 2586 to 2414 Ma (mean 2513 Ma) and from 2676 to 2465 Ma (mean 2557 Ma) for samples LYN-3/2 and LY-40/1. The $\epsilon_{\text{Hf}}(t)$ values are all negative and fall between -22.1 to -19.4 with an average value of -20.9 for sample LYN-3/2 and -23.5 to -20.2 with an average value of -21.6. The similar uniform Hf isotopic compositions suggest that they may share the same single magma source.

6.1.2 Granitoids

A total of forty-nine zircon grains from granitoids including ten from quartz monzonite (sample LY-21/1), twenty from syenogranite (samples LY-33/1 and LY-36/1), fourteen from monzonite (sample LY-42/1), and five from monzogranite (sample LYN-1/3) were analyzed for their Hf isotopic compositions. The variations of Hf isotopic compositions among different rock types are very small with narrow ranges of analytical results indicating the source similarity for the granitoids. The initial $^{176}\text{Hf}/^{177}\text{Hf}$ ratios vary from 0.282077 to 0.282213 (average value of 0.282132)

with $\epsilon_{\text{Hf}}(t)$ values ranging from -21.8 to -16.8. The T_{DM}^{C} show a range of 2564–2255 Ma (mean 2441 Ma).

6.1.3 Dyke suites

6.1.3.1 Lamprophyre

Twenty-six zircon grains were analyzed from lamprophyre including 7 from sample LY-8/1, 5 from sample LY-16/1, 6 from sample LYN-1/1, and 8 from sample LYN-2/1 (Fig. 5-4). Because of the multiple age groups, the features of Lu-Hf isotopes are different. Zircon grains with ages below 116 Ma show initial $^{176}\text{Hf}/^{177}\text{Hf}$ ratios in the range of 0.282215 to 0.282597. Their Hf crustal model ages (T_{DM}^{C}) show a range of 2268–1412 Ma (mean 2016 Ma). The $\epsilon_{\text{Hf}}(t)$ values are between -17.2 to -3.7 with an average value of -13.3 (Fig. 6-1). The variable $\epsilon_{\text{Hf}}(t)$ values of lamprophyres suggest that the source of lamprophyres is heterogeneous, and probably include mantle materials and crustal materials. The remaining zircon grains can be classified as two groups (Fig. 5-4). One population showing ages between 119 to 116 Ma is consistent with the emplacement ages of dolerite, with initial $^{176}\text{Hf}/^{177}\text{Hf}$ ratios in a tight cluster of 0.282126 to 0.282230. The T_{DM}^{C} show a range of 2462–2231 Ma (mean 2395 Ma). The $\epsilon_{\text{Hf}}(t)$ values are all negative ranging from -20.3 to -16.6 with a mean value of -19.2. The oldest group whose ages are above 126 Ma shows $\epsilon_{\text{Hf}}(t)$ values in the range of -21.3 to -19.4 with an average of -20.3. The T_{DM}^{C} range from 2534 to 2414 Ma (mean 2476 Ma), respectively. The initial $^{176}\text{Hf}/^{177}\text{Hf}$ ratios are between 0.282092 and 0.282146.

6.1.3.2 Dolerite

Twenty-six zircon grains were analyzed from dolerite or dolerite porphyry including 5 from sample LY-15/1, 6 from sample LY-16/2, 5 from sample LY-18/1, 6 from sample LY-26/1, and 4 from sample LYN-4/1 (Fig. 5-5). The results show initial $^{176}\text{Hf}/^{177}\text{Hf}$ ratios in the tight range of 0.282038 to 0.282298, and $\epsilon_{\text{Hf}}(t)$ values between -23.3 to -14.2 with an average value of -19.5 (Fig. 6-1). The T_{DM}^{C} show a range of 2656–2080 Ma (mean 2415 Ma). The Lu-Hf features are similar to the second group of zircons of lamprophyre suggesting that these zircon grains were

derived from the dolerites.

6.1.3.3 Felsic dykes

Ten zircon grains from felsic dykes (samples LY-34/1 and LYN-1/4) were analyzed for Lu-Hf isotopes (Fig. 5-6). The initial $^{176}\text{Hf}/^{177}\text{Hf}$ ratios vary from 0.282062 to 0.282205. The T_{DM}^{C} range from 2599 to 2279 Ma (mean 2482 Ma). The $\epsilon_{\text{Hf}}(t)$ values are all negative and fall between -22.3 to -17.2 with an average value of -20.4.

6.2 Source variations between diverse magmatic suites

The Lu-Hf isotopic composition of zircon provides significant imprints on the magma source variations. The variations and linkages of Hf isotopic compositions are brought out through the zircon $\epsilon_{\text{Hf}}(t)$ values vs. age diagram (Fig. 6-1). On the whole, the $\epsilon_{\text{Hf}}(t)$ values and Hf crustal model ages for the Laiyuan magmatic rocks are majorly in the ranges of -22.5 to -15.0 and 2.5 to 2.0 Ga, respectively. The negative zircon $\epsilon_{\text{Hf}}(t)$ values generally suggest that the magmas were not solely sourced from juvenile components such as juvenile crust or asthenospheric mantle, and may be primarily sourced from enriched lithospheric mantle with or without additions from fertile mafic lower crust. This inference is also supported by previous studies of Sr-Nd isotopes for various magmatic suites from the Laiyuan complex. The ultramafic cumulates, mafic intrusions, intermediate-felsic granitoids, and volcanic and sub-volcanic rocks fell near the EMI field in the Sr-Nd isotope diagram (Fig. 6-2) suggesting they may share a common basaltic magma derived from an enriched lithospheric mantle probably previously modified due to subduction (Foley et al., 2000; Hawkesworth et al., 1993; Schmidt et al., 2009). The contribution from the enriched lithospheric mantle plays a significant role in the formation of this complex, and this is the source connection throughout different magmatic units.

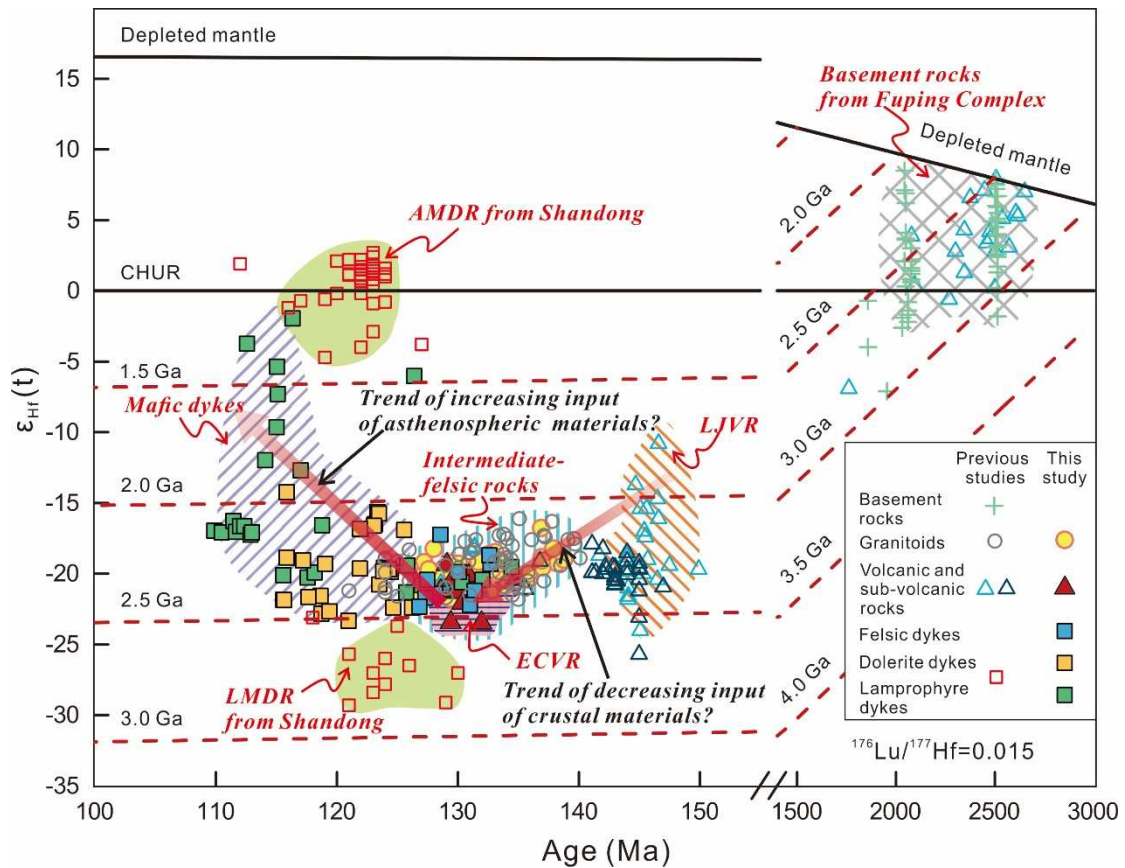


Fig. 6-1 Zircon $\epsilon_{\text{Hf}}(t)$ values vs. age diagram for the Laiyuan Mesozoic magmatic rocks compiled from previous studies and this study. Data sources: Basemen rocks of the Fuping Complex (Tang et al., 2015; Tang et al., 2016); Granitoids from the Laiyuan complex (this study; Shen et al., 2015a; Yang et al., 2019a); Late Jurassic volcanic rocks (Duan et al., 2016); Sub-volcanic rocks (Qu, 2012; Shen et al., 2015b); Early Cretaceous volcanic rocks (this study); Dyke suites from the Laiyuan complex (this study) and Shandong Peninsula (Ma et al., 2014a; Ma et al., 2016).

Despite the similarity in their source, the complexities in the source materials are also recorded in the changes of Hf isotopic compositions (Fig. 6-1). It is apparent that the zircon $\epsilon_{\text{Hf}}(t)$ values display reverse variation trends at ~130 Ma. From 150 to 130 Ma, the zircon $\epsilon_{\text{Hf}}(t)$ values are decreasing and changing from variable to uniform through time, whereas these values are increasing and changing from uniform to variable from 130 to 110 Ma. The distinct variation trends probably result from the involvement of multiple materials including crustal and asthenospheric components. The Late Jurassic volcanic rocks (LJVR) which were formed at ~146 Ma exhibit a

variable zircon $\epsilon_{\text{Hf}}(t)$ values ranging from -25 to -10 (Fig. 6-1). Besides, inherited zircon cores from basement rocks with ages in the range of ~2.65-2.08 Ga are common in these andesitic-dacitic rocks with positive $\epsilon_{\text{Hf}}(t)$ values (0-10) consistent with the values of basement rocks of the Fuping Complex (Fig. 6-1) suggesting juvenile source synchronous with the major crustal growth in the NCC (Geng et al., 2012; Tang et al., 2015; Tang et al., 2016; Zhao et al., 2012). In terms of the published Sr-Nd-Pb isotopic features, the ~146 Ma volcanic rocks are characterized by low radiogenic Pb and high radiogenic Sr isotopic composition which might result from enriched mantle-derived melts and lower crust melts (Gao et al., 2012). Therefore, the magma source for the LJVR involved both enriched lithospheric mantle and lower crustal components.

After ~140 Ma, the intermediate-felsic magmatism which generated the granitoids, the felsic dykes and the Early Cretaceous volcanic rocks (ECVR), was intensive and culminated at ~130 Ma. The zircon $\epsilon_{\text{Hf}}(t)$ values for the rocks during this period show a transformation to values ranging from -23.5 to -16.8 especially the ECVR (-23.5 to -19.4). Considering the major lithospheric mantle source, this variation trend could be interpreted as the decreasing contribution of crustal materials to the source. As illustrated in the whole rock Sr-Nd isotope diagram (Fig. 6-2), the granitoids are plotted in the field closer to the lower crustal components of the NCC than the LJVR suggesting the change of crustal materials. As a result, the decreasing input of lower crustal components account for the decreasing trend of zircon $\epsilon_{\text{Hf}}(t)$ values from the Laiyuan magmatic rocks.

The mafic dyke events took place in the complex after ~130 Ma and generated dolerites and lamprophyres showing disparate zircon Hf isotopic compositions. As illustrated in $\epsilon_{\text{Hf}}(t)$ vs. age diagram (Fig. 6-1), the Laiyuan lamprophyres show a wider range of zircon $\epsilon_{\text{Hf}}(t)$ values from -17.2 to -3.7 compared with dolerites (-23.3 to -14.2) suggesting that the sources of lamprophyres are mixed and different from that of the dolerites whose limited negative zircon $\epsilon_{\text{Hf}}(t)$ values suggest that the dolerites were mainly sourced from an ancient enriched lithospheric mantle. This excludes the

possibility of a single source for the lamprophyres, but instead, indicates the involvement of multiple sources. In general, the enriched zircon Hf isotope compositions may not directly indicate the different input of asthenospheric components. The different incorporation of crustal materials into the lithospheric or asthenospheric mantles can both explain the variable and enriched zircon Hf isotope compositions in the mafic dykes. However the detailed geochemical data (discussed in Chapter 9) show that the crustal contamination did not play a key role in the ascent of lamprophyres excluding the possibility of much incorporation of crustal materials. And, the $\epsilon_{\text{Hf}}(t)$ values of the Laiyuan mafic dykes shows a systematic change from highly negative to nearly positive compared with mafic dykes from Jiaodong area (Liu et al., 2018; Liu et al., 2017b; Ma et al., 2014a; Ma et al., 2014b). The increasing input of asthenospheric material through time is evident in mafic dykes, as indicated by the increasing zircon $\epsilon_{\text{Hf}}(t)$ values from dolerites to lamprophyres. The variation trend is also shown by the signature of whole Sr-Nd isotope compositions (Zhang et al., 2003b). The dolerites show more depleted Nd isotopic composition ($\epsilon_{\text{Nd}}(t)$ values ranging from -15.2 to -10.5) and high initial $^{87}\text{Sr}/^{86}\text{Sr}$ ratios ranging from 0.70523 to 0.70683 than the lamprophyres ($\epsilon_{\text{Nd}}(t)$ ranging from -8.3 to -8.6 and initial $^{87}\text{Sr}/^{86}\text{Sr}$ ratios ranging from 0.7052 to 0.70554) suggesting that the lithospheric mantle source for mafic dykes and some input of asthenospheric mantle for lamprophyres in Laiyuan area as well (Fig. 6-2). As a consequence, in terms of isotopic evidence, the increasing trend of zircon $\epsilon_{\text{Hf}}(t)$ values from dolerites to lamprophyres demonstrates the increasing involvement of asthenospheric mantle into lithospheric mantle through time contributed to source of mafic dykes.

In summary, the enriched lithospheric mantle accounts for the major magma source for the ultramafic-mafic rocks, intermediate-felsic granitoids, volcanic rocks and mafic dyke suites from ~150-110 Ma. Over the long time, multiple sources e.g. asthenospheric materials and crustal melts, involved in this formation process. From 150-130 Ma, the lower crustal contribution to the source shows a decrease from the LJVR, through granitoids, to the ECVR and felsic dykes whereas the asthenospheric

mantle contribution is increasing through time from dolerites to lamprophyres during 130-110 Ma. In the following chapters, the petrogenesis of different units will be discussed individually, and their generalities and connections will be clarified by comparing with previous studies in the NCC.

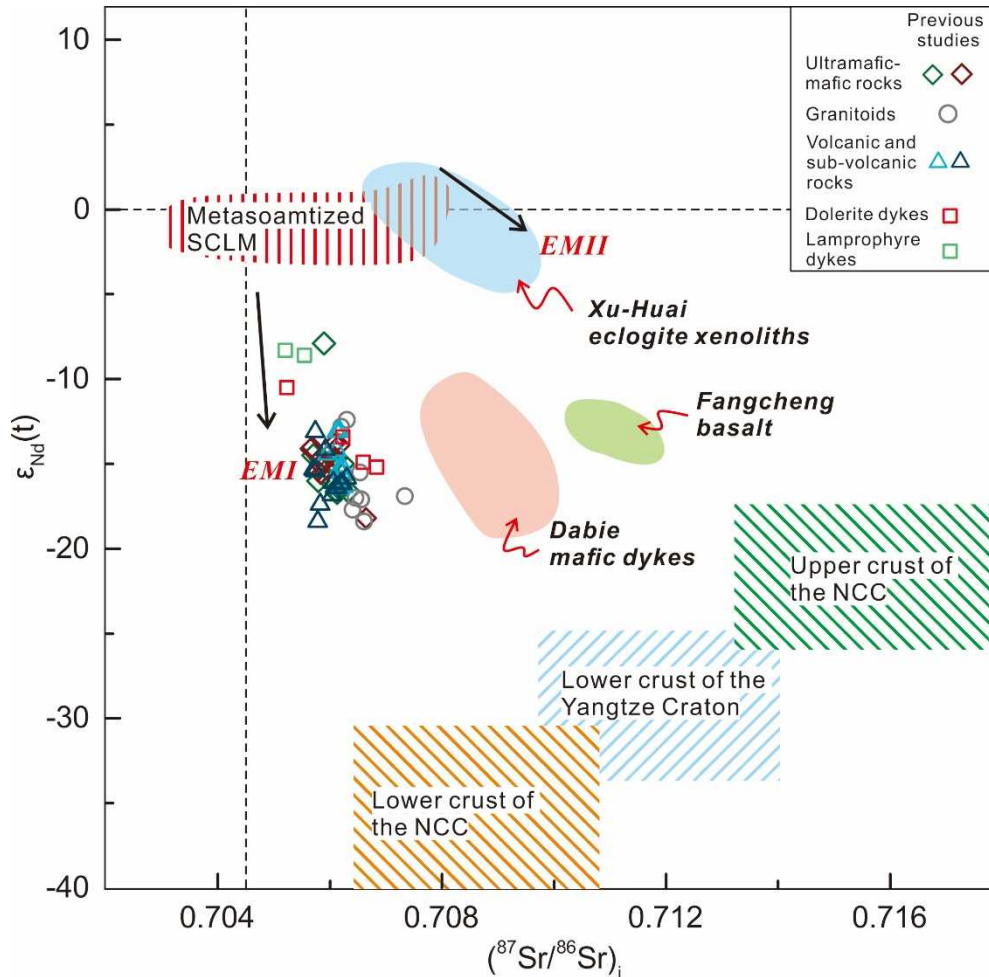


Fig. 6-2 Sr-Nd isotope diagram for magmatic rocks from the Laiyuan complex. The fields of EMI and EMII are after DePaolo (1981). The metasomatized sub-continental lithospheric mantle (SCLM) field is modified after Zhang et al. (2008a). Lower and upper crust of the NCC, and lower crust of the Yangtze Craton are after Jahn et al. (1999), Fan et al. (2001), and Gao et al. (2004), respectively. Isotopic data of Dabie mafic dykes (Jahn et al., 1999), Fangcheng basalt (Zhang et al., 2002), and Xu-Huai eclogites xenoliths (Gao et al., 2004) are given for comparison. Data source for the magmatic rocks in the Laiyuan complex: Gao et al., 2012; Gao et al., 2013; Hou et al., 2015; Liu et al., 2010; Zhang et al., 2016; Zhang et al., 2003b.

Chapter 7 Petrogenesis of volcanic rocks

7.1 Introduction

The compositional diversities of magmatic suites are derived from a conjunction of the difference in source composition and magmatic evolution such as fractional crystallization and magma mixing (Chen et al., 2013; Gao et al., 2012; Li et al., 2019a). Magmatic rocks with distinctive geochemical affinities, such as high Sr/Y and high Ba-Sr contents, have attracted considerable attention as they provide important clues on petrogenesis and tectonic setting (Defant and Drummond, 1990; Fowler et al., 2001). These rocks have been generally correlated to adakites which are intermediate-felsic igneous rocks with high Sr, low Y and Yb contents, and high Sr/Y and La/Yb ratios (Defant and Drummond, 1990; Drummond et al., 1996). The petrogenesis of adakites provides important insights into various processes that contribute to lithospheric evolution (Castillo et al., 1999; Defant and Drummond, 1990; Gao et al., 2004; Kröner et al., 2005; Martin et al., 2005; Rapp, 2002). Similarly, high Ba-Sr magmatic rocks which are characterized by alkali-rich, high Ba-Sr and LREE contents have also attracted considerable attention (Fowler et al., 2001; Tarney and Jones, 1994). Tarney and Jones (1994) defined the “high Ba-Sr granite” and correlated their origin to the partial melting of subducted oceanic islands, underplated basaltic magmas, or veined lithospheric mantle. Wang et al. (2014) and Ye et al. (2008) argued that high Ba-Sr rocks can be produced by partial melting of mafic lower crust with minor of enriched lithospheric mantle-sourced magmas. Other studies emphasized the role of fractional crystallization of enriched lithospheric mantle-derived magma (Fowler et al., 2001; Li et al., 2019a).

Following its final cratonization during late Paleoproterozoic, the NCC remained quiescent for a long time until Mesozoic, when voluminous magmatism (Zhang et al., 2014) and associated metallogeny generating some of the world-class deposits (Yang and Santosh, 2020) in the eastern and central parts, referred to as craton destruction or

decratonization (Zhu et al., 2011). The Mesozoic magmatic rocks with adakitic features and high Ba-Sr concentrations occur in the central and eastern parts of the NCC are important targets to understand craton destruction (Chen et al., 2013). Gao et al. (2004) investigated the high Mg[#] adakites from Western Liaoning in the northern margin of the NCC and proposed that the high Sr/Y and La/Yb ratios of these rocks resulted from the partial melting of the delaminated lower crust. This process has also been invoked for similar rock types along the northern and southern domains (Gao et al., 2004; Wang et al., 2007), and the Sulu belt (Huang et al., 2008) in the eastern NCC. In the central NCC, the delamination model was applied to explain the formation of high Sr/Y volcanic and plutonic rocks (Cai et al., 2003; Zhang et al., 2016), although these rocks show different petrological and isotopic features as compared to those in the eastern NCC, suggesting diverse mechanisms during craton destruction. Based on geochemical and Sr-Nd-Os isotopic studies of the intrusions in north Taihang Mountain of the central NCC, Chen et al. (2013) suggested a magma mixing model between felsic crustal melts and basaltic magma as an alternative to the delamination model. Similarly, the Cretaceous magmatic rocks with high Ba-Sr contents in the NCC are also indicators of magmatic evolution, specific sources and geodynamic settings (Li et al., 2019a; Wang et al., 2014).

The origin of magmatic rocks with adakitic affinity in the NTM remains debated. Cai et al. (2003) and Zhang et al. (2016) assumed that the adakitic feature of the Laiyuan granitoids were sourced from the partial melting of thickened lower crust. Some researchers also regarded fractional crystallization as the possible mechanism which generated adakitic features of the Late Jurassic volcanic rocks (Gao et al., 2012; Gao et al., 2013). With view to understand the petrogenesis of adakitic rocks, the Early Cretaceous volcanic rocks from the Laiyuan complex are investigated. The high Ba-Sr magmatic rocks from this area are reported for the first time. The petrological, geochemical, and zircon U-Pb and Lu-Hf data are presented which provide insights into: (1) two volcanic episodes in the Laiyuan complex; (2) magma sources; (3) origin of adakitic features and high Ba-Sr contents.

7.2 Petrography

The petrographic features of the volcanic rocks were described earlier. The Early Cretaceous (~130 Ma) volcanic rocks belong to andesite-dacite series as exhibited by [Fig. 3-2](#) and [Table 3-1](#).

7.3 Geochemistry

Based on the field observations and petrological studies, seven representative rock samples were analyzed for their major and trace elements and the results are presented in [Table 7-1](#). The rocks show intermediate to felsic geochemical features and are classified as trachyandesite, andesite, trachydacite, and dacite in TAS diagram ([Fig. 7-1a](#)). As revealed by K_2O - SiO_2 diagram ([Fig. 7-1b](#)), they belong to high-K calc-alkaline series. These rocks are characterized by moderate SiO_2 contents (59.13-66.46 wt. %, average 62.70 wt. %) and low contents of MgO (1.34-2.93 wt. %, average 2.21 wt. %) and variable TFe_2O_3 contents (0.99-6.36 wt. %, average 4.97 wt. %) as well as low-high $Mg^\#$ ranging from 36 to 73. The total alkali (Na_2O+K_2O) contents range from 6.48 to 9.56 wt. % with average concentration of 7.65 wt. %. They have 14.56-17.73 wt. % Al_2O_3 , 3.06-5.15 wt. % CaO, 0.49-0.89 wt. % TiO_2 , and 0.21-0.42 P_2O_5 with low concentration of LOI (0.69-2.58 wt. %).

In the chondrite-normalized REE patterns ([Fig. 7-1c](#)), the volcanic rocks are all enriched in LREEs relative to HREEs as suggested by moderate LREE/HREE and $(La/Yb)_N$ values of 14.61-24.35 and 19.45-47.07, respectively, without significant Eu anomalies, similar to the features of adakitic rocks. As shown in the primitive mantle-normalized spidergram ([Fig. 7-1d](#)), except the trachydacite (sample LYN-3/2), the other volcanic rocks all show similar characteristics of enrichment in large ion lithophile elements (LILEs; e.g., Ba and Pb), and strong depletion in high field strength elements (HFSEs; e.g., Ti and Ta-Nb). The trachydacite shows distinct Sr negative anomaly whereas other rocks have Sr positive anomalies indicating that they might have experienced different magmatic process.

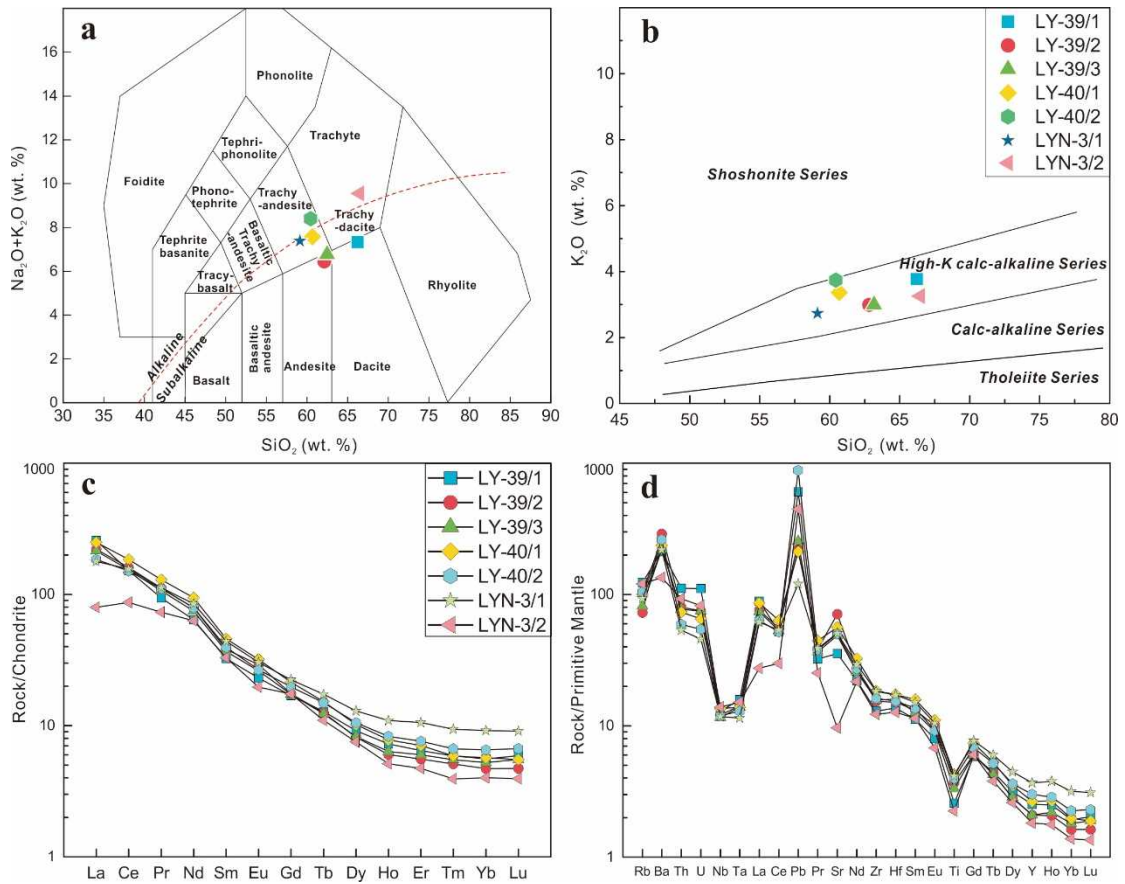


Fig. 7-1 (a) TAS diagram for classification (Middlemost, 1994). (b) K_2O vs. SiO_2 diagram (Peccerillo and Taylor, 1975). (c) Chondrite-normalized REE distribution diagrams. (d) Primitive mantle-normalized trace element diagrams. Normalized values: chondrite (Mcdonough and Sun, 1995), primitive mantle (Sun and Mcdonough, 1989).

7.4 Petrogenesis

7.4.1 Crustal contamination

Before evaluating the source and petrogenesis using geochemical and isotopic data, it is essential to consider the effects of crustal contamination. Firstly, the compiled isotopic data from literature show that all magmatic rocks from the Wanganzhen pluton share similar Sr-Nd isotopic compositions close to enriched mantle component excluding the major effect of contamination by the upper crustal materials (Gao et al., 2012; Hou et al., 2015). The $^{87}\text{Sr}/^{86}\text{Sr}$ ratios for coeval granitoids from the Wanganzhen pluton show consistent values with increasing SiO_2 indicating

the absence of crustal contamination during the magma evolution in the Laiyuan complex (Zhang et al., 2016). Geochemically, the Ba and Sr contents of the volcanic rocks show a range of 1484-2025 ppm and 748-1493 ppm, respectively, which are notably higher than the average Ba (390 ppm) and Sr (325 ppm) contents of continental crust (Rudnick and Fountain, 1995). As revealed in Fig. 7-5a, the Rb/Nb ratios also do not show any obvious change with against SiO₂. However, compared with other samples, sample LYN-3/2 might have experienced albitization and crustal contamination as it shows the highest Na₂O (6.31 wt. %) and LOI (2.58 wt. %), and lowest TFe₂O₃ (0.99 wt. %), Ba (942 ppm), and Sr (204 ppm) concentrations (Li et al., 2013a). In conclusion, crustal contamination cannot be totally ruled out for volcanic rocks, and does not appear to be an important factor affecting magma composition in these rocks. This is also consistent with the absence of inherited ages in the zircon grains.

7.4.2 Fractional crystallization

The compiled data of volcanic rocks reflect clear correlation between SiO₂ with other major elements and some trace elements (Fig. 7-2 and Fig. 7-3), reflecting the significant role of fractional crystallization during magma evolution. As shown in the diagrams, with SiO₂ increasing from ~52 to 70 wt. %, the TFe₂O₃, MgO, and CaO show decreasing trend, whereas Al₂O₃ and Na₂O contents remain slightly flat indicating the dominance of ferromagnesian mineral fractionation and the minor role of feldspar separation in the early stage of the magma evolution. The absence of Eu anomalies in the Laiyuan volcanic rocks also suggests that the fractional crystallization of feldspar was minor. In addition, TiO₂, and P₂O₅ contents are stable when SiO₂ content is less than 57 wt. % (Fig. 7-2a, d), but they show distinct negative linear correlation with increasing SiO₂ contents when silica concentration is more than 57 wt. %, suggesting that the onset of fractional crystallization of accessory minerals, such as apatite and Fe-Ti oxides, was at about 57 wt. % SiO₂. The contents of compatible elements, e.g., V and Ni, show decrease with increasing SiO₂ contents, whereas the incompatible elements including Rb and Ba display reverse trend (Fig.

7-3a, b, c, d). These variations are interpreted to represent the fractional crystallization of amphibole and pyroxene. The Sr and Y contents display different trends at 57 wt. % SiO₂ which may represent the initiation of plagioclase fractionation (Gao et al., 2012; Li et al., 2019a) (Fig. 7-3g, h).

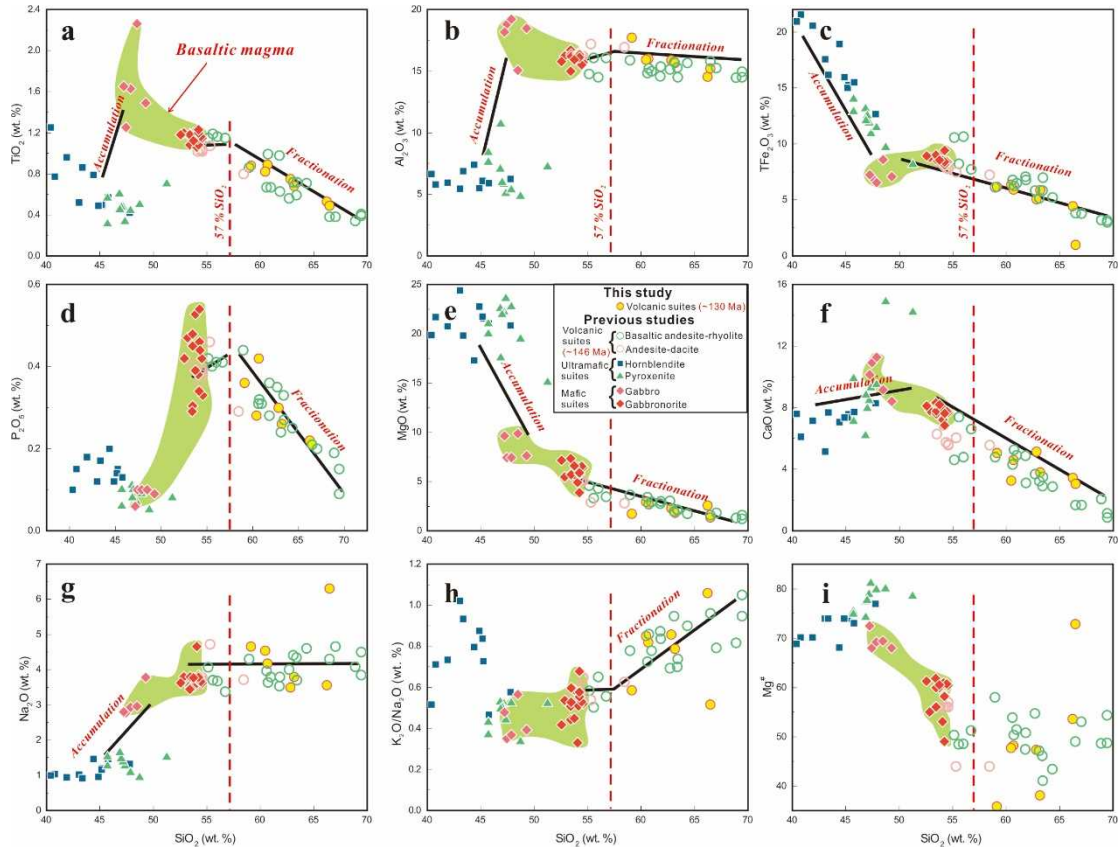


Fig. 7-2 Major elemental variation diagrams for the Laiyuan volcanic, mafic and ultramafic rocks compiled from previous studies and this study. Data sources: volcanic suites (Gao et al., 2012; Hou et al., 2015); mafic suites (Hou et al., 2015; Liu et al., 2010); ultramafic suites (Gao et al., 2012; Hou et al., 2015; Liu et al., 2010).

The existence of crystal fractionation was also confirmed by the formation of synchronous late Mesozoic pyroxenites (Yaogou, Zhai et al., 2014) and hornblendites occurring as ultramafic-mafic plutons along the periphery of the Laiyuan complex (Fig. 3-1). These ultramafic rocks display typical magmatic cumulate texture (Gao et al., 2012; Hou et al., 2015). Their petrological features suggest fractional crystallization of olivine, pyroxene, hornblende, and interstitial plagioclase, which is

also supported by chemical variation trends (Fig. 7-2 and Fig. 7-3). As a corollary, the fractional crystallization of ferromagnesian minerals has played a significant role in the formation of Laiyuan andesitic-dacitic magma, whereas the fractional crystallization of feldspar was not dominant in the early stage of magma evolution.

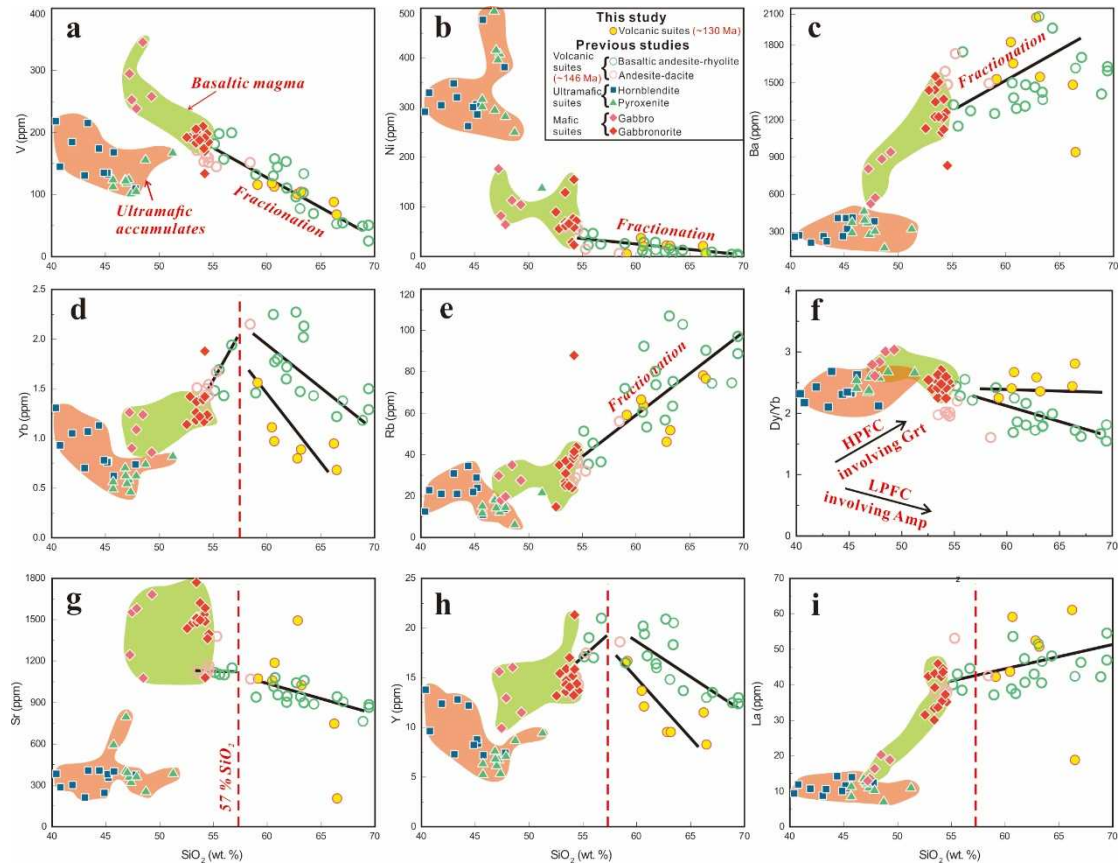


Fig. 7-3 Trace elemental variation diagrams. Symbols and data sources are same as in Fig. 7-2.

7.4.3 Nature of magma source

Considering the high TFe_2O_3 and MgO contents, and high $\text{Mg}^\#$ values (Fig. 7-2c, e, i), the primary magma for the Laiyuan andesites and dacites might have originated from the mantle. Geochemically, the Nb/Yb ratio is useful to trace the mantle source as to whether it is depleted (MORB) or enriched (OIB) (Pearce, 2008). As illustrated in Th/Yb - Nb/Yb diagram (Fig. 7-4a), the studied rocks exhibit high Th/Yb (2.91-11.59) and Nb/Yb (5.37-14.57) ratios suggesting an enriched mantle source. In addition, the geochemical affinities for the Laiyuan volcanic rocks, such as enrichment in LILEs and LREEs and depletion in HFSEs, exclude the possibility of

asthenospheric mantle source, but indicate that the magma was derived possibly from enriched lithospheric mantle (Li et al., 2019a; Yan et al., 2019). These rocks also contain abundant amphibole phenocrysts and microcrystals (Fig. 3-2) suggesting that the parental magma contained considerable amount of water which may be result of the mantle metasomatism. Previous studies show that prior to Mesozoic lithospheric destruction and extensive magmatism, the lithospheric mantle beneath the NCC experienced large-scale metasomatism and therefore was hydrated (Liu et al., 2019; Xia et al., 2017). Some studies argued that the fluid released by the stagnant horizontal Paleo-Pacific slab in the mantle transition zone might be responsible for the mantle metasomatism (Chen et al., 2005; Liu et al., 2018; Ma et al., 2014a). As shown in Fig. 7-4b, the Laiyuan volcanic rocks and adjacent mafic-ultramafic suites exhibit a tight correlation to fluid-related subduction metasomatism (Zhang et al., 2003b).

The Laiyuan andesites-dacites are characterized by high K_2O contents ranging from 2.73 to 3.86 wt. % and are enriched in LILEs and LREEs implying the presence of volatile-bearing minerals such as amphibole and phlogopite in the mantle source. Rb and Ba are compatible in phlogopite, whereas Rb, Sr, and Ba are moderately compatible in amphibole; thus melts in equilibrium with amphibole are expected to have significantly lower Rb/Sr (<0.1) and higher Ba/Rb (>20) ratios. Comparatively, melts of a phlogopite-bearing source may have extremely low Ba contents and Ba/Rb ratios (Furman and Graham, 1999). The low Rb/Sr (<0.1) and high Ba/Rb (>25) values for the Laiyuan andesitic-dacitic rocks (Fig. 7-4c) suggest that it is amphibole rather than phlogopite that dominated the mantle source. In addition, partial melting in garnet stability field contributes to high Dy/Yb ratios (>2.5), while melting in spinel stability field produces low Dy/Yb ratios (<1.5). When the Dy/Yb ratios are between 1.5 and 2.5, partial melting is inferred to occur in the garnet-spinel transition zone. The studied samples (except sample LYN-3/2) have Dy/Yb ratios varying from 2.11 to 2.67 which fall in the garnet-spinel transitional field (Fig. 7-4d), suggesting both spinel and garnet lherzolite in the mantle source (Yang et al., 2014).

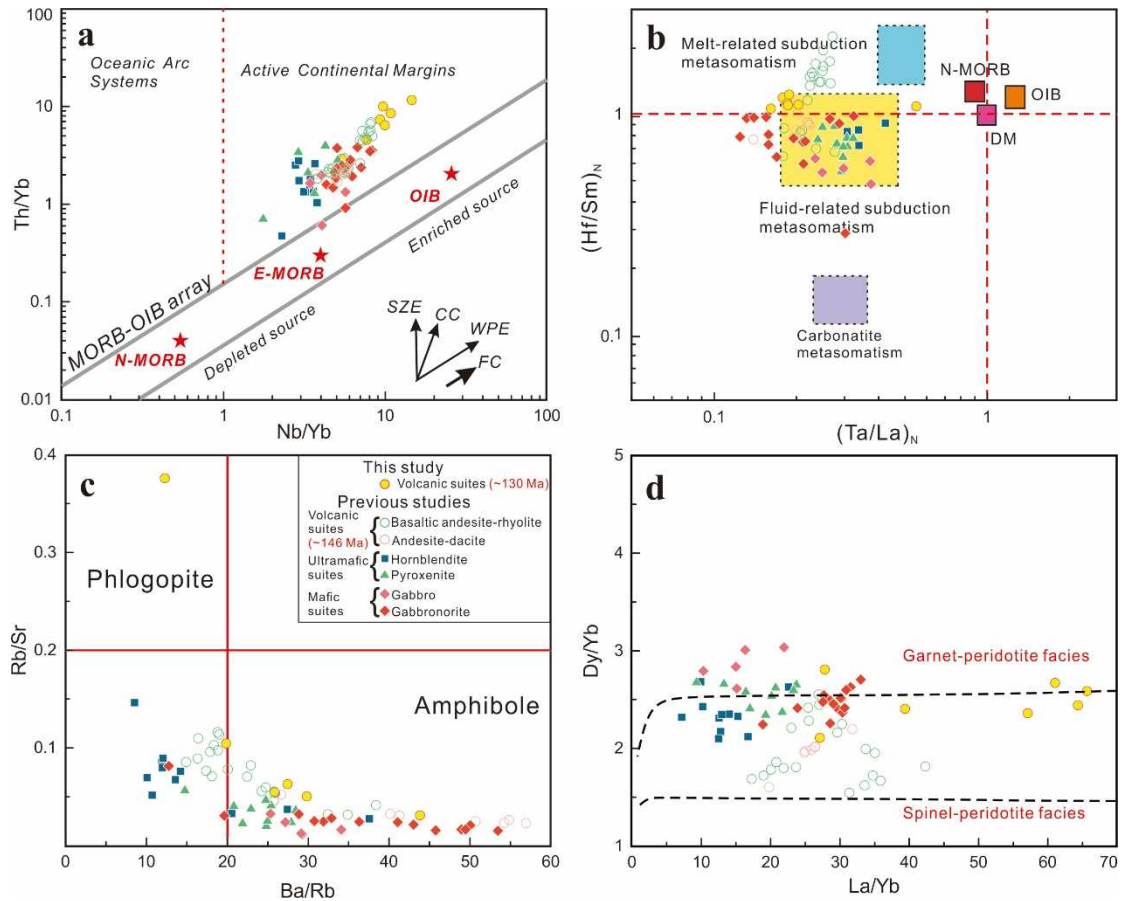


Fig. 7-4 (a) Th/Yb vs. Nb/Yb diagram (after Pearce, 2008). (b) $(\text{Hf}/\text{Sm})_N$ vs. $(\text{Ta}/\text{La})_N$ diagram (La Flèche et al., 1998). (c) Rb/Sr vs. Ba/Rb diagram. (d) Dy/Yb vs. La/Yb diagram (after Jung et al., 2006). Symbols and data sources are same as in Fig. 7-2. Abbreviation: MORB, mid-ocean-ridge basalt; E-MORB, enriched mid-ocean-ridge basalt; OIB, oceanic-island basalt; SZE, subduction zone enrichment; CC, crustal contamination; WPE, within-plate enrichment; FC, fractional crystallization.

The Lu-Hf isotopic composition of zircon also provides significant imprints on the mantle source. The rocks have uniform $\epsilon_{\text{Hf}}(t)$ values (-23.5 to -19.4) and Paleoproterozoic Hf model ages (ca. 2.6-2.4 Ga) indicating that they were mainly generated from ancient enriched lithospheric mantle, and not a single juvenile lithospheric mantle or asthenospheric mantle. However, the Tiaojishan volcanic rocks which formed at ~146 Ma exhibit variable $\epsilon_{\text{Hf}}(t)$ values ranging from -25 to -10 (Fig. 6-1). Besides, inherited zircon cores from basement rocks with ages in the range of

~2.65-2.08 Ga are common in these andesitic-dacitic rocks with positive $\epsilon_{\text{Hf}}(t)$ values (0-10) suggesting juvenile source synchronous with the major crustal growth in the NCC (Geng et al., 2012; Tang et al., 2015; Tang et al., 2016; Zhao et al., 2012). In terms of Sr-Nd-Pb isotopic features, the ~146 Ma volcanic rocks are characterized by low radiogenic Pb and high radiogenic Sr isotopic composition which might result from enriched mantle-derived melts and lower crust melts (Gao et al., 2012). Therefore, it is concluded that the magma source for the Late Jurassic volcanic rocks involved both enriched lithospheric mantle and lower crustal components.

In summary, the parental magma of the studied Laiyuan andesitic-dacitic rocks were derived from the partial melting of an ancient enriched lithospheric mantle which experienced fluid-related metasomatism in the amphibole-bearing garnet-spinel transition stability field.

7.4.4 Origin of high Ba-Sr and adakitic signatures

The rocks in this study are characterized by high Ba (942-2025 ppm with average of 1573 ppm) and Sr (748-1493 ppm with average of 1098 ppm) contents, which are akin to typical high Ba-Sr magmatic rocks (Tarney and Jones, 1994). In addition, these samples (except sample LYN-3/2) display high Sr/Y (64-157) and La/Yb (27-66) ratios, and high Sr (748-1493 ppm), low Y (9.52-16.70 ppm), and Yb (0.80-1.56 ppm) contents with no obvious Eu anomalies, falling in the adakite domain (Defant and Drummond, 1990; Moyen, 2009) (Fig. 7-5c, d).

Adakites include high-silica adakites (HSA) and low silica adakites (LSA) as defined by Martin et al. (2005), continental adakites (Gao et al., 2007; Rapp, 2002; Xiao and Clemens, 2007), and Archean adakites (Naqvi et al., 2006; Polat and Kerrich, 2000). The typical adakitic characteristics (high Sr/Y and La/Yb ratios) not only reflect the source nature, but also can be achieved through multiple petrogenetic process including melting, fractionation, and interaction (Moyen, 2009) (Fig. 7-6). In the NCC, the widespread occurrences of adakitic rocks mostly belong to the continental adakites, or can be referred as potassium-rich adakites (Rapp, 2002) or K-adakites (Xiao and Clemens, 2007) exhibiting high K_2O contents and $\text{K}_2\text{O}/\text{Na}_2\text{O}$

ratios (Fig. 7-2h). These rocks were produced within intra-plate reactivation setting in the eastern margin of the NCC, rather than in an active subduction system. Diverse models were proposed for the genesis of the adakitic rocks in the NCC including partial melting of thickened lower continental crust (Cai et al., 2003; Jiang et al., 2007), partial melting of delaminated mafic crust (Gao et al., 2004), mixing and mingling of siliceous crustal melts and mafic magma (Chen et al., 2013), and fractional crystallization of mantle-derived magma (Gao et al., 2012; Li et al., 2019a).

Table 7-2 Starting compositions and partition coefficients used in the geochemical modeling. Mineral abbreviation: Amp-amphibole; Cpx-clinopyroxene; Ol-olivine; Pl-plagioclase; Sph-Sphene; Zrn-zircon.

Simple mixing model							
Sample	Lithology	SiO ₂ (wt. %)	Rb (ppm)	Nb (ppm)	Zr (ppm)	La (ppm)	References
JN0918	Mafic granulite	49.58	6.09	0.21	17.9	1.93	(Jiang et al., 2011)
JN0919	Intermediate granulite	60.33	21.2	2.89	65.7	22.8	(Jiang et al., 2011)
ZB-20	Felsic granulite	72.95	156	12.4	681	11.6	(Liu et al., 2001)
LMT-3	Avid lava	68.89	74.7	8.49	178	42.3	(Gao et al., 2012)
ZJ014	Gabbro	49.29	27.6	4.87	62.6	18.88	(Liu et al., 2010)
Rayleigh fractional crystallization model							
Elements	Kd						Start composition
	Amp	Pl	Sph	Zrn	Cpx	Ol	LWB-6 (ppm)
Sr	0.40	12.50	0.37	0.01	0.02	0.09	1042.00
Y	13.50	0.02	633.00	181.00	0.01	1.20	20.90
La	1.40	0.40	113.00	0.10	0.05	0.40	43.10
Yb	9.60	0.01	393.00	465.00	0.02	1.30	2.27
References	(Bachmann et al., 2005)						(Gao et al., 2012)

The studied volcanic rocks show characteristics of K-adakites (Moyen, 2009), such as high K₂O contents ranging from 2.73 to 3.86 wt. %, and high K₂O/Na₂O ratios varying from 0.52 to 1.06 (Fig. 7-2h). Here the evaluation of the possible petrogenetic processes that may account for the adakitic features of these rocks was

conducted. The possibility of partial melting of young subducted lithosphere can be ruled out because the Laiyuan volcanic rocks have different geochemical (lower La/Yb ratios) and isotopic composition (enriched Sr-Nd-Hf isotopes) (Castillo, 2012). Also, if they were sourced from partial melting of delaminated mafic lower crust, the rocks will be characterized by high differentiation in HREE related to garnet in the restites (Gao et al., 2004), whereas these samples do not exhibit a flat HREE pattern (Fig. 7-1c). Additionally, the geochemical and isotopic evidence indicates that the enriched lithospheric mantle acted as the major source, excluding the possibility of involvement of any significant mafic lower crustal materials (Fig. 6-1).

Mixing and mingling of siliceous crustal melts and mafic magma has been regarded to play a key role in the formation of magmatic rocks in the NTM (Chen et al., 2009b; Chen et al., 2013). In this context, some samples are used to represent the components of lower crust and enriched lithospheric mantle to model the mixing between crust- and mantle-derived magmas. The neighboring Longmengou gabbro (Fig. 3-1) was formed during Early Cretaceous and the magma was directly sourced from enriched sub-continental lithospheric mantle (SCLM) (sample ZJ014; Liu et al., 2010). The mafic granulite xenolith (sample JN0918), intermediate granulite xenolith (sample JN0919), and felsic granulite xenolith (sample ZB-20), dated at Late Jurassic to Early Cretaceous, from Hannuoba basalts in Zhangjiakou area are considered to represent the components of lower crust beneath the TNCO (Jiang et al., 2011; Liu et al., 2001). The rhyolite (sample LMT-3) from Mujicun area in the northern Laiyuan complex represents the felsic end-member in the mixing model (Gao et al., 2012). The detailed parameters and starting compositions in the modeling are listed in Table 7-2. As revealed by the modeling results (Fig. 7-5a, b), the rock samples do not match well with the calculated mixing curves suggesting that the formation of the Laiyuan andesitic-dacitic rocks cannot solely be attributed to the mixing between mantle-derived magma and intermediate-felsic magma.

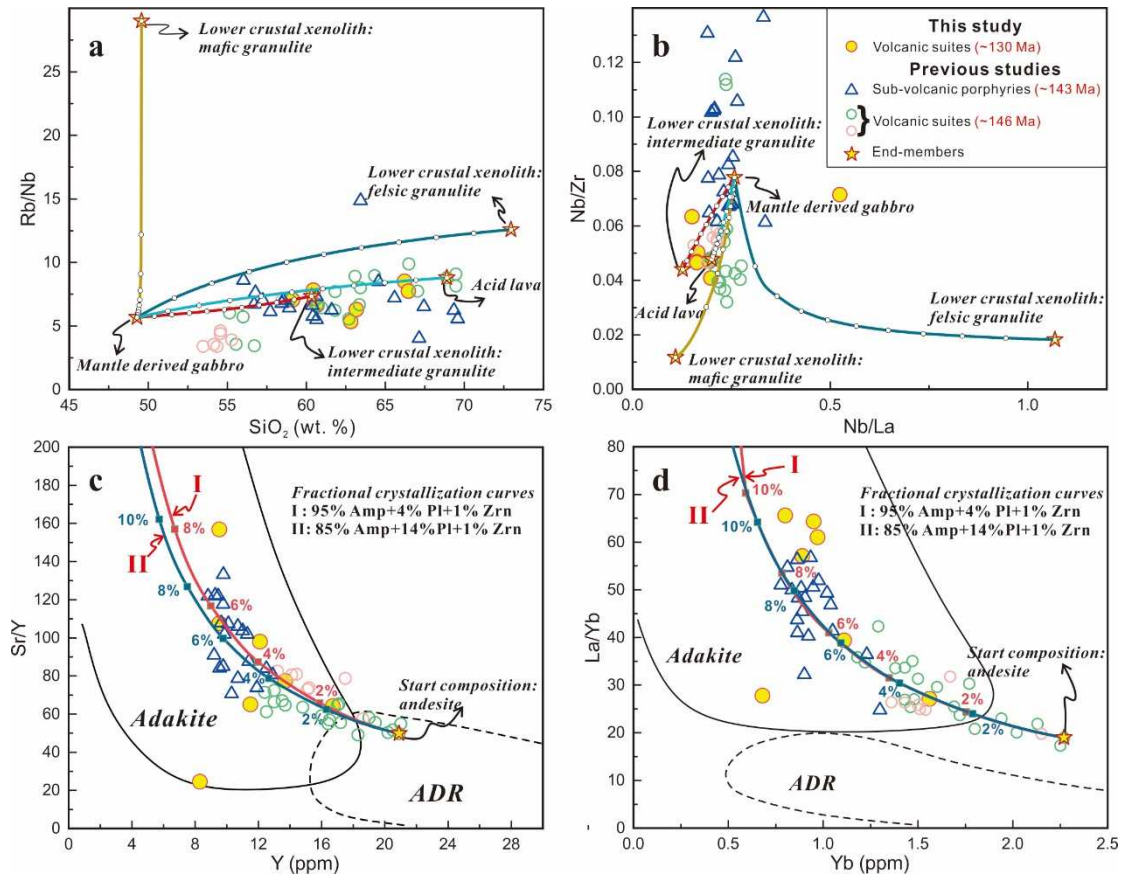


Fig. 7-5 Variation diagrams for the Laiyuan volcanic and sub-volcanic rocks compiled from this study and previous literature. (a) Rb/Nb vs. SiO₂ and (b) Nb/Zr vs. Nb/La, showing calculated curves corresponding to magmatic evolution by simple mixing. Ticks on these curves represent 10% increments. (c) Sr/Y vs. Y (after Defant and Drummond, 1990) and (d) La/Yb vs. Yb (after Castillo, 2012) diagrams exhibiting the calculated curves of Rayleigh fractional crystallization modeling. The detailed parameters and start compositions in the modeling are listed in Table 7-2. Data sources: volcanic suites (Gao et al., 2012; Hou et al., 2015); sub-volcanic porphyries (Gao et al., 2013). Abbreviation: ADR-normal arc andesite-dacite-rhyolite; Amp-amphibole; Pl-plagioclase; Zrn-zircon.

Finally, the effects of fractional crystallization in generating high Ba-Sr and adakitic features are also considered. The crystal fractionation of enriched lithospheric mantle-derived magmas is considered as a possible mechanism for high Ba-Sr magmatic rocks (Fowler et al., 2001; Li et al., 2019a). The above discussion shows that fractionation of ferromagnesian minerals (hornblende and clinopyroxene)

occurred during earlier stage of magma evolution. The ultramafic cumulates, mafic intrusions (gabbro and gabbro-norite), intermediate-felsic lava, and related sub-volcanic porphyries in the Laiyuan complex have variable Ba-Sr contents, but these rocks share a similar Sr-Nd-Pb-Hf pattern suggesting the varying geochemical features were controlled by magmatic evolution, rather than the source process. The Ba and Sr values can increase during the fractional crystallization of hornblende, whereas the fractionation of feldspar would lead to the decrease of Sr contents and variable Ba concentrations. In conclusion, it is inferred that fractional crystallization was the key factor which generated the high Ba-Sr concentrations.

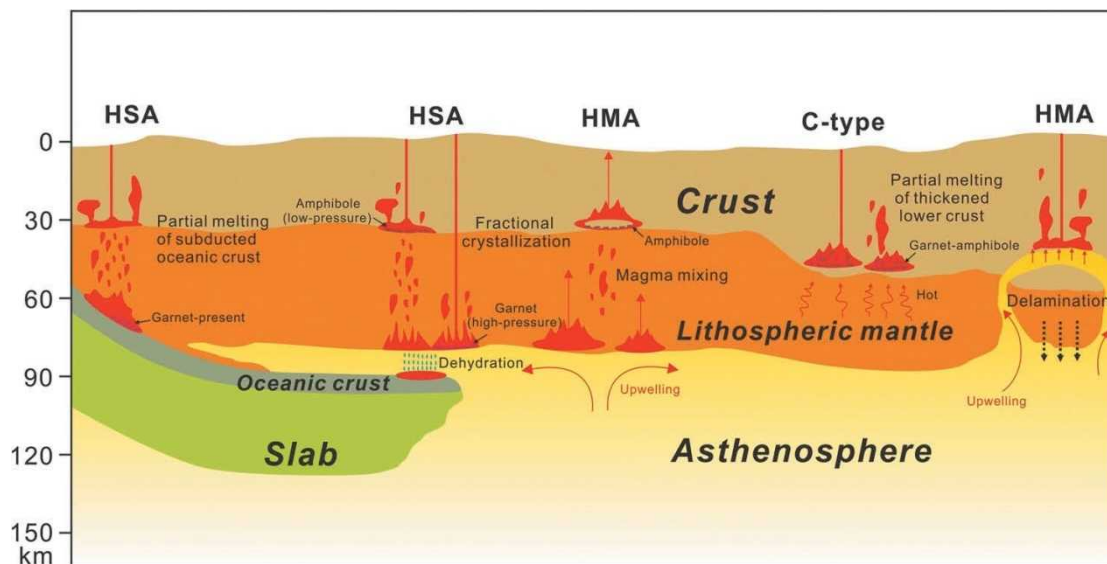


Fig. 7-6 Cartoon of the five genetic models for the formation of adakites or adakitic rocks (modified after Zhang et al., 2019). Adakitic signature may be produced under different tectonic settings. HSA: high-SiO₂ adakites, HMA: high-Mg[#] adakitic rocks, C-type: C-type adakitic rocks.

The adakitic affinities (high Sr/Y and La/Yb ratios) can also result from the fractionation of amphibole-rich cumulates (Gao et al., 2012). Recent experimental studies show that two types of fractional crystallization trends can produce the adakitic signature: low-pressure amphibole fractionation and high-pressure garnet fractionation of hydrous basaltic melts (Castillo, 2012; Davidson et al., 2007; Moyen, 2009; Richards and Kerrich, 2007). The mafic rocks, volcanic rocks, and associated sub-volcanic porphyries exhibit continuous changes in composition from basaltic or

gabbroic, through andesitic to rhyolitic, suggesting the net effect of magmatic evolution and source nature on the origin of adakitic affinity (Fig. 7-2 and Fig. 7-3). As shown in the adakite discrimination diagrams (Fig. 7-5c, d), the volcanic and sub-volcanic rocks from the Laiyuan complex display apparent sequential trends from normal arc volcanic rocks to adakites, matching well with fractional path of mineral assemblage of garnet+amphibole+titanite+zircon defined by Castillo et al. (1999). The garnet fractionation was negligible because the Dy/Yb ratios do not increase with increasing SiO₂ contents, showing a stable or decreasing trend (Fig. 7-3f). Thus, such distinct adakitic features could be achieved through large amount of amphibole fractionation and minor degree of fractionation of HREE-rich accessory minerals, such as titanite and zircon. Using andesite from the Laiyuan complex (sample LWB-6) as the start composition, the fractional crystallization procedure was modeled (Fig. 7-5c, d; Table 7-2). The modeled Rayleigh fractional crystallization curves (95%Amp+4%Pl+1%Zrn; 85%Amp+14%Pl+1%Zrn) are well correlated with the trends defined by the samples, which emphasize the role of amphibole-dominated crystal fractionation in controlling the Sr/Y and La/Yb ratios. Therefore, major amphibole and minor titanite and zircon fractional crystallization of in the early stage is considered to have resulted in the adakitic features of the Laiyuan volcanic rocks.

In conclusion, the distinct geochemical signature of the Laiyuan volcanic rocks such as high Ba-Sr concentrations and adakitic affinities (e.g., high Sr/Y and La/Yb ratios) not only resulted from inheritance from their magma source, but was also principally controlled by fractional crystallization during magma evolutionary process.

7.5 Summary

(1) Zircon geochronology of the Laiyuan volcanic rocks yielded weighted mean ages of 131.4 Ma, 130.3 Ma, and 127.1 Ma with $\varepsilon_{\text{Hf}}(t)$ values ranging from -23.5 to -19.4 and limited T_{DM}^{C} range of 2676 to 2414 Ma indicating single enriched ancient mantle source.

(2) The volcanic suites show compositional range from andesite to dacite,

enrichment in LREE and LILE, depletion in HFSE, and no obvious Eu anomalies. Geochemical data exhibit clear correlation between SiO₂ with other major and some trace elements, reflecting the significant role of fractional crystallization in the petrogenesis of the Laiyuan volcanic rocks.

(3) Geochemical and isotopic data obtained in this study indicate that the parental magma of the Laiyuan andesitic-dacitic rocks were primarily derived from the partial melting of an enriched SCLM which experienced fluid-related subduction metasomatism in the amphibole-bearing garnet-spinel transition stability field.

(4) The high Ba-Sr concentrations and adakitic affinities resulted not only from inheritance from their magma source, but also through fractional crystallization during magma evolution. Major amphibole fractionation and minor fractional crystallization of titanite and zircon occurred at depth, with limited plagioclase segregation at shallow levels.

Chapter 8 Petrogenesis of granitoids

8.1 Introduction

Granitoids are the most widely distributed rocks in the continental crust of the Earth, which provide important clues on the crustal growth and evolution being one of the most essential discussed topics in geology (Brown, 2013; Petford et al., 2000). The giant igneous complexes comprising various types of granitoids (including diorite, quartz diorite, monzonite, quartz monzonite, granodiorite, monzogranite, syenogranite, and alkali granite) are important targets to investigate the magmatic differentiation contributing to the compositional variations from mafic to felsic. Some magmatic complexes are concentric with normal zoning sequences showing a variation from outer mafic to inner felsic (Coleman et al., 2004; Miller et al., 2007) whereas others show reverse zoning (Wu et al., 2017). Several mechanisms have been proposed to interpret the petrological and geochemical variation, such as aggregation of numerous pulses of magmas from partial melting, fractional crystallization of magma, magma mixing and mingling, assimilation and contamination of surrounding rocks, and liquid immiscibility (Clemens and Stevens, 2012). Magma mixing, assimilation and contamination, and liquid immiscibility may generate stock-scale to enclave-scale intrusions but could not have the power to cause a pluton-scale intrusion with compositional variations (Wu et al., 2017). In contrast, partial melting and crystal fractionation are the primary mechanisms to devote to the differentiation of granite (Gao et al., 2016). Partial melting means that the different portions of various types in the granitoid complex were directly crystallized from incremental batches of the magma (Glazner et al., 2004; Walker Jr et al., 2007; Žák and Paterson, 2005). Under this condition, the compositional changes of different magmatic suites could be regarded as the variations of the melting source (Hu et al., 2018). Crystal fractionation means that different types of rocks were sourced from the same batch of magma by crystal separation and were crystallized in the magma chamber at different periods

(Bateman and Chappell, 1979; Pitcher, 1997; Wilson, 1993). Therefore, the compositional characteristics of rocks generated by fractional crystallization do not necessarily equate to the source features, but it could reveal much physicochemical condition of the magma and its variation during crystallization (Xu et al., 2019).

The Laiyuan complex consisting of granitoids and mafic intrusions, and volcanic rocks offers the opportunity to investigate the history of magmatic evolution and its implications on the petrogenesis and tectonic setting. Several researches have concentrated on the petrogenesis of the magmatic rocks of the Laiyuan complex. Some favored that the granitoids with adakitic affinity were formed by partial melting of the thickened mafic lower crust (Cai et al., 2003; He and Santosh, 2014; Zhang et al., 2016), whereas others highlighted the role of fractional crystallization of magmas sourced from partial melting of the ancient enriched lithospheric mantle on the formation of variable magmatic suites (Gao et al., 2012; Hou et al., 2015; Li et al., 2019a). Liu et al. (2010) also suggested that the formation of ultramafic-mafic intrusions was controlled by the fractional crystallization of olivine+pyroxene+hornblende, while plagioclase separation is insignificant. In addition, magma mixing and mingling between mantle-derived basaltic magmas and siliceous crustal melts was also thought the possible petrogenesis for granitoids with adakitic feature (Chen et al., 2013).

The petrogenesis for magmatic rocks in the Laiyuan complex is still debated. Therefore, in this research, based on detailed field investigations and sampling of granitoids, combining previous data of other magmatic units, the brand-new analytical results whole-rock major, trace and REE geochemistry, zircon U-Pb geochronology, and in-situ Lu-Hf isotopes are presented with objectives to (1) to document precisely the emplacement ages of the granitoids; (2) to understand the petrogenesis and magma source characteristics; and (3) to investigate the petrogenetic linkages of diverse magmatic rocks and magmatic evolutionary process of the Laiyuan complex.

8.2 Petrography

The studied granitoids could be classified as two series: granite including monzogranite and syenogranite, and monzonite including monzonite and quartz monzonite as illustrated in Fig. 3-4 and Fig. 3-5. The two MME samples belong to the quartz monzonite in lithology.

8.3 Geochemistry

The geochemical data of the Laiyuan granitoids are shown in Table 8-1. Detailed field and petrographical observations indicate that the studied rocks have not experienced significant alteration with only a few amounts of secondary kaolinite, sericite and epidote (Fig. 3-5). In addition, most of these samples have low LOI (<2% wt. %) except for one sample LYN-1/2 that has moderate LOI values (2.88 wt. %). As a corollary, these features indicate that the elemental and isotopic compositions of granitoids were not primarily affected by epigenetic alteration after their crystallization, and the geochemical data can be used for petrological discussion.

Based on the geochemical affinities (Fig. 8-1a, b), considering the field and petrographical characteristics as well, the granitoids from the Laiyuan complex could be classified as syenogranite, monzogranite, quartz monzonite, and monzonite, and most of them belong to high-K calc-alkaline series in K_2O-SiO_2 diagram (Fig. 8-1c). The syenogranite samples are characterized by the highest SiO_2 (74.93-75.95 wt. %) and alkaline contents (8.75-9.28 wt. %), lowest Al_2O_3 (13.03-13.21 wt. %), TFe_2O_3 (0.96-1.11 wt. %), MgO (0.11-0.21 wt. %), and TiO_2 (0.11-0.23 wt. %) contents compared to other groups of rocks. They are also very weakly peraluminous with A/CNK ratios varying from 0.98 to 1.04 (Fig. 8-1d). Comparing with syenogranites, the monzogranite, quartz monzonite, and monzonite samples are all showing metaluminous features with A/CNK ratios ranging from 0.82 to 0.97. The SiO_2 , Al_2O_3 , TFe_2O_3 , MgO , and TiO_2 contents for monzogranites are in the range of 69.17-71.34 wt. %, 14.07-14.90 wt. %, 2.14-3.14 wt. %, 0.78-1.17 wt. %, and 0.36-0.57 wt. %, respectively, whereas the quartz monzonite and monzonite samples have lower SiO_2 concentrations (55.01-65.23 wt. %), and higher Al_2O_3 (15.69-16.86 wt. %), TFe_2O_3 (3.35-8.46 wt. %), MgO (1.36-3.76 wt. %), and TiO_2 (0.49-1.08 wt. %) contents.

Chondrite-normalized REE patterns for the Laiyuan granitoids are strongly fractionated with high $(La/Yb)_N$ and LREE/HREE ratios of 10.63-85.10 and 8.35-32.58, respectively (Fig. 8-2a, c). The syenogranite samples exhibit strong negative Eu anomalies ($\delta Eu=0.3-0.52$) different from no obvious Eu anomalies in other studied rocks with δEu of 0.59 to 1.04. In primitive mantle-normalized spider-diagrams (Fig. 8-2b, d), these samples are roughly enriched in LILEs (e.g., Rb, K, Th and U) and are distinctively depleted in HFSEs (e.g., Nb, Ta, P and Ti). In addition, the syenogranite samples exhibit more negative P and Ti anomalies indicative of possible more evolved magmas.

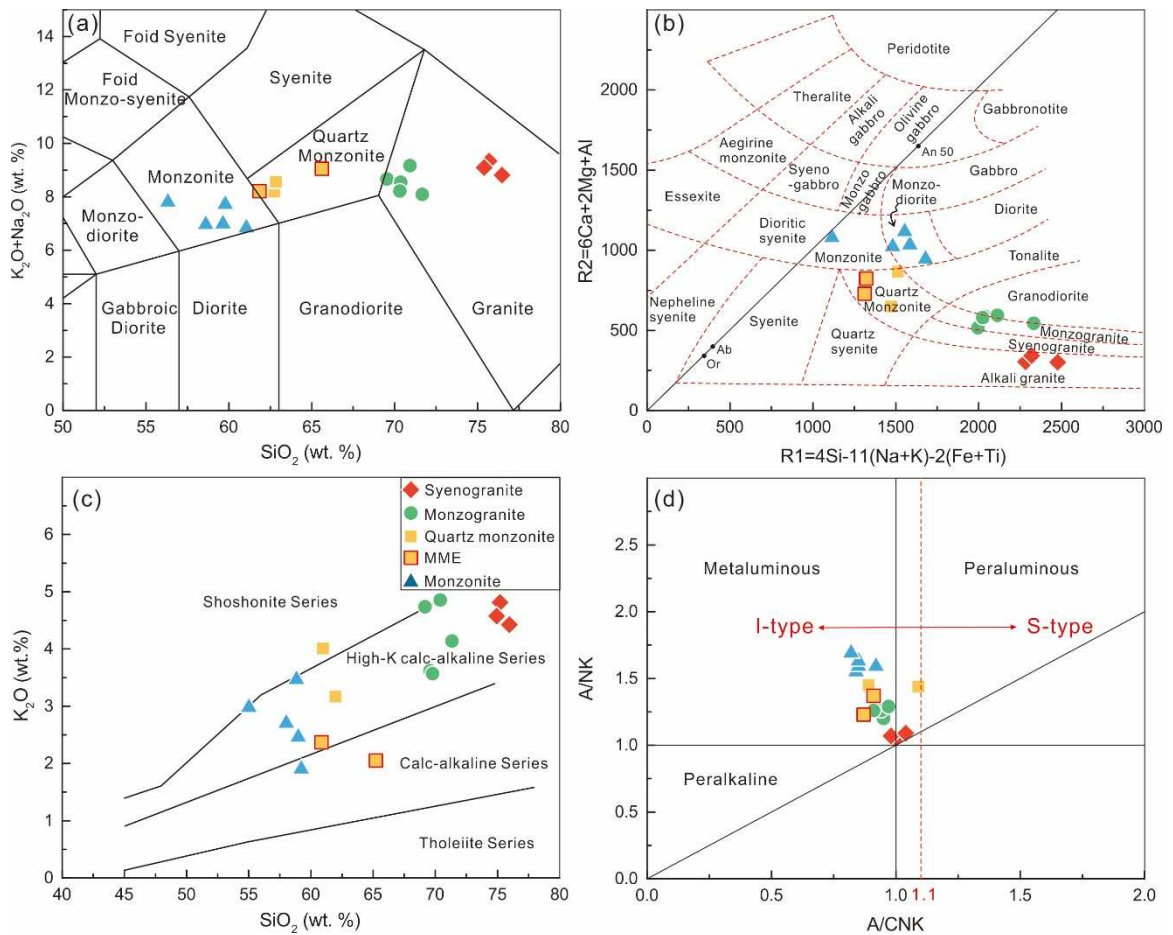


Fig. 8-1 (a) TAS diagram for classification of the Laiyuan dykes (Middlemost, 1994). (b) R1 vs. R2 classification diagram (De La Roche et al., 1980). (c) K_2O vs. SiO_2 classification diagram (Peccerillo and Taylor, 1975). (d) A/NK vs. A/CNK classification diagram (Rickwood, 1989).

8.4 Petrogenesis

8.4.1 Genetic types

The genetic types of granites are generally classified as I-, S-, and A-type granites based on mineralogy, petrology, and geochemistry (Chappell and White, 1992; Chappell and White, 2001). Among the studied granitoid samples, the syenogranites are apparently different from the other three rock types according to their mineralogical, petrological, and geochemical characteristics indicating their different genetic types. In terms of minerals, I-, S-, and A-type granites are characterized by the existence of calcium-bearing ferromagnesian minerals such as hornblende and clinopyroxene, cordierite (garnet, muscovite, tourmaline), and sodic ferromagnesian minerals such as arfvedsonite and riebeckite, respectively (Miller, 1985). The monzogranites, quartz monzonites (including MMEs), and monzonites contain abundant hornblende minerals and are absent of typical alkaline mafic minerals for A-type granites to manifest they are not A-type granites (Fig. 3-5). The absence of enrichment in HFSE including Zr, Nb and Y, and negative Eu anomalies for monzogranites, quartz monzonites, and monzonites also deprive the possibility of A-type granitoid (Fig. 8-2). As shown in the genetic type discrimination diagrams (Fig. 8-3), these granitoids are plotted in the fields of I- and S-type granitoids indicating their similar genetic types. Furthermore, the metaluminous features with A/CNK ratios ranging from 0.82-0.97 (Barbarin, 1999) and abundance of hornblende and biotite minerals (Chappell and White, 2001) validate they are I-type granitoids rather than S-type (Fig. 8-1d). The I-type characteristics are also confirmed by the decreasing P₂O₅ contents with increasing SiO₂ contents (Chappell and White, 1992; Wolf and London, 1994).

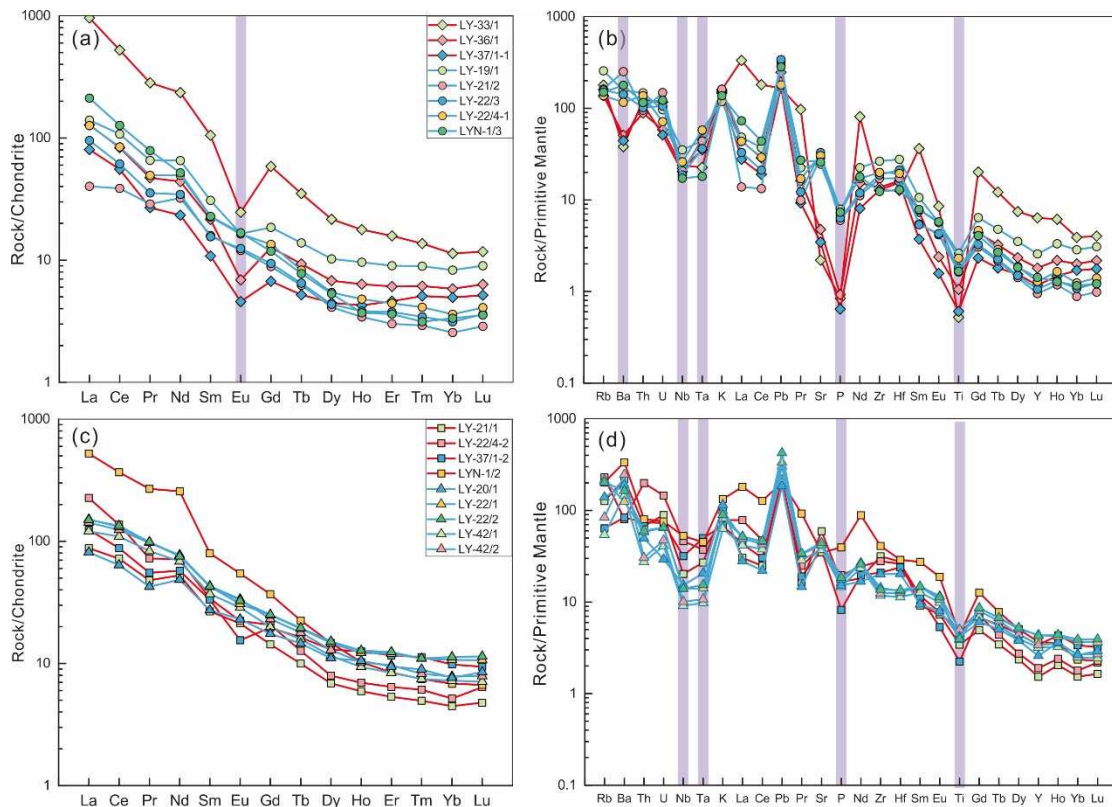


Fig. 8-2 (a), (c) Chondrite-normalized REE distribution diagrams, and (b), (d) Primitive mantle-normalized trace element diagrams for granite and monzonite series, respectively.

Normalized values: chondrite (McDonough and Sun, 1995), primitive mantle (Sun and McDonough, 1989).

It is still a problem to distinguish between highly fractionated granite and A-type granite (Gao et al., 2016; King et al., 2001; Wu et al., 2017). In general, A-type granites are low in Al but high in Ga and Zr concentrations which could be used as the discrimination indexes (Whalen et al., 1987), but quite a few highly fractionated granites also have high $10000 \times \text{Ga}/\text{Al}$ ratio like A-type granites (Breiter et al., 2013). Similarly, A-type granite, if intensively fractionated, is geochemically overlapped with the highly fractionated granite (King et al., 2001). The studied syenogranites show weakly peraluminous features, strongly negative Eu anomalies, and fell into the A-type field in the discriminative diagram (Fig. 8-3a). However, several lines of evidence prove that the Laiyuan syenogranite coincides with highly fractionated granites. Firstly, the Zr contents (141.64-153.19 ppm) for syenogranites are lower

than the values of typical A-type granites (average of 301 ppm) and similar to highly fractionated I-type granites (average of 151 ppm) in the famous Lachlan Fold Belt (King et al., 1997). Secondly, they all fell into the highly fractionated granite fields in other discriminative diagrams (Fig. 8-3c, d). As illustrated in the TFeO/MgO vs. 10000Ga/Al diagram (Fig. 8-3b), they also show I- and S-type granitic characteristics. The abundant K-feldspar minerals in the syenogranites could account for the high alkaline contents similar to A-type granites (Fig. 8-3a). Thirdly, the A-type granite is characterized by high-temperature magma (900 °C, Clemens et al., 1986) while the zircon saturation temperatures for the Laiyuan syenogranite are ranging from 774 to 781 °C same with the zircon saturation temperatures for highly fractionated I-type granites in the Lachlan Fold Belt (Chappell and White, 1992; King et al., 1997). Collectively, the conclusion is made that the syenogranite belong to highly fractionated I-type granites rather than S- or A-type, which is consistent with previous studies on leucogranites in the Laiyuan complex (Chen et al., 2003), and monzogranites, quartz monzonites (including MME), and monzonites are identified as normal I-type granitoids.

8.4.2 Fractional crystallization

The crustal contamination is a negative factor to assess the petrogenesis using geochemical data, and thus it is essential to eliminate the impact of crustal contamination. Firstly, according to field observation, the Laiyuan granitoids intruded into the Paleozoic sedimentary rocks and Archean basement rocks, and carried diverse xenoliths from the country rocks with distinct contact boundaries (Fig. 3-4c, d), suggesting the melts were derived from the deep lithosphere and the magmas crystallized to emplace rapidly. Meanwhile, the uniform Sr-Nd isotopic compositions from the Laiyuan magmatic rocks don't vary with increasing SiO₂ contents depriving the possibility of significant contamination during the magmatic evolution (Fig. 6-2). Thirdly, except for the highly fractionated syenogranites, all rock samples have higher Ba and Sr contents (Fig. 8-5a, e) showing a range of 562-2347 ppm (mean 787 ppm) and 517-1251 ppm (mean 1217 ppm), respectively, which are notably higher than the

average Ba (390 ppm) and Sr (325 ppm) contents of continental crust (Rudnick and Fountain, 1995). These features suggest that the melt assimilation with the wall rock did not play a significant role before emplacement.

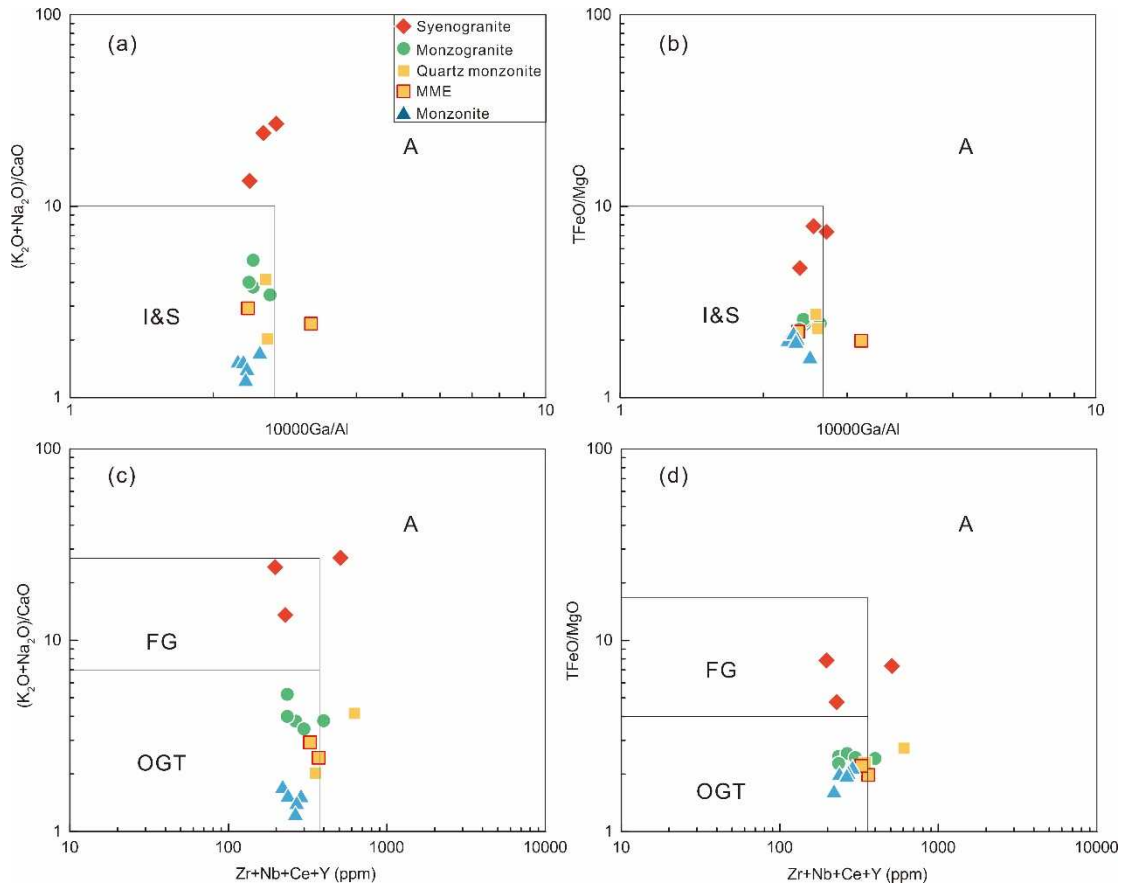


Fig. 8-3 Genetic type discrimination diagrams for the Laiyuan granitoids (modified after Whalen et al., 1987). Abbreviation: A-type, A-type granite; FG, fractionated felsic granite; OGT, unfractionated M-, I-, and S-type granite.

Some degree of fractional crystallization was involved in the magmatic evolution of the granitoids as indicated by linear correlations between some elements with increasing SiO_2 contents (Fig. 8-4 and Fig. 8-5). As illustrated in the major elemental variation diagrams, with the SiO_2 contents varying from ~53-70 wt. %, the TFe_2O_3 , MgO, and CaO contents show decreasing trend (Fig. 8-4c, d, e), indicating an essential role of ferromagnesian mineral fractionation such as pyroxene and amphibole which was also identified by the variations of Ni and Cr (Fig. 8-5c, d). The fractionation of titanite is also shown by the related elemental variations in the TiO_2

contents. The Al_2O_3 , Na_2O , Ba, and Sr contents display board distributions (Fig. 8-4b, f and Fig. 8-5a, e), and Al_2O_3 , Ba, and Sr contents don't decrease with increasing SiO_2 concentrations until silica concentration is more than 65 wt. %. Combined with the variations of Eu anomalies, it is suggested that during the magma evolution of intermediate rocks (e.g., diorite, monzonite, quartz monzonite, and MME), the plagioclase fractionation is suppressed while the fractional crystallization of plagioclase becomes intense during the granitic magmatic evolution (e.g., granodiorite, monzogranite, and syenogranite). This transformation may imply that the monzogranitic and the more evolved syenogranitic magmas may not be derived from the dioritic or monzonitic magmas through crystal fractionation, namely there are two series of magmas for granitoids. Similarly, the difference between the two series of magmas could also be distinguished in the variations of P_2O_5 and Zr contents (Fig. 8-4g and Fig. 8-5i). From monzonite to quartz monzonite, the P_2O_5 and Zr contents are increasing, whereas they are decreasing with increasing SiO_2 contents from monzogranite to syenogranite, indicating the fractional crystallization of apatite and zircon. The substantial variations of some trace elements (Fig. 8-5) may also indicate the existence of magma mixing and mingling during the magma differentiation of intermediate rocks, not only the fractional crystallization. According to the different magmatic evolution, with available geochemical and isotopic data from this study and literatures, the Laiyuan granitoids could be classified as two types of rock series: Group I rocks are majorly intermediate including diorite, monzonite, quartz diorite, quartz monzonite, and variable MME, while Group II are mainly felsic consisting of granodiorite, monzogranite, and syenogranite. These two groups of granitoids exhibit distinct magmatic evolutionary processes which will be discussed below.

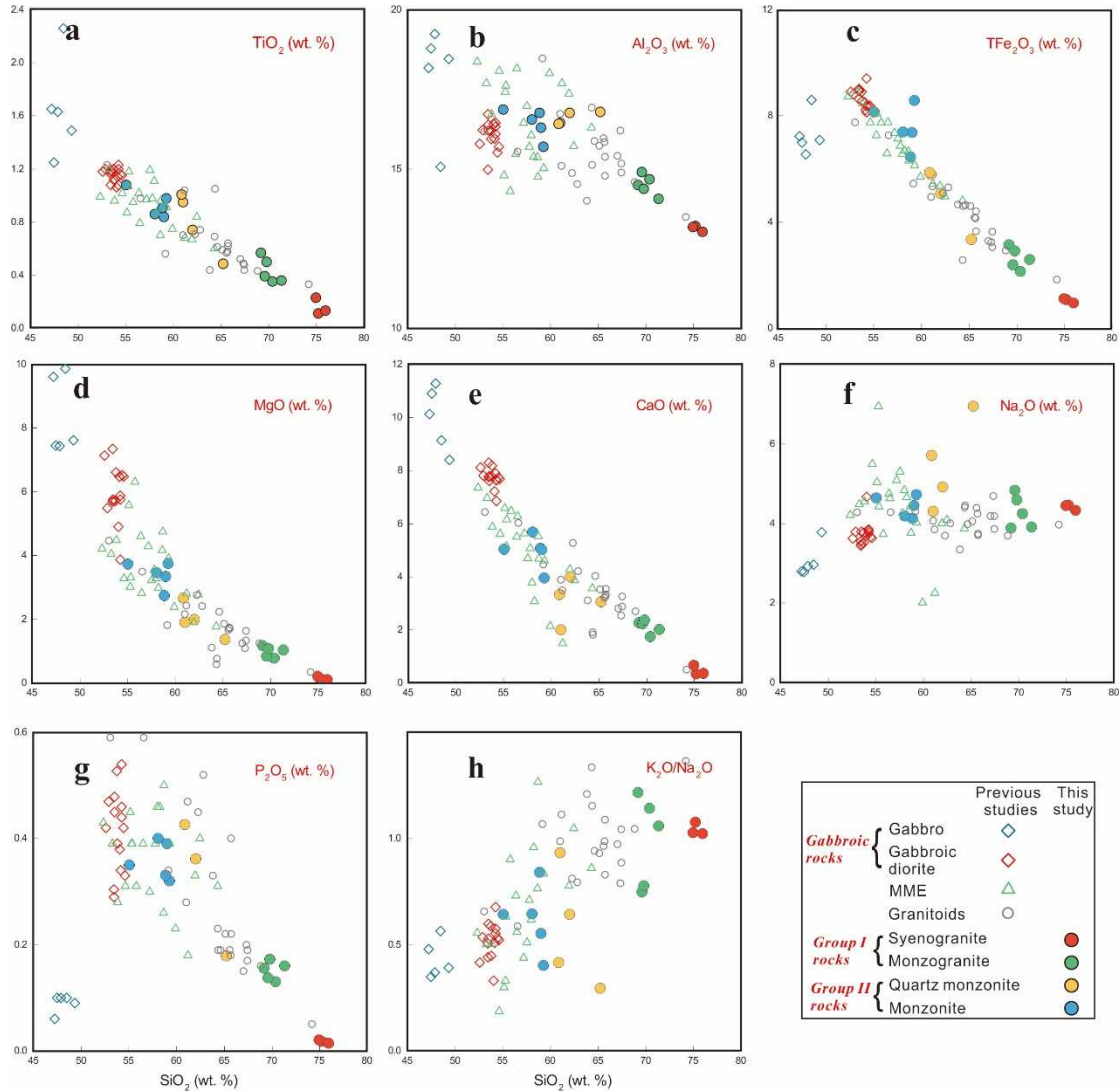


Fig. 8-4 Major elemental variation diagrams for the Laiyuan magmatic rocks from previous studies and this study. Data sources: gabbroic rocks (Hou et al., 2015; Liu et al., 2010); MME (Chen et al., 2009b; Zhang et al., 2016); granitoids (Zhang et al., 2016).

8.4.3 Two types of magmatic evolution

8.4.3.1 Group I rocks: Mixing and mingling of mantle- and crustal-derived magmas

Group I rocks are mainly dioritic with lower SiO_2 (55-65 wt. %), higher Al_2O_3 (>15 wt. %), TFe_2O_3 (4-8 wt. %), $\text{Mg}^\#$ (>45 wt. %), and P_2O_5 (>0.3 wt. %) than Group II rocks (Fig. 8-4). The features of enrichment of LILEs (e.g., Rb, Ba, Th and U), depletion in HFSEs (e.g., Nb, Ta and Ti), and fractionated REE patterns with

(La/Yb)_N varying from 11 to 77, are similar to the arc magmas (Pearce, 1984). Geochemically, the volcanic suites exposed in the Laiyuan complex also belong to Group I rocks (see Chapter 7) as well as the abundant MMEs and some felsic dykes (see Chapter 9). Although the Group I rocks existed in diverse forms (dykes, enclaves, and stocks), the scale of this type of magmatism is much smaller than the felsic magmatism, whose exposure areas are accounting for over 80% of the Laiyuan complex (Fig. 3-1), indicating the back burner of this type of magmatism to cause the heterogeneity in the magmatic complex.

For the magmatic evolution of Group I rocks, a model could be presented that incorporates two-step processes of initial fractional crystallization (FC) and subsequent mixing and mingling between two end-member (MM) from different sources. The above detailed study of synchronous ECVR (~130 Ma) has demonstrated that the enriched lithospheric mantle beneath the TM during Late Jurassic to Early Cretaceous acted as the source for the andesitic-dacitic magmas. The ECVR and Group I rocks share similar geochemical affinities, such as high mafic components indicating they may have similar parental magma derived from the mantle. The Group I rocks exhibit high Th/Yb (1-25) and Nb/Yb (5-30) ratios suggesting an enriched mantle source (Pearce, 2008). Thus, the parental mafic magma for the Group I rocks was derived from partial melting of an ancient enriched lithospheric mantle which experienced fluid-related metasomatism in the amphibole-bearing garnet-spinel transition stability field. Similarly, the FC process should be responsible for the high Sr/Y ratios and Ba-Sr contents of the Group I rocks. This hypothesis was tested by geochemical modeling based on Rayleigh fractionation (Fig. 8-8c). The modeling results show that the Group I rocks match well with the calculated curves of the FC process with the residual mineral assemblage of amphibole(95%)+plagioclase(4%)+zircon(1%). Notably, the Group I rocks show moderately fractionated LREE patterns relative to MREE, suggesting the significant removal of MREE-enriched minerals (e.g., hornblende, clinopyroxene, and zircon) (Castillo, 2012). Therefore, hornblende-dominated crystallization fractionation

probably controlled the limited magmatic differentiation of the Group I rocks magmas and caused their adakitic affinities.

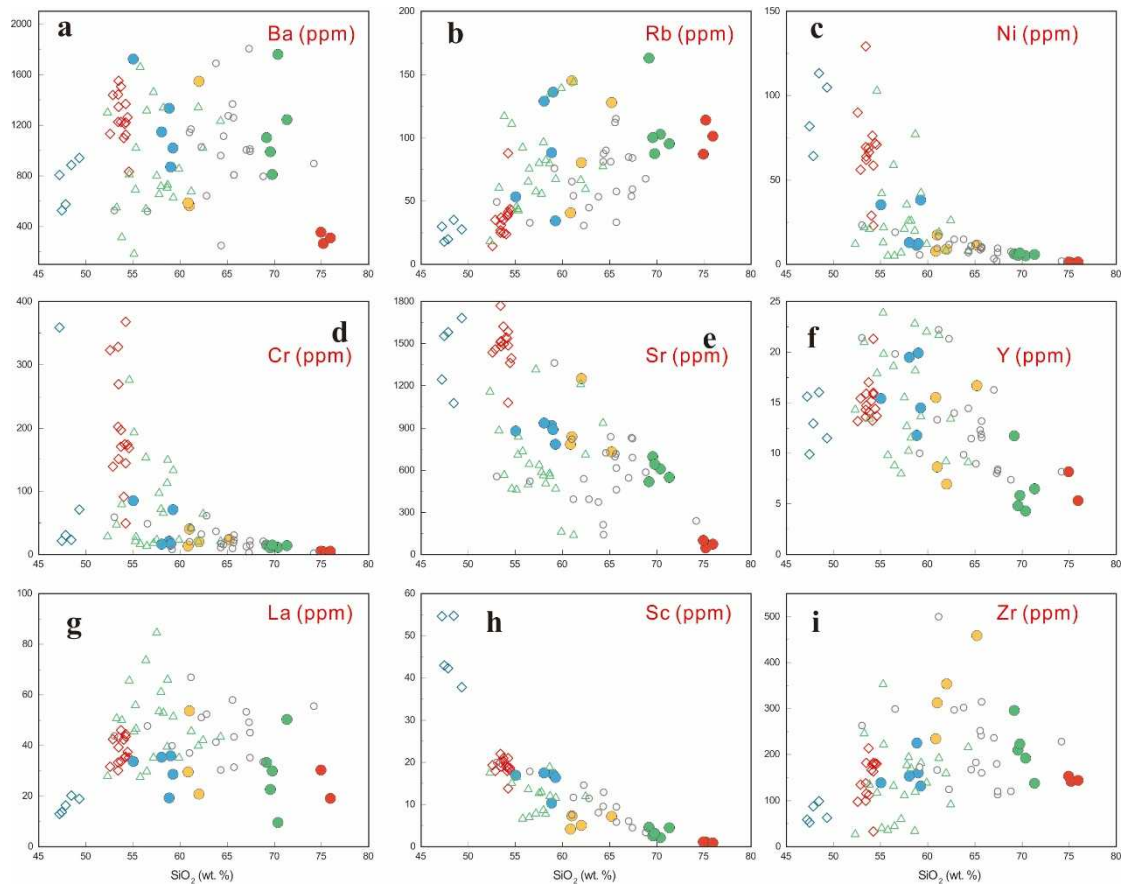


Fig. 8-5 Trace elemental variation diagrams for the Laiyuan magmatic rocks from previous studies and this study. Date sources and legend are as same as in Fig. 8-4.

Rather than the limited FC process, the MM process may play a more significant role in contributing to the variable compositions of the Group I rocks. The significant variations of trace elements cannot be attributed to the simple FC process but imply the multiple sources involved in the magmatic evolution (Fig. 8-5). The direct evidence is the immanent MMEs in the host granitoids which are regarded as the direct evidence of the MM process (Baxter and Feely, 2002; Reubi and Blundy, 2009). In general, there are three hypothesizes interpreting the origin of MMEs, i.e., fragments of recrystallized and refractory metamorphic rocks or melt residues from a granite source (Chappell et al., 1987; Vernon, 1990; White et al., 1999), cognate

fragments of cumulate minerals or early formed crystals from the host magma (Clemens and Wall, 1988; Donaire et al., 2005), and more mafic magma that was injected into and mingled with felsic magma (Barbarin, 2005; Chen et al., 2013). The metamorphic and sedimentary fabric from basement rocks have been identified in the host monzonite, indicating the possible restite model, but the distinct irregular contact lines between these fragments with host granitoids suggest they may be just captured from wall rocks when magma ascent (Fig. 3-4c, d). Furthermore, this type of xenolith is not commonly distributed in the host granitoids compared with the widespread MMEs having regular rounded or rod-like shapes and igneous textures (Fig. 3-4). The geochronological researches on the MMEs (Chen et al., 2005; Chen et al., 2007a) and host granitoids (this study) have verified that they were formed synchronously excluding the restite mechanism. Although the MMEs have mineral assemblages and isotopic ages similar to those of their host rocks (Fig. 3-5k, l), a cognate origin for the enclaves from the host magma is still not the dominant mechanism because of the lack of cumulate textures in the enclaves from widespread Group II rocks (Fig. 3-5k, l). Moreover, the collected enclaves and host syenogranite (LY-37/1) and monzogranite (LY-22/4) have different geochemical compositions (Fig. 8-2, Fig. 8-4, and Fig. 8-5) and therefore inconsistent with the autolith model. Thus, the most sensible explanation for the formation of MMEs is linked to the injected magmatic globules from pre-injection evolved magmas into host granitic magmas.

Based on detailed investigations on the chemical and mechanical transfer of crystals between MMEs and host granitoids, Chen et al. (2009b) proposed that the MMEs in the NTM were formed through remote and deep pre-injection MM process and post-injection local hybridization with host granitic magma. In this study, the MME sample (LY-37/1-2) was hosted by the syenogranite and showed similar geochemical characteristics to Group II rocks revealing the post-injection local hybridization (Fig. 8-4 and Fig. 8-5). The MMEs and Group I rocks are similar in mineral assemblages (Fig. 3-5, Table 3-1) and geochemistry (Fig. 8-4 and Fig. 8-5) indicating their magma consistency, but the variations of chemical and isotopic

compositions for MMEs is greater than the Group I rocks, e.g., the $Mg^\#$ (majorly 45-60), Al_2O_3 contents (14-18 wt. %), and zircon Hf isotopes (-22 to -6) (Chen et al., 2009b; Chen et al., 2007a). The variations result from the post-injection major elemental chemical exchange and crystal mechanical transfer between MMEs and host granitic magma. To result in broad distributions of MMEs in the complex, a mixed evolved magma reservoir is needed which should be the magmas of Group I rocks. Thus, the deep pre-injection MM process between basaltic magma and granitic magma contributed to the hybrid intermediate magma to form the Group I rocks.

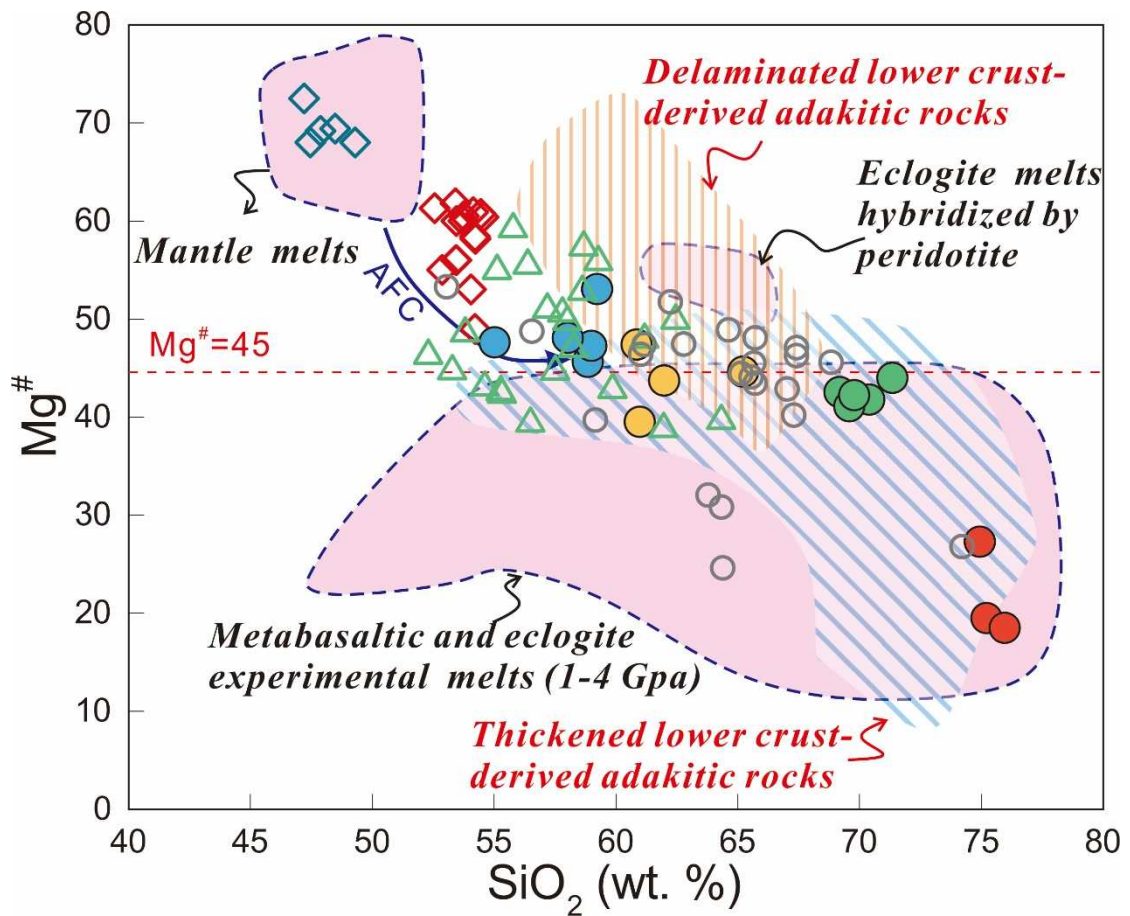


Fig. 8-6 $Mg^\#$ vs. SiO_2 (wt. %) diagram. AFC curve is modified after (Stern and Kilian, 1996).

Fields of metabasaltic and eclogite experimental melts hybridized with peridotite are after (Rapp et al., 1999). Field of metabasaltic and eclogitic melts (1-4 GPa) is after (Wang et al., 2006) and (Rapp and Watson, 1995). Fields of delaminated and thick lower crust-derived adakitic rocks are after (Wang et al., 2006). Date sources and legend are as same as in Fig. 8-4.

There are several lines of evidence to support the mixing origin for the Group I rocks. Firstly, unique petrological textures to witness the MM such as poikilitic texture, normal or reverse oscillatory zoning texture in the plagioclase grains, and quartz ocelli rimmed by ferromagnesian minerals could be identified in the Group I rocks (Fig. 3-5i, j, n, p). Secondly, geochemical data support the magma mixing origin. The Group I rocks have a range of intermediate compositions between those of the gabbroic rocks and host Group II rocks (monzogranite), indicating that they formed by mixing the mafic and felsic magmas (Ghaffari et al., 2015). In addition, Langmuir et al. (1978) showed that on a ratio–ratio plot, data consistent with mixing lie along a hyperbolic curve, while a linear trend occurs when the ratios of the concentrations of the two denominators are the same for all data points. In this study, linear trends are observed on SiO_2/MgO vs. $\text{Al}_2\text{O}_3/\text{MgO}$, and $\text{Na}_2\text{O}/\text{CaO}$ vs. $\text{Al}_2\text{O}_3/\text{CaO}$ plots (Fig. 8-7a, c), and hyperbolic mixing curves are observed on SiO_2/MgO vs. $\text{MgO}/\text{Al}_2\text{O}_3$ and Sc/Ga vs. Sr/Sc plots (Fig. 8-7b, d). Furthermore, Group I intrusions have high $\text{Mg}^\#$ values (up to 60), higher than experimental melts ($\text{Mg}^\# < 45$) of basaltic sources with similar silica contents (Fig. 8-6b; Rapp and Watson, 1995). This rules out partial melting of lower crust as the sole origin for these plutons, as an additional source of relatively high-Mg magmas is required. The gabbroic rocks in this area exhibit high-Mg characteristics which may be the mafic end-member during mixing. The simple mixing modeling between the gabbro sample LY-12/1 from the Laiyuan complex (unpublished data) and the monzogranite sample LY-21/2 (this study) shows that the Group I rocks match well with the calculated mixing curve indicating their mixing sources. These diagrams also exhibit the huge compositional gap between the Group II syenogranites and Group I rocks depriving the possibility that the magmas for syenogranites were highly evolved from the magmas for Group II rocks through magmatic differentiation. Finally, in sample LY-42/1 (monzonite), two clusters of zircons have been identified with mean ages of 137 Ma and 132 Ma. This older age of 137 Ma is consistent with the formation age of gabbroic rocks from the Longmengou mafic intrusions (Chen et al., 2005; Zhang, 2014) suggesting the existence of MM.

In summary, the parental mafic magma for the Group I intermediate rocks were derived from the enriched lithospheric mantle and subsequently experienced the hornblende-dominated FC process to form the LJVR and some monzonitic/dioritic magmas, then the magma mixing and mingling with the crustal melts/magmas generated the hybrid magmas to form the MMEs and variable intermediate suites.

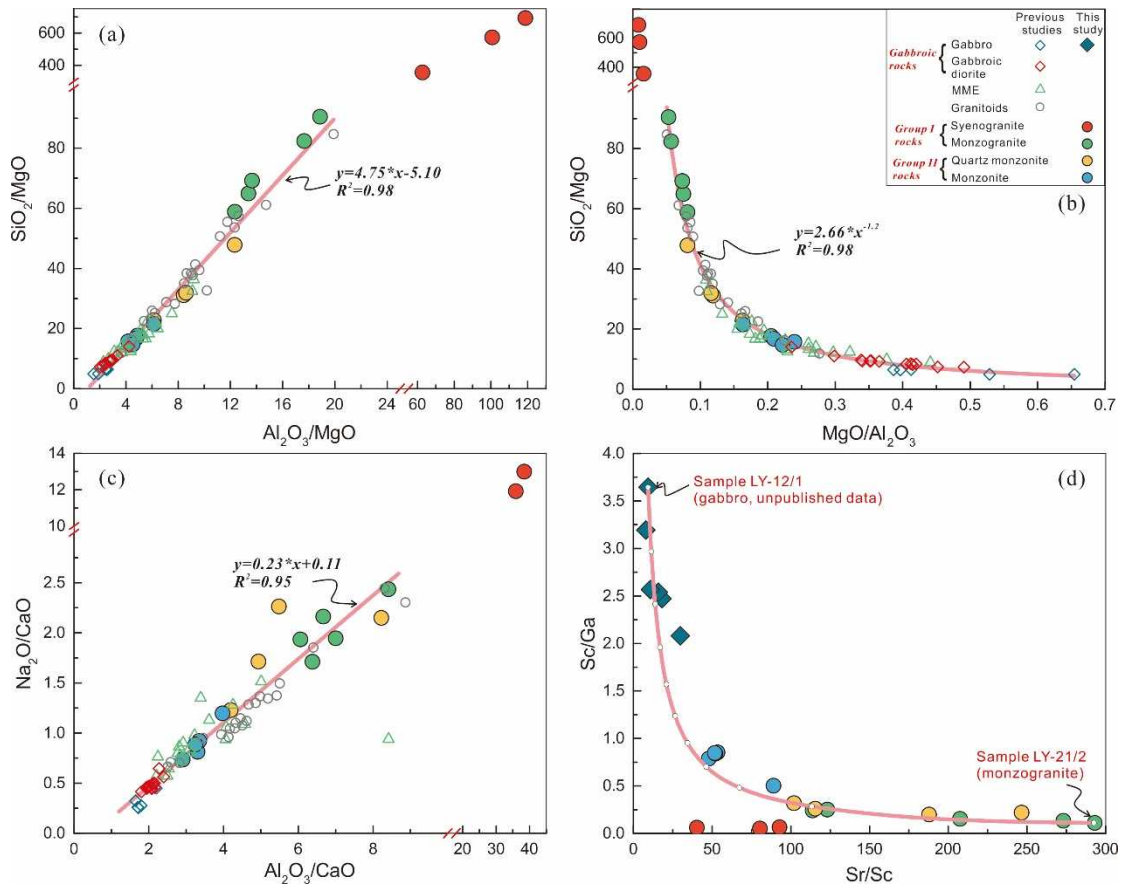


Fig. 8-7 Elemental ratio-ratio diagrams showing the magma mixing process in the Laiyuan magmatic rock. (a) SiO_2/MgO vs. $\text{Al}_2\text{O}_3/\text{MgO}$. (b) SiO_2/MgO vs. $\text{MgO}/\text{Al}_2\text{O}_3$. (c) $\text{Na}_2\text{O}/\text{CaO}$ vs. $\text{Al}_2\text{O}_3/\text{CaO}$. (d) Sc/Ga vs. Sr/Sc displaying the calculated curves corresponding to magmatic evolution by simple mixing. The gabbro sample LY-12/1 (unpublished data, $\text{Sr}=299.30$ ppm, $\text{Sc}=32.22$ ppm, $\text{Ga}=8.84$ ppm) represents mafic end-member, and the monzogranite sample LY-21/2 (this study, $\text{Sr}=608.40$ ppm, $\text{Sc}=2.08$ ppm, $\text{Ga}=18.85$ ppm) represents the felsic end-member. Ticks on these curves represent 10% increments.

8.4.3.2 Group II: Partial melting of thickened mafic lower crust

Group II rocks are classified as high-K calc-alkali I-type suite with higher SiO_2

(70-75 wt. %) and lower MgO (0.11-1.17 wt. %) contents and Mg[#] (19-44) than Group I rocks (Fig. 8-4 and Fig. 8-6) indicating their magmatic evolution difference. Several hypotheses have been proposed to explain the generation of calc-alkaline I-type granitoids, including (1) assimilation and fractional crystallization of mantle-derived basaltic or andesitic magmas ((DePaolo, 1981; Grove et al., 1997; Jagoutz, 2010; Lee and Bachmann, 2014); (2) reworking of sedimentary materials modified by mantle-like magmas (Collins and Richards, 2008; Kemp et al., 2007); and (3) partial melting of mafic lower crustal rocks with (i.e., magma mixing) or without the addition of mantle-derived mafic magmas (Chappell and White, 2001; Ratajeski et al., 2005; Sisson et al., 2005).

Group II samples have isotopic compositions that are almost indistinguishable from Group I samples (Fig. 6-1 and Fig. 6-2). This result, together with their similar emplacement ages (137-128 Ma), might indicate that Group II monzogranite represents differentiated Group I magmas. However, an interpretation whereby Group II rocks are derived from the partial melting of thickened lower crust with contributions from mantle-derived mafic magmas was more acceptable for the following reasons. Firstly, in some Harker diagrams (e.g., SiO₂ versus K₂O, Na₂O, Sr, and Ba) (Fig. 8-4 and Fig. 8-5), the monzogranites do not follow the trends shown by the Group I samples, but show a compositional gap between them and plot in isolated fields, implying that they were not derived from the Group I magmas. Secondly, although hornblende-dominated FC of basaltic magmas has been identified in the formation of the ECVR and Group I rocks, the much smaller volumes of mafic rocks in this complex cannot provide enough energy and materials to generate a much larger amount of granitic magmas to form the major igneous body of the complex. Moreover, modeling the processes of fractional crystallization using whole-rock chemical data also precludes the possibility of Group II monzogranitic rocks having been derived from the differentiation of Group I rocks (Fig. 8-8a, b, c). The Group II rocks don't follow the fractional crystallization trend defined by the Group I rocks.

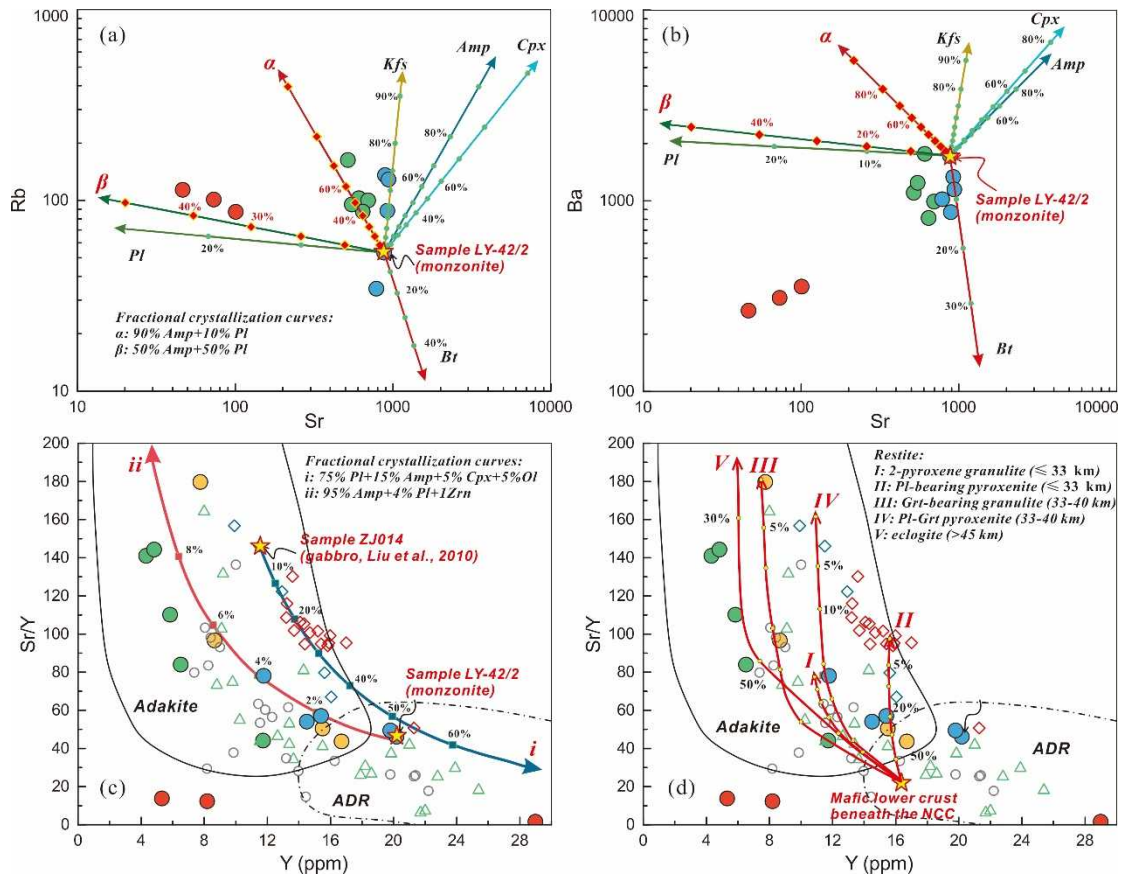


Fig. 8-8 Variation diagrams for the Laiyuan magmatic rocks compiled from this study and previous literature. (a) Rb vs. Sr and (b) Ba vs. Sr diagrams showing modeling of fractional crystallization for the Laiyuan granitoids. (c), (d) Sr/Y vs. Y diagrams exhibiting the calculated curves of Rayleigh fractional crystallization modeling, and calculated curves of batch partial melting of the mafic lower crust of the NCC ($Y=16.5$ ppm and $Sr/Y=21$) with different restites after [Ma et al. \(2015\)](#), respectively. The detailed parameters and start compositions in the modeling are listed in Table 7-2. Fields of adakites and classical island andesite–dacite–rhyolite rocks are modified from [Defant and Drummond \(1990\)](#). Abbreviation: ADR-normal arc andesite-dacite-rhyolite; Amp-amphibole; Bt-biotite; Cpx-clinopyroxene; Kfs-K-feldspar; Pl-plagioclase; Zrn-zircon. Date sources and legend are as same as in Fig. 8-4.

Thirdly, the monzogranites are characterized by high Sr contents (> 500 ppm), high Sr/Y ratios (> 40), low Y and HREE (<12 ppm) contents and are plotted in the adakite field in the Sr/Y-Y diagram showing different variation trend with the Group I rocks ([Fig. 8-8c, d](#)). The adakitic affinities for Group II rocks are unlikely to have

derived from the partial melting of subducted oceanic crust, because the higher K_2O contents (>3.50 wt. %) and $(^{87}Sr/^{86}Sr)_i$ ratios (>0.7060), low MgO (<1.20 wt. %), Cr (<15 ppm), Co (<7 ppm), and Ni (<7 ppm), and lower whole-rock $\epsilon_{Nd}(t)$ (<-12) and zircon $\epsilon_{Hf}(t)$ values (<-19) of the Group I rocks differ from the geochemical and isotopic features of the typical slab-derived adakites (Drummond et al., 1996; Li et al., 2016). This adakitic feature can also be originated from the partial melting of thickened mafic lower crust at sufficient depth (≥ 40 km) where garnet is stable within the residual assemblage (e.g., residues of garnet–amphibolite, amphibole-bearing eclogite, and/or eclogite) (Defant and Drummond, 1990; Moyen, 2009; Richards and Kerrich, 2007). As shown in the discriminative diagram (Fig. 8-6b), the studied low-Mg monzogranites all fell into the field for adakitic rocks derived from partial melting of the thickened lower crust. In addition, the Group II monzogranite samples plot along the calculated batch partial melting curves for the eclogite (>45 km) in Sr/Y-Y diagram (Fig. 8-8d) suggesting that these rocks formed from melts generated by partial melting of a thickened lower crustal source, leaving an eclogite restite (Atherton and Petford, 1993; Defant and Drummond, 1990; Ma et al., 2015). Therefore, it is concluded that the Group II monzogranite probably formed via partial melting of thickened mafic crustal sources rather than by fractional crystallization of the Group I dioritic magmas.

Another question remaining is the origin of high $Mg^\#$ for the Group II rocks. The Mg numbers of the monzogranites are higher than those of experimental melts from basalts at the same silica contents (Rapp and Watson, 1995; Sen and Dunn, 1994) suggesting the source cannot be the pure crustal melts. The contribution from mantle materials is needed. The studies of high-Mg andesites from the eastern NCC have demonstrated that the melts derived from the delaminated mafic lower crust and interaction with the overlying lithospheric mantle can result in the high Mg numbers (Gao et al., 2004; Jiang et al., 2007; Xu et al., 2008; Xu et al., 2009b). However, the absence of peridotite xenoliths in the studied rocks doesn't support the delamination model. Therefore, the parental basaltic magma should also involve in the formation of

the anatectic felsic melts, not only providing thermal energy for crustal melting (Chen et al., 2013). This hypothesis was also supported by the modeled mixing process between the lower crust of the NCC and the enriched lithospheric mantle using whole-rock Sr-Nd isotopes (Zhang et al., 2016). The granitoids plot along the modeling mixing curve and displays that ~30 % mantle materials were involved in the lower crust-derived magmas for the Group I rocks (Fig. 6-2), which was also supported by the simple mixing modeling (~10%, Fig. 8-7).

The highly fractionated syenogranites are also included in the Group II rocks and show similarities in their crustal magma source. It is suggested that the highly-fractionated granites are evolved from felsic magmas through intense FC process such as Himalayan leucogranites (Guo and Wilson, 2012; Le Fort et al., 1987) and some Mesozoic granites in southeastern China (Li et al., 2007). Leucogranites were also identified in the NTM from the Wanganzhen and Dahenan plutons which show similar geochemical features to these studied syenogranites (Cai et al., 2003; Chen et al., 2003; Zhang et al., 2016). Identical to these leucogranites, the syenogranite rocks experienced strong plagioclase mineral removal as revealed by the strong depletion in Eu, negative correlation between SiO₂ and Al₂O₃, and rare plagioclase crystals in the rocks. The fractional crystallization of hornblende, pyroxene, and Fe-Ti oxides are also revealed in the elemental variation diagrams (Fig. 8-4, Fig. 8-5, and Fig. 8-7).

Based on the above discussion, it is concluded that the granites were most likely generated by partial melting of the thickened mafic lower crust at high pressure, with some addition of the mafic magma from an enriched mantle, and followed by intense crystal fractionations of plagioclase, hornblende, pyroxene, and accessory minerals such as apatite. The compositional variabilities of the Laiyuan granitoids result from the multiple involved sources, chaotic mixing and mingling process and the complicated fractional crystallization (Fig. 8-9).

8.4.4 Crust-mantle interaction

Intense mantle and crustal magmatic process have been identified in the

formation of the Laiyuan magmatic complex suggesting the significant role of crust-mantle interaction to contribute to the formation of voluminous plutonic rocks in the central NCC (Chen et al., 2007b; He et al., 2017a; Li et al., 2019a). In many cases, the mantle-derived underplated mafic magmas act as not only the thermal source to induce the crustal melting, but also the mafic end-member to interact with the felsic melts/magmas derived from the crust (Annen et al., 2006; Wang et al., 2017). Multiple magmatic processes are involved throughout the crust-mantle interaction, including the partial melting of variable sources, fractional crystallization, magma mixing and mingling, crystal accumulation and compaction, assimilation and contamination, and chemical exchange and mixing (Ma et al., 2019; Turnbull et al., 2010). As a result, a series of magmatic rocks with contrasting compositions were formed, including mafic-ultramafic rocks and felsic rocks in forms of eruption, plutonic emplacement, enclave, and dyke. These rocks constitute the enormous magmatic complex with petrological, compositional, and textural variations that could trace the deep crust-mantle interaction and multiple magmatic evolutions. The petrological complexities in the Laiyuan magmatic complex account for the chance to investigate the crust-mantle interaction in the central NCC. Above detailed petrological, geochemical, isotopic, and geochronological researches have illustrated that the incorporation of the thickened lower crust and enriched lithospheric mantle in the source, and the involvement of diverse magmatic processes, have played a significant role in the petrogenesis of the Laiyuan igneous complex arousing the heterogeneities (Fig. 8-9). In the central NCC, such magmatic complexes (plutons) similar to the Laiyuan complex, such as the Dahenan complex (Chen et al., 2009b) and Mapeng pluton (He and Santosh, 2014) from the NTM, and the Fushan pluton (Li et al., 2019a) from the STM, are widespread indicating that the intense crust-mantle interaction is the common deep process beneath the intra-domain of the NCC. The crust-mantle interaction took place during Late Mesozoic, peaking at Early Cretaceous, consistent with the NCC destruction peaking period (Liu et al., 2019; Wu et al., 2019; Zhang et al., 2014) revealing the tight internal genetic relationship

between the magmatism, interaction, and destruction. In brief, the deep crust-mantle interaction holds important clues to the Mesozoic tectonic setting and craton destruction mechanism in the central NCC which will be discussed in the following chapter.

8.5 Summary

(1) Zircon geochronology of the Laiyuan granitoids showed that they were formed during the Early Cretaceous at 137-128 Ma with $\epsilon_{\text{Hf}}(t)$ values and T_{DM}^{C} ages ranging from -21.8 to -16.8 and 2564 to 2255 Ma, respectively, indicating the mixed source of lithospheric mantle and mafic lower crustal materials.

(2) The granitoids display variable compositions and can be classified into two groups. The Group I rocks with low SiO_2 concentrations, high MgO contents, and $\text{Mg}^{\#}$ comprise monzonite, quartz monzonite, and diorite in forms of enclaves and intrusions. The parental mafic magma for the Group I rocks were derived from the enriched lithospheric mantle and subsequently experienced the hornblende-dominated fractional crystallization to form the monzonitic/dioritic magmas, then the magma mixing and mingling with the crustal melts/magmas generated the hybrid magmas to form the MMEs and variable intermediate suites.

(3) Group II rocks are classified as high-K calc-alkaline I-type suites with higher SiO_2 and lower MgO contents and $\text{Mg}^{\#}$ than Group I rocks, including monzogranites and syenogranites. These granitic rocks were most likely generated by partial melting of the thickened mafic lower crust at high pressure, with some addition of mafic magma from an enriched mantle, and followed by intense crystal fractionations of plagioclase, hornblende, pyroxene, and accessory minerals such as apatite to form the highly-fractionated syenogranites.

(4) The crust-mantle interaction accounts for the petrogenesis of the Laiyuan magmatic complex. The compositional heterogeneities of the igneous complex resulted from the multiple involved mantle and crustal sources, chaotic mixing and mingling process, and the complex fractional crystallization during the deep interaction process.

Chapter 9 Petrogenesis of dyke suites

9.1 Introduction

Lamprophyres are small-volume, mesocratic to melanocratic, mostly hypabyssal, volatile-rich mafic-ultramafic igneous rocks, occurring as sills, dykes, or pipes. Porphyritic texture with large ferromagnesian minerals (olivine, clinopyroxene, amphibole, and biotite) set in a fine-grained groundmass is typical of these rocks (Wooley et al., 1996). Rock (1987) defined five subgroups of lamprophyre clan, including ultramafic lamprophyres (UL), alkali lamprophyres (AL), calc-alkali lamprophyres (CAL), lamproites (LL), and kimberlites. However, according to the IUGS standard, lamproites and kimberlites are different from the lamprophyres and should not be classified as lamprophyres (Wooley et al., 1996). Lamprophyres, kimberlites, dolerites, and carbonatites derived from mantle sources provide windows to investigate the nature of deep mantle (Foley et al., 1987). They are also considered as important proxies for mantle-derived magmatism within intra-cratonic rift settings or post-orogenic settings along craton margins, with significant implications to track mantle plumes (Lu et al., 2015), asthenosphere plume-lithosphere interaction (Kerr et al., 2010), and mantle metasomatism (Woodard et al., 2014).

As discussed above, the NCC has experienced extensive craton destruction during Mesozoic. Voluminous intrusive and extrusive rock suites were well documented in the Jiaodong region within the eastern NCC, and the TM within the central NCC. Recent studies have revealed that the present lithosphere beneath the central NCC and eastern NCC are different indicating that the lithosphere experienced distinct evolutionary process (Liu et al., 2019). Therefore, it is of great importance to study the nature of lithosphere at Mesozoic in the NCC which could be recorded by deep mantle-derived mafic dykes. In this context, mantle-derived mafic dykes assume importance in gaining insights on the nature of the mantle and crust-mantle interaction processes beneath the NCC. Mesozoic mafic dykes in the NCC are dominantly

dolerite and lamprophyre distributed in over 300 localities (Liu et al., 2017b). However, compared with their equivalents in south China (Lu et al., 2015), most of the detailed-studied mafic dykes in the NCC are confined to the Shandong region in the eastern margin of the craton (Deng et al., 2017a; Liang et al., 2017), with only a few investigations from the other regions. The TM region occurs within the Trans-North China Orogen in the central part of the NCC, and is an important province for Mesozoic magmatism and metallogeny (Li and Santosh, 2017). A few previous studies reported mafic dykes within some intrusive plutons such as in the Mapeng pluton (Li et al., 2015a). A large number of mafic dykes occur within the Laiyuan complex, although only few studies have so far focused on the geochemical and isotopic features of these rocks (Yang, 1989; Yang, 1991; Zhang et al., 2003b).

In this study, detailed field investigations and sampling were carried out in the Laiyuan complex, focusing on the various suites of dykes including typical lamprophyre and dolerites, as well as felsic dykes. Brand-new results are presented from detailed petrology and mineral chemistry, whole major, trace and REE geochemistry, zircon U-Pb geochronology, and in-situ Lu-Hf isotopes. The objectives of this study are: (1) to document precisely the emplacement ages of the various dyke suites; (2) to assess the nature and variation of mantle sources beneath the NTM during Mesozoic; (3) to understand the petrogenesis and magma source characteristics; and (4) to evaluate the implications of the results on the lithospheric evolution and destruction of the NCC.

9.2 Petrography and mineral chemistry

The petrographic features of these rocks were described in Chapter 3. The mafic dykes are lamprophyres and dolerite or dolerite porphyry, and the felsic dykes include diorite porphyry and granodiorite as exhibited in Fig. 3-6, Fig. 3-7, and Table 3-1.

Representative minerals in samples LY-13/2 (dolerite), LY-16/1 (lamprophyre), and LYN-1/4 (granodiorite) were selected for EPMA analysis and the result are listed in Table 9-1 to Table 9-4, including pyroxene, amphibole, plagioclase, and mica.

9.2.1 Pyroxenes

Clinopyroxenes occur in the mafic dykes (samples LY-13/2 and LY-16/1) (Table 9-1). Clinopyroxene minerals from lamprophyre are classified as diopside in the classification diagram (Fig. 9-1a) whereas clinopyroxene from dolerite falls in the augite field consistent with the microscope observation. They are all characterized by Mg-rich [$X_{Mg}=Mg/(Fe+Mg)=0.67-0.83$] nature with only small composition difference between the two rocks. Diopside with zoning texture is very pronounced in lamprophyres (sample LY-16/1) occurring as idiomorphic phenocrysts with thick core and mantle and a thin rim (Fig. 3-7c). However, the compositional zoning is not prominent as demonstrated by the narrow range of X_{Mg} from 0.83 to 0.72 (Table 9-1). Augite phenocrysts from the dolerite also do not show any marked compositional zoning (Fig. 3-7h).

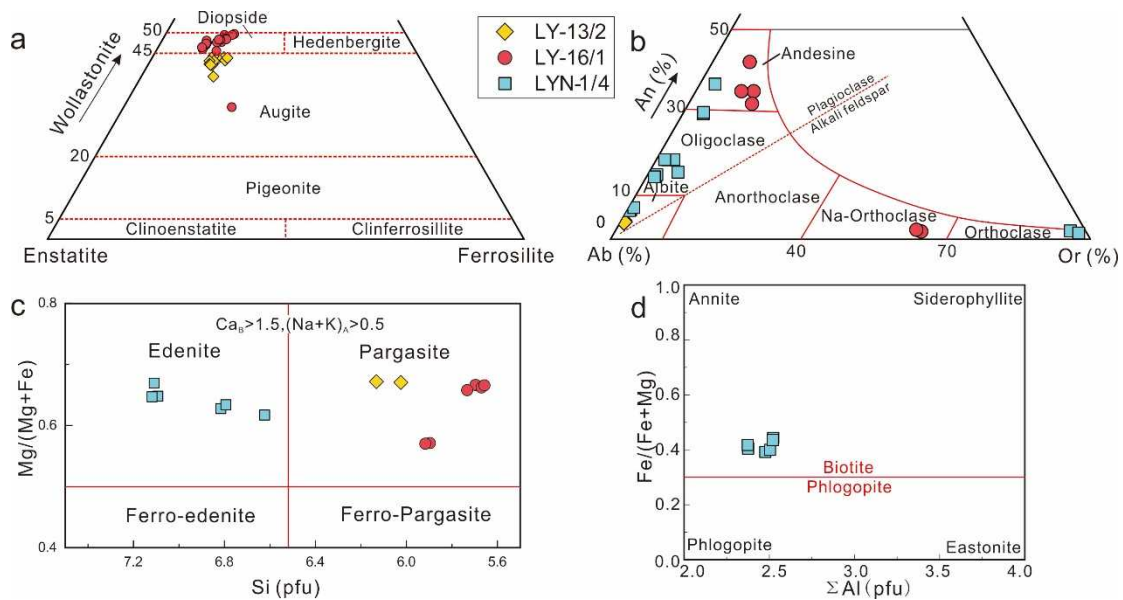


Fig. 9-1 Classification diagrams for minerals. (a) Enstatite-Ferrosilite-Wollastonite ternary diagram for pyroxene (Lindsley and Andersen, 1983). (b) Anorthite-Orthoclase-Albite ternary classification diagram for feldspar (Smith and Brown, 1974). (c) Mg/(Mg+Fe) vs. Si classification diagram for amphibole (Leake et al., 1997). (d) Mg/(Mg+Fe) vs. ΣAl classification plot for biotite (Barbarin, 1999).

9.2.2 Feldspars

Feldspars in the studied rocks are almost plagioclase except two spots from the

lamprophyre (sample LY-16/1) and two from the granodiorite (sample LYN-1/4) which plot in the alkali feldspar field (Fig. 9-1b). The plagioclase minerals in lamprophyres fall in the field of andesine and slightly albite-rich ($An_{33-43} Ab_{50-55} Or_{8-13}$) whereas the plagioclase from dolerite (sample LY-13/2) is classified as albite ($An_4 Ab_{95} Or_1$) (Fig. 9-1b). Plagioclase grains in granodiorite (sample LY-1/4) exhibit compositional variations from andesine to albite (Ab_{60-93}) depending on their textural association such as plagioclase inclusions in biotite and euhedral phenocrysts (Fig. 3-7l). Overall, the compositional difference between core and rim is not significant. Alkali feldspars from lamprophyre and granodiorite fall in the Na-orthoclase and orthoclase fields in anorthite-albite-orthoclase diagram (Fig. 9-1b), respectively. K-feldspar is not common in the lamprophyre and rarely occurs as fine-grained minerals in matrix.

9.2.3 Amphibole

Amphiboles from lamprophyre (sample LY-16/1) and dolerite (sample LY-13/2) are classified as pargasite, and amphiboles from the granodiorite (sample LYN-1/4) plot in the edenite field indicating notable compositional variation depending on their occurrences (Fig. 9-1c). They are all characterized by high Ca (1.757-1.955 pfu), moderate Mg (2.702-3.179 pfu) and limited range of X_{Mg} (0.57-0.67), with pargasite composition in the mafic rocks (2.017-2.574 pfu) and Al-rich than edenite in the felsic rocks (1.070-1.452 pfu) (Table 9-3). Pargasite in the lamprophyre forms xenomorphic to subhedral grains and sometimes occurs as small matrix minerals (Fig. 3-7a, b, c, d).

9.2.4 Biotite

Biotite is not common in the mafic dykes but is the main mafic mineral in granodiorite (sample LYN-1/4; Fig. 3-7l). It is characterized by Mg-rich ($X_{Mg}=0.56-0.61$), Ti-poor (0.267-0.443 pfu), and Fe-rich (FeO=16.00-17.69 wt. %) compositions (Table 9-4). The Fe/(Fe+Mg) ratios show a narrow range from 0.392 to 0.443 indicating that post-magmatic alteration is negligible. Biotites are also Ca-free or Ca-poor, indicating that they were least affected by chloritization and sericitization

through meteoric fluid circulation or post-magmatic deuteric alteration. They are plotted in the biotite field near the annite end member (Fig. 9-1d).

9.3 Geochemistry

Seventeen dyke samples, including four lamprophyres, ten dolerites and dolerite porphyry, and three felsic dykes from the Laiyuan complex were analyzed for geochemistry. The results are listed in Table 9-5.

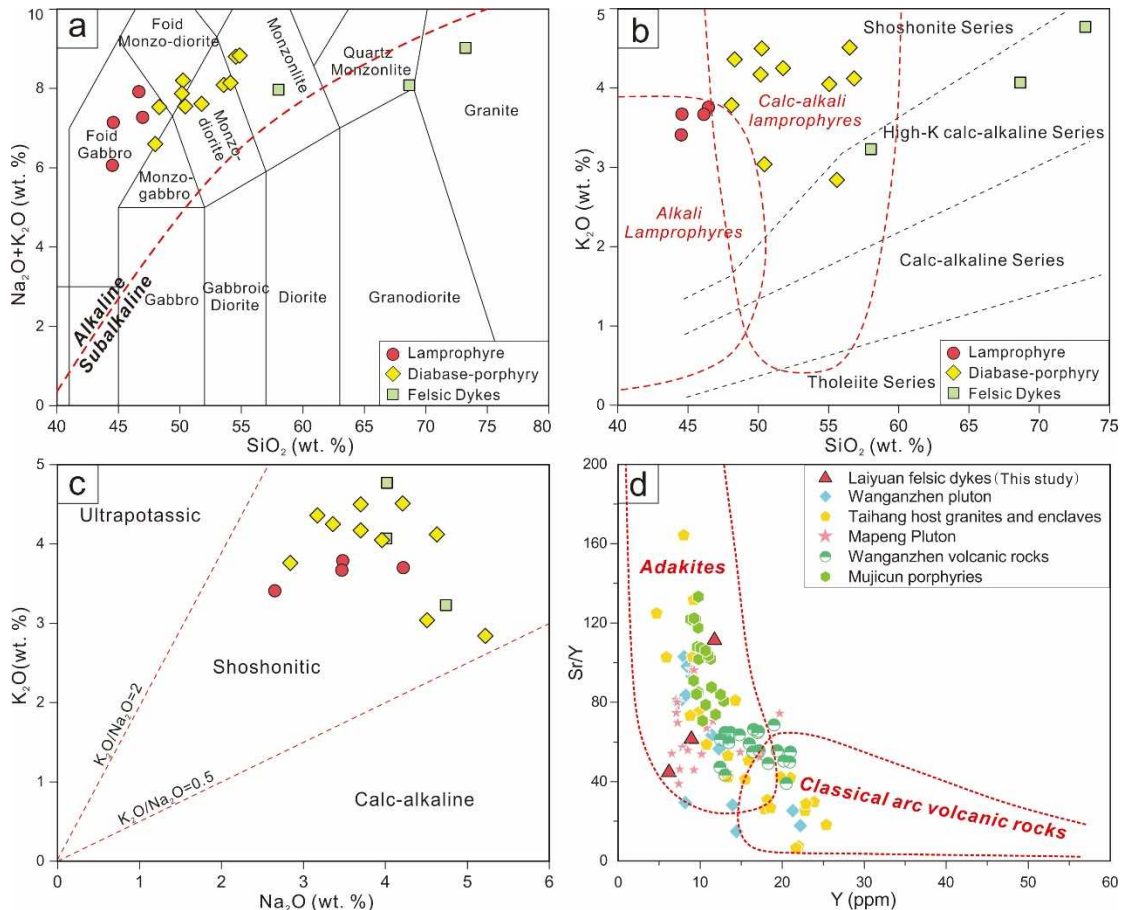


Fig. 9-2 (a) TAS diagram for classification of the Laiyuan dykes (Middlemost, 1994). (b) K_2O vs. SiO_2 classification diagram (Peccerillo and Taylor, 1975). The fields of alkali lamprophyres and calc-alkali lamprophyres are modified after Rock (1987). (c) K_2O vs. Na_2O classification diagram.

(d) Sr/Y-Y classification diagram for adakite (Defant and Drummond, 1990). Data sources:

Wanganzhen pluton (Zhang et al., 2016); Taihang host granite and mafic enclaves (Chen et al., 2009b); Mapeng pluton (Li et al., 2015a); Wanganzhen volcanic rocks (Gao et al., 2012); Mujicun porphyries (Gao et al., 2013).

The lamprophyres (samples LY-8/1, LY-16/1, LYN-1/1, and LYN-2/1) show low concentrations of SiO₂ (44.51-47.97 wt. %, average 45.68 wt. %) and high contents of MgO (4.47-8.37 wt. %, average 5.61 wt. %) as well as relatively high Mg[#] ranging from 49 to 62 with an average of 53, which are typical of mafic magma. The lamprophyres have total alkali (Na₂O+K₂O) contents of 6.06-7.92 wt. % and plot in the Foid-gabbro field in the TAS diagram (Middlemost, 1994) (Fig. 9-2a). The lamprophyres also show shoshonitic characteristics (Fig. 9-2b, c), and belong to the alkali lamprophyre field in the K₂O vs. SiO₂ plot (Fig. 9-2b). As shown in Fig. 9-3, they have relatively high Fe₂O₃ (3.34-4.51 wt. %, average 4.04 wt. %), FeO (3.83-5.44 wt. %, 4.82 wt. %), CaO (6.03-9.20 wt. %, average 7.72 wt. %), and TiO₂ (1.44-2.01 wt. %, average 1.65 wt. %) contents but show low Na₂O (2.65-4.22 wt. %, average 3.46 wt. %) and K₂O (3.41-3.79 wt. %, average 3.64 wt. %). The high concentrations of CO₂ and LOI range from 0.86 to 4.20 wt. % with average of 2.85 wt. %, and 3.65-6.88 wt. % with average of 5.39 wt. %, respectively.

Compared with lamprophyres, the dolerites and dolerite porphyries (samples LY-7/1, LY-13/1, LY-13/2, LY-15/1, LY-15/2, LY-16/2, LY-18/1, LY-26/1, LY-26/2, and LYN-4/1) display a broad compositional change from foid gabbro, foid monzo-diorite, to monzo-diorite in the total alkali versus SiO₂ diagram (Fig. 9-2a). Their SiO₂ and MgO contents range from 47.98 to 56.82 wt. % and 2.50 to 5.22 wt. %, respectively, which are lower than those of lamprophyres. Their Mg[#] (44-54, average 49) are also not higher than those of lamprophyres. They also exhibit shoshonitic features in diagrams of K₂O vs. SiO₂ and K₂O vs. Na₂O similar to lamprophyres (Fig. 9-2b, c). They are characterized by 1.97-4.88 wt. % Fe₂O₃ (average 3.76 wt. %), 3.00-5.05 wt. % FeO (average 3.99 wt. %), 3.48-6.07 wt. % CaO (average 4.94 wt. %), 1.09-2.08 wt. % TiO₂ (average 1.57 wt. %), 14.39-16.01 wt. % Al₂O₃ (average 15.52 wt. %), 2.84-5.22 wt. % Na₂O (average 3.93 wt. %), and 2.84-4.51 wt. % K₂O (average 3.96 wt. %), with low concentrations of MnO (0.07-0.12 wt. %), P₂O₅ (0.86-1.14 wt. %), and moderate LOI (2.08-7.39 wt. %) and CO₂ (0.17-4.97 wt. %).

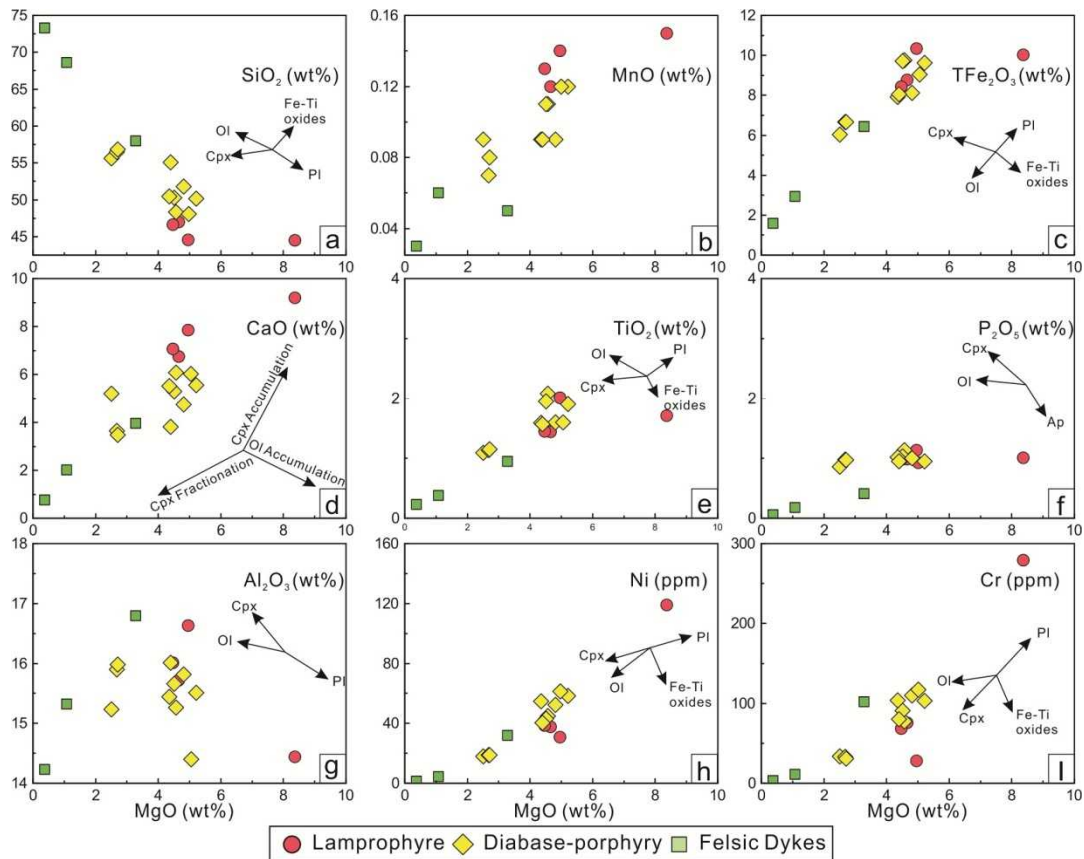


Fig. 9-3 Elemental variation diagrams for the Laiyuan dykes showing possible fractionating phases during magma evolution (Guo et al., 2004).

Unlike the mafic dykes, major elements of felsic dykes show obviously different features of higher silica contents (58.02-73.27 wt. %), alkali contents (7.97-8.79 wt. %), and lower MgO (0.37-3.28 wt. %, average 1.57 wt. %), TiO₂ (0.23-0.95 wt. %, average 0.52 wt. %), TFe₂O₃ (1.58-6.44 wt. %, average 3.65 wt. %), CaO (0.76-3.97 wt. %, average 2.25 wt. %), P₂O₅ (0.06-0.41 wt. %, average 0.22 wt. %), and Mg[#] (32-50, average 41). In terms of volatiles, the CO₂ contents of felsic dykes range from 0.26 to 0.77 wt. %, and are much lower than those of the mafic dykes with an average of 2.85 wt. %. Their composition varies from monzonite, quartz monzonite, to granite as shown by plots in TAS diagram (Fig. 9-2a). They all belong to high-K calc alkaline series (Fig. 9-2b) and are characterized by shoshonitic features (Fig. 9-2c).

In chondrite-normalized REE patterns (Fig. 9-4a, c, e), all of the studied rocks show features of enrichment in light rare earth elements (LREEs) with (La/Yb)_N of

lamprophyres, dolerites and felsic dykes ranging from 35.70 to 47.40, 26.72 to 79.42 and 36.77 to 44.83, respectively which are significantly higher than that of lower continental crust (5.3). However, total contents of REEs of the mafic dyke (average 418 ppm) samples are higher than that of the felsic dyke samples (average 178 ppm). All the samples are characterized by the lack of obvious Eu anomalies. In the primitive mantle-normalized spidergram (Fig. 9-4b, d, f), the mafic dyke samples show enrichment in fluid-mobile LILEs (e.g., Ba, K, and Pb). The dolerites show strong depletion in HFSEs. However, Th-U and Ta-Nb depletions in lamprophyres are not obvious, implying the different sources of dolerites and lamprophyres. The lamprophyres exhibit geochemical signatures characteristics of OIB-type alkali basalt (Fig. 9-4b). Compared with mafic rocks, the felsic dyke samples show stronger Nb-Ta and Ti depletion and Pb enrichment indicating their crustal origin.

9.4 Petrogenesis

9.4.1 Effects of crustal contamination and fractional crystallization

The lamprophyres and dolerites (dolerite porphyries) from Laiyuan show typical features of mantle-derived rocks with low SiO₂ contents (44.51 to 46.97 wt. % for lamprophyres and 48.32 to 56.82 wt. % for dolerites), and high concentrations of MgO (4.47 to 8.37 wt. % for lamprophyres and 2.50 to 5.22 wt. % for dolerites). Therefore, the compositional features of mafic rocks can be used to explore the nature of mantle source (Ma et al., 2014a). Although it is difficult to contaminate the rapidly rising and low viscosity mafic magma, it is essential to evaluate the effects of crustal contamination before trying to assess the mantle source characteristics.

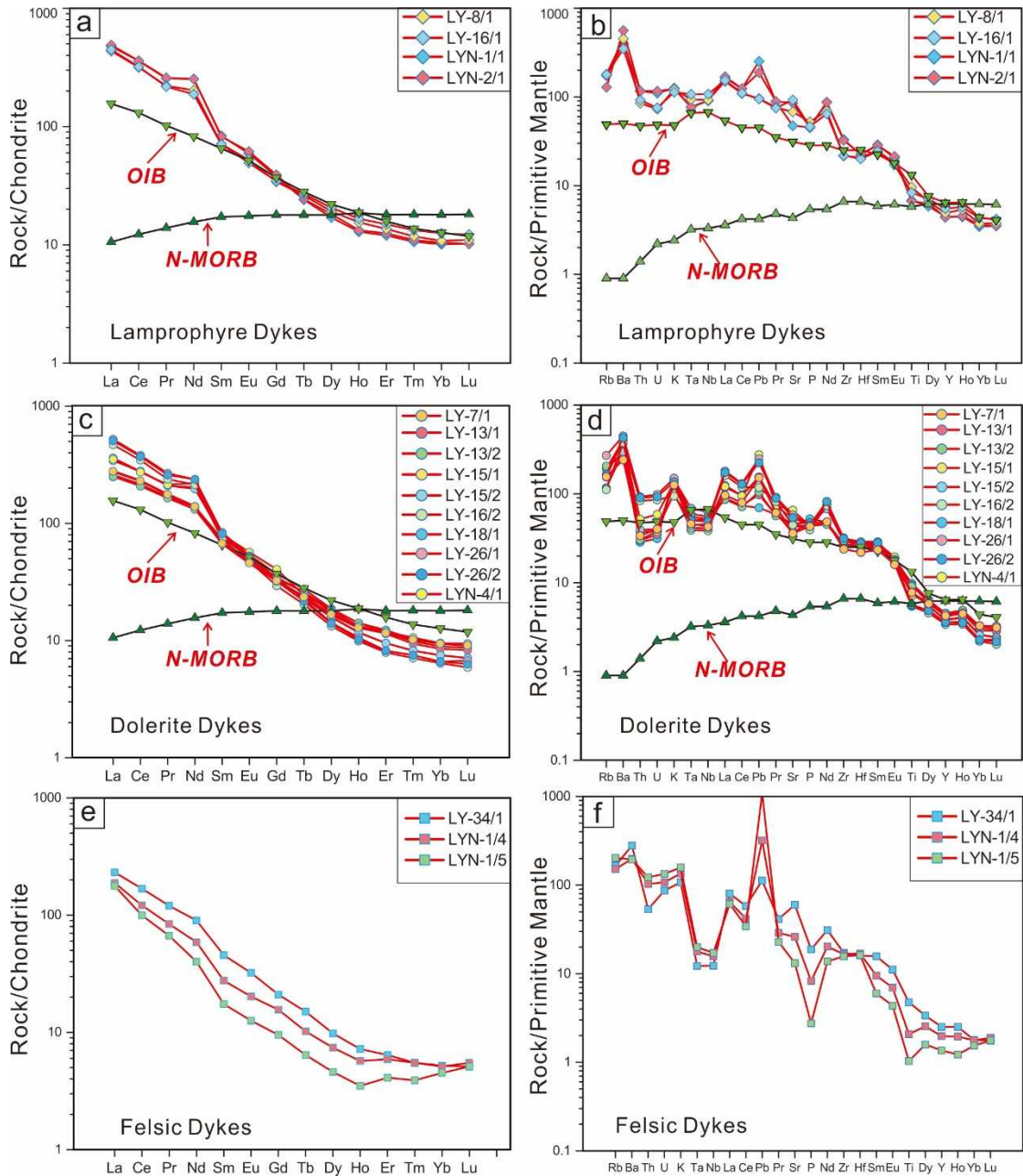


Fig. 9-4 Chondrite-normalized rare earth element (REE) distribution diagrams (a, c, e) and primitive mantle-normalized multi-element variation diagrams (b, d, f). Normalized values: chondrite (McDonough and Sun, 1995), primitive mantle (Sun and McDonough, 1989) and N-MORB and OIB (Sun and McDonough, 1989).

Among the zircon grains of lamprophyres and dolerites, inherited zircon cores are not common, but multiple groups of different ages can be identified in lamprophyres and older zircon xenocrysts from basement rocks in dolerites which

might suggest the presence of limited crustal contamination during magma ascent. These also mark the difference between the sources of lamprophyres and dolerites. The involvement of continental components in the magma source of the mafic dykes is also indicated by the crust-like trace element features, including enrichment in LILEs and LREEs, positive Pb anomalies and depletion in HFSEs, and negative Ta-Nb anomalies. However, the following evidence suggests that these lamprophyres and dolerites may have only experienced a limited crustal contamination. The Ba (1672-3910 ppm) and Sr (754-1949) contents are markedly higher than the average continental crust value (390 ppm of Ba and 325 ppm of Sr; [Rudnick and Fountain, 1995](#)) precluding any significant input of crustal components. Low HREE ratios (Lu/Yb=0.14-0.16) also indicate a mantle-derived magma. Higher Lu/Yb ratios (0.16-0.18) are considered as an indicator of crustal involvement ([Sun and Mcdonough, 1989](#)), whereas the data from the mafic dykes display only a lower range of 0.14-0.15 indicating minor effects of crustal contamination. The Nb/U ratio and Nb concentration are also good indicators to assess the extent of crustal contamination. [Hofmann et al. \(1986\)](#) identified that Nb/U ratios are uniform at 47 ± 10 , in both uncontaminated MORB and OIB around the world. As shown in [Fig. 9-5](#), the Nb/U ratios of these mafic rocks show a variable range of 16.79-67.12 which are not totally uniform. But most of the samples are plotted close to the MORB and OIB fields and similar to the asthenospheric mantle-derived mafic dykes (AMDR), especially the lamprophyres. The lamprophyres experienced less incorporation of crustal materials than dolerites in Laiyuan area revealed by the negative Th-U anomalies in dolerite dykes and no Th-U anomalies in lamprophyre dykes ([Li et al., 2017](#)). Therefore, the large variation of Nb/U ratios of mafic dykes suggests the existence of crustal contamination, but the relative concentration also indicates limited role of the crustal contamination. Notably, they are different from the lithospheric mantle-derived mafic dykes (LMDR) from the Jiaodong Peninsula which are caused by lower crustal recycling ([Ma et al., 2014a](#); [Ma et al., 2016](#); [Ma et al., 2014b](#)) implying the minor role of lower crustal on the source of mafic dykes from the Laiyuan complex. According

to the above discussion, although the effects of crustal contamination cannot be totally eliminated, it is evident that such process did not play any significant role in the composition of mafic magma during its ascent. Therefore, the compositional signatures of the mafic dykes were mainly inherited from original mantle sources. Among these studied rocks, sample LY-16/1 may represent the most primitive composition.

The fractional crystallization process is another important factor. The mafic dykes in this study show a large variation in $Mg^{\#}$ ranging from 40 to 62 (Table 8-1) and there are clear correlations between MgO and some major and trace elements suggesting fractional crystallization during the mafic magma evolution. In the Harker diagram (Fig. 9-3), clear positive linear correlations between MgO and Cr, Ni, and TFe_2O_3 , and negative correlation between MgO and SiO_2 indicate olivine and clinopyroxene fractionation. Based on the absence of Eu anomalies and lack of any linear correlation between MgO and Al_2O_3 (Fig. 9-3 and Fig. 9-4), significant plagioclase fractionation is excluded. As well, the indistinct correlation between MgO versus TiO_2 and P_2O_5 suggests that accessory minerals such as apatite and Fe-Ti oxides were not significantly fractionated. In the case of lamprophyres and dolerites, they do not show any distinct difference in terms of the fractionating phases such as olivine and clinopyroxene as inferred from the compositional changes. Compared with the mafic dykes from the Jiaodong peninsula, the fractional crystallization feature of these rocks are similar to the asthenospheric mantle-derived diabase porphyries but distinct from asthenospheric mantle-derived high-Ti lamprophyres. These rocks also resemble the mafic dykes generated from magmas sourced from the lithosphere mantle reported from the Jiaodong peninsula and western Shandong.

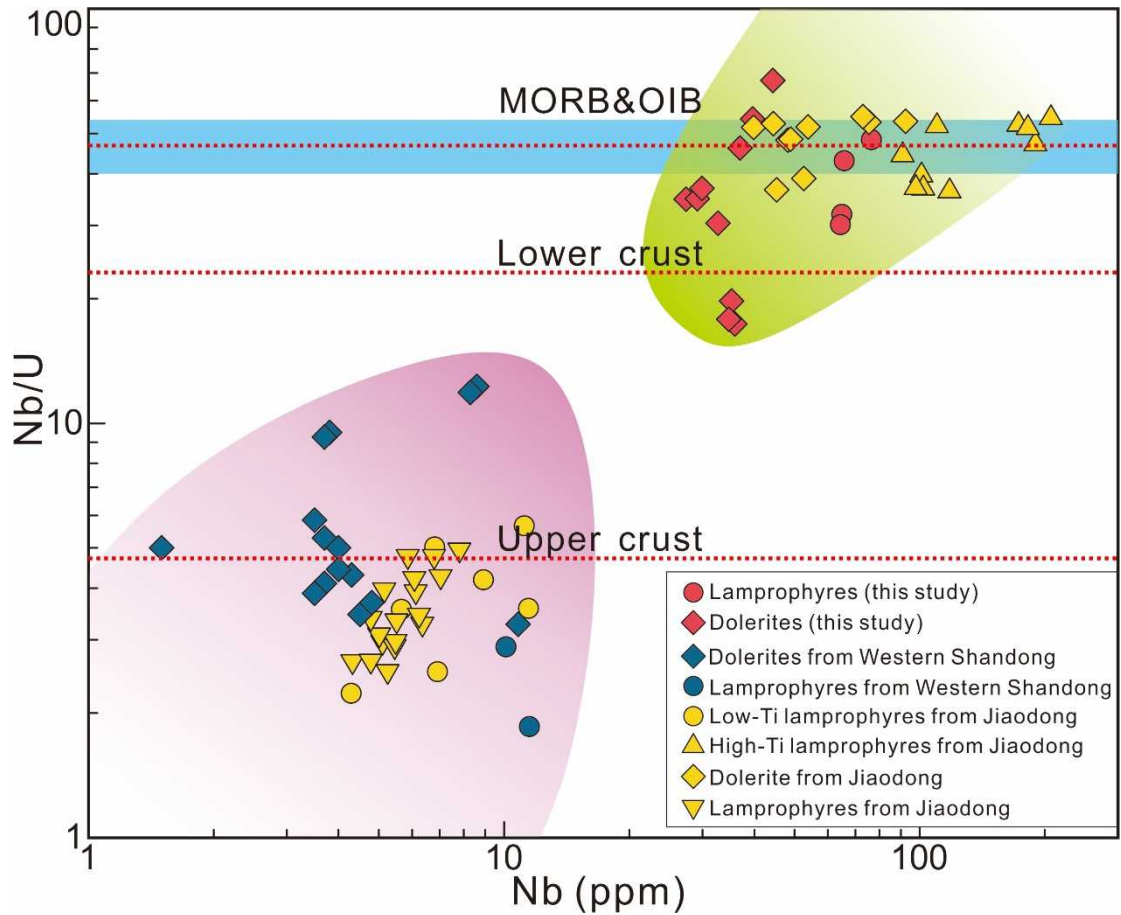


Fig. 9-5 Nb/U vs. Nb diagram for mafic dykes from the NCC. Data sources: dolerites and lamprophyres from western Shandong (Li et al., 2017); Low-Ti and high-Ti lamprophyres (Ma et al., 2014a), dolerites (Ma et al., 2016), other lamprophyres (Ma et al., 2014b) from Jiaodong area; MORB and OIB (Hofmann et al., 1986); Lower and upper crust (Rudnick and Gao, 2003).

9.4.2 Implication of U-Pb ages

Although the mafic dykes in the Laiyuan complex have been investigated in terms of their geochemical features, precise age data are scanty (Yang, 1991; Zhang et al., 2003b). This study is the first comprehensive attempt to obtain U-Pb ages from the various dykes in this complex and to investigate the implications of Cretaceous dyke activity in the NTM.

In this study, zircon grains from the felsic dykes yield weighted-mean ages of 130.6 ± 1.0 Ma (sample LY-34/1) and 126.9 ± 0.8 Ma (sample LYN-1/4). The zircon grains show typical growth zoning and euhedral grain morphology suggesting that the

ages represent the timing of emplacement of the felsic dyke magma. One group of zircon grains in the lamprophyres with similar oscillatory zoning (sample LYN-2/1) show weighted mean $^{206}\text{Pb}/^{238}\text{U}$ age of ~ 129 Ma, and is regarded as zircon antecrysts from the 129 Ma magmatic pulse. This study identifies an intermediate-felsic magmatism at ~ 131 -127 Ma, consistent with the emplacement ages of large and concentrically-zoned granitoid intrusions at 137-126 Ma in this region (Chen et al., 2009b; Shen et al., 2015a; Zhang et al., 2016). Compared with the felsic dykes, the dolerite and dolerite porphyries represent a younger mafic magmatic event, which is distinct from the much earlier mafic magmatism in the Laiyuan complex (Hou et al., 2015). The weighted-mean $^{206}\text{Pb}/^{238}\text{U}$ ages of five samples show ~ 117 Ma, 120 Ma, 123 Ma, 124 Ma, and 125 Ma (Fig. 5-8 and Fig. 5-9). Zircon grains of similar ages are identified in lamprophyres including one group of ~ 117 Ma (sample LY-8/1) and two groups of ~ 119 Ma and ~ 126 Ma (sample LYN-1/1) (Fig. 5-5 and Fig. 5-6). Hence, obtained data suggest a long-lived mafic magmatic event in the Laiyuan complex from 125 to 117 Ma generating the dolerite dyke suite (Fig. 3-1). In contrast to the dolerites, the lamprophyres are characterized by a limited and younger range of ages from 115-110 Ma (Fig. 3-1).

The isotopic age data suggest that the Mesozoic dykes in the Laiyuan complex were generated in three stages, 131-127 Ma for felsic dykes, 125-117 Ma for dolerite dykes, and 115-110 Ma for lamprophyre dykes. The Early Cretaceous magmatic pulses match well with the synchronous widespread magmatism elsewhere in the NCC. More than 300 mafic dykes were identified in the Liaoning, Shanxi, Hebei, Shandong, Henan, Gansu, Shaanxi Provinces, and Inner Mongolia Autonomous Region in China (Liu et al., 2017b). Numerous mafic dykes have also been reported from the Jiaodong area, Luxi area, Taihang Mountain, and southern Hebei area (Fig. 9-6a). Compilation of the available ages shows that the peak mafic dyke emplacement occurred at ~ 123 Ma and the magmatism culminated at ~ 113 Ma. It has also been proposed that the Early Cretaceous giant igneous event and destruction of the NCC reached their peak at ~ 125 Ma (Yang et al., 2008; Zhu et al., 2011). In the Laiyuan

complex, the lamprophyres emplaced during late Early Cretaceous at 115-110 Ma mark the end of the extensive Mesozoic magmatism in eastern China. Compared with the formation ages of mafic dykes from the Jiaodong, Luxi, and southern Hebei areas, the Laiyuan lamprophyres are younger whereas the Laiyuan dolerites are contemporaneous with the other mafic event, suggesting that the Laiyuan lamprophyres and dolerites had a different petrogenetic history (Fig. 9-6a).

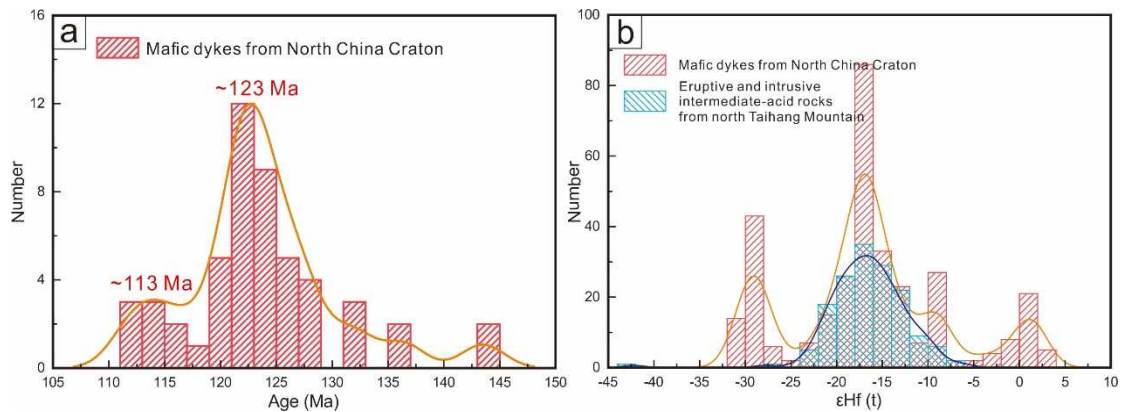


Fig. 9-6 (a) Histogram and probability curves of age data from Early Cretaceous mafic dykes compiled from previous studies and this study in the NCC. (b) Histograms and probability curves of compiled $\epsilon_{HF}(t)$ data from Early Cretaceous mafic dykes compiled from previous studies and this study in the NCC, as well, histograms and probability curves of compiled $\epsilon_{HF}(t)$ data from Early Cretaceous eruptive and intrusive intermediate-felsic rocks compiled from previous studies in north Taihang Mountain. Data sources: Wanganzhen pluton (Zhang et al., 2016); Mapeng pluton (Li et al., 2015a); Laiyuan volcanic rocks (Gao et al., 2012); Chiwawu pluton (He and Santosh, 2014); Luxi mafic dykes (Li et al., 2017; Liu et al., 2008); Hebei mafic dykes (Liu et al., 2018); Taihang-Da Hinggan mafic dykes (Liu et al., 2017b); Jiaodong mafic dykes (Deng et al., 2017b; Guo et al., 2004; Liu et al., 2009b; Ma et al., 2014a; Ma et al., 2016; Tan et al., 2008; Yang et al., 2004).

9.4.3 Petrogenesis of felsic dykes

Similar to the granitoids of the Wanganzhen pluton, the felsic dykes in this study show adakitic features such as: $\text{SiO}_2 > 56\%$ wt. %, high Sr contents (277-1262 ppm), low Y contents (6.21-11.40 ppm), low Yb (0.76-0.88 ppm) with high Sr/Y ratios

(45-111) and La/Yb ratios (55-63) (Drummond et al., 1996; Moyen, 2009). The felsic dykes also show adakitic affinity in Sr/Y-Sr diagram (Fig. 9-2d). In the last chapter, the multiple origins of adakitic features have been discussed including partial melting of young and hot oceanic slab subduction, the melting of a high Sr/Y source, deep melting with abundant residual garnet, fractional crystallization, and interactions of felsic melts with the mantle. The fractional crystallization of lithospheric mantle-derived magmas controlled the origin of adakitic features of volcanic rocks from the Laiyuan complex, which is the possible petrogenesis for felsic dykes. However, compared with the large exposure areas of volcanic rocks, the scale of felsic dyke suites is very small which is similar to the mafic-intermediate magmatic enclaves hosted by the granitic plutons. In the NTM, the widely distributed plutons carry some mafic magmatic enclaves, suggesting mixing and mingling between basaltic and felsic magmas. The mafic magmas experienced fractionation of ferromagnesian minerals, and were injected into the granitic magma chambers. This model argues against the delamination model and highlights the significant role of asthenosphere upwelling during Early Cretaceous. He and Santosh (2014) studied the granitoids (~130 Ma) and dioritic enclaves (~128 Ma) in the Chiwawu and Mapeng plutons from the NTM and identified magma mixing, although they argued that the magma was sourced from the reworked Neoproterozoic to Paleoproterozoic basement rocks which were formed during the earlier subduction-collision event between the Eastern Block and the Western Blocks along the ~1.8–1.9 Ga TNCO. In this study, the presence of older zircon xenocryst with a $^{207}\text{Pb}/^{206}\text{Pb}$ age of 1973 Ma (sample LY-34/1, Fig. 5-11) and emplacement ages of 127 Ma and 131 Ma combined with the similar geochemical features with the Chiwawu pluton (He and Santosh, 2014) and Mapeng felsic porphyry dykes which were formed at ~129-124 Ma (Li et al., 2015a), it is suggested that the felsic dykes probably share a same genetic history with magma mixing and mingling of siliceous crustal melts from reworked older continental crust and basaltic magma derived from metasomatized mantle (Chen et al., 2013). The non-porphyrific and very fine-grained mafic enclaves were found enclosed in the

felsic (dioritic) dykes from Laiyuan (see Fig. 11 in [Chen et al., 2009b](#)), providing the field evidence to support the magma mixing and mingling model. The mafic enclaves from the Laiyuan complex are mainly dioritic ([Fig. 3-6e](#), [Fig. 3-4](#)), same with these studied felsic dykes in mineral composition and geochemistry ([Fig. 3-7](#)). As shown in [Fig. 3-6e](#), the diorite porphyry dyke shows tight contact correlation with the enclaves hosted by the surrounding monzogranite. Combining with the similar forming ages, it is reasonable to consider that the dioritic enclaves and the felsic dykes are of the same genetic history, but they are of different forms.

9.4.4 Magma source of mafic dykes

The mafic dykes are characterized by high MgO and Fe₂O₃ contents with high Mg[#] ([Table 8-1](#)) as well as low SiO₂ contents and enrichment in compatible elements, suggesting mantle source. The Nb/Yb ratio is considered as indicator of the degree of depletion (MORB like) or enrichment (OIB like) of the mantle source. The Th/Yb ratio is also indicator of crustal input. Thus these two ratios are sensitive to crustal input and can be used to fingerprint the basalt types ([Pearce, 2008](#)). In the Th/Yb-Nb/Yb diagram ([Fig. 9-7a](#)), mafic dykes from the Laiyuan complex show a limited range of high Th/Yb and Nb/Yb values and are plotted in the OIB-like mantle array exhibiting enriched character similar to high-Ti lamprophyres and diabase-porphyrines in the Jiaodong peninsula which originated from asthenosphere ([Ma et al., 2014a](#); [Ma et al., 2016](#); [Ma et al., 2014b](#)). These features suggest that the mafic dykes in the Laiyuan complex were derived from an enriched mantle source in within-plate setting. This inference is also supported by the Nb/U ratios ([Fig. 9-5](#)). However there is key difference between the mafic dykes in Laiyuan and asthenosphere-derived high-Ti lamprophyre from the Jiaodong area. Compared with the limited variation on Nb/U ratios of high-Ti lamprophyres, the Nb/U ratios of the Laiyuan mafic rocks are not totally uniform (16.79-67.12) indicating that the mafic dykes in Laiyuan area are not likely to totally sourced from the asthenosphere like the high-Ti lamprophyre from Jiaodong area ([Ma et al., 2014a](#)).

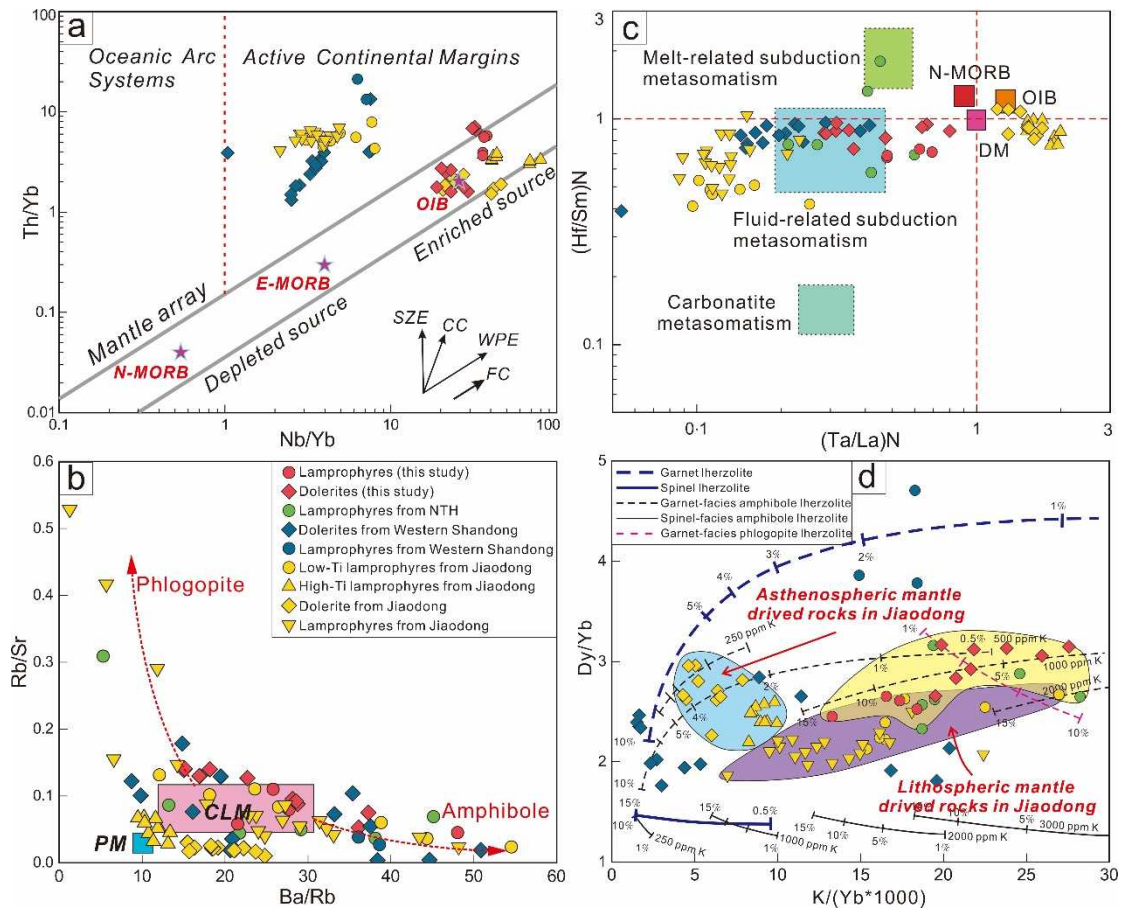


Fig. 9-7 (a) Th/Yb vs. Nb/Yb (after Pearce, 2008), (b) (Hf/Sm)_N vs. (Ta/La)_N (La Flèche et al., 1998), (c) Rb/Sr vs. Ba/Rb, and (d) K/Yb vs. Dy/Yb diagrams for mafic dykes in the NCC.

Melting curves for garnet lherzolite, spinel lherzolite, garnet-facies phlogopite lherzolite, garnet-facies amphibole lherzolite and spinel-facies amphibole lherzolite are after Duggen et al. (2005) and reference therein. Data sources are same with Fig. 9-5.

The mafic dykes sampled from the Laiyuan complex are also characterized by high K₂O contents (2.84-4.51 wt. %) and significant LILE and LREE enrichment suggesting the presence of volatile-bearing minerals such as phlogopite and amphibole in the mantle source region. The incompatible element ratios such as Rb/Sr and Ba/Sr are employed to identify the mineralogy and composition of the mantle source where there is no significant magma differentiation. The partition coefficient for Ba is higher than Rb in amphibole, whereas in phlogopite, these elements have the reverse partition coefficient. Consequently, melts in equilibrium with amphibole

display significantly lower Rb/Sr (<0.1) and higher Ba/Rb (>20) ratios than those formed from amphibole-bearing sources (Furman and Graham, 1999). The mafic dykes from the NTM have low Rb/Sr ratios (0.05-0.13 of lamprophyres and 0.05-0.14 of dolerites) and high Ba/Rb ratios (16.97-48.03 of lamprophyres and 15.04-37.29 of dolerites), suggesting the predominance of amphibole rather than phlogopite in the melting source (Fig. 9-7b). Mafic dykes from the Shandong Peninsula also display amphibole-bearing source region, whereas the mafic lava and lamprophyres from western Yunnan Province are characterized by a phlogopite-bearing source as indicated by the presence of phlogopite-bearing peridotite xenoliths (Lu et al., 2015). The nature of the source mantle is also confirmed by the abundance of amphibole in the studied rocks (Fig. 3-7). The identification of amphibole in the source region of these rocks implies that metasomatism by fluids occurred prior to melting (Ma et al., 2014a). This metasomatism may be related to the fluid released by the stagnant horizontal Pacific slab in the mantle transition zone beneath the NCC not the subducted oceanic crusts (Chen et al., 2005; Liu et al., 2018). As shown in Fig. 9-7c, the metasomatism may be a fluid-related rather than melt and carbonatite-related processes. Ma et al. (2014a) argued that metasomatism induced by slab-derived hydrous fluids was responsible for the enriched lithospheric mantle beneath the NCC.

Furthermore, the Dy/Yb ratios are widely used to constrain the nature of mantle source and degree of partial melting (Li et al., 2019a; Ma et al., 2014a). In the Dy/Yb vs. $K/(Yb \cdot 1000)$ diagram (Fig. 9-7d), the partial melting in the spinel and garnet stability fields of a phlogopite- and/or amphibole-bearing lherzolite is distinguished. Partial melts which were generated in the garnet stability zone are expected to have Dy/Yb ratios higher than 2.5 whereas those in the spinel stability field have lower Dy/Yb ratios (<1.5). Where the Dy/Yb ratios are between 1.5 and 2.5, partial melting is inferred in the garnet-spinel transition zone. Lamprophyres and dolerites from the Laiyuan complex show Dy/Yb ratios in the range of 2.45-2.65 and 2.66-3.21, respectively, suggesting that partial melting occurred in the garnet stability field. They are plotted in the garnet-facies amphibole lherzolite curves (3-14%), in contrast to

lamprophyres in the Shandong peninsula which fall between the curves of garnet-facies lherzolite and spinel-facies lherzolite. It is estimated that garnet in peridotite is stable at depths >70-80 km which generally marks the depth (~75-85 km) for the spinel–garnet transition zone (Duggen et al., 2005; Mckenzie and O'Nions, 1991; Robinson and Wood, 1998; Yang et al., 2010). Since amphibole will become unstable at depths below 70-100 km, garnet-facies amphibole peridotite can exist only in a narrow zone between 85 and 100 km depth probably near the mechanical boundary layer of the continental lithosphere in the north Taihang Mountain (Fig. 1-2) (Zhu et al., 2011). Furthermore, the Laiyuan lamprophyres experienced a higher degree of partial melting up to 8-14%. The variable degrees of partial melting between the mafic dykes are consistent with the wide range of their formation ages from 125 to 110 Ma. As discussed above, the lamprophyres and dolerites in the Laiyuan complex were probably derived from partial melting of different degrees of enriched mantle in the amphibole-bearing garnet-facies amphibole stability zone at 80-100 km depth. The asthenosphere mantle cannot melt until the thickness of the lithosphere has been reduced to less than about 80 km. Therefore, it is possible that the upwelling asthenosphere melted beneath the TM.

In summary, it is concluded that the dolerites and lamprophyres in the Laiyuan complex were probably derived from different degrees of partial melting (~3-14%) of an enriched lithospheric mantle in the amphibole-bearing garnet-facies amphibole stability zone at 80-100 km depth which experienced fluid metasomatism related to subduction. And the source magmas of the lamprophyres also involved asthenospheric input.

9.4.5 Lithosphere-asthenosphere interaction

The above discussion also illustrates the contribution of asthenosphere in the petrogenesis of mafic dykes. The mechanism of origin also varies in lamprophyres and dolerites. As shown in the primitive mantle-normalized spidergram (Fig. 9-4b, d), the dolerite dykes are enriched in LILEs, LREEs, and Pb, and have negative Nb-Ta and Th-U anomalies, whereas the lamprophyre dykes are enriched with LILEs and

LREEs with without negative Nb-Ta anomalies. The dolerite dykes are quite similar to lithosphere-derived low-Ti lamprophyre from the Jiaodong area except for the negative Th-U anomalies which may result from the minor incorporation of enriched crustal materials. As well, the geochemical features of lamprophyres are between the asthenosphere-derived high-Ti mafic rocks (Ma et al., 2016) and dolerites from Laiyuan area indicating that the mantle sources for lamprophyres are not homogeneous. The lamprophyres have slightly negative Th-U anomalies indicating very limited input of crustal materials, and no positive Ta-Nb anomalies which may suggest the injection of asthenospheric mantle (Li et al., 2017).

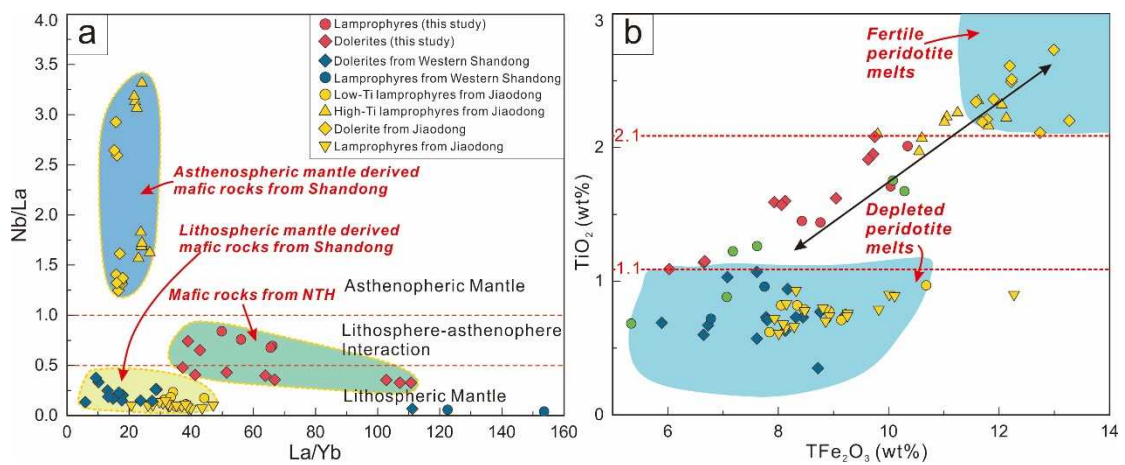


Fig. 9-8 (a) Nb/La vs. La/Yb (Smith et al., 1999) and (b) TiO₂ vs. TFe₂O₃ diagrams for mafic dykes in the NCC. Data sources are same with Fig. 7-4. Fertile peridotite melts and refractory peridotite melts are defined by the study of experimental melts (after Falloon et al., 1988).

The Lu-Hf isotopic features of zircon grains in the lamprophyres and dolerites provide some important clues on the mantle source variations. The Laiyuan lamprophyres show a wider range of $\epsilon_{\text{Hf}}(t)$ values from -17.2 to -3.7 compared with dolerites (-23.3 to -14.2) and felsic dykes (-22.3 to -17.2) suggesting that the sources of lamprophyres are mixed and different from that of the dolerites whose limited negative zircon $\epsilon_{\text{Hf}}(t)$ values suggest that the dolerites were mainly sourced from an ancient enriched lithospheric mantle. As illustrated in $\epsilon_{\text{Hf}}(t)$ vs. age diagram (Fig. 6-1) and interpreted in Chapter 6, in terms of geochemical and isotopic evidence, the lithospheric mantle with increasing involvement of asthenospheric mantle contributed

to source of lamprophyres.

Compared with $\epsilon_{\text{Hf}}(t)$ values of zircons of AMDR and LMDR from Jiaodong areas, the $\epsilon_{\text{Hf}}(t)$ values for zircons from mafic dykes from the NTM show typical transition feature with moderate $\epsilon_{\text{Hf}}(t)$ values (Fig. 6-1 and Fig. 9-6b). Some geochemical indexes are also characterized by transitional feature which may imply the existence of lithosphere-asthenosphere interaction (Fig. 9-8). The Nb is generally depleted in the lithospheric mantle relative to La. Therefore, low Nb/La ratios for mafic magmas are in favor of lithospheric mantle source and higher ratios suggest an OIB-like asthenospheric mantle source (Smith et al., 1999). As illustrated in the Nb/La versus La/Yb diagram (Fig. 9-8a), the lamprophyres all fall in the lithosphere-asthenosphere interaction field indicating the involvement of both asthenosphere and lithosphere in the origin of the Laiyuan mafic dykes (Santosh et al., 2018). However, most of the dolerites fall in the lithospheric mantle field whereas just two samples fall in the interaction field implying the change from lithospheric mantle source to asthenospheric mantle source with time from 125 to 110 Ma. The mafic dykes from the Laiyuan complex fall between the fields of simultaneous AMDR and LMDR from the Shandong Peninsula, which also suggest interaction of asthenosphere mantle and lithospheric mantle. This transitional feature is also identified in the diagram of TiO_2 - TFe_2O_3 relationship where TiO_2 contents of the Laiyuan dykes are between 1.1 to 2.1 whereas those of the LMDR are below 1.1 and those of AMDR exceed 2.1 (Fig. 9-8b). Furthermore, the composition of studied rocks shows a transition from fertile peridotite melts to refractory peridotite melts as defined from experimental melts (Falloon et al., 1988). These features argue that the melts were probably extracted from a mixture of enriched mantle source and depleted mantle source (Lu et al., 2015). As a corollary, the lithosphere-asthenosphere interaction could be interpreted as the possible petrogenesis for mafic dykes in the central NCC similar to the Datong Cenozoic basalts from Datong Volcanic Field near Laiyuan area (Xu et al., 2005).

9.5 Summary

(1) The lamprophyre dykes, dolerite dykes and felsic dykes in the Laiyuan complex were formed at 115-110 Ma, 125-117 Ma, and 131-127 Ma. The $\epsilon_{\text{HF}}(t)$ values ranging from -17.2 to -3.7, -23.3 to -14.2, and -22.3 to -17.2, respectively, indicate the increasing input of asthenospheric materials in the younger magmatic pulses.

(2) The mafic dyke samples exhibit enrichment in LILE and no obvious Eu anomalies, and the dolerites show strong depletion in HFSE whereas the Th-U and Ta-Nb depletions in lamprophyres are not obviously similar to OIB-type. The felsic dykes have stronger Nb-Ta and Ti depletion and Pb enrichment indicating their crustal origin.

(3) Mafic dykes in the Laiyuan complex were probably derived from different degrees of partial melting of an enriched lithospheric mantle in the amphibole-bearing garnet-facies amphibole stability zone at 80-100 km depth which experienced fluid metasomatism related to subduction.

(4) In terms of geochemical and isotopic evidence, through time, increasing involvement of asthenospheric mantle involved in the source of lamprophyres. The lithosphere-asthenosphere interaction could be interpreted as the possible petrogenesis for mafic dykes in the central NCC.

Chapter 10 Tectonic implications

10.1 Tectonic regime transition from compression to extension

In the eastern and central NCC, three metallogenic pulses are identified, i.e. 200-160 Ma, ca. 140 Ma, and 130-110 Ma when the tectonic regime was under post-collisional setting, transforming from compression to extension, and intense extensional setting, respectively (Mao et al., 2005). These episodic metallogenic events demonstrate that the tectonic regime in TM region was under compressional setting during Late Jurassic, transformed from compression to extension from Late Jurassic to Early Cretaceous, and was experiencing extension at Early Cretaceous. The significant tectonic regime transformation was also recorded by the widespread metamorphic core complex in the NCC (Wang et al., 2012) (Fig. 10-1a). Detailed geochronological studies of the Yunmengshan metamorphic core complex illustrate a rapid change in the tectonic setting from NNE-SSW compression to NW-SE extension in the earliest Cretaceous (Zhu et al., 2015a). In the study area, the LJVR, associated sub-volcanic rocks and skarn-porphyry type Cu-Mo deposits may be the products under the transforming tectonic setting. Geochronological studies on the Mujicun deposit show that the volcanic rocks, porphyry intrusion and porphyry-type and skarn-type of mineralization were formed during the same event at 145-140 Ma consistent with the important tectonic regime changing period (Dong et al., 2013; Gao et al., 2012; Gao et al., 2013; Hou et al., 2015). Commonly, the skarn-porphyry Cu-Mo and Mo-W mineralizations are often related to the transforming tectonic regime in eastern China, such as Jiaodong area (Goldfarb and Santosh, 2014; Li et al., 2015b) and East Qinling orogen (Li et al., 2018; Yang et al., 2019b). Furthermore, the LJVR belong to the Tiaojishan Formation which was also regarded as the intra-plate volcanism induced by the transition in the tectonic regime (Dong et al., 2018). Therefore, the early formation of the Laiyuan complex was associated with the

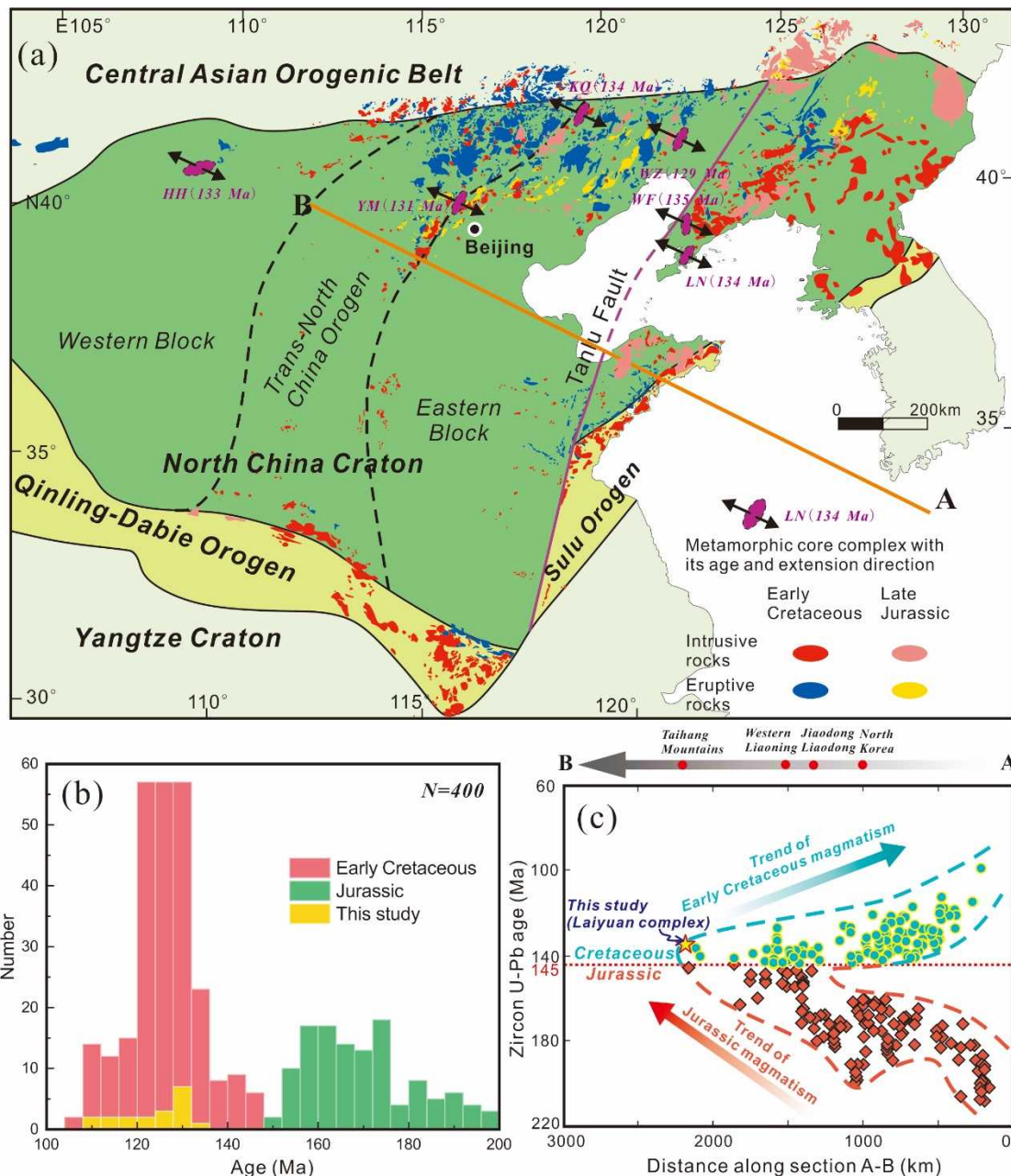


Fig. 10-1 (a) Tectonic map of the North China Craton and surrounding regions showing the metamorphic core complex (modified after Zhu et al., 2015a) and Early Cretaceous and Late Jurassic magmatic rocks (Zhang et al., 2014; Zhao et al., 2005). (b) Histogram of zircon U-Pb ages of Late Mesozoic igneous rocks in the NCC. (c) Projection of zircon U-Pb ages along the section A-B (in Fig. 10-1a) cross the NCC. The combinations of the zircon U-Pb ages are modified after Wu et al. (2019) and reference therein. Metamorphic core complex: KQ-Kalaqing metamorphic core complex; WZ-Waziyu metamorphic core complex; LN-Liaonan metamorphic core complex; WF- Wanfu metamorphic core complex; YM-Yunmengshan metamorphic core complex; FS-Fangshan metamorphic core complex; HH-Hohhot metamorphic core complex.

tectonic regime transition from compression to extension accompanied with the formation of LJVR, sub-volcanic rocks and hosted Cu-Mo mineralization.

The Early Cretaceous witnessed a widespread extensional tectonic regime in the NCC from the eastern Jiaodong area to the central TM. Lithospheric extension beneath eastern China is supported by several lines of evidence, including a series of fault basins, numerous detachment faults, metamorphic core complexes, and associated voluminous magmatism (Fig. 10-1a) (Zhu et al., 2011). Compared with the Jurassic magmatism, the Early Cretaceous magmatism was more intense and widespread throughout the eastern and central NCC marking the peak of the extension (Fig. 10-1a, b). Extensional tectonic setting has also been identified in the NTM (He and Santosh, 2014; Hou et al., 2015). The mafic dyke events indicate crustal extension and lithospheric thinning because they are products of lower-degree partial melting of enriched lithospheric mantle under a rifting or extensional setting (Campos et al., 2012; Deng et al., 2017a; Li et al., 2014; Orozco-Garza et al., 2013). Various mafic dykes were found in the Laiyuan complex and adjacent plutons (Li et al., 2015a) suggesting the NTM underwent the extensive crustal extension during Early Cretaceous. Furthermore, crust-mantle interaction also reveals the deep extension architecture. Apparently, the Early Cretaceous intense magmatism in the study area displays a close relationship with the extensional setting. To interpret the trigger of the extensional tectonic regime, several mechanisms have been presented. Among the two popular models, one relates the Triassic collision between the NCC and Yangtze Block with the intra-continental extensional regime during the post-collision (Zhang et al., 2002). The other model proposes the nearly W-E subduction of the Paleo-Pacific Ocean which changed the geodynamic regime from N-S transpressional setting to nearly W-E extensional setting (Li and Santosh, 2014). A marked age polarity has been identified in the East Asian magmatic suites with a northwestward younging trend from Japanese islands (~210 Ma), through the Jiaodong and Liaodong areas (180 Ma), to the Taihang Mountain in central NCC (138 Ma), which has been linked with the subduction process of Paleo-Pacific Plate (Chen et al., 2005), with

extension of the NCC triggered by the subduction process.

10.2 Geodynamic trigger for the NCC destruction

The large-scale crustal extension and voluminous magmatism in the NCC are often regarded as the evidence of the NCC destruction during Mesozoic (Gao et al., 2002; Griffin et al., 1998). Detailed geological and geophysical studies have proved that more than 100 km of the ancient refractory lithospheric mantle has been eroded and replaced by young and fertile mantle materials beneath the eastern portion of the NCC since Mesozoic (Gao et al., 2002; Liu et al., 2019; Liu et al., 2017a; Wu et al., 2019). It is widely accepted that the eastern NCC has experienced extensive cratonic destruction during Mesozoic evidenced by large-scale volcanic eruptions (Dong et al., 2018), mafic-granitic intrusions (Zhang et al., 2014; Zheng et al., 2018), mafic dykes (Ma et al., 2014a), crustal deformation (Li et al., 2019b; Wang et al., 2018), basin sedimentation (Li et al., 2012), and the formation of world-class polymetallic mineralization (Deng et al., 2017b; Xue et al., 2019a). To interpret how the lithospheric root was replaced, several mechanisms have been proposed, and the two most popular models are continental delamination (Gao et al., 2004) and chemical-mechanical erosion (Xu, 2001). Before discussing the possible mechanism for the NCC destruction, the prior focus is the tectonic triggering forces for the destruction. Previous studies show that the subduction of oceanic plate and plume erosion act as the major driving force for craton destruction in the margins or within continental interiors, respectively (Menzies et al., 2007; Wilde et al., 2003). As shown in the tectonic setting discriminative diagrams (Fig. 10-2d), the studied rocks from the Laiyuan complex are showing subduction-related characteristics. As well, the rocks exhibit geochemical features similar to the rocks generated in active continental margin (Fig. 10-2a, b, c, e). However, these rocks were formed far from any active continental margin arc setting during the Mesozoic, and shows an intra-plate setting as also suggested in previous studies from the TM and north Hebei Province (Dong et al., 2018; Gao et al., 2011; He et al., 2017b; Li et al., 2019a; Yang et al., 2020). The arc-like characteristics might be an inheritance from the lithosphere beneath the

central NCC which was influenced by the oceanic plate subduction through far-field effects (He et al., 2017b). As well, the granitoids plotted in the VAG field (Fig. 10-2a),

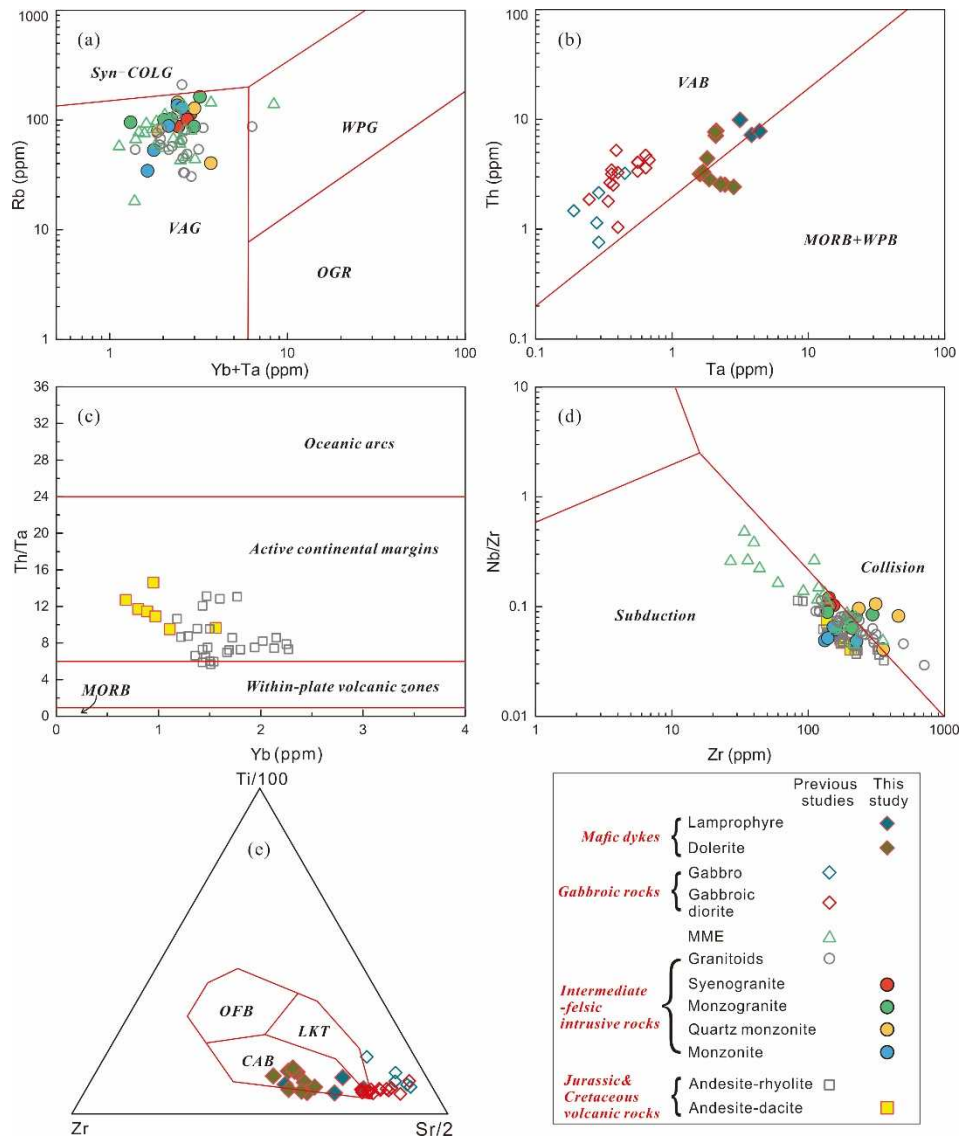


Fig. 10-2 Tectonic discriminative diagrams for magmatic rocks from the Laiyuan complex. (a) Rb vs. Yb+Ta diagram (Pearce, 1984). (b) Th vs. Ta diagram (Pearce and Peate, 1995). (c) Th/Ta vs. Yb diagram (Pearce and Peate, 1995). (d) Nb/Zr vs. Zr diagram (Tarney and Jones, 1994). (e) Ti/100-Zr-Sr/2 ternary diagram (Pearce and Cann, 1973). Field abbreviations: syn-COLG, syn-collisional granitoids; VAG, volcanic arc granitoids; post-COLG, post-collisional granitoids; WPG, within plate granitoids; ORG, orogenic granitoids; VAB, volcanic arc basalt; WPB, within-plate basalt; MORB, mid-ocean ridge basalt; CAB, calc-alkali basalt; LKT, low-potassium tholeiite; OFB, ocean-floor basalt. Data sources are same as in Fig. 8-4 and Fig. 7-2.

and the mafic rocks fell in the field of active continental margin (Fig. 10-2c) indicating the primary controlling effect exerted by subduction to form the magmatic rocks in the central NCC.

During Paleozoic to Mesozoic, the NCC underwent multiple tectonic events, and was surrounded by multiple subduction zones (Windley et al., 2010) (Fig. 10-3). However, the following lines of evidence support that the NCC destruction was triggered by the subduction of Paleo-Pacific Plate, neither by the subduction of Paleo-Asian oceanic plate to the north nor the subduction of Paleo-Tethys and following continental collision between the NCC and Yangtze Craton to the south. Firstly, the NCC experienced extensive destruction in its eastern and central part showing a gradual thinning trend from west to east whereas the western part still have a thick and stable lithosphere suggesting the subduction effect came from the east (Fig. 1-2) (Chen, 2010). Secondly, combined age data of Mesozoic magmatic rocks from the NCC (Fig. 10-1c) show that the Jurassic calc-alkali magmatism exhibits a westward younging trend, whereas the Cretaceous calc-alkali magmatism show a reverse eastward younging trend, indicating the role of subduction and rollback of the Paleo-Pacific Plate in the spatial–temporal migration of Mesozoic magmatism in the NCC (Wu et al., 2019). Thirdly, there are northeast-extending belts of the Mesozoic magmatic rocks and contemporaneous sedimentary basins which distributed parallel to the subduction zone of the Paleo-Pacific Plate (Fig. 10-1a) (Li et al., 2012; Wang et al., 2012). According to the above observations, the subduction of Paleo-Pacific Plate exerted principle influence on the thinning, extension and destruction of the NCC. Because of the important role of the westward subduction of Paleo-Pacific slab, some researchers considered the subduction as the first-order mechanism whereas the erosion and foundering are only the second-order mechanism in contributing to the NCC destruction (Zheng et al., 2018).

Based on previous studies and this study, some key stages associated with the subduction of the Paleo-Pacific Plate can be recognized: initiation of the subduction beneath the Northeast China between ~200-190, low-angle flat subduction between

~170-145 Ma, the sinking or rollback between ~145-110, stagnancy and vanish of Paleo-Pacific slab in mantle transition zone at ~110-50 Ma (Liu et al., 2019; Wu et al., 2019; Zhu and Xu, 2019). During Late Jurassic, at ca. 155 Ma, the Paleo-Pacific Plate began to roll back, with the tectonic setting changing from compression to extension. By ~145 Ma, the slab had mostly rolled back contributing to unstable mantle flows and upwelling of asthenosphere. The subduction, retreat, roll back, and stagnation of the Paleo-Pacific slab result in the heterogeneous lithosphere and various evolutionary processes in the deep beneath the NCC, furthermore manifested as distinct magmatic rocks series in the shallow.

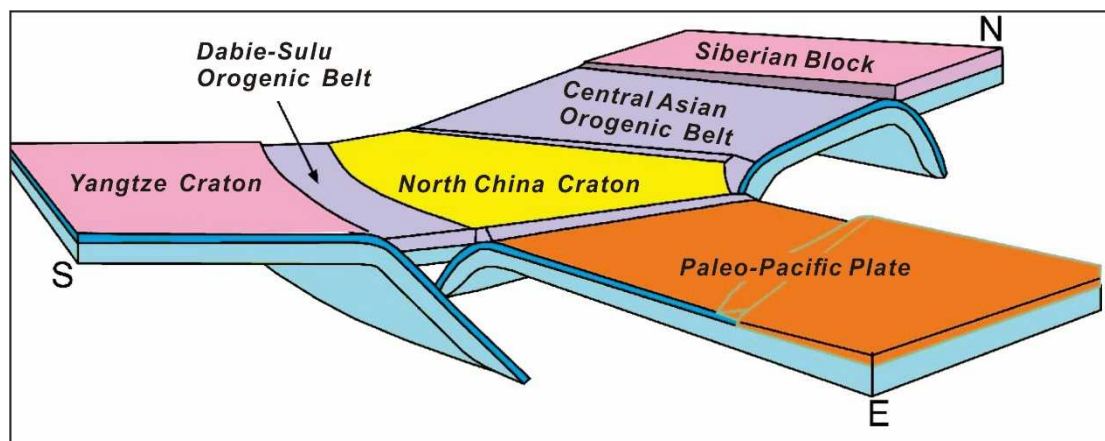


Fig. 10-3 The North China Craton and its adjacent plates in the Paleozoic to Mesozoic (modified after Windley et al., 2010).

10.3 Different lithospheric evolution beneath the eastern and central NCC

Seismic data indicate that the present lithospheric thickness of the NCC becomes gradually reduced from the Western Block (~200 km in the Ordos basin) through the central region (120 km in the TM) to the Eastern Block (only 70 km in the Bohai Bay region) (Fig. 1-2) (Chen, 2010). The geophysical data also reveals the crustal structure is varying from the eastern to the central NCC, with thickness of the lower crust decreasing from ~20 km in the TM to only 6 km in the Bohai Bay (Zheng et al., 2007b). These features essentially reflect the spatial variation of the thinning and

destruction throughout the NCC.

Due to the subduction of Paleo-Pacific Plate from the east at Jurassic and multiple Phanerozoic collisional orogenies from the north and the south, the lower crust of the NCC would be thickened, especially the eastern NCC. From ~200-145 Ma, the magmatism shows a westward younging trend and the igneous rocks are characterized by intermediate to felsic with adakitic affinities and low Mg[#] (Wu et al., 2019). These rocks were derived from the partial melting of the thickened lower crust in a subduction-related setting (Wu et al., 2005; Zhang et al., 2014; Zheng et al., 2018). The LJVR from the Laiyuan complex also show similar geochemical and petrological characteristics to this group of rocks (Duan et al., 2016; Gao et al., 2012) indicating the flat subducted Paleo-Pacific slab has reached the position beneath the TM at ~145 Ma. Given the rare distributions of Jurassic magmatic rocks to the west of the central NCC, the TM may represent the westernmost domain where the slab reached. This hypothesis is supported by the geophysical evidence. As revealed by the velocity structures of the mantle transition zone of the NCC (Fig. 10-4a), at present, there is an eastward-subducted plate beneath the eastern margin of the Euroasia continent called Pacific Plate (Huang and Zhao, 2006) which didn't reach the mantle transition zone until 20 Ma (Zhu et al., 2015b). In this regard, the presently observed modern stagnated Pacific oceanic slab has nothing to do with the Cretaceous thinning and destruction of the NCC. Although the current observations just reveal the Cenozoic subduction process of the Pacific Plate, it can be used as a reference to reconstruct the subduction of Paleo-Pacific Plate based on the reconstruction of global plates and numerical modeling of oceanic basin dynamics (Müller et al., 2008; Seton et al., 2012). The studies indicate that the modern Pacific Plate at the Japan Trench is ca. 130 Myrs. old with estimated subduction rate of ca. 10 cm/yr. According to the subduction rate, about 20 Myrs. were required for the Paleo-Pacific Plate to move from the Japan Trench to the westernmost part of the stagnant slab. It is reasonable that the Paleo-Pacific Plate has come to the mantle transition zone at Early Cretaceous. Furthermore, this is also revealed by the tomographic images in which there are three

relatively high-velocity bodies in the transition zone or the lower mantle (Fig. 10-4a). These bodies can be assumed as the remnants of the Paleo-Pacific Plate during the Early Cretaceous (Huang and Zhao, 2006). In summary, during Early Cretaceous, the destruction process should have been associated with the subduction and stagnancy of the Paleo-Pacific Plate.

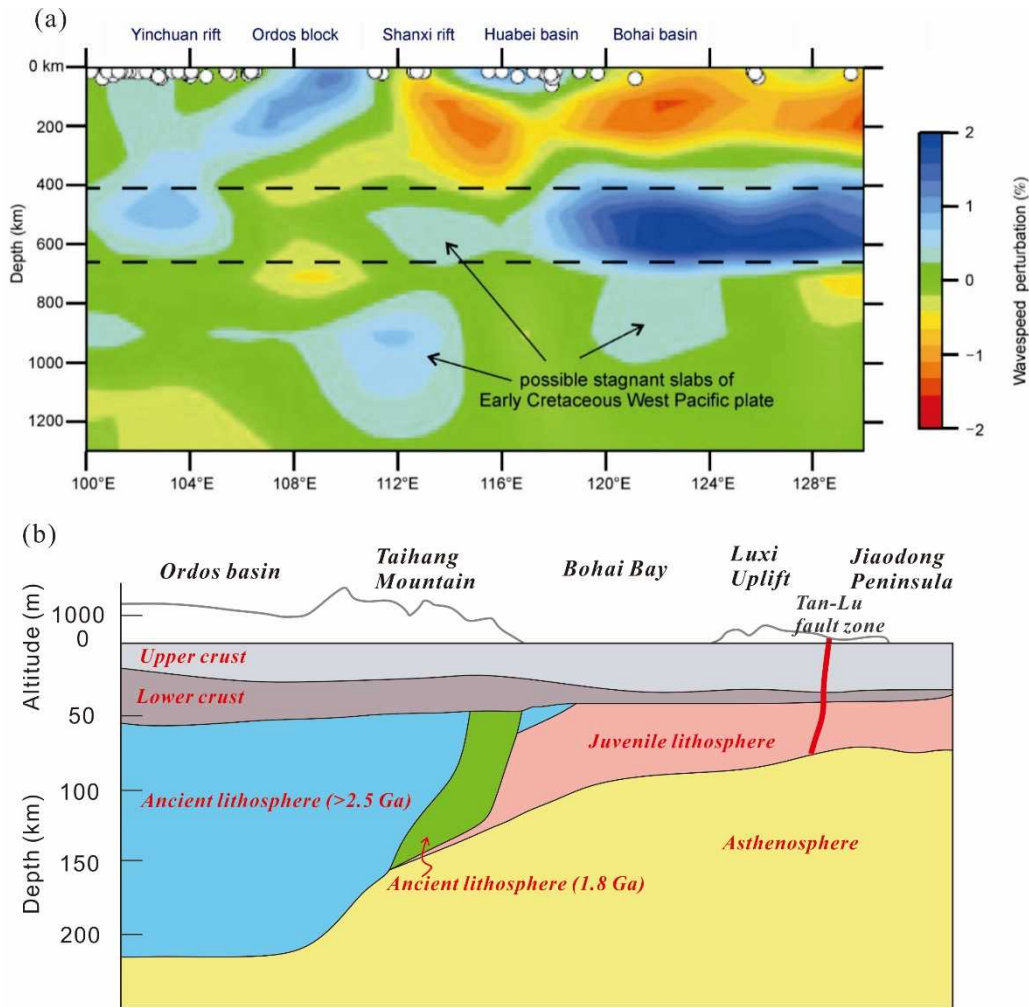


Fig. 10-4 (a) Tomographic images to show the velocity structures of the present mantle transition zone of the NCC (modified after Huang and Zhao, 2006). (b) The schematic lithospheric structure of the current NCC from the eastern Jiaodong Peninsula through the central Taihang Mountain (not to scale) to the western Ordos Basin revealing the lithosphere heterogeneity beneath the NCC (modified after Liu et al., 2019).

The magmatic similarities in both central and eastern NCC reveal the consistency of lithospheric evolution by Late Jurassic. Distinct from the Jurassic magmatism, the Early Cretaceous magmatism occurred more widely, resulted in extremely variable rock types and chemical compositions, and involved multiple crustal and mantle sources (Wu et al., 2019; Zheng et al., 2018). The crust-mantle interaction played significant role during their formation in both central and eastern NCC, but may be of different forms. As discussed in this study, the underplated basaltic magma derived from the enriched lithospheric mantle interacted with the thickened lower crust to account for the variable magmatic rocks in the central NCC, whereas the melts derived from delaminated lower crust interacted with the mantle peridotite contributed to the formations of high-Mg andesites and adakites in the eastern NCC (Gao et al., 2004; Gao et al., 2009; Jiang et al., 2007; Xu et al., 2013). The different forms of crust-mantle interaction are consistent with the thickness variations of the lithosphere.

Notably, the mafic dyke events occurred in both regions offered direct evidence to identify the distinct lithospheric evolution. Two types of lamprophyres with same emplacement ages of ca. 121 Ma have been discovered in the Jiaojia gold deposit from the Jiaodong region (Deng et al., 2017a; Ma et al., 2014a): one is the high-Ti lamprophyres sourced from the partial melting of an asthenospheric mantle with juvenile and depleted isotopic characteristics ($\epsilon_{\text{HF}}(t)$ values ranging from -4.7 to 2.1), another is the low-Ti lamprophyres sourced from the lithospheric mantle with ancient and enriched isotopic features ($\epsilon_{\text{HF}}(t)$ values ranging from -29.3 to -23.1) (Fig. 6-1). The co-occurrence of the two types of lamprophyres record a rapid transition from lithospheric to asthenospheric mantle sources, indicating the rapid detachment of the lithosphere and rapid upwelling of the asthenosphere beneath the eastern NCC (Deng et al., 2017a; Ma et al., 2014a; Ma et al., 2016; Ma et al., 2014b). However, as revealed by the increasing input of asthenospheric materials through time for the source of lamprophyres from 115-110 Ma, and the relatively uniform enriched lithospheric mantle source for the dolerites from 125-117 Ma, a progressive and slow lithospheric thinning and asthenospheric upwelling process occurred at the central

NCC. The distinct lithospheric evolutionary processes in the central and eastern NCC may result from the different destruction mechanisms and lead to different lithospheric structure beneath the central and eastern NCC at present (Fig. 10-4b).

10.4 Destruction mechanism in the central NCC

Several models were proposed to interpret the destruction process including convective destabilization (Houseman et al., 1981; Morency et al., 2002), tectonic erosion (Maruyama et al., 2007; Santosh, 2010), destabilization due to the Indo-Eurasian collision (Menzies et al., 2007), thermo-mechanical erosion (Griffin et al., 1998; Xu, 2001), and continental delamination (Gao et al., 2004; Windley et al., 2010). Among these models, thermo-mechanical erosion and lithospheric delamination modes are the more accepted mechanisms to explain the lithospheric thinning process. These two models have contrasting characteristics of magmatic imprints. In the case of thermo-mechanical erosion, the upwelling asthenosphere gradually heats up, weakens and erodes the lowermost lithosphere (Xu et al., 2009a; Xu et al., 2005). Progressive removal would contribute to considerable thinning of the lithosphere (Ma et al., 2016). The magmatism related to this process will have lithospheric mantle features at the beginning, followed by asthenospheric mantle characteristics with progressive thinning (Cai et al., 2013; Xu et al., 2009a). In contrast, the delamination model hypothesizes that thickened lower crust and the coupled lithosphere sunk into the convective asthenospheric mantle to produce simultaneous lithospheric and asthenospheric mantle-derived magmas as well as mixed felsic magmas (Gao et al., 2004; Wu et al., 2008). The two types of mafic dykes in the Jiaodong area (Deng et al., 2017a; Ma et al., 2014a), and the formation of high-Mg adakitic rocks and mafic dykes from different sources in the proximal western Shandong region (Li et al., 2017; Liu et al., 2017b) indicate the delamination of lithosphere can be well demonstrated in the eastern NCC. Furthermore, it is also supported by the subsequent magmatic pulses showing an asthenospheric source, such as the Fuxin basalt (107-97 Ma) in Liaoning Province (Zhang et al., 2003a) and the Pishikou mafic dikes (86-78 Ma) in the Jiaodong Peninsula (Zhang et al., 2008b).

Early Cretaceous (145-110 Ma)

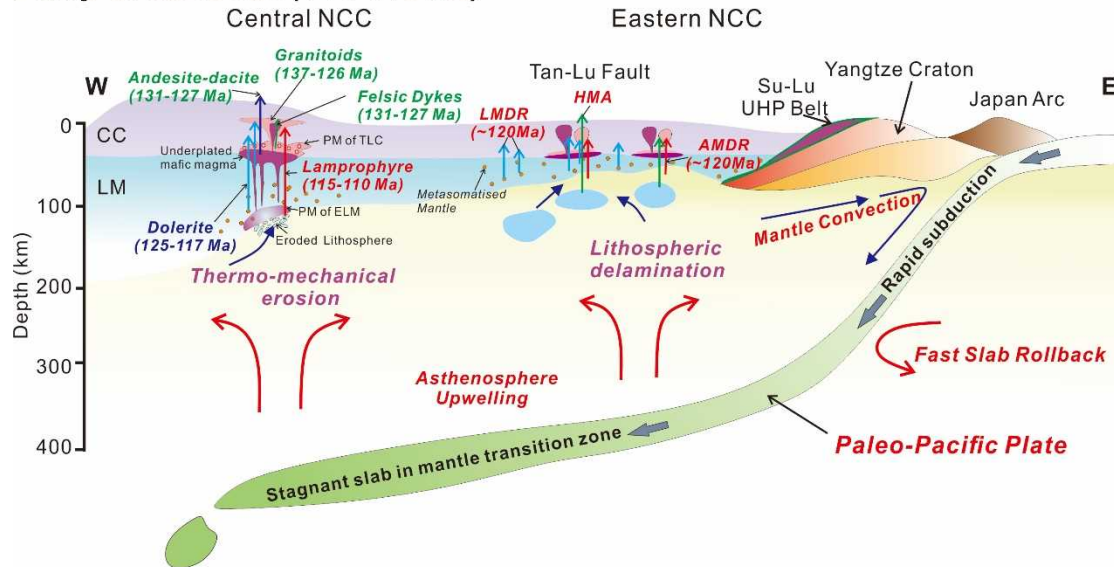


Fig. 10-5 Schematic plate tectonic model to explain the lithospheric destruction of the North China Craton during Early Cretaceous through thermal-mechanical erosion and lithospheric delamination. Detailed discussions are in the text. AMDR, asthenospheric mantle-derived rocks; CC, continental crust; ELM, enriched lithospheric mantle; HMA, high-Mg adakites; LM, lithospheric mantle; LMDR, lithospheric mantle-derived rocks; TLC, thickened lower crust.

Given the different lithospheric nature (Fig. 10-4b), it is difficult to use the delamination model to interpret the formation of Mesozoic magmatic rocks in the central NCC whereas it is reasonable to apply the thermal-mechanical erosion to account for the craton destruction in the study area. The lithosphere-asthenosphere and crust-mantle interactions constitute the vertical craton destruction phenomenon induced by the thermal-mechanical erosion. The delaminated lower crust cannot pass through the thick lithospheric mantle to founder into the asthenosphere because of the buoyancy and strength in the central NCC. Although the two mechanisms certainly differ from each other, the connection between them cannot be eliminated. The rapid and intense lithospheric delamination would trigger thermo-mechanical erosion within the interior domains of the NCC, and the slow and gradual erosion would act as the prelude of large-scale delamination. Both of the two mechanisms combined with the Paleo-Pacific slab played a significant role in the NCC destruction process to form

variable magmatic rocks (Fig. 10-5).

10.5 An integrated petrogenetic model for the Laiyuan complex

Combining the spatial, temporal, genetic, and tectonic linkages, considering the state change of the Paleo-Pacific slab beneath the NCC, an integrated petrogenetic model has been proposed to describe the formation mechanism of the Laiyuan magmatic complex (Fig. 10-5).

During Early Jurassic (~200 Ma), the initiation of subduction of the Paleo-Pacific Plate occurred beneath the Northeast Asia. Until ~150 Ma, the slab has reached the position beneath the central NCC. The cold slab lowered the geothermal gradient of the mantle beneath the craton and depressed direct mantle melting. During this period, the central NCC was under compression which thickened the lithosphere in the central NCC. The LJVR with the sub-volcanic suites corresponding to Tiaojishan Formation were formed during this period whose petrogenesis could be attributed to the MASH process (melting, assimilation, storage, homogenization) highlighting the important role of partial melting of thickened lower crust (Gao et al., 2012; Hildreth and Moor bath, 1988). The deep hornblende-dominated fractional crystallization process accounts for the sporadic ultramafic cumulates and evolved andesitic magmas with adakitic affinities which ascend through the crust to erupt.

Throughout the NCC, between the two main stages of Late Jurassic and the Early Cretaceous igneous activities, the sedimentary Tuchengzi/Houchengzi Formation was deposited with a magmatic gap indicating that the sub-horizontal subducted Paleo-Pacific Plate have been able to sequester the asthenospheric mantle out of the preexisting lithospheric mantle and the subducted slab which depressed the magmatic events in the central NCC (Wu et al., 2019). During 145-140 Ma, fast slab rollback occurred leading to hot asthenosphere upwelling and extensional setting in the central NCC. This intense mantle convection transformed from central to eastern NCC identified by the eastward younging trend of magmatism after ~140 Ma (Fig. 10-1c).

Induced by the upwelling of hot asthenosphere, the pre-weakened metasomatized lithospheric mantle would be heated and eroded, which would lead to partial melting, producing the parental basaltic magma. These magmas would be underplated beneath the base of thickened lower crust, acting as not only the thermal source to induce the crustal melting, but also the mafic end-member to interact with the felsic melts/magmas derived from the crust. The intense and consistent crust-mantle interaction accounts for the petrogenesis for the formation of the Laiyuan magmatic complex, including granitoids (137-126 Ma), MMEs (129-126 Ma), ECVR (131-127 Ma), and felsic dykes (131-127 Ma). The compositional heterogeneities of the igneous complex resulted from the multiple involved mantle and crustal sources, chaotic mixing and mingling process, and the complicated fractional crystallization during the deep interaction process.

From 145-110 Ma, the lithosphere in the central NCC underwent continued thinning and erosion. Through time, the lithosphere became substantially thin that lithospheric mantle-derived magmas could migrate through the lithospheric faults and intruded the plutons or country rocks leading to the formation of dolerite dykes at 125-117 Ma. The continuous asthenospheric upwelling caused heterogeneous erosion along weak zones resulting in non-uniform destruction of the lithosphere. In the eastern NCC, at ~120 Ma, delamination of the eclogitic lower crust occurred and the evacuated mantle was replaced by hot asthenosphere. However in the central NCC, the delamination didn't happen but the thermal-mechanical erosion took place to generate eroded lithosphere. Following delamination in the Jiaodong area at ~120 Ma, and the rapid slab rollback induced intense mantle convection, with further input from the accumulating slab graveyards in the mantle transition zone, the mantle upwelling and thermo-mechanical erosion reached their peak. More asthenosphere mantle began to melt with eroded lithospheric mantle. The partial melting of asthenospheric mantle and its interaction with the lithospheric mantle material produced the lamprophyre with both of arc-type and OIB-type characteristics dykes from ~115 Ma to 110 Ma.

Thus, the above discussion interprets the integrated formation process of the

Laiyuan magmatic complex. This formation mechanism could be also used to account for the petrogenesis of the magmatic plutons in the central. It is favored that both of the lithospheric delamination and thermo-mechanical erosion together played a key role in the destruction of the cratonic architecture of the NCC ([Fig. 10-5](#)).

Chapter 11 Summary and conclusions

(1) The Laiyuan magmatic complex is composed of variable magmatic suites including volcanic sequence (andesite-dacite), intermediate-felsic granitoids (syenogranite, monzogranite, quartz monzonite, and monzonite), mafic-ultramafic intrusions, and some dyke suites (felsic dykes, dolerites, and lamprophyres). The contact relationships between different magmatic suites indicate their tight genetic linkages.

(2) The detailed zircon geochronological studies of the Laiyuan magmatic rocks show that the volcanic rocks, granitoids, felsic dykes, dolerites, and lamprophyres were formed at 131-127 Ma, 137-128 Ma, 131-127 Ma, 125-117 Ma, and 115-110 Ma, respectively. The complicated history of magmatism for the Laiyuan complex is defined, beginning with ultramafic cumulate formation at ~154 Ma, then the first proceeding to the eruption of andesitic-dacitic lavas at ~146 Ma, reaching the peak with the intrusion of granitoid and simultaneous small mafic rocks from ~137-126 Ma, following the second episode of volcanism at ~130 Ma, and concluding with the tiny but widespread mafic dyking events from ~125-110 Ma.

(3) The zircon $\epsilon_{\text{Hf}}(t)$ values ranges from -23.5 to -19.4, -21.8 to -16.8, -22.3 to -17.2, -23.3 to -14.2, and -17.2 to -3.7 for studied volcanic rocks, granitoids, felsic dykes, dolerites, and lamprophyres, respectively. The isotopic studies show that the enriched lithospheric mantle accounts for the major parental magma source for the Laiyuan magmatic rocks ~150-110 Ma. Over a long time, multiple sources e.g., asthenospheric materials and crustal melts, are involved in this formation process. From 150-130 Ma, the lower crustal contribution to the source decreases from LJVR, through granitoids, to ECVR and felsic dykes, whereas the asthenospheric mantle contribution is increasing through time from dolerites to lamprophyres during 130-110 Ma.

(4) The Early Cretaceous volcanic suites show compositional range from andesite

to dacite, enrichment in LREE and LILE, depletion in HFSE, no apparent Eu anomalies, and adakitic geochemical features. The parental magma of the andesitic-dacitic rocks was primarily derived from the partial melting of an enriched lithospheric mantle which experienced fluid-related subduction metasomatism. The geochemical modeling reveals that adakitic affinities resulted not only from inheritance from their magma source but also through fractional crystallization during magma evolution. Significant amphibole fractionation and minor fractional crystallization of titanite and zircon occurred at depth, with limited plagioclase segregation at shallow levels.

(5) The granitoids display variable compositions and can be classified as two groups. The parental mafic magma for the Group I rocks were derived from the enriched lithospheric mantle and subsequently experienced the hornblende-dominated fractional crystallization to form the monzonitic/dioritic magmas, then the magma mixing and mingling with the crustal melts/magmas generated the hybrid magmas to form the MMEs and variable intermediate suites. Group II rocks are classified as high-K calc-alkaline I-type suite with higher SiO₂ content, and lower MgO content and Mg[#] than Group I rocks, including monzogranites and syenogranites. These granitic rocks were most likely generated by partial melting of the thickened mafic lower crust at high pressure, with some addition of the mafic magma from an enriched mantle, and followed by intense plagioclase-dominated fractional crystallization to form the highly-fractionated syenogranites. The compositional heterogeneities of the igneous complex resulted from the intense crust-mantle interaction which involved multiple mantle and crustal sources, and complicated magmatic evolutionary process.

(6) The mafic dyke samples exhibit enrichment in LILE and no obvious Eu anomalies, and the dolerites show strong depletion in HFSE, whereas the Th-U and Ta-Nb depletions in lamprophyres are not obviously similar to OIB-type. Mafic dykes in the Laiyuan complex were probably derived from different degrees of partial melting (3-14%) of an enriched lithospheric mantle in the amphibole-bearing garnet-facies amphibole stability zone at 80-100 km depth which experienced fluid

metasomatism related to subduction. Through time, increasing involvement of the asthenospheric mantle involved in the source of lamprophyres leading to the transitional geochemical feature indicating the key role of lithosphere-asthenosphere interaction in the central NCC.

(7) The Laiyuan area experienced the tectonic regime transition from compression to extension at Late Jurassic to Early Cretaceous. The intense magmatism to form the Laiyuan complex was under the extension tectonic setting triggered by the subduction of Paleo-Pacific Plate. The subduction, retreat, roll back, and stagnation of the Paleo-Pacific slab resulted in the heterogeneous lithosphere and various evolutionary processes in the deep beneath the NCC. The different lithospheric evolution beneath the eastern and central NCC during the Early Cretaceous resulted from different destruction mechanisms. The slow and gradual thermal-mechanical erosion occurred at the central NCC, whereas the rapid and intense lithospheric delamination occurred at the eastern NCC. Both of the two mechanisms combined with the Paleo-Pacific slab played a significant role in the NCC destruction process to form variable magmatic rocks.

Acknowledgements

First of all, I would like to sincerely appreciate my PhD supervisor Professor Toshiaki Tsunogae and Professor M. Santosh for their excellent supervision, kind encouragement and support on my PhD research project. I would like to express my gratefulness to Professor Toshiaki Tsunogae for his guidance, immense supervision and experimental support on my PhD research project in University of Tsukuba, Japan. The study in Japan broadened my vision, enriched my knowledge and improved my communicative competence.

I am very grateful to Prof. M. Santosh for his excellent suggestions in my research career and life, for his kind help to provide international cooperation platform in South Korea and Japan, and for the great efforts to improve my spoken and written English. These obtained experiences during my PhD study not only broadened my view, but also taught me how to think and solve scientific problems.

Special thanks to Professor Sheng-Rong Li for his kind help in the fieldwork and financial support, and to Dr. Juquan Zhang for his useful advice and support during my PhD study. I appreciate Dr. Sung Won Kim and Professor Hongying Zhou for their help in the zircon U-Pb and Lu-Hf analyses in the Korea Basic Research Institute, South Korea, and Tianjin center, China geological survey, China. Many thanks are given to my group members Fan Yang, Li Tang, Shan-Shan Li, Xiao-Fang He, Yuesheng Han, Chengxue Yang, Cun Zhang, Xueming Teng and Zhiwei Shen for their useful discussion, kind help in the field, together with laboratory analyses. Several members of University of Tsukuba, such as Qian Liu, Wang Ding, Yaping Hu, Sam Uthup, Md. Sazzadur Rahman and Yusuke Takamura, are also thanked for their kind help in my PhD study career in Japan.

This research was financially supported by the Talent Award to M. Santosh under the 1000 Talents Plan of the Chinese Government, the Basic Research Project (GP2017- 021; Development of integrated geological information based on digital mapping) of the Korea Institute of Geoscience and Mineral Resources, funded by the

Ministry of Science, ICT, and Future Planning, Korea to Sung Won Kim, the National Key Research and Development Program (No. 2016YFC0600106) to Sheng-Rong Li together with the China Scholarship Council (No. 201806400026), and the Fundamental Research Funds for the Central Universities (No. 2652016066).

At last, I am very much grateful to my parents and every family members for their fully support and encourage in my life. Without them, I would not have got the power to continue my research.

References

- Annen C, Blundy J D, Sparks R. The genesis of intermediate and silicic magmas in deep crustal hot zones. *Journal of Petrology*, 2006, 47(3): 505-539.
- Arndt N T, Coltice N, Helmstaedt H, et al. Origin of Archean subcontinental lithospheric mantle: Some petrological constraints. *Lithos*, 2009, 109(1-2): 61-71.
- Atherton M P, Petford N. Generation of sodium-rich magmas from newly underplated basaltic crust. *Nature*, 1993, 362(6416): 144-146.
- Bachmann O, Dungan M A, Bussy F. Insights into shallow magmatic processes in large silicic magma bodies: the trace element record in the Fish Canyon magma body, Colorado. *Contributions to Mineralogy and Petrology*, 2005, 149(3): 338-349.
- Barbarin B. A review of the relationships between granitoid types, their origins and their geodynamic environments. *Lithos*, 1999, 46(3): 605-626.
- Barbarin B. Mafic magmatic enclaves and mafic rocks associated with some granitoids of the central Sierra Nevada batholith, California: nature, origin, and relations with the hosts. *Lithos*, 2005, 80(1-4): 155-177.
- Bateman P C, Chappell B W. Crystallization, fractionation, and solidification of the Tuolumne intrusive series, Yosemite National Park, California. *Geological Society of America Bulletin*, 1979, 90(5): 465-482.
- Baxter S, Feely M. Magma mixing and mingling textures in granitoids: examples from the Galway Granite, Connemara, Ireland. *Mineralogy and Petrology*, 2002, 76(1-2): 63-74.
- Boyd F R, Pokhilenko N P, Pearson D G, et al. Composition of the Siberian cratonic mantle: evidence from Udachnaya peridotite xenoliths. *Contributions to Mineralogy and Petrology*, 1997, 128(2-3): 228-246.
- Breiter K, Gardenová N, Kanický V, et al. Gallium and germanium geochemistry during magmatic fractionation and post-magmatic alteration in different types of granitoids: A case study from the Bohemian Massif (Czech Republic). *Geologica Carpathica*, 2013, 64(3): 171-180b.
- Brown M. Granite: From genesis to emplacement. *GSA bulletin*, 2013, 125(7-8): 1079-1113.
- Cai J H, Yan G H, Chang Z S, et al. Petrological and geochemical characteristics of the

- Wanganzhen complex and discussion on its genesis. *Acta Petrologica Sinica*, 2003, 19(1): 81-92.
- Cai Y C, Fan H R, Santosh M, et al. Decratonic gold mineralization: Evidence from the Shangzhuang gold deposit, eastern North China Craton. *Gondwana Research*, 2018, 54: 1-22.
- Cai Y, Fan H, Santosh M, et al. Evolution of the lithospheric mantle beneath the southeastern North China Craton: Constraints from mafic dikes in the Jiaobei terrain. *Gondwana Research*, 2013, 24(2): 601-621.
- Campos R S D, Philipp R P, Massonne H, et al. Early post-collisional Brasiliano magmatism in Botuverá region, Santa Catarina, southern Brazil: Evidence from petrology, geochemistry, isotope geology and geochronology of the diabase and lamprophyre dikes. *Journal of South American Earth Sciences*, 2012, 37: 266-278.
- Castillo P R. Adakite petrogenesis. *Lithos*, 2012, 134: 304-316.
- Castillo P R, Janney P E, Solidum R U. Petrology and geochemistry of Camiguin Island, southern Philippines: insights to the source of adakites and other lavas in a complex arc setting. *Contributions to Mineralogy and Petrology*, 1999, 134(1): 33-51.
- Chappell B W, White A J R. I-and S-type granites in the Lachlan Fold Belt. *Earth and Environmental Science Transactions of the Royal Society of Edinburgh*, 1992, 83(1-2): 1-26.
- Chappell B W, White A J R. Two contrasting granite types: 25 years later. *Australian Journal of Earth Sciences*, 2001, 48(4): 489-499.
- Chappell B W, White A J R, Wyborn D. The importance of residual source material (restite) in granite petrogenesis. *Journal of Petrology*, 1987, 28(6): 1111-1138.
- Chen B, Chen Z C, Jahn B M. Origin of mafic enclaves from the Taihang Mesozoic orogen, north China craton. *Lithos*, 2009b, 110(1-4): 343-358.
- Chen B, Jahn B M, Arakawa Y, et al. Petrogenesis of the Mesozoic intrusive complexes from the southern Taihang Orogen, North China Craton: elemental and Sr–Nd–Pb isotopic constraints. *Contributions to Mineralogy and Petrology*, 2004, 148(4): 489-501.
- Chen B, Jahn B M, Suzuki K. Petrological and Nd-Sr-Os isotopic constraints on the origin of high-Mg adakitic rocks from the North China Craton: Tectonic implications. *Geology*, 2013, 41(1): 91-94.

- Chen B, Tian W, Jahn B M, et al. Zircon SHRIMP U–Pb ages and in-situ Hf isotopic analysis for the Mesozoic intrusions in South Taihang, North China craton: Evidence for hybridization between mantle-derived magmas and crustal components. *Lithos*, 2008, 102(1): 118-137.
- Chen B, Tian W, Zhai M G, et al. Zircon U-Pb geochronology and geochemistry of Mesozoic magmatism in the Taihang Mountains and other places of the North China Craton, with implications for petrogenesis and geodynamic setting. *Acta Petrologica Sinica*, 2005, 21(1): 13-24.
- Chen B, Zhai M, Shao J A. Petrogenesis and significance of the Mesozoic North Taihang complex: major and trace element evidence. *Science in China Series D: Earth Sciences*, 2003, 46(9): 941-953.
- Chen B, Zhai M, Tian W. Origin of the Mesozoic magmatism in the North China Craton: constraints from petrological and geochemical data. *Geological Society, London, Special Publications*, 2007b, 280(1): 131-151.
- Chen L. Concordant structural variations from the surface to the base of the upper mantle in the North China Craton and its tectonic implications. *Lithos*, 2010, 120(1): 96-115.
- Chen L, Cheng C, Wei Z. Seismic evidence for significant lateral variations in lithospheric thickness beneath the central and western North China Craton. *Earth and Planetary Science Letters*, 2009a, 286(1): 171-183.
- Chen L, Zheng T Y, Xu W W. A thinned lithospheric image of the Tanlu Fault Zone, eastern China: constructed from wave equation based receiver function migration. *Journal of Geophysical Research: Solid Earth*, 2006, 111(B9).
- Chen Z C, Chen B, Tian W. Hf isotopic compositions and geological significance; a case study of Mesozoic batholiths and mafic enclaves in North Taihang. *Acta Petrologica Sinica*, 2007a, 23(2): 295-306.
- Chu N, Taylor R N, Chavagnac V, et al. Hf isotope ratio analysis using multi-collector inductively coupled plasma mass spectrometry: an evaluation of isobaric interference corrections. *Journal of Analytical Atomic Spectrometry*, 2002, 17(12): 1567-1574.
- Clemens J D, Holloway J R, White A. Origin of an A-type granite; experimental constraints. *American Mineralogist*, 1986, 71(3-4): 317-324.

- Clemens J D, Stevens G. What controls chemical variation in granitic magmas? *Lithos*, 2012, 134: 317-329.
- Clemens J D, Wall V J. Controls on the mineralogy of S-type volcanic and plutonic rocks. *Lithos*, 1988, 21(1): 53-66.
- Coleman D S, Gray W, Glazner A F. Rethinking the emplacement and evolution of zoned plutons: Geochronologic evidence for incremental assembly of the Tuolumne Intrusive Suite, California. *Geology*, 2004, 32(5): 433-436.
- Collins W J, Richards S W. Geodynamic significance of S-type granites in circum-Pacific orogens. *Geology*, 2008, 36(7): 559-562.
- Corfu F. Atlas of Zircon Textures. *Reviews in Mineralogy & Geochemistry*. 2003, 53(1): 469-500.
- Davidson J, Turner S, Handley H, et al. Amphibole “sponge” in arc crust? *Geology*, 2007, 35(9): 787-790.
- De La Roche H, Leterrier J, Grandclaude P, et al. A classification of volcanic and plutonic rocks using r1r2-diagram and major-element analyses-its relationships with current nomenclature. *Chemical Geology*, 1980, 29: 183-210.
- Defant M J, Drummond M S. Derivation of some modern arc magmas by melting of young subducted lithosphere. *Nature*, 1990, 347(6294): 662-665.
- Deng J, Liu X F, Wang Q F, et al. Isotopic characterization and petrogenetic modeling of Early Cretaceous mafic diking—Lithospheric extension in the North China craton, eastern Asia. *Geological Society of America Bulletin*, 2017a, 129(11-12): 1379-1407.
- Deng J, Wang Q F, Li G J. Tectonic evolution, superimposed orogeny, and composite metallogenic system in China. *Gondwana Research*, 2017b, 50: 216-266.
- DePaolo D J. Radiogenic isotopes and crustal evolution. In: R.J. O’Connell, W.S. Fyfe (Eds.), *Evolution of the Earth. Geodynamics Series*, American Geophysical Union, Washington, DC, United States, 1981, pp. 59-68.
- Donaire T, Pascual E, Pin C, et al. Microgranular enclaves as evidence of rapid cooling in granitoid rocks: the case of the Los Pedroches granodiorite, Iberian Massif, Spain. *Contributions to Mineralogy and Petrology*, 2005, 149(3): 247-265.
- Dong S W, Zhang Y Q, Li H L, et al. The Yanshan orogeny and late Mesozoic multi-plate

- convergence in East Asia—Commemorating 90th years of the “Yanshan Orogeny”. *Science China Earth Sciences*, 2018, 61(12): 1888-1909.
- Drummond M S, Defant M J, Kepezhinskas P K. Petrogenesis of slab-derived trondhjemite-tonalite-dacite/adakite magmas. *Transactions of the Royal Society of Edinburgh Earth Sciences*, 1996, 87(1-2): 205-215.
- Duan C, Mao J W, Xie G Q, et al. Zircon U-Pb Geochronological and Hf isotope study on Tiaojishan volcanic Formation, Mujicun, North Taihang Mountain and implications for regional metallogeny and magmatism. *Acta Geologica Sinica*, 2016, 90(2): 250-266.
- Duggen S, Hoernle K, Van D B P, et al. Post-Collisional Transition from Subduction- to Intraplate-type Magmatism in the Westernmost Mediterranean: Evidence for Continental-Edge Delamination of Subcontinental Lithosphere. *Journal of Petrology*, 2005, 46(6): 1155-1201.
- Elhlou S, Belousova E, Griffin W L, et al. Trace element and isotopic composition of GJ-red zircon standard by laser ablation. *Geochimica et Cosmochimica Acta*, 2006, 70(18): A158-A158.
- Ernst R E, Buchan K L. Recognizing mantle plumes in the geological record. *Annual Review of Earth and Planetary Sciences*, 2003, 31(1): 469-523.
- Falloon T J, Green D H, Hatton C J, et al. Anhydrous Partial Melting of a Fertile and Depleted Peridotite from 2 to 30 kb and Application to Basalt Petrogenesis. *Journal of Petrology*, 1988, 29(6): 1257-1288.
- Fan W M. Destruction of aged lower lithosphere and accretion of asthenosphere mantle beneath eastern China. *Geotectonica et Metallogenia*, 1992, 16: 171-180.
- Fan W, Guo F, Wang Y, et al. Post-orogenic bimodal volcanism along the Sulu orogenic belt in eastern China. *Physics and Chemistry of the Earth, Part A: Solid Earth and Geodesy*, 2001, 26(9-10): 733-746.
- Foley S F, Barth M G, Jenner G A. Rutile/melt partition coefficients for trace elements and an assessment of the influence of rutile on the trace element characteristics of subduction zone magmas. *Geochimica et Cosmochimica Acta*, 2000, 64(5): 933-938.
- Foley S F, Venturelli G, Green D H, et al. The ultrapotassic rocks: Characteristics, classification,

- and constraints for petrogenetic models. *Earth-Science Reviews*, 1987, 24(2): 81-134.
- Fowler M B, Henney P J, Darbyshire D, et al. Petrogenesis of high Ba–Sr granites: the Rogart pluton, Sutherland. *Journal of the Geological Society*, 2001, 158(3): 521-534.
- Furman T, Graham D. Erosion of lithospheric mantle beneath the East African Rift system: geochemical evidence from the Kivu volcanic province. *Developments in Geotectonics*, 1999, 24: 237-262.
- Gao P, Zheng Y F, Zhao Z F. Experimental melts from crustal rocks: A lithochemical constraint on granite petrogenesis. *Lithos*, 2016, 266: 133-157.
- Gao S, Rudnick R L, Carlson R W, et al. Re–Os evidence for replacement of ancient mantle lithosphere beneath the North China craton. *Earth & Planetary Science Letters*, 2002, 198(3-4): 307-322.
- Gao S, Rudnick R L, Yuan H, et al. Recycling lower continental crust in the North China craton. *Nature*, 2004, 432(7019): 892.
- Gao S, Zhang J, Xu W, et al. Delamination and destruction of the North China Craton. *Chinese Science Bulletin*, 2009, 54(19): 3367-3378.
- Gao Y F, Hou Z Q, Kamber B S, et al. Adakite-like porphyries from the southern Tibetan continental collision zones: evidence for slab melt metasomatism. *Contributions to Mineralogy and Petrology*, 2007, 153(1): 105-120.
- Gao Y F, Santosh M, Hou Z Q, et al. High Sr/Y magmas generated through crystal fractionation: Evidence from Mesozoic volcanic rocks in the northern Taihang orogen, North China Craton. *Gondwana Research*, 2012, 22(1): 152-168.
- Gao Y F, Santosh M, Wei R H, et al. Origin of high Sr/Y magmas from the northern Taihang Mountains: Implications for Mesozoic porphyry copper mineralization in the North China Craton. *Journal of Asian Earth Sciences*, 2013, 78(12): 143-159.
- Gao Y F, Wei R H, Hou Z Q, et al. Mujicun porphyry copper mineralization: response to Mesozoic thinning of lithosphere in North China Craton. *Mineral Deposits*, 2011, 30(5): 890-902.
- Geng J Z, Li H K, Zhang J, et al. Zircon Hf isotope analysis by means of LA-MC-ICP-MS. *Geological Bulletin of China*, 2011, 30(10): 1508-1513.

- Geng Y S, Du L L, Ren L D. Growth and reworking of the early Precambrian continental crust in the North China Craton: constraints from zircon Hf isotopes. *Gondwana Research*, 2012, 21(2-3): 517-529.
- Ghaffari M, Rashidnejad-Omran N, Dabiri R, et al. Interaction between felsic and mafic magmas in the Salmas intrusive complex, Northwestern Iran: Constraints from petrography and geochemistry. *Journal of Asian Earth Sciences*, 2015, 111: 440-458.
- Glazner A F, Bartley J M, Coleman D S, et al. Are plutons assembled over millions of years by amalgamation from small magma chambers? *GSA today*, 2004, 14(4/5): 4-12.
- Goldfarb R J, Santosh M. The dilemma of the Jiaodong gold deposits: Are they unique? *Geoscience Frontiers*, 2014, 5(2): 139-153.
- Griffin W L, Andi Z, O'Reilly S Y, et al. Phanerozoic Evolution of the Lithosphere Beneath the Sino - Korean Craton. *American Geophysical Union*, 1998. 107-126.
- Griffin W L, Kobussen A F, Babu E, et al. A translithospheric suture in the vanished 1-Ga lithospheric root of South India: evidence from contrasting lithosphere sections in the Dharwar Craton. *Lithos*, 2009, 112: 1109-1119.
- Griffin W L, Pearson N J, Belousova E, et al. The Hf isotope composition of cratonic mantle: LAM-MC-ICPMS analysis of zircon megacrysts in kimberlites. *Geochimica et cosmochimica acta*, 2000, 64(1): 133-147.
- Griffin W L, Wang X, Jackson S E, et al.. Zircon chemistry and magma mixing, SE China: in-situ analysis of Hf isotopes, Tonglu and Pingtan igneous complexes. *Lithos*, 2002, 61(3-4): 237-269.
- Grove T L, Donnelly-Nolan J M, Housh T. Magmatic processes that generated the rhyolite of Glass Mountain, Medicine Lake volcano, N. California. *Contributions to Mineralogy and Petrology*, 1997, 127(3): 205-223.
- Groves D I, Santosh M. The giant Jiaodong gold province: The key to a unified model for orogenic gold deposits? *Geoscience Frontiers*, 2016, 7(3): 409-417.
- Guo F, Fan W M, Wang Y J, et al. Origin of early Cretaceous calc-alkaline lamprophyres from the Sulu orogen in eastern China: implications for enrichment processes beneath continental collisional belt. *Lithos*, 2004, 78(3): 291-305.

- Guo Z F, Wilson M. The Himalayan leucogranites: constraints on the nature of their crustal source region and geodynamic setting. *Gondwana Research*, 2012, 22(2): 360-376.
- Hawkesworth C J, Cawood P A, Dhuime B, et al. Earth's continental lithosphere through time. *Annual Review of Earth and Planetary Sciences*, 2017, 45: 169-198.
- Hawkesworth C J, Gallagher K, Hergt J M, et al. Mantle and slab contributions in arc magmas. *Annual Review of Earth and Planetary Sciences*, 1993, 21(1): 175-204.
- He X F, Kobayashi A, Santosh M, et al. Crust–mantle interaction and craton destruction: evidence from Late Mesozoic plutons in the North China Craton. *Journal of the Geological Society*, 2017a, 174(6): 1070-1089.
- He X F, Santosh M. Crustal recycling through intraplate magmatism: Evidence from the Trans-North China Orogen. *Journal of Asian Earth Sciences*, 2014, 95: 147-163.
- He X F, Santosh M, Ganguly S. Mesozoic felsic volcanic rocks from the North China craton: Intraplate magmatism associated with craton destruction. *GSA Bulletin*, 2017b, 129(7-8): 947-969.
- Hildreth W, Moorbath S. Crustal contributions to arc magmatism in the Andes of Central Chile. *Contributions to Mineralogy and Petrology*, 1988, 98(4): 455-489.
- Hofmann A W, Jochum K P, Seufert M, et al. Nb and Pb in oceanic basalts: new constraints on mantle evolution. *Earth & Planetary Science Letters*, 1986, 79(1-2): 33-45.
- Hou Z Q, Li Q Y, Gao Y F, et al. Lower-Crustal Magmatic Hornblendite in North China Craton: Insight into the Genesis of Porphyry Cu Deposits. *Economic Geology*, 2015, 110(7): 1879-1904.
- Houseman G A, Mckenzie D P, Molnar P. Convective instability of a thickened boundary layer and its relevance for the thermal evolution of continental convergent belts. *Journal of Geophysical Research Solid Earth*, 1981, 86(B7): 6115-6132.
- Hu F Y, Liu S W, Ducea M N, et al. Interaction among magmas from various sources and crustal melting processes during continental collision: insights from the Huayang intrusive complex of the South Qinling Belt, China. *Journal of Petrology*, 2018, 59(4): 735-770.
- Huang F, Li S G, Dong F, et al. High-Mg adakitic rocks in the Dabie orogen, central China: implications for foundering mechanism of lower continental crust. *Chemical Geology*, 2008,

255(1-2): 1-13.

Huang J L, Zhao D P. High - resolution mantle tomography of China and surrounding regions.

Journal of Geophysical Research Solid Earth, 2006, 111(B9): 1-21.

Huang S W. The relationship between magmatic rocks and mineralization of the Dawan Porphyry

Mo deposit in the north of Taihang mountain: [Master Thesis]. Beijing: China University of Geosciences (Beijing), 2014.

Jackson S E, Pearson N J, Griffin W L, et al. The application of laser ablation-inductively coupled

plasma-mass spectrometry to in situ U–Pb zircon geochronology. *Chemical Geology*, 2004, 211(1-2): 47-69.

Jagoutz O E. Construction of the granitoid crust of an island arc. Part II: a quantitative

petrogenetic model. *Contributions to Mineralogy and Petrology*, 2010, 160(3): 359-381.

Jahn B, Wu F, Lo C, et al. Crust–mantle interaction induced by deep subduction of the continental

crust: geochemical and Sr–Nd isotopic evidence from post-collisional mafic–ultramafic intrusions of the northern Dabie complex, central China. *Chemical Geology*, 1999, 157(1-2): 119-146.

Jiang N, Carlson R W, Guo J H. Source of Mesozoic intermediate-felsic igneous rocks in the

North China craton: Granulite xenolith evidence. *Lithos*, 2011, 125(1-2): 335-346.

Jiang N, Liu Y S, Zhou W G, et al. Derivation of Mesozoic adakitic magmas from ancient lower

crust in the North China craton. *Geochimica et Cosmochimica Acta*, 2007, 71(10): 2591-2608.

Jung C, Jung S, Hoffer E, et al. Petrogenesis of Tertiary mafic alkaline magmas in the Hocheifel,

Germany. *Journal of Petrology*, 2006, 47(8): 1637-1671.

Karmalkar N R, Duraiswami R A, Rao N C, et al. Mantle-derived mafic-ultramafic xenoliths and

the nature of Indian sub-continental lithosphere. *Journal of the Geological Society of India*, 2009, 73(5): 657.

Kemp A, Hawkesworth C J, Foster G L, et al. Magmatic and crustal differentiation history of

granitic rocks from Hf-O isotopes in zircon. *Science*, 2007, 315(5814): 980-983.

Kerr A C, Khan M, Mahoney J J, et al. Late Cretaceous alkaline sills of the south Tethyan suture

zone, Pakistan: Initial melts of the Réunion hotspot? *Lithos*, 2010, 117(1): 161-171.

- King P L, Chappell B W, Allen C M, et al. Are A - type granites the high - temperature felsic granites? Evidence from fractionated granites of the Wangrah Suite. *Australian Journal of Earth Sciences*, 2001, 48(4): 501-514.
- King P L, White A, Chappell B W, et al. Characterization and origin of aluminous A-type granites from the Lachlan Fold Belt, southeastern Australia. *Journal of Petrology*, 1997, 38(3): 371-391.
- Kröner A, Wilde S A, Li J H, et al. Age and evolution of a late Archean to Paleoproterozoic upper to lower crustal section in the Wutaishan/Hengshan/Fuping terrain of northern China. *Journal of Asian Earth Sciences*, 2005, 24(5): 577-595.
- Krystopowicz N J, Currie C A. Crustal eclogitization and lithosphere delamination in orogens. *Earth & Planetary Science Letters*, 2013, 361: 195-207.
- La Flèche M R, Camiré G, Jenner G A. Geochemistry of post-Acadian, Carboniferous continental intraplate basalts from the Maritimes Basin, Magdalen Islands, Québec, Canada. *Chemical Geology*, 1998, 148(3-4): 115-136.
- Langmuir C H, Jr. Vocke R D, Hanson G N, et al. A general mixing equation with applications to Icelandic basalts. *Earth and Planetary Science Letters*, 1978, 37(3): 380-392.
- Le Fort P, Cuney M, Deniel C, et al. Crustal generation of the Himalayan leucogranites. *Tectonophysics*, 1987, 134(1-3): 39-57.
- Leake B E, Woolley A R, Arps C E S, et al, 1997. Nomenclature of amphiboles; Report of the Subcommittee on Amphiboles of the International Mineralogical Association, Commission on New Minerals and Mineral Names, International Conference on Formal Concept Analysis, pp. 181-196.
- Lee C A, Bachmann O. How important is the role of crystal fractionation in making intermediate magmas? Insights from Zr and P systematics. *Earth and Planetary Science Letters*, 2014, 393: 266-274.
- Lee C A, Luffi P, Chin E J. Building and destroying continental mantle. *Annual Review of Earth and Planetary Sciences*, 2011, 39: 59-90.
- Li L, Santosh M, Li S R. The 'Jiaodong type' gold deposits: Characteristics, origin and prospecting. *Ore Geology Reviews*, 2015b, 65: 589-611.

- Li N, Chen Y, Santosh M, et al. Late Mesozoic granitoids in the Qinling Orogen, Central China, and tectonic significance. *Earth-Science Reviews*, 2018, (182): 141-173.
- Li Q, Santosh M, Li S R. Stable isotopes and noble gases in the Xishimen gold deposit, central North China Craton: metallogeny associated with lithospheric thinning and crust-mantle interaction. *International Geology Review*, 2013a, 55(14): 1728-1743.
- Li Q, Santosh M, Li S R, et al. Petrology, geochemistry and zircon U–Pb and Lu–Hf isotopes of the Cretaceous dykes in the central North China Craton: Implications for magma genesis and gold metallogeny. *Ore Geology Reviews*, 2015a, 67(67): 57-77.
- Li S R, Santosh M. Metallogeny and craton destruction: Records from the North China Craton. *Ore Geology Reviews*, 2014, 56(1): 376-414.
- Li S R, Santosh M. Geodynamics of heterogeneous gold mineralization in the North China Craton and its relationship to lithospheric destruction. *Gondwana Research*, 2017, 50: 267-292.
- Li S Z, Suo Y H, Li X Y, et al. Mesozoic tectono-magmatic response in the East Asian ocean-continent connection zone to subduction of the Paleo-Pacific Plate. *Earth-Science Reviews*, 2019b, 192: 91-137.
- Li S Z, Zhao G C, Dai L M, et al. Mesozoic basins in eastern China and their bearing on the deconstruction of the North China Craton. *Journal of Asian Earth Sciences*, 2012, 47: 64-79.
- Li S, Santosh M, Zhang H, et al. Inhomogeneous lithospheric thinning in the central North China Craton: zircon U–Pb and S–He–Ar isotopic record from magmatism and metallogeny in the Taihang Mountains. *Gondwana Research*, 2013b, 23(1): 141-160.
- Li S, Zhu D, Wang Q, et al. Slab-derived adakites and subslab asthenosphere-derived OIB-type rocks at 156 ± 2 Ma from the north of Gerze, central Tibet: Records of the Bangong–Nujiang oceanic ridge subduction during the Late Jurassic. *Lithos*, 2016, 262: 456-469.
- Li X H, Li Z X, Li W X, et al. U–Pb zircon, geochemical and Sr–Nd–Hf isotopic constraints on age and origin of Jurassic I- and A-type granites from central Guangdong, SE China: a major igneous event in response to foundering of a subducted flat-slab? *Lithos*, 2007, 96(1-2): 186-204.
- Li X Y, Li S Z, Huang F, et al. Petrogenesis of high Ba–Sr plutons with high Sr/Y ratios in an intracontinental setting: evidence from Early Cretaceous Fushan monzonites, central North

- China Craton. *Geological Magazine*, 2019a: 1-17.
- Li X Y, Li S Z, Suo Y H, et al. Early Cretaceous diabases, lamprophyres and andesites-dacites in western Shandong, North China Craton: Implications for local delamination and Paleo-Pacific slab rollback. *Journal of Asian Earth Sciences*, 2018, 160: 426-444.
- Li X Y, Zheng J P, Ma Q, et al. From enriched to depleted mantle : evidence from Cretaceous lamprophyres and Paleogene basaltic rocks in eastern and central Guangxi Province, western Cathaysia block of South China. *Lithos*, 2014, 184: 300-313.
- Liang Y Y, Liu X F, Qin C, et al. Petrogenesis of early cretaceous mafic dikes in southeastern Jiaolai basin, Jiaodong Peninsula, China. *International Geology Review*, 2017, 59(2): 131-150.
- Liégeois J, Abdelsalam M G, Ennih N, et al. Metacraton: nature, genesis and behavior. *Gondwana Research*, 2013, 23(1): 220-237.
- Lindsley D H, Andersen D J. A two - pyroxene thermometer. *Journal of Geophysical Research Solid Earth*, 1983, 88(S02): A887-A906.
- Liu A K, Chen B, Suzuki K, et al. Petrogenesis of the Mesozoic Zijinguan mafic pluton from the Taihang Mountains, North China Craton: Petrological and Os–Nd–Sr isotopic constraints. *Journal of Asian Earth Sciences*, 2010, 39(4): 294-308.
- Liu D Y, Nutman A P, Compston W, et al. Remnants of ≥ 3800 Ma crust in the Chinese part of the Sino-Korean craton. *Geology*, 1992, 20(4): 339-342.
- Liu D Y, Page R W, Compston W, et al. U-Pb zircon geochronology of late Archaean metamorphic rocks in the Taihangshan—Wutaishan area, North China. *Precambrian Research*, 1984, 27(1): 85-109.
- Liu J G, Cai R H, Pearson D G, et al. Thinning and destruction of the lithospheric mantle root beneath the North China Craton: A review. *Earth-Science Reviews*, 2019, 196: 102873.
- Liu L, Chen B, Liu A K. Petrogenesis of the Zijinguan mafic pluton, northern Taihang orogen: Constraints from petrology and geochemistry. *Earth Science*, 2009a, 34: 165-178.
- Liu S, Feng C X, Santosh M, et al. Integrated elemental and Sr-Nd-Pb-Hf isotopic studies of Mesozoic mafic dykes from the eastern North China Craton: implications for the dramatic transformation of lithospheric mantle. *Journal of Geodynamics*, 2018, 114: 19-40.

- Liu S, Feng C, Feng G, et al. Timing, mantle source and origin of mafic dykes within the gravity anomaly belt of the Taihang-Da Hinggan gravity lineament, central North China Craton. *Journal of Geodynamics*, 2017b, 109: 41-58.
- Liu S, Hu R Z, Gao S, et al. Zircon U–Pb geochronology and major, trace elemental and Sr–Nd–Pb isotopic geochemistry of mafic dykes in western Shandong Province, east China: Constrains on their petrogenesis and geodynamic significance. *Chemical Geology*, 2008, 255(3): 329-345.
- Liu S, Hu R Z, Gao S, et al. Petrogenesis of Late Mesozoic mafic dykes in the Jiaodong Peninsula, eastern North China Craton and implications for the foundering of lower crust. *Lithos*, 2009b, 113(3-4): 621-639.
- Liu X, Zhao D P, Li S Z, et al. Age of the subducting Pacific slab beneath East Asia and its geodynamic implications. *Earth and Planetary Science Letters*, 2017a, 464: 166-174.
- Liu Y S, Gao S, Jin S Y, et al. Geochemistry of lower crustal xenoliths from Neogene Hannuoba Basalt, North China Craton: Implications for petrogenesis and lower crustal composition. *Geochimica et Cosmochimica Acta*, 2001, 65(15): 2589-2604.
- Lu Y J, Mccuaig T C, Li Z X, et al. Paleogene post-collisional lamprophyres in western Yunnan, western Yangtze Craton: Mantle source and tectonic implications. *Lithos*, 2015, 233: 139-161.
- Ludwig K R. ISOPLOT, a geochronological toolkit for Microsoft Excel 3.00. 2003.
- Ma L, Jiang S Y, Hofmann A W, et al. Lithospheric and asthenospheric sources of lamprophyres in the Jiaodong Peninsula: A consequence of rapid lithospheric thinning beneath the North China Craton? *Geochimica et Cosmochimica Acta*, 2014a, 124(1): 250-271.
- Ma L, Jiang S Y, Hofmann A W, et al. Rapid lithospheric thinning of the North China Craton: New evidence from cretaceous mafic dikes in the Jiaodong Peninsula. *Chemical Geology*, 2016, 432: 1-15.
- Ma L, Jiang S Y, Hou M L, et al. Geochemistry of Early Cretaceous calc-alkaline lamprophyres in the Jiaodong Peninsula: Implication for lithospheric evolution of the eastern North China Craton. *Gondwana Research*, 2014b, 25(2): 859-872.
- Ma Q, Zheng J P, Xu Y G, et al. Are continental “adakites” derived from thickened or foundered

- lower crust? *Earth and Planetary Science Letters*, 2015, 419: 125-133.
- Ma X, Chen C, Zhao J, et al. Late Permian intermediate and felsic intrusions in the eastern Central Asian Orogenic Belt: Final-stage magmatic record of Paleo-Asian Oceanic subduction? *Lithos*, 2019, 326: 265-278.
- Mao J W, Xie G Q, Zhang Z H, et al. Mesozoic large-scale metallogenic pulses in North China and corresponding geodynamic settings. *Acta Petrologica Sinica*, 2005, 21(1): 169-188.
- Martin H, Smithies R H, Rapp R, et al. An overview of adakite, tonalite–trondhjemite–granodiorite (TTG), and sanukitoid: relationships and some implications for crustal evolution. *Lithos*, 2005, 79(1-2): 1-24.
- Maruyama S, Santosh M, Zhao D. Superplume, supercontinent, and post-perovskite: Mantle dynamics and anti-plate tectonics on the Core–Mantle Boundary. *Gondwana Research*, 2007, 11(1–2): 7-37.
- Mcdonough W F, Sun S S. The composition of the Earth ☆. *Chemical Geology*, 1995, 120(3-4): 223-253.
- Mckenzie D, O'Nions R K. Partial Melt Distributions from Inversion of Rare Earth Element Concentrations. *Journal of Petrology*, 1991, 32(5): 1021-1091.
- Menzies M, Xu Y, Zhang H, et al. Integration of geology, geophysics and geochemistry: A key to understanding the North China Craton. *Lithos*, 2007, 96(1-2): 1-21.
- Middlemost E A K. Naming materials in the magma/igneous rock system. *Earth-Science Reviews*, 1994, 37(3-4): 215-224.
- Miller C F. Are strongly peraluminous magmas derived from pelitic sedimentary sources? *The Journal of Geology*, 1985, 93(6): 673-689.
- Miller J S, Matzel J E P, Miller C F, et al. Zircon growth and recycling during the assembly of large, composite arc plutons. *Journal of Volcanology & Geothermal Research*, 2007, 167(1): 282-299.
- Morency C, Doin M P, Dumoulin C. Convective destabilization of a thickened continental lithosphere. *Earth and Planetary Science Letters*, 2002, 202(2): 303-320.
- Moyen J F. High Sr/Y and La/Yb ratios: The meaning of the “adakitic signature”. *Lithos*, 2009, 112(3-4): 556-574.

- Müller R D, Sdrolias M, Gaina C, et al. Long-term sea-level fluctuations driven by ocean basin dynamics. *Science*, 2008, 319(5868): 1357-62.
- Naqvi S M, Khan R, Manikyamba C, et al. Geochemistry of the NeoArchaean high-Mg basalts, boninites and adakites from the Kushtagi–Hungund greenstone belt of the Eastern Dharwar Craton (EDC); implications for the tectonic setting. *Journal of Asian Earth Sciences*, 2006, 27(1): 25-44.
- Niu Y L. Generation and evolution of basaltic magmas: some basic concepts and a new view on the origin of Mesozoic–Cenozoic basaltic volcanism in eastern China. *Geological Journal of China Universities*, 2005, 11(1): 9-46.
- Orozco-Garza A, Dostal J, Keppie J D, et al. Mid-Tertiary (25-21 Ma) lamprophyres in NW Mexico derived from subduction-modified subcontinental lithospheric mantle in an extensional backarc environment following steepening of the Benioff zone. *Tectonophysics*, 2013, 590: 59-71.
- Paton C, Hellstrom J, Paul B, et al. Iolite: Freeware for the visualisation and processing of mass spectrometric data. *Journal of Analytical Atomic Spectrometry*, 2011, 26(12): 2508-2518.
- Pearce J A. Trace Element Discrimination Diagrams for the Tectonic Interpretation of Granitic Rocks. *Journal of Petrology*, 1984, 25(4): 956-983.
- Pearce J A. Geochemical fingerprinting of oceanic basalts with applications to ophiolite classification and the search for Archean oceanic crust. *Lithos*, 2008, 100(1-4): 14-48.
- Pearce J A, Cann J R. Tectonic setting of basic volcanic rocks determined using trace element analyses. *Earth and Planetary Science Letters*, 1973, 19(2): 290-300.
- Pearce J A, Peate D W. Tectonic implications of the composition of volcanic arc magmas. *Annual Review of Earth and Planetary sciences*, 1995, 23(1): 251-285.
- Pearson D G, Carlson R W, Shirey S B, et al. Stabilisation of Archaean lithospheric mantle: A ReOs isotope study of peridotite xenoliths from the Kaapvaal craton. *Earth and Planetary Science Letters*, 1995, 134(3-4): 341-357.
- Peccerillo A, Taylor S R. Geochemistry of eocene calc-alkaline volcanic rocks from the Kastamonu area, Northern Turkey. *Contributions to Mineralogy and Petrology*, 1975, 58(1): 63-81.

- Petford N, Cruden A R, McCaffrey K, et al. Granite magma formation, transport and emplacement in the Earth's crust. *Nature*, 2000, 408(6813): 669-673.
- Pitcher W S. *The nature and origin of granite*. Springer Science & Business Media, 1997.
- Polat A, Kerrich R. Archean greenstone belt magmatism and the continental growth–mantle evolution connection: constraints from Th–U–Nb–LREE systematics of the 2.7 Ga Wawa subprovince, Superior Province, Canada. *Earth and Planetary Science Letters*, 2000, 175(1-2): 41-54.
- Qu K. *Geology and mineralization in Mujicun porphyry Cu-Mo deposit, Northern Taihang Mt., China*: [Master Thesis]. Beijing: China University of Geosciences (Beijing), 2012.
- Rapp R P. Experimental constraints on the origin of potassium-rich adakite in eastern China. *Acta Petrol, Sinica*, 2002, 18: 293-311.
- Rapp R P, Shimizu N, Norman M D, et al. Reaction between slab-derived melts and peridotite in the mantle wedge: experimental constraints at 3.8 GPa. *Chemical Geology*, 1999, 160(4): 335-356.
- Rapp R P, Watson E B. Dehydration melting of metabasalt at 8-32 kbar: implications for continental growth and crust-mantle recycling. *Journal of Petrology*, 1995, 36(4): 891-931.
- Ratajeski K, Sisson T W, Glazner A F. Experimental and geochemical evidence for derivation of the El Capitan Granite, California, by partial melting of hydrous gabbroic lower crust. *Contributions to Mineralogy and Petrology*, 2005, 149(6): 713-734.
- Reubi O, Blundy J. A dearth of intermediate melts at subduction zone volcanoes and the petrogenesis of arc andesites. *Nature*, 2009, 461(7268): 1269-1273.
- Richards J P, Kerrich R. Special paper: adakite-like rocks: their diverse origins and questionable role in metallogenesis. *Economic geology*, 2007, 102(4): 537-576.
- Rickwood P C. Boundary lines within petrologic diagrams which use oxides of major and minor elements. *Lithos*, 1989, 22(4): 247-263.
- Robinson J A C, Wood B J. The depth of the spinel to garnet transition at the peridotite solidus. *Earth and Planetary Science Letters*, 1998, 164(1-2): 277-284.
- Rock N M S. The nature and origin of lamprophyres: some definitions, distinctions, and derivations. *Earth-Science Reviews*, 1977, 13(2): 123-169.

- Rock N M S. The nature and origin of lamprophyres: an overview. Geological Society of London Special Publications, 1987, 30(1): 191-226.
- Rudnick R L. Making continental crust. Nature, 1995, 378(6557): 571.
- Rudnick R L, Fountain D M. Nature and composition of the continental crust: A lower crustal perspective. Reviews of Geophysics, 1995, 33(3): 267-309.
- Rudnick R L, Gao S. Composition of the Continental Crust. Treatise Geochem 3:1-64, 2003.
- Santosh M. Assembling North China Craton within the Columbia supercontinent: The role of double-sided subduction. Precambrian Research, 2010, 178(1-4): 149-167.
- Santosh M, Hari K R, He X, et al. Oldest lamproites from Peninsular India track the onset of Paleoproterozoic plume-induced rifting and the birth of Large Igneous Province. Gondwana Research, 2018, 55: 1-20.
- Schmidt A, Weyer S, John T, et al. HFSE systematics of rutile-bearing eclogites: new insights into subduction zone processes and implications for the earth's HFSE budget. Geochimica et Cosmochimica Acta, 2009, 73(2): 455-468.
- Scott J M, Liu J, Pearson D G, et al. Continent stabilisation by lateral accretion of subduction zone-processed depleted mantle residues; insights from Zealandia. Earth and Planetary Science Letters, 2019, 507: 175-186.
- Sen C, Dunn T. Dehydration melting of a basaltic composition amphibolite at 1.5 and 2.0 GPa: implications for the origin of adakites. Contributions to Mineralogy and Petrology, 1994, 117(4): 394-409.
- Seton M, Müller R D, Zahirovic S, et al. Global continental and ocean basin reconstructions since 200 Ma. Earth-Science Reviews, 2012, 113(3-4): 212-270.
- Shen Z C, Hou Z Q, Chen Z K, et al. Molybdenite Re-Os isotopic dating and zircon SHRIMP U-Pb and Hf isotopic compositions of the Mujicun porphyry deposit. Acta Petrologica Et Mineralogica, 2015b, 4(34): 526-538.
- Shen Z C, Hou Z Q, Yu F, et al. SHRIMP zircon U-Pb ages and Hf isotopes of the intermediate-acidic rocks of Wanganzhen complex in northern part of Taihang Mountains and their geological implications. Acta Petrologica Sinica, 2015a, 31(5): 1409-1420.
- Sisson T W, Ratajeski K, Hanks W B, et al. Voluminous granitic magmas from common

- basaltic sources. *Contributions to Mineralogy and Petrology*, 2005, 148(6): 635-661.
- Sláma J, Košler J, Condon D J, et al. Plešovice zircon—a new natural reference material for U–Pb and Hf isotopic microanalysis. *Chemical Geology*, 2008, 249(1-2): 1-35.
- Smith E I, Sánchez A, Walker J D, et al. Geochemistry of Mafic Magmas in the Hurricane Volcanic Field, Utah: Implications for Small - and Large - Scale Chemical Variability of the Lithospheric Mantle. *Journal of Geology*, 1999, 107(4): 433-448.
- Smith J V, Brown W L. *Feldspar Minerals*. Springer-Verlag, 1974. 388-389.
- Song Y, Ding H Y, Qu X M, et al. Re–Os and U–Pb Geochronology of the Dawan Mo–Zn–Fe Deposit in Northern Taihang Mountains, China. *Resource Geology*, 2014, 64(2): 117-135.
- Spera F J, Bohron W A. Energy-constrained open-system magmatic processes I: General model and energy-constrained assimilation and fractional crystallization (EC-AFC) formulation. *Journal of Petrology*, 2001, 42(5): 999-1018.
- Stern C R, Kilian R. Role of the subducted slab, mantle wedge and continental crust in the generation of adakites from the Andean Austral Volcanic Zone. *Contributions to Mineralogy and Petrology*, 1996, 123(3): 263-281.
- Sun S S, McDonough W F. *Chemical and Isotopic Systematics of Oceanic Basalts; Implications for Mantle Composition and Processes*. Geological Society London Special Publications, 1989, 42(1): 313-345.
- Tan J, Wei J H, Guo L L, et al. LA-ICP-MS zircon U-Pb dating and phenocryst EPMA of dikes, Guocheng, Jiaodong Peninsula: Implications for North China Craton lithosphere evolution. *Science China Earth Sciences*, 2008, 51(10): 1483-1500.
- Tang L, Santosh M. Neoproterozoic-Paleoproterozoic terrane assembly and Wilson cycle in the North China Craton: an overview from the central segment of the Trans-North China Orogen. *Earth-Science Reviews*, 2018, 182: 1-27.
- Tang L, Santosh M, Teng X. Paleoproterozoic (ca. 2.1–2.0 Ga) arc magmatism in the Fuping Complex: implications for the tectonic evolution of the Trans-North China Orogen. *Precambrian Research*, 2015, 268: 16-32.
- Tang L, Santosh M, Tsunogae T, et al. Late Neoproterozoic arc magmatism and crustal growth associated with microblock amalgamation in the North China Craton: evidence from the

- Fuping Complex. *Lithos*, 2016, 248: 324-338.
- Tarney J, Jones C E. Trace element geochemistry of orogenic igneous rocks and crustal growth models. *Journal of the Geological Society*, 1994, 151(5): 855-868.
- Turnbull R, Weaver S, Tulloch A, et al. Field and geochemical constraints on mafic–felsic interactions, and processes in high-level arc magma chambers: an example from the Halfmoon Pluton, New Zealand. *Journal of Petrology*, 2010, 51(7): 1477-1505.
- Vernon R H. Crystallization and hybridism in microgranitoid enclave magmas: microstructural evidence. *Journal of Geophysical Research: Solid Earth*, 1990, 95(B11): 17849-17859.
- Walker Jr B A, Miller C F, Claiborne L L, et al. Geology and geochronology of the Spirit Mountain batholith, southern Nevada: Implications for timescales and physical processes of batholith construction. *Journal of Volcanology and Geothermal Research*, 2007, 167(1-4): 239-262.
- Wang H Z, Mo X X. An outline of the tectonic evolution of China. *Episodes*, 1995, 18: 6-16.
- Wang Q, Wyman D A, Xu J, et al. Early Cretaceous adakitic granites in the Northern Dabie Complex, central China: implications for partial melting and delamination of thickened lower crust. *Geochimica et Cosmochimica Acta*, 2007, 71(10): 2609-2636.
- Wang Q, Xu J, Jian P, et al. Petrogenesis of Adakitic Porphyries in an Extensional Tectonic Setting, Dexing, South China: Implications for the Genesis of Porphyry Copper Mineralization. *Journal of Petrology*, 2006, 47(1): 119-144.
- Wang R, Qiu J, Yu S, et al. Crust–mantle interaction during Early Jurassic subduction of Neo-Tethyan oceanic slab: Evidence from the Dongga gabbro–granite complex in the southern Lhasa subterrane, Tibet. *Lithos*, 2017, 292: 262-277.
- Wang T, Guo L, Zheng Y, et al. Timing and processes of late Mesozoic mid-lower-crustal extension in continental NE Asia and implications for the tectonic setting of the destruction of the North China Craton: Mainly constrained by zircon U–Pb ages from metamorphic core complexes. *Lithos*, 2012, 154: 315-345.
- Wang Y, Zhou L Y, Liu S F, et al. Post-cratonization deformation processes and tectonic evolution of the North China Craton. *Earth-Science Reviews*, 2018, 177: 320-365.
- Wang Z L, Yang L Q, Deng J, et al. Gold-hosting high Ba-Sr granitoids in the Xincheng gold

- deposit, Jiaodong Peninsula, East China: Petrogenesis and tectonic setting. *Journal of Asian Earth Sciences*, 2014, 95: 274-299.
- Wang Z, Cheng H, Zong K, et al. Metasomatized lithospheric mantle for Mesozoic giant gold deposits in the North China craton. *Geology*, 2020, 2(48): 169-173.
- Wei C J, Qian J H, Zhou X W. Paleoproterozoic crustal evolution of the Hengshan–Wutai–Fuping region, North China craton. *Geoscience Frontiers*, 2014, 5(4): 485-497.
- Whalen J B, Currie K L, Chappell B W. A-type granites: geochemical characteristics, discrimination and petrogenesis. *Contributions to Mineralogy and Petrology*, 1987, 95(4): 407-419.
- White A J, Chappell B W, Wyborn D. Application of the Restite Model to the Deddick Granodiorite and its Enclaves—a Reinterpretation of the Observations and Data of Mass et al. (1997). *Journal of Petrology*, 1999, 40(3): 413-421.
- Wiedenbeck M, Alle P, Corfu F, et al. Three natural zircon standards for U - Th - Pb, Lu - Hf, trace element and REE analyses. *Geostandards newsletter*, 1995, 19(1): 1-23.
- Wilde S A, Zhou X, Nemchin A A, et al. Mesozoic crust-mantle interaction beneath the North China craton: A consequence of the dispersal of Gondwanaland and accretion of Asia. *Geology*, 2003, 31(9): 817-820.
- Wilson M. Magmatic differentiation. *Journal of the Geological Society*, 1993, 150(4): 611-624.
- Windley B F, Maruyama S, Xiao W J. Delamination/thinning of sub-continental lithospheric mantle under Eastern China: The role of water and multiple subduction. *American Journal of Science*, 2010, 310(10): 1250-1293.
- Wolf M B, London D. Apatite dissolution into peraluminous haplogranitic melts: an experimental study of solubilities and mechanisms. *Geochimica et Cosmochimica Acta*, 1994, 58(19): 4127-4145.
- Woodard J, Kietäväinen R, Eklund O. Svecofennian post-collisional shoshonitic lamprophyres at the margin of the Karelia Craton: Implications for mantle metasomatism. *Lithos*, 2014, 205(9): 379-393.
- Woodhead J D, Hergt J M. A Preliminary Appraisal of Seven Natural Zircon Reference Materials for In Situ Hf Isotope Determination. *Geostandards & Geoanalytical Research*, 2005, 29(2):

183–195.

- Wooley, R A, Bergman S C, et al. Classification of lamprophyres, lamproites, kimberlites, and the kalsilitic, melilitic, and leucitic rocks. *Canadian Mineralogist*, 1996, 34(2): 175-186.
- Wu F Y, Lin J Q, Wilde S A, et al. Nature and significance of the Early Cretaceous giant igneous event in eastern China. *Earth and Planetary Science Letters*, 2005, 233(1): 103-119.
- Wu F Y, Liu X C, Ji W Q, et al. Highly fractionated granites: Recognition and research. *Science China Earth Sciences*, 2017, 60(7): 1201-1219.
- Wu F Y, Xu Y G, Gao S, et al. Lithospheric thinning and destruction of the North China Craton. *Acta Petrologica Sinica*, 2008, 24(6): 1145-1174.
- Wu F Y, Xu Y G, Zhu R X, et al. Thinning and destruction of the cratonic lithosphere: A global perspective. *Science China Earth Sciences*, 2014, 57(12): 2878-2890.
- Wu F, Yang J, Xu Y, et al. Destruction of the North China Craton in the Mesozoic. *Annual Review of Earth and Planetary Sciences*, 2019, 47(1): 173-195.
- Xia Q K, Liu J, Kovács I, et al. Water in the upper mantle and deep crust of eastern China: concentration, distribution and implications. *National Science Review*, 2017, 6(1): 125-144.
- Xiao L, Clemens J D. Origin of potassic (C-type) adakite magmas: experimental and field constraints. *Lithos*, 2007, 95(3-4): 399-414.
- Xu W L, Hergt J M, Gao S, et al. Interaction of adakitic melt-peridotite: implications for the high-Mg[#] signature of Mesozoic adakitic rocks in the eastern North China Craton. *Earth and Planetary Science Letters*, 2008, 265(1-2): 123-137.
- Xu W L, Yang D B, Pei F P, et al. Petrogenesis of Fushan high-Mg-# diorites from the southern Taihang Mts. in the central North China Craton: Resulting from interaction of peridotite-melt derived from partial melting of delaminated lower continental crust. *Acta Petrologica Sinica*, 2009b, 25(8): 1947-1961.
- Xu W, Zhou Q, Pei F, et al. Destruction of the North China Craton: Delamination or thermal/chemical erosion? Mineral chemistry and oxygen isotope insights from websterite xenoliths. *Gondwana Research*, 2013, 23(1): 119-129.
- Xu W, Zhu D, Wang Q, et al. Constructing the Early Mesozoic Gangdese Crust in Southern Tibet by Hornblende-dominated Magmatic Differentiation. *Journal of Petrology*, 2019, 60(3):

515-552.

- Xu Y G. Thermo-tectonic destruction of the archaean lithospheric keel beneath the Sino-Korean Craton in China: Evidence, timing and mechanism. *Physics and Chemistry of the Earth Part A-Solid Earth and Geodesy*, 2001, 26(9-10): 747-757.
- Xu Y G, Li H Y, Pang C J, et al. On the timing and duration of the destruction of the North China Craton. *Chinese Science Bulletin*, 2009a, 54(19): 3379.
- Xu Y G, Ma J L, Frey F A, et al. Role of lithosphere–asthenosphere interaction in the genesis of Quaternary alkali and tholeiitic basalts from Datong, western North China Craton. *Chemical Geology*, 2005, 224(4): 247-271.
- Xue F, Santosh M, Li S, et al. Early Cretaceous cryptoexplosive breccia-related gold mineralization in the North China Craton: Evidence from the Puziwan gold deposit. *Ore Geology Reviews*, 2019a, 111: 102986.
- Xue F, Santosh M, Tsunogae T, et al. Geochemical and isotopic imprints of early cretaceous mafic and felsic dyke suites track lithosphere-asthenosphere interaction and craton destruction in the North China Craton. *Lithos*, 2019b, 326-327: 174-199.
- Xue F, Santosh M, Tsunogae T, et al. The genesis of high Ba - Sr adakitic rocks: Insights from an Early Cretaceous volcanic suite in the central North China Craton. *Geological Journal*, 2020, doi.org/10.1002/gj.3720.
- Xue F, Wang G, Santosh M, et al. Geochemistry and geochronology of ore-bearing and barren intrusions in the Luanchuan ore fields of East Qinling metallogenic belt, China: diverse tectonic evolution and implications for mineral exploration. *Journal of Asian Earth Sciences*, 2018, 157: 57-77.
- Yan H Y, Long X P, Li J, et al. Arc Andesitic Rocks Derived From Partial Melts of Mélange Diapir in Subduction Zones: Evidence From Whole - Rock Geochemistry and Sr - Nd - Mo Isotopes of the Paleogene Linzizong Volcanic Succession in Southern Tibet. *Journal of Geophysical Research: Solid Earth*, 2019, 124(1): 456-475.
- Yang C X, Santosh M. Ancient deep roots for Mesozoic world-class gold deposits in the north China craton: An integrated genetic perspective. *Geoscience Frontiers*, 2020, 11(1): 203-214.
- Yang F, Santosh M, Kim S W, et al. Early Cretaceous adakitic granitoids from the Zhijiazhuang

- skarn iron deposit, North Taihang Mountain, China: Implications for petrogenesis and metallogenesis associated with craton destruction. *Geological Journal*, 2019a, 54(6): 3189-3211.
- Yang F, Santosh M, Kim S W, et al. Late Mesozoic intraplate rhyolitic volcanism in the North China Craton: Far-field effect of the westward subduction of the Paleo-Pacific Plate. *GSA Bulletin*, 2020, (132): 291-309.
- Yang F, Xue F, Santosh M, et al. Late Mesozoic magmatism in the East Qinling Orogen, China and its tectonic implications. *Geoscience Frontiers*, 2019b, 10(5): 1803-1821.
- Yang J H, Chung S L, Zhai M G, et al. Geochemical Sr–Nd–Pb isotopic compositions of mafic dikes from the Jiaodong Peninsula, China: evidence for vein-plus-peridotite melting in the lithospheric mantle. *Lithos*, 2004, 73(3-4): 145-160.
- Yang J H, Wu F Y, Wilde S A, et al. Mesozoic decratonization of the North China block. *Geology*, 2008, 36(6): 467-470.
- Yang J. The Petrological Studies on Lamprophyres in Laiyuan and Fuping Area, Hebei. *Acta Petrologica Et Mineralogica*, 1989, (8): 12-24.
- Yang J. The geochemical features and their genesis of lamprophyres in Laiyuan-Fuping area, Hebei Province, China. *Geoscience*, 1991, 3(5): 330-337.
- Yang J, O'Reilly S, Walker R J, et al. Diachronous decratonization of the Sino-Korean craton: Geochemistry of mantle xenoliths from North Korea. *Geology*, 2010, 38(9): 799-802.
- Yang W B, Niu H C, Shan Q, et al. Geochemistry of primary-carbonate bearing K-rich igneous rocks in the Awulale Mountains, western Tianshan: Implications for carbon-recycling in subduction zone. *Geochimica et Cosmochimica Acta*, 2014, 143: 143-164.
- Yang Y, Wu F, Wilde S A, et al. In situ perovskite Sr–Nd isotopic constraints on the petrogenesis of the Ordovician Mengyin kimberlites in the North China Craton. *Chemical Geology*, 2009, 264(1-4): 24-42.
- Ye H M, Li X H, Li Z X, et al. Age and origin of high Ba–Sr appinite–granites at the northwestern margin of the Tibet Plateau: Implications for early Paleozoic tectonic evolution of the Western Kunlun orogenic belt. *Gondwana Research*, 2008, 13(1): 126-138.
- Žák J, Paterson S R. Characteristics of internal contacts in the Tuolumne Batholith, central Sierra

- Nevada, California (USA): Implications for episodic emplacement and physical processes in a continental arc magma chamber. *Geological Society of America Bulletin*, 2005, 117(9-10): 1242-1255.
- Zhai M G, Santosh M. The early Precambrian odyssey of the North China Craton: A synoptic overview. *Gondwana Research*, 2011, 20(1): 6-25.
- Zhai Y Y, Xie J C, Dong G C. The genetic significance of amphiboles from the ultramafic rocks of Wang'anzen batholith in northern Taihang Mountains. *Acta Petrologica Et Mineralogica*, 2014, 33(2): 273-282.
- Zhang C H, Li C M, Deng H L, et al. Mesozoic contraction deformation in the Yanshan and northern Taihang mountains and its implications to the destruction of the North China Craton. *Science China Earth Sciences*, 2011, 54(6): 798-822.
- Zhang H D, Liu J C, Santosh M, et al. Ultra-depleted peridotite xenoliths in the Northern Taihang Mountains: Implications for the nature of the lithospheric mantle beneath the North China Craton. *Gondwana Research*, 2017, 48: 72-85.
- Zhang H D, Liu J C, Wang J Y, et al. Petrology, geochronology and geochemistry characteristics of Wang'anzen complex in the northern Taihang Mountain and their geological significance. *Acta Petrologica Sinica*, 2016, 32(3): 727-745.
- Zhang H, Goldstein S L, Zhou X, et al. Evolution of subcontinental lithospheric mantle beneath eastern China: Re–Os isotopic evidence from mantle xenoliths in Paleozoic kimberlites and Mesozoic basalts. *Contributions to Mineralogy and Petrology*, 2008a, 155(3): 271-293.
- Zhang H, Sun M, Zhou X, et al. Mesozoic lithosphere destruction beneath the North China Craton: evidence from major-, trace-element and Sr–Nd–Pb isotope studies of Fangcheng basalts. *Contributions to Mineralogy and Petrology*, 2002, 144(2): 241-254.
- Zhang H, Sun M, Zhou X, et al. Secular evolution of the lithosphere beneath the eastern North China Craton: evidence from Mesozoic basalts and high-Mg andesites. *Geochimica et Cosmochimica Acta*, 2003a, 67(22): 4373-4387.
- Zhang J, Li S, Santosh M, et al. Mineral chemistry of high-Mg diorites and skarn in the Han-Xing Iron deposits of South Taihang Mountains, China: Constraints on mineralization process. *Ore Geology Reviews*, 2015, 64: 200-214.

- Zhang J, Zhang H F, Ying J F, et al. Contribution of subducted Pacific slab to Late Cretaceous mafic magmatism in Qingdao region, China: A petrological record. *Island Arc*, 2008b, 17(2): 231-241.
- Zhang L Y, Li S C, Zhao Q Y. A review of research on adakites. *International Geology Review*, 2019: 1-18.
- Zhang S H, Zhao Y, Davis G A, et al. Temporal and spatial variations of Mesozoic magmatism and deformation in the North China Craton: Implications for lithospheric thinning and decratonization. *Earth-Science Reviews*, 2014, 131(4): 49-87.
- Zhang S N. Geochemical Characteristics and Genetic Mechanism of Wanganzhen Complex in Taihang Mountains: [Master Thesis]. Beijing: China University of Geosciences (Beijing), 2014.
- Zhang Y, Chen B, Shao J A, et al. Geochemistry and origin of Late Mesozoic lamprophyre dykes in Taihang Mountains, North China. *Acta Petrologica Et Mineralogica*. 2003b, 22(1): 29-33.
- Zhao G C, Cawood P A, Li S Z, et al. Amalgamation of the North China Craton: key issues and discussion. *Precambrian Research*, 2012, 222: 55-76.
- Zhao G C, Sun M, Wilde S A, et al. Late Archean to Paleoproterozoic evolution of the North China Craton: key issues revisited. *Precambrian Research*, 2005, 136(2): 177-202.
- Zhao G C, Sun M, Wilde S A, et al. Some key issues in reconstructions of Proterozoic supercontinents. *Journal of Asian Earth Sciences*, 2006, 28(1): 3-19.
- Zheng J P. Mesozoic-Cenozoic mantle replacement and lithospheric thinning beneath the eastern China. China University of Geosciences Press, Wuhan. 1999, 126.
- Zheng J P, Griffin W L, O Reilly S Y, et al. Mechanism and timing of lithospheric modification and replacement beneath the eastern North China Craton: peridotitic xenoliths from the 100 Ma Fuxin basalts and a regional synthesis. *Geochimica et Cosmochimica Acta*, 2007a, 71(21): 5203-5225.
- Zheng J P, O'Reilly S Y, Griffin W L, et al. Relict refractory mantle beneath the eastern North China block: significance for lithosphere evolution. *Lithos*, 2001, 57(1): 43-66.
- Zheng T Y, Chen L, Zhao L, et al. Crustal structure across the Yanshan belt at the northern margin of the North China Craton. *Physics of the Earth and Planetary Interiors*, 2007b, 161(1):

36-49.

Zheng Y F, Xu Z, Zhao Z F, et al. Mesozoic mafic magmatism in North China: Implications for thinning and destruction of cratonic lithosphere. *Science China Earth Sciences*, 2018, 61(4): 353-385.

Zhu G, Chen Y, Jiang D, et al. Rapid change from compression to extension in the North China Craton during the Early Cretaceous: Evidence from the Yunmengshan metamorphic core complex. *Tectonophysics*, 2015a, 656: 91-110.

Zhu R X, Chen L, Wu F Y, et al. Timing, scale and mechanism of the destruction of the North China Craton. *Science China Earth Sciences*, 2011, 54(6): 789-797.

Zhu R X, Fan H R, Jianwei L I, et al. Decratonic gold deposits. *Science China Earth Sciences*, 2015b, 58(9): 1523-1537.

Zhu R X, Xu Y G. The subduction of the west Pacific plate and the destruction of the North China Craton. *Science China Earth Sciences*, 2019: 1-11.

Zhu R X, Yang J, Wu F Y. Timing of destruction of the North China Craton. *Lithos*, 2012, 149: 51-60.

Appendix I: Analytical data

Table 5-1 LA-MC-ICPMS zircon U-Pb data of the Laiyuan volcanic rocks analyzed in this study.

Identifier	Elements Concentrations				Isotopic ratios ($\pm 2\sigma$)							Age (Ma) ($\pm 2\sigma$)						Concordance
	Pb*	²³⁸ U	²³² Th	Th/U	²⁰⁶ Pb/ ²³⁸ U	2 σ	²⁰⁷ Pb/ ²³⁵ U	2 σ	Rho	²⁰⁷ Pb/ ²⁰⁶ Pb	2 σ	²⁰⁶ Pb/ ²³⁸ U	2 σ	²⁰⁷ Pb/ ²³⁵ U	2 σ	²⁰⁷ Pb/ ²⁰⁶ Pb	2 σ	
	ppm	ppm	ppm		abs		abs			abs		abs		abs		abs		%
LYN-3/2																		
LYN-3/2-01	8	351	347	0.99	0.0198	0.0004	0.1322	0.0078	0.35	0.0486	0.0028	126.1	2.6	126.1	7.4	126.4	136.7	100
LYN-3/2-04	5	226	268	1.19	0.0203	0.0005	0.1348	0.0196	0.16	0.0481	0.0071	129.6	3.1	128.4	18.6	105.6	346.4	101
LYN-3/2-05	6	256	258	1.00	0.0200	0.0004	0.1368	0.0101	0.29	0.0496	0.0035	127.6	2.8	130.2	9.6	177.7	166.8	98
LYN-3/2-06	5	221	136	0.61	0.0202	0.0005	0.1347	0.0136	0.23	0.0484	0.0048	128.9	3.0	128.3	13.0	116.9	232.3	100
LYN-3/2-07	6	280	202	0.72	0.0202	0.0004	0.1385	0.0102	0.29	0.0498	0.0037	128.6	2.7	131.7	9.7	187.8	171.5	98
LYN-3/2-08	3	132	84	0.64	0.0201	0.0004	0.1396	0.0233	0.13	0.0504	0.0084	128.1	2.8	132.7	22.1	215.0	385.7	97
LYN-3/2-09	6	290	209	0.72	0.0207	0.0004	0.1350	0.0171	0.16	0.0473	0.0059	132.1	2.7	128.6	16.3	63.0	297.8	103
LYN-3/2-10	3	117	82	0.70	0.0202	0.0005	0.1381	0.0292	0.11	0.0497	0.0107	128.7	3.1	131.4	27.8	179.8	502.7	98
LYN-3/2-11	3	116	91	0.78	0.0207	0.0005	0.1374	0.0300	0.10	0.0482	0.0110	131.9	2.9	130.8	28.5	109.5	536.8	101
LYN-3/2-12	6	254	221	0.87	0.0203	0.0004	0.1355	0.0098	0.29	0.0483	0.0035	129.8	2.7	129.0	9.4	114.0	168.8	101
LYN-3/2-13	10	426	448	1.05	0.0202	0.0005	0.1363	0.0082	0.40	0.0490	0.0026	128.8	3.1	129.7	7.8	146.7	125.9	99
LYN-3/2-14	4	194	133	0.68	0.0202	0.0004	0.1367	0.0139	0.21	0.0490	0.0049	129.1	2.8	130.1	13.3	148.6	235.3	99
LYN-3/2-15	3	154	103	0.67	0.0201	0.0005	0.1349	0.0161	0.19	0.0485	0.0057	128.6	2.9	128.5	15.4	126.1	275.9	100
LYN-3/2-16	3	138	82	0.60	0.0205	0.0005	0.1378	0.0197	0.16	0.0487	0.0069	131.0	3.0	131.1	18.8	133.1	334.3	100
LYN-3/2-17	2	113	69	0.61	0.0206	0.0005	0.1395	0.0281	0.12	0.0490	0.0100	131.8	3.3	132.6	26.7	147.4	477.3	99
LYN-3/2-18	11	471	295	0.63	0.0212	0.0004	0.1445	0.0111	0.26	0.0493	0.0037	135.5	2.7	137.0	10.5	163.3	175.6	99
LYN-3/2-19	4	180	103	0.57	0.0203	0.0004	0.1370	0.0207	0.14	0.0489	0.0073	129.6	2.7	130.3	19.7	143.8	350.0	99

LYN-3/2-20	3	133	59	0.44	0.0204	0.0005	0.1399	0.0230	0.14	0.0497	0.0081	130.4	2.9	133.0	21.8	179.5	380.9	98
LYN-3/2-21	6	253	240	0.95	0.0199	0.0004	0.1324	0.0108	0.25	0.0482	0.0038	127.3	2.6	126.3	10.3	107.6	186.7	101
LYN-3/2-22	5	241	175	0.73	0.0205	0.0004	0.1354	0.0144	0.20	0.0478	0.0050	131.1	2.7	129.0	13.7	90.2	246.5	102
LYN-3/2-23	4	198	142	0.72	0.0202	0.0004	0.1315	0.0126	0.23	0.0472	0.0044	128.9	2.8	125.5	12.0	61.6	222.9	103
LYN-3/2-24	4	203	129	0.64	0.0198	0.0004	0.1354	0.0109	0.27	0.0497	0.0039	126.2	2.7	128.9	10.4	179.8	183.7	98
LYN-3/2-25	5	237	147	0.62	0.0199	0.0004	0.1399	0.0097	0.31	0.0510	0.0036	127.1	2.7	133.0	9.2	239.6	161.1	96
LYN-3/2-26	7	324	248	0.77	0.0200	0.0004	0.1381	0.0086	0.32	0.0501	0.0031	127.7	2.5	131.4	8.2	198.4	141.7	97
LYN-3/2-27	3	119	57	0.48	0.0208	0.0005	0.1345	0.0185	0.16	0.0469	0.0064	132.8	2.9	128.1	17.6	42.6	328.1	104
LYN-3/2-28	4	179	116	0.65	0.0204	0.0004	0.1332	0.0150	0.19	0.0474	0.0052	130.0	2.8	126.9	14.3	69.3	263.0	102
LYN-3/2-29	5	218	145	0.67	0.0208	0.0004	0.1330	0.0112	0.25	0.0464	0.0038	132.5	2.8	126.8	10.7	20.2	195.8	105
LYN-3/2-30	3	156	91	0.58	0.0207	0.0005	0.1358	0.0162	0.19	0.0475	0.0056	132.2	2.9	129.3	15.4	75.3	278.6	102
LYN-3/2-31	7	318	238	0.75	0.0207	0.0004	0.1360	0.0082	0.33	0.0476	0.0028	132.3	2.6	129.5	7.8	78.4	138.1	102
LYN-3/2-32	5	203	139	0.68	0.0211	0.0005	0.1407	0.0156	0.23	0.0485	0.0052	134.3	3.4	133.6	14.9	121.9	250.9	100
LYN-3/2-33	4	179	112	0.62	0.0211	0.0005	0.1414	0.0132	0.23	0.0487	0.0045	134.4	2.9	134.3	12.6	132.7	218.3	100
LYN-3/2-34	5	212	136	0.64	0.0207	0.0005	0.1373	0.0155	0.21	0.0481	0.0053	132.0	3.1	130.6	14.7	105.8	258.6	101
LYN-3/2-35	9	395	284	0.72	0.0206	0.0005	0.1351	0.0099	0.30	0.0475	0.0034	131.6	2.9	128.7	9.4	74.3	171.8	102
LYN-3/2-36	5	208	126	0.61	0.0206	0.0006	0.1388	0.0191	0.22	0.0489	0.0061	131.4	3.9	132.0	18.2	143.3	292.6	100
LYN-3/2-37	4	167	118	0.70	0.0205	0.0005	0.1397	0.0160	0.19	0.0495	0.0060	130.6	2.9	132.7	15.2	170.5	281.3	98
LYN-3/2-38	6	280	186	0.66	0.0207	0.0005	0.1377	0.0094	0.35	0.0483	0.0031	131.9	3.2	131.0	8.9	115.4	152.9	101
LYN-3/2-39	7	335	205	0.61	0.0210	0.0004	0.1336	0.0128	0.22	0.0462	0.0046	133.9	2.8	127.3	12.2	6.3	239.5	105

LY-40/1

LY-40/1-01	4	162	111	0.68	0.0216	0.0005	0.1445	0.0329	0.10	0.0486	0.0110	137.7	3.1	137.1	31.2	126.7	531.5	100
LY-40/1-03	2	74	67	0.91	0.0207	0.0007	0.1445	0.0591	0.08	0.0506	0.0218	132.2	4.2	137.0	56.1	221.1	995.8	96
LY-40/1-04	3	114	83	0.73	0.0205	0.0005	0.1376	0.0230	0.13	0.0487	0.0083	130.9	2.9	130.9	21.9	132.4	399.1	100
LY-40/1-05	3	125	91	0.73	0.0208	0.0005	0.1423	0.0385	0.09	0.0497	0.0138	132.4	3.1	135.1	36.6	182.2	645.8	98
LY-40/1-06	2	63	46	0.73	0.0201	0.0007	0.1463	0.0632	0.08	0.0528	0.0238	128.3	4.4	138.7	59.9	320.2	1024.8	93

LY-40/1-07	2	101	94	0.93	0.0207	0.0005	0.1539	0.0431	0.09	0.0539	0.0151	132.1	3.5	145.4	40.7	367.5	630.3	91
LY-40/1-08	3	146	139	0.95	0.0207	0.0005	0.1319	0.0258	0.11	0.0463	0.0091	131.8	2.9	125.8	24.6	13.1	474.6	105
LY-40/1-09	3	152	106	0.70	0.0207	0.0005	0.1373	0.0173	0.18	0.0482	0.0060	132.0	2.9	130.6	16.4	107.0	294.6	101
LY-40/1-10	4	175	167	0.96	0.0211	0.0005	0.1392	0.0156	0.20	0.0478	0.0053	134.7	3.0	132.3	14.8	89.5	262.0	102
LY-40/1-11	3	138	108	0.78	0.0212	0.0005	0.1415	0.0176	0.19	0.0485	0.0060	135.1	3.2	134.4	16.7	121.6	290.7	101
LY-40/1-12	4	154	141	0.92	0.0205	0.0004	0.1377	0.0177	0.16	0.0487	0.0063	130.9	2.8	131.0	16.9	133.0	303.5	100
LY-40/1-13	8	354	274	0.77	0.0211	0.0005	0.1417	0.0173	0.21	0.0487	0.0056	134.7	3.5	134.6	16.5	131.7	269.1	100
LY-40/1-14	1	56	42	0.76	0.0209	0.0006	0.1554	0.0581	0.08	0.0539	0.0213	133.5	3.9	146.6	54.8	365.0	893.3	91
LY-40/1-15	3	110	91	0.83	0.0209	0.0005	0.1431	0.0262	0.12	0.0497	0.0092	133.1	2.9	135.8	24.9	182.7	432.4	98
LY-40/1-16	3	124	101	0.82	0.0205	0.0005	0.1406	0.0221	0.14	0.0497	0.0077	131.0	2.9	133.6	21.0	179.6	360.4	98
LY-40/1-17	3	120	144	1.20	0.0213	0.0005	0.1408	0.0220	0.16	0.0480	0.0075	135.8	3.4	133.8	20.9	97.0	367.8	102
LY-40/1-18	2	75	58	0.78	0.0212	0.0005	0.1470	0.0362	0.10	0.0503	0.0126	135.1	3.5	139.3	34.3	210.8	580.9	97
LY-40/1-19	2	86	96	1.12	0.0198	0.0005	0.1364	0.0391	0.09	0.0498	0.0146	126.7	3.2	129.8	37.2	187.7	682.6	98
LY-40/1-20	2	88	71	0.81	0.0206	0.0005	0.1384	0.0311	0.11	0.0486	0.0111	131.8	3.4	131.6	29.5	128.9	539.3	100
LY-40/1-21	1	46	42	0.91	0.0205	0.0007	0.1520	0.0778	0.07	0.0538	0.0322	130.8	4.6	143.6	73.6	360.8	1352.0	91
LY-40/1-22	2	93	72	0.78	0.0208	0.0005	0.1432	0.0322	0.11	0.0498	0.0120	133.0	3.4	135.9	30.5	186.9	558.9	98
LY-40/1-23	3	111	96	0.86	0.0207	0.0005	0.1444	0.0298	0.12	0.0506	0.0110	132.1	3.4	137.0	28.3	222.4	501.9	96
LY-40/1-24	2	105	92	0.87	0.0204	0.0005	0.1441	0.0347	0.11	0.0512	0.0141	130.2	3.4	136.7	32.9	251.8	631.6	95
LY-40/1-26	2	100	67	0.68	0.0198	0.0005	0.1382	0.0295	0.11	0.0505	0.0112	126.7	3.1	131.5	28.1	218.8	513.1	96
LY-40/1-27	4	202	214	1.06	0.0201	0.0004	0.1368	0.0155	0.20	0.0493	0.0056	128.5	2.9	130.2	14.8	161.3	267.3	99
LY-40/1-28	1	54	63	1.17	0.0208	0.0006	0.1416	0.0550	0.07	0.0493	0.0200	132.9	3.6	134.5	52.2	161.6	947.7	99
LY-40/1-29	5	212	211	0.99	0.0206	0.0005	0.1358	0.0188	0.16	0.0478	0.0066	131.5	2.9	129.3	17.9	90.2	327.9	102
LY-40/1-30	4	181	182	1.01	0.0198	0.0004	0.1335	0.0239	0.12	0.0489	0.0089	126.3	2.8	127.2	22.8	144.7	427.8	99
LY-40/1-32	4	179	217	1.21	0.0209	0.0004	0.1372	0.0177	0.16	0.0475	0.0061	133.6	2.8	130.5	16.9	75.4	307.4	102
LY-40/1-33	3	130	113	0.86	0.0207	0.0005	0.1386	0.0208	0.16	0.0487	0.0072	131.8	3.2	131.8	19.7	132.8	349.9	100
LY-40/1-34	2	79	73	0.93	0.0207	0.0005	0.1405	0.0344	0.11	0.0492	0.0123	132.2	3.4	133.5	32.7	157.8	584.7	99

LY-40/1-35	2	96	73	0.76	0.0201	0.0006	0.1326	0.0362	0.10	0.0479	0.0136	128.3	3.6	126.5	34.5	92.7	674.7	101
LY-40/1-36	1	58	51	0.88	0.0203	0.0006	0.1452	0.0482	0.09	0.0518	0.0193	129.8	4.0	137.6	45.7	275.5	853.3	94
LY-40/1-37	5	192	236	1.23	0.0203	0.0004	0.1368	0.0129	0.23	0.0489	0.0047	129.4	2.8	130.2	12.3	143.8	223.1	99
LY-40/1-38	5	208	166	0.80	0.0206	0.0004	0.1426	0.0130	0.23	0.0502	0.0045	131.6	2.8	135.3	12.3	202.4	207.4	97
LY-40/1-39	3	154	119	0.77	0.0203	0.0005	0.1404	0.0176	0.18	0.0501	0.0063	129.6	2.9	133.4	16.7	201.6	291.0	97
LY-40/1-40	3	116	82	0.70	0.0200	0.0005	0.1431	0.0216	0.16	0.0520	0.0080	127.5	3.1	135.8	20.5	283.9	350.1	94

LY-39/1

LY-39/1-03	3	144	106	1.36	0.0194	0.0019	0.1557	0.0677	0.23	0.0567	0.0240	123.9	12.1	146.9	59.5	479.7	840.7	84
LY-39/1-06	5	210	203	1.03	0.0195	0.0006	0.1243	0.0254	0.16	0.0464	0.0098	124.5	4.0	119.0	22.9	20.5	474.0	105
LY-39/1-08	5	228	182	1.26	0.0195	0.0008	0.1245	0.0283	0.18	0.0493	0.0115	124.5	4.9	119.1	25.5	161.2	503.6	105
LY-39/1-09	5	165	190	0.87	0.0194	0.0010	0.1604	0.0523	0.16	0.0643	0.0209	123.6	6.4	151.1	45.7	750.0	696.2	82
LY-39/1-10	4	121	126	0.96	0.0201	0.0013	0.1342	0.0423	0.21	0.0505	0.0177	128.5	8.4	127.8	37.9	220.4	737.0	101
LY-39/1-11	8	449	235	1.91	0.0202	0.0007	0.1463	0.0224	0.22	0.0540	0.0087	128.8	4.4	138.6	19.9	368.6	366.6	93
LY-39/1-12	4	151	146	1.04	0.0198	0.0008	0.1657	0.0313	0.22	0.0629	0.0127	126.5	5.1	155.7	27.3	705.6	433.3	81
LY-39/1-13	4	160	144	1.11	0.0204	0.0008	0.1350	0.0266	0.20	0.0485	0.0102	130.0	5.1	128.6	23.8	120.5	459.2	101
LY-39/1-16	5	178	166	1.07	0.0205	0.0015	0.1347	0.0364	0.27	0.0499	0.0142	130.9	9.4	128.3	32.5	187.1	625.8	102
LY-39/1-17	3	162	114	1.42	0.0203	0.0010	0.1288	0.0383	0.17	0.0493	0.0149	129.3	6.4	123.0	34.4	161.2	644.4	105
LY-39/1-18	5	139	185	0.75	0.0205	0.0011	0.1505	0.0411	0.20	0.0566	0.0173	130.7	7.2	142.4	36.3	476.0	694.4	92
LY-39/1-20	5	161	182	0.88	0.0206	0.0008	0.1490	0.0268	0.22	0.0539	0.0097	131.2	5.0	141.0	23.7	364.9	416.6	93
LY-39/1-21	5	147	200	0.73	0.0193	0.0019	0.1731	0.0573	0.30	0.0662	0.0224	123.4	12.0	162.1	49.6	813.0	719.4	76
LY-39/1-22	6	246	236	1.04	0.0200	0.0008	0.1440	0.0323	0.18	0.0552	0.0149	127.7	5.0	136.6	28.6	420.4	607.3	93
LY-39/1-23	4	152	151	1.01	0.0192	0.0009	0.1628	0.0330	0.23	0.0647	0.0146	122.6	5.8	153.1	28.8	764.8	478.7	80
LY-39/1-24	5	193	202	0.96	0.0197	0.0007	0.1299	0.0245	0.18	0.0501	0.0103	125.9	4.3	124.0	22.1	211.2	444.4	102
LY-39/1-25	5	193	190	1.02	0.0203	0.0008	0.1471	0.0275	0.22	0.0543	0.0102	129.4	5.2	139.4	24.4	387.1	416.6	93
LY-39/1-26	6	351	210	1.67	0.0191	0.0013	0.1552	0.0405	0.26	0.0613	0.0173	121.7	8.1	146.5	35.6	650.0	605.5	83
LY-39/1-28	2	85	88	0.97	0.0203	0.0013	0.1267	0.0509	0.16	0.0505	0.0204	129.8	8.3	121.1	45.8	216.7	822.1	107

Table 5-2 LA-MC-ICPMS zircon U-Pb data of the Laiyuan granitoids analyzed in this study.

Identifier	Elements Concentrations				Isotopic ratios ($\pm 2\sigma$)							Age (Ma) ($\pm 2\sigma$)						Concordance
	Pb*	²³⁸ U	²³² Th	Th/U	²⁰⁶ Pb/ ²³⁸ U	2 σ	²⁰⁷ Pb/ ²³⁵ U	2 σ	Rho	²⁰⁷ Pb/ ²⁰⁶ Pb	2 σ	²⁰⁶ Pb/ ²³⁸ U	2 σ	²⁰⁷ Pb/ ²³⁵ U	2 σ	²⁰⁷ Pb/ ²⁰⁶ Pb	2 σ	
	ppm	ppm	ppm		abs			abs			abs		abs		abs		%	
LY-21/1																		
LY-21/1-01	13	168	222	1.32	0.0199	0.0004	0.1351	0.0064	0.38	0.0490	0.0011	127.1	2.2	128.9	2.8	193.0	26.0	99
LY-21/1-02	22	533	397	0.75	0.0199	0.0003	0.1340	0.0036	0.51	0.0494	0.0006	126.9	1.7	127.7	1.6	175.0	18.0	99
LY-21/1-03	7	185	131	0.72	0.0199	0.0004	0.1328	0.0064	0.13	0.0485	0.0012	126.7	2.4	126.6	2.9	175.0	29.0	100
LY-21/1-04	21	526	385	0.74	0.0201	0.0005	0.1358	0.0050	0.77	0.0495	0.0007	128.3	3.2	129.2	2.2	163.0	15.0	99
LY-21/1-05	15	336	257	0.79	0.0204	0.0003	0.1369	0.0044	0.33	0.0488	0.0008	130.2	1.9	130.2	2.0	162.0	15.0	100
LY-21/1-06	13	229	245	1.08	0.0198	0.0003	0.1348	0.0054	0.13	0.0496	0.0011	126.3	2.2	128.3	2.4	184.0	20.0	98
LY-21/1-07	16	296	280	0.94	0.0203	0.0003	0.1365	0.0048	0.50	0.0488	0.0008	129.6	2.2	130.1	2.1	170.0	18.0	100
LY-21/1-08	24	381	400	1.05	0.0209	0.0004	0.1408	0.0048	0.49	0.0492	0.0007	133.1	2.6	133.9	2.1	170.0	17.0	99
LY-21/1-09	17	470	297	0.62	0.0205	0.0006	0.1403	0.0050	0.74	0.0500	0.0006	131.0	3.4	133.3	2.2	200.0	17.0	98
LY-21/1-10	7	184	125	0.68	0.0203	0.0004	0.1362	0.0056	0.33	0.0484	0.0010	129.5	2.2	129.6	2.5	192.0	24.0	100
LY-21/1-11	19	290	353	1.21	0.0202	0.0003	0.1357	0.0046	0.30	0.0489	0.0008	129.1	1.6	129.4	2.1	166.0	24.0	100
LY-21/1-12	6	154	108	0.66	0.0204	0.0005	0.1379	0.0060	0.42	0.0496	0.0011	129.8	3.0	131.1	2.7	206.0	25.0	99
LY-21/1-13	8	185	144	0.78	0.0202	0.0006	0.1368	0.0078	0.35	0.0491	0.0013	128.7	3.6	130.1	3.5	195.0	28.0	99
LY-21/1-14	9	182	168	0.95	0.0202	0.0004	0.1356	0.0062	0.43	0.0491	0.0009	128.7	2.4	129.3	2.8	181.0	21.0	100
LY-21/1-15	8	140	150	1.06	0.0201	0.0004	0.1358	0.0062	0.21	0.0492	0.0011	128.2	2.2	129.5	2.7	211.0	28.0	99
LY-21/1-16	13	446	245	0.55	0.0198	0.0004	0.1330	0.0038	0.61	0.0485	0.0006	126.3	2.2	126.8	1.7	145.0	17.0	100
LY-21/1-17	9	223	164	0.73	0.0201	0.0003	0.1347	0.0050	0.32	0.0488	0.0008	128.0	2.2	128.2	2.2	178.0	18.0	100
LY-21/1-18	30	308	557	1.72	0.0197	0.0004	0.1331	0.0050	0.40	0.0492	0.0008	125.6	2.2	126.9	2.2	172.0	19.0	99
LY-21/1-19	7	168	129	0.72	0.0200	0.0004	0.1356	0.0054	0.32	0.0487	0.0010	127.7	2.4	129.3	2.4	181.0	21.0	99

LY-21/1-20	17	297	301	1.02	0.0199	0.0003	0.1332	0.0046	0.37	0.0488	0.0008	127.1	2.2	127.4	2.1	164.0	17.0	100
LY-21/1-21	23	480	426	0.76	0.0198	0.0004	0.1332	0.0036	0.60	0.0489	0.0006	126.3	2.6	126.9	1.6	157.0	13.0	100
LY-21/1-22	5	119	89	0.72	0.0198	0.0004	0.1306	0.0064	0.28	0.0478	0.0012	126.0	2.4	124.6	2.9	166.0	23.0	101
LY-21/1-23	4	84	65	0.79	0.0199	0.0005	0.1362	0.0094	0.21	0.0497	0.0017	126.9	3.0	129.4	4.2	253.0	30.0	98
LY-21/1-24	46	909	803	0.90	0.0199	0.0003	0.1344	0.0030	0.53	0.0487	0.0004	127.2	2.0	128.2	1.4	133.0	12.0	99
LY-21/1-25	8	225	136	0.63	0.0197	0.0003	0.1332	0.0042	0.26	0.0488	0.0008	126.0	1.7	126.9	1.8	171.0	17.0	99
LY-21/1-26	53	930	980	1.07	0.0199	0.0006	0.1336	0.0050	0.84	0.0485	0.0005	126.9	3.6	127.3	2.2	118.0	15.0	100
LY-21/1-27	9	100	158	1.62	0.0198	0.0004	0.1317	0.0076	0.32	0.0486	0.0014	126.6	2.6	125.8	3.4	208.0	23.0	101
LY-21/1-28	13	251	219	0.89	0.0202	0.0003	0.1345	0.0042	0.43	0.0481	0.0007	128.8	1.7	128.0	1.9	128.0	16.0	101
LY-21/1-29	17	247	260	1.03	0.0220	0.0004	0.1475	0.0066	0.54	0.0486	0.0010	140.4	2.4	140.0	3.0	170.0	25.0	100
LY-21/1-30	16	288	286	1.01	0.0201	0.0003	0.1355	0.0042	0.31	0.0491	0.0007	128.3	1.8	129.2	1.8	174.0	19.0	99

LY-33/1

LY-33/1-01	70	533	1225	2.24	0.0209	0.0004	0.1406	0.0034	0.55	0.0487	0.0005	133.1	2.2	133.7	1.5	138.0	13.0	100
LY-33/1-02	31	400	539	1.36	0.0210	0.0003	0.1413	0.0038	0.52	0.0485	0.0006	133.9	1.9	134.2	1.7	147.0	14.0	100
LY-33/1-03	141	747	2420	3.13	0.0210	0.0003	0.1433	0.0034	0.58	0.0492	0.0005	134.1	1.8	136.2	1.5	156.0	13.0	98
LY-33/1-04	37	187	646	3.42	0.0207	0.0004	0.1381	0.0056	0.42	0.0479	0.0009	131.8	2.6	131.6	2.5	150.0	21.0	100
LY-33/1-05	32	464	586	1.25	0.0205	0.0003	0.1383	0.0048	0.54	0.0487	0.0006	130.8	2.0	131.7	2.1	144.0	15.0	99
LY-33/1-06	22	238	381	1.55	0.0210	0.0004	0.1399	0.0060	0.45	0.0483	0.0009	133.9	2.8	132.9	2.7	151.0	22.0	101
LY-33/1-07	69	615	1214	1.93	0.0210	0.0003	0.1424	0.0042	0.54	0.0490	0.0006	133.8	1.9	135.1	1.9	149.0	12.0	99
LY-33/1-08	123	663	2160	3.23	0.0209	0.0003	0.1473	0.0036	0.61	0.0507	0.0005	133.4	1.7	139.5	1.6	222.0	12.0	96
LY-33/1-09	30	234	515	2.17	0.0206	0.0004	0.1376	0.0054	0.25	0.0482	0.0010	131.6	2.6	130.8	2.4	168.0	20.0	101
LY-33/1-10	24	267	409	1.54	0.0209	0.0005	0.1400	0.0058	0.45	0.0480	0.0009	133.3	3.2	133.0	2.6	143.0	19.0	100
LY-33/1-11	22	300	383	1.28	0.0207	0.0003	0.1393	0.0044	0.55	0.0489	0.0008	132.2	2.0	132.4	2.0	164.0	18.0	100
LY-33/1-12	41	508	717	1.40	0.0209	0.0003	0.1408	0.0036	0.53	0.0486	0.0005	133.5	1.8	133.7	1.6	141.0	12.0	100
LY-33/1-13	27	329	470	1.43	0.0210	0.0004	0.1416	0.0048	0.35	0.0486	0.0008	134.1	2.2	134.4	2.1	150.0	19.0	100
LY-33/1-14	8	147	143	0.98	0.0206	0.0003	0.1387	0.0060	0.40	0.0486	0.0010	131.4	1.9	131.8	2.6	164.0	23.0	100

LY-33/1-15	13	76	218	2.85	0.0208	0.0004	0.1398	0.0096	0.08	0.0487	0.0017	132.4	2.8	132.6	4.3	242.0	38.0	100
LY-33/1-16	36	458	616	1.34	0.0205	0.0003	0.1387	0.0038	0.63	0.0492	0.0005	130.8	2.0	131.8	1.7	165.0	13.0	99
LY-33/1-17	79	684	1426	2.07	0.0205	0.0003	0.1369	0.0034	0.46	0.0485	0.0005	130.6	2.0	130.3	1.5	127.0	12.0	100
LY-33/1-18	35	417	607	1.44	0.0209	0.0003	0.1407	0.0040	0.51	0.0490	0.0006	133.5	1.8	133.6	1.7	154.0	15.0	100
LY-33/1-19	19	252	326	1.29	0.0210	0.0005	0.1389	0.0062	0.29	0.0479	0.0010	134.2	2.8	132.0	2.7	126.0	18.0	102
LY-33/1-20	44	605	770	1.27	0.0209	0.0004	0.1415	0.0042	0.67	0.0493	0.0006	133.6	2.4	134.4	1.8	153.0	15.0	99
LY-33/1-21	30	389	541	1.38	0.0210	0.0003	0.1415	0.0044	0.44	0.0486	0.0006	133.8	2.2	134.3	2.0	131.0	15.0	100
LY-33/1-22	40	460	710	1.53	0.0206	0.0003	0.1384	0.0038	0.40	0.0489	0.0006	131.7	1.9	131.6	1.7	142.0	16.0	100
LY-33/1-23	56	659	1013	1.53	0.0206	0.0003	0.1380	0.0042	0.47	0.0487	0.0006	131.6	1.9	131.3	1.8	144.0	16.0	100
LY-33/1-24	97	691	1701	2.43	0.0211	0.0003	0.1411	0.0038	0.58	0.0488	0.0006	134.4	2.2	134.0	1.7	145.0	15.0	100
LY-33/1-25	19	340	323	0.93	0.0210	0.0002	0.1401	0.0040	0.29	0.0486	0.0007	133.8	1.5	133.1	1.8	154.0	20.0	101
LY-33/1-26	19	305	331	1.07	0.0212	0.0004	0.1413	0.0046	0.42	0.0486	0.0008	135.3	2.4	134.2	2.0	144.0	19.0	101
LY-33/1-27	62	584	1073	1.75	0.0210	0.0003	0.1405	0.0040	0.57	0.0490	0.0006	133.8	1.8	133.6	1.7	150.0	14.0	100
LY-33/1-28	12	211	203	0.97	0.0210	0.0003	0.1423	0.0050	0.23	0.0493	0.0009	133.8	1.8	135.0	2.3	185.0	22.0	99
LY-33/1-29	125	706	2112	2.92	0.0210	0.0002	0.1406	0.0026	0.45	0.0489	0.0004	134.0	1.3	133.5	1.2	137.0	12.0	100
LY-33/1-30	32	393	561	1.38	0.0208	0.0002	0.1412	0.0048	0.38	0.0498	0.0008	132.4	1.4	134.0	2.2	188.0	24.0	99
LY-36/1																		
LY-36/1-01	41	532	707	1.33	0.0210	0.0002	0.1416	0.0032	0.35	0.0490	0.0005	133.9	1.4	134.4	1.4	154.0	14.0	100
LY-36/1-02	23	288	410	1.30	0.0205	0.0003	0.1361	0.0048	0.31	0.0481	0.0008	130.8	1.8	130.0	2.1	154.0	19.0	101
LY-36/1-03	13	220	220	0.99	0.0208	0.0003	0.1443	0.0056	0.35	0.0506	0.0009	132.5	1.7	136.8	2.5	225.0	22.0	97
LY-36/1-04	20	364	352	0.96	0.0203	0.0003	0.1370	0.0048	0.38	0.0488	0.0008	129.3	1.8	130.3	2.2	167.0	24.0	99
LY-36/1-05	11	204	201	0.98	0.0200	0.0003	0.1354	0.0058	0.26	0.0488	0.0010	127.4	1.9	128.9	2.6	170.0	28.0	99
LY-36/1-06	27	376	497	1.30	0.0205	0.0003	0.1376	0.0048	0.36	0.0484	0.0007	130.9	1.9	130.9	2.1	156.0	16.0	100
LY-36/1-07	22	436	410	0.93	0.0199	0.0003	0.1324	0.0046	0.41	0.0479	0.0008	127.0	1.8	126.3	2.1	131.0	18.0	101
LY-36/1-08	11	228	214	0.94	0.0197	0.0003	0.1335	0.0070	0.29	0.0488	0.0012	125.9	2.0	127.1	3.1	218.0	28.0	99
LY-36/1-09	23	407	441	1.07	0.0198	0.0004	0.1320	0.0044	0.51	0.0484	0.0007	126.4	2.4	125.9	2.0	132.0	15.0	100

LY-36/1-10	11	238	203	0.86	0.0206	0.0002	0.1391	0.0044	0.32	0.0490	0.0007	131.6	1.5	132.2	2.0	162.0	20.0	100
LY-36/1-11	17	252	306	1.19	0.0208	0.0002	0.1411	0.0046	0.26	0.0490	0.0008	132.7	1.5	134.2	2.1	177.0	16.0	99
LY-36/1-12	14	217	261	1.20	0.0208	0.0003	0.1380	0.0050	0.37	0.0484	0.0008	132.4	1.9	131.1	2.2	142.0	16.0	101
LY-36/1-13	22	343	405	1.14	0.0201	0.0003	0.1327	0.0034	0.16	0.0481	0.0006	128.1	1.7	126.5	1.6	120.0	15.0	101
LY-36/1-14	43	517	810	1.51	0.0202	0.0003	0.1350	0.0040	0.51	0.0489	0.0007	128.8	2.2	128.6	1.8	138.0	16.0	100
LY-36/1-15	18	165	338	1.97	0.0196	0.0003	0.1312	0.0062	0.49	0.0486	0.0011	125.3	1.8	125.1	2.7	186.0	24.0	100
LY-36/1-16	22	355	392	1.09	0.0207	0.0003	0.1394	0.0042	0.37	0.0488	0.0007	132.2	1.8	132.4	1.9	156.0	16.0	100
LY-36/1-17	64	704	1154	1.64	0.0203	0.0002	0.1358	0.0028	0.40	0.0485	0.0005	129.5	1.1	129.3	1.3	130.0	12.0	100
LY-36/1-18	127	886	2308	2.57	0.0203	0.0003	0.1349	0.0030	0.64	0.0486	0.0004	129.2	1.9	128.5	1.3	125.0	10.0	101
LY-36/1-19	12	259	221	0.85	0.0201	0.0002	0.1354	0.0050	0.23	0.0490	0.0009	128.3	1.5	128.9	2.2	195.0	21.0	100
LY-36/1-20	23	454	430	0.94	0.0198	0.0002	0.1341	0.0034	0.41	0.0490	0.0006	126.6	1.3	127.7	1.6	158.0	13.0	99
LY-36/1-21	22	305	374	1.22	0.0209	0.0003	0.1445	0.0040	0.36	0.0502	0.0007	133.2	1.7	137.2	1.8	216.0	20.0	97
LY-36/1-22	11	204	195	0.95	0.0207	0.0003	0.1413	0.0054	0.23	0.0496	0.0010	132.1	1.8	134.1	2.4	217.0	24.0	99
LY-36/1-23	15	279	271	0.92	0.0208	0.0003	0.1399	0.0050	0.41	0.0490	0.0008	132.8	2.0	133.1	2.2	178.0	18.0	100
LY-36/1-24	12	209	226	1.07	0.0203	0.0003	0.1358	0.0050	0.21	0.0487	0.0009	129.5	1.9	129.2	2.2	185.0	21.0	100
LY-36/1-25	41	570	741	1.29	0.0204	0.0002	0.1383	0.0028	0.28	0.0492	0.0005	130.5	1.3	131.5	1.3	152.0	14.0	99
LY-36/1-26	15	279	271	0.96	0.0200	0.0003	0.1343	0.0042	0.29	0.0487	0.0007	127.6	1.7	127.9	1.8	170.0	20.0	100
LY-36/1-27	35	479	634	1.26	0.0198	0.0003	0.1336	0.0038	0.48	0.0491	0.0006	126.6	1.8	127.5	1.7	178.0	15.0	99
LY-36/1-28	14	186	251	1.10	0.0206	0.0006	0.1404	0.0066	0.47	0.0494	0.0011	131.7	3.6	133.3	2.9	198.0	25.0	99
LY-36/1-29	21	285	383	1.31	0.0208	0.0003	0.1383	0.0042	0.25	0.0482	0.0008	132.8	1.9	131.5	1.9	137.0	18.0	101
LY-36/1-30	8	102	143	1.38	0.0216	0.0004	0.1471	0.0076	0.30	0.0497	0.0012	137.5	2.4	139.2	3.4	204.0	24.0	99

LY-42/1

LY-42/1-02	25	316	415	1.31	0.0217	0.0004	0.1456	0.0044	0.38	0.0489	0.0007	138.2	2.4	138.2	1.9	155.0	16.0	100
LY-42/1-03	48	571	819	1.44	0.0220	0.0003	0.1479	0.0042	0.56	0.0487	0.0006	140.0	2.2	140.0	1.8	136.0	14.0	100
LY-42/1-04	35	460	598	1.31	0.0214	0.0003	0.1505	0.0048	0.35	0.0511	0.0008	136.3	1.7	142.3	2.1	232.0	25.0	96
LY-42/1-05	80	813	1345	1.69	0.0218	0.0004	0.1456	0.0034	0.73	0.0489	0.0004	138.8	2.4	138.0	1.5	151.0	12.0	101

LY-42/1-06	79	555	1340	2.44	0.0215	0.0002	0.1445	0.0034	0.38	0.0491	0.0005	136.9	1.3	137.0	1.5	157.0	13.0	100
LY-42/1-07	20	356	358	0.80	0.0217	0.0006	0.1468	0.0074	0.62	0.0494	0.0009	138.6	3.6	139.3	3.3	193.0	17.0	99
LY-42/1-08	17	228	293	1.28	0.0208	0.0003	0.1394	0.0058	0.21	0.0487	0.0010	132.5	2.0	132.4	2.6	182.0	25.0	100
LY-42/1-09	22	287	364	1.28	0.0213	0.0003	0.1445	0.0044	0.22	0.0496	0.0007	135.6	1.6	137.2	2.0	174.0	17.0	99
LY-42/1-10	32	422	542	1.30	0.0215	0.0003	0.1437	0.0036	0.55	0.0487	0.0006	136.9	1.9	136.3	1.6	133.0	14.0	100
LY-42/1-11	30	666	504	0.76	0.0216	0.0002	0.1449	0.0030	0.49	0.0486	0.0004	137.9	1.5	137.4	1.4	133.0	11.0	100
LY-42/1-12	5	129	90	0.70	0.0215	0.0003	0.1464	0.0066	0.35	0.0495	0.0010	137.0	2.2	138.6	2.9	196.0	26.0	99
LY-42/1-13	4	109	73	0.67	0.0219	0.0005	0.1503	0.0080	0.62	0.0498	0.0013	139.7	3.2	142.0	3.5	212.0	30.0	98
LY-42/1-14	11	180	187	1.01	0.0214	0.0004	0.1459	0.0062	0.45	0.0493	0.0009	136.5	2.4	138.2	2.7	187.0	22.0	99
LY-42/1-15	26	336	457	1.37	0.0217	0.0004	0.1449	0.0056	0.21	0.0487	0.0010	138.5	2.4	137.3	2.5	157.0	17.0	101
LY-42/1-16	54	715	928	1.31	0.0201	0.0004	0.1390	0.0060	0.47	0.0503	0.0009	128.1	2.4	132.1	2.6	206.0	32.0	97
LY-42/1-17	6	123	103	0.84	0.0205	0.0005	0.1415	0.0098	0.23	0.0498	0.0017	130.5	3.4	135.1	4.6	232.0	43.0	97
LY-42/1-18	43	674	764	1.15	0.0204	0.0003	0.1370	0.0034	0.51	0.0487	0.0005	130.1	1.7	130.3	1.5	131.0	13.0	100
LY-42/1-19	7	157	119	0.76	0.0203	0.0005	0.1381	0.0070	0.39	0.0500	0.0012	129.3	3.0	131.3	3.1	203.0	29.0	98
LY-42/1-20	33	404	561	1.40	0.0209	0.0002	0.1411	0.0032	0.26	0.0489	0.0005	133.6	1.4	134.0	1.4	143.0	14.0	100
LY-42/1-21	5	126	90	0.67	0.0205	0.0004	0.1401	0.0060	0.35	0.0491	0.0009	130.9	2.4	133.1	2.7	189.0	21.0	98
LY-42/1-22	11	158	186	1.14	0.0208	0.0003	0.1386	0.0054	0.21	0.0482	0.0010	132.6	2.0	131.7	2.4	164.0	21.0	101
LY-42/1-23	8	150	138	0.83	0.0207	0.0004	0.1410	0.0076	0.36	0.0492	0.0013	132.1	2.4	133.8	3.3	220.0	25.0	99
LY-42/1-24	109	1083	1945	1.78	0.0206	0.0002	0.1392	0.0026	0.47	0.0490	0.0004	131.5	1.4	132.3	1.2	144.0	10.0	99
LY-42/1-25	34	408	569	1.39	0.0214	0.0003	0.1433	0.0040	0.45	0.0483	0.0006	136.3	1.8	136.0	1.8	142.0	16.0	100
LY-42/1-26	56	566	886	1.56	0.0220	0.0003	0.1472	0.0038	0.49	0.0482	0.0006	140.2	1.6	139.4	1.7	109.0	13.0	101
LY-42/1-28	12	235	219	0.91	0.0208	0.0003	0.1389	0.0054	0.36	0.0488	0.0009	132.5	1.9	132.0	2.4	170.0	18.0	100
LY-42/1-29	42	483	734	1.52	0.0212	0.0003	0.1489	0.0048	0.31	0.0509	0.0008	135.4	1.9	140.9	2.1	238.0	19.0	96
LY-42/1-30	28	415	466	1.12	0.0213	0.0003	0.1439	0.0034	0.43	0.0485	0.0005	135.9	1.6	136.5	1.5	136.0	14.0	100
LY-42/1-31	23	514	378	0.74	0.0213	0.0002	0.1437	0.0034	0.44	0.0486	0.0005	135.8	1.5	136.3	1.5	135.0	12.0	100
LY-42/1-32	23	276	377	1.24	0.0209	0.0002	0.1392	0.0048	0.17	0.0483	0.0008	133.5	1.5	132.5	2.1	162.0	17.0	101

LY-42/1-33	34	581	561	0.95	0.0206	0.0002	0.1391	0.0034	0.61	0.0486	0.0005	131.7	1.5	132.2	1.6	142.0	12.0	100
LY-42/1-34	36	470	588	1.24	0.0215	0.0003	0.1438	0.0036	0.44	0.0486	0.0006	137.0	1.6	136.4	1.6	139.0	12.0	100
LY-42/1-35	19	340	301	0.89	0.0217	0.0004	0.1460	0.0038	0.47	0.0486	0.0006	138.1	2.4	138.3	1.7	146.0	14.0	100
LY-42/1-36	5	109	73	0.67	0.0215	0.0004	0.1463	0.0078	0.25	0.0495	0.0013	136.9	2.2	138.5	3.4	180.0	23.0	99
LY-42/1-37	3	71	39	0.53	0.0219	0.0005	0.1502	0.0090	0.26	0.0496	0.0014	139.6	3.4	142.3	4.0	250.0	29.0	98

LYN-1/3

LYN-1/3-01	3	117	72	0.61	0.0199	0.0005	0.1473	0.0271	0.13	0.0537	0.0101	127.0	3.0	139.5	25.7	358.4	423.1	91
LYN-1/3-02	3	135	76	0.56	0.0199	0.0004	0.1484	0.0254	0.13	0.0540	0.0094	127.1	2.8	140.5	24.1	372.9	390.3	90
LYN-1/3-03	5	199	176	0.88	0.0200	0.0004	0.1304	0.0183	0.15	0.0473	0.0068	127.5	2.6	124.5	17.5	66.0	339.7	102
LYN-1/3-04	4	181	117	0.65	0.0198	0.0004	0.1411	0.0182	0.16	0.0517	0.0064	126.4	2.7	134.0	17.3	271.5	282.1	94
LYN-1/3-05	4	168	134	0.80	0.0209	0.0005	0.1437	0.0345	0.10	0.0499	0.0119	133.2	3.1	136.4	32.8	191.5	554.4	98
LYN-1/3-06	4	169	113	0.67	0.0204	0.0004	0.1531	0.0156	0.20	0.0544	0.0054	130.2	2.7	144.7	14.8	389.7	222.4	90
LYN-1/3-07	5	215	150	0.70	0.0195	0.0004	0.1457	0.0117	0.26	0.0542	0.0043	124.6	2.6	138.1	11.1	377.7	179.7	90
LYN-1/3-08	2	107	79	0.74	0.0194	0.0005	0.1509	0.0221	0.16	0.0564	0.0083	123.9	2.9	142.7	20.9	469.0	324.7	87
LYN-1/3-09	2	85	52	0.61	0.0194	0.0005	0.1325	0.0315	0.11	0.0494	0.0117	124.1	3.2	126.3	30.0	168.7	554.9	98
LYN-1/3-10	3	125	79	0.63	0.0200	0.0005	0.1316	0.0228	0.13	0.0477	0.0085	127.7	2.9	125.5	21.7	85.0	423.6	102
LYN-1/3-11	3	142	84	0.59	0.0201	0.0005	0.1366	0.0212	0.15	0.0494	0.0079	128.0	2.9	130.0	20.2	166.0	374.5	98
LYN-1/3-12	4	194	185	0.95	0.0200	0.0004	0.1468	0.0186	0.17	0.0532	0.0069	127.7	2.7	139.1	17.6	337.9	292.3	92
LYN-1/3-13	6	290	199	0.69	0.0202	0.0004	0.1410	0.0107	0.28	0.0507	0.0039	128.8	2.8	133.9	10.2	226.2	178.0	96
LYN-1/3-14	2	101	85	0.84	0.0206	0.0005	0.1406	0.0267	0.13	0.0496	0.0094	131.1	3.2	133.6	25.4	177.8	441.8	98
LYN-1/3-15	2	79	88	1.12	0.0196	0.0006	0.1413	0.0480	0.08	0.0523	0.0173	125.2	3.5	134.2	45.6	297.0	756.5	93
LYN-1/3-16	2	95	54	0.57	0.0194	0.0005	0.1407	0.0381	0.10	0.0526	0.0145	123.8	3.2	133.6	36.2	311.6	629.2	93
LYN-1/3-17	3	125	77	0.61	0.0196	0.0004	0.1351	0.0223	0.14	0.0501	0.0083	124.9	2.8	128.7	21.2	199.6	383.4	97
LYN-1/3-18	3	154	98	0.64	0.0204	0.0005	0.1330	0.0267	0.11	0.0474	0.0094	130.0	2.9	126.8	25.4	68.2	470.7	102
LYN-1/3-19	2	74	38	0.51	0.0202	0.0005	0.1493	0.0423	0.09	0.0536	0.0165	128.9	3.3	141.3	40.1	355.4	695.9	91
LYN-1/3-20	2	100	88	0.88	0.0202	0.0005	0.1369	0.0264	0.12	0.0491	0.0095	129.0	3.0	130.3	25.1	154.9	454.7	99

LYN-1/3-21	3	126	79	0.63	0.0200	0.0005	0.1341	0.0203	0.16	0.0487	0.0072	127.6	3.1	127.8	19.3	131.6	347.3	100
LYN-1/3-22	3	131	78	0.60	0.0203	0.0005	0.1397	0.0210	0.15	0.0498	0.0075	129.8	2.9	132.8	20.0	186.4	348.8	98
LYN-1/3-23	3	139	102	0.73	0.0203	0.0005	0.1390	0.0193	0.16	0.0497	0.0070	129.5	2.9	132.1	18.3	179.1	326.6	98
LYN-1/3-24	2	88	45	0.51	0.0201	0.0005	0.1410	0.0281	0.12	0.0508	0.0104	128.4	3.0	134.0	26.7	233.6	470.9	96
LYN-1/3-25	3	157	126	0.81	0.0202	0.0004	0.1365	0.0159	0.19	0.0490	0.0056	128.9	2.8	130.0	15.1	148.8	269.2	99
LYN-1/3-26	3	131	129	0.98	0.0201	0.0005	0.1422	0.0201	0.16	0.0514	0.0074	128.1	2.9	135.0	19.1	258.6	329.8	95
LYN-1/3-27	3	155	96	0.62	0.0202	0.0004	0.1408	0.0157	0.20	0.0505	0.0056	129.1	2.8	133.7	15.0	217.2	257.6	97
LYN-1/3-28	4	187	111	0.59	0.0207	0.0005	0.1471	0.0378	0.09	0.0517	0.0127	131.8	3.1	139.4	35.8	270.3	564.5	95
LYN-1/3-29	4	185	127	0.68	0.0203	0.0004	0.1354	0.0139	0.20	0.0484	0.0049	129.5	2.7	128.9	13.2	118.0	236.7	100
LYN-1/3-30	3	141	78	0.55	0.0204	0.0004	0.1364	0.0171	0.17	0.0484	0.0060	130.4	2.9	129.9	16.3	119.6	294.3	100
LYN-1/3-31	5	209	130	0.62	0.0203	0.0004	0.1456	0.0128	0.25	0.0521	0.0045	129.3	2.8	138.0	12.1	291.5	197.5	94
LYN-1/3-32	3	164	89	0.55	0.0203	0.0005	0.1357	0.0180	0.18	0.0485	0.0064	129.5	3.2	129.2	17.2	124.3	311.3	100
LYN-1/3-33	3	128	70	0.55	0.0200	0.0005	0.1371	0.0227	0.14	0.0497	0.0081	127.8	3.0	130.4	21.6	179.0	380.3	98
LYN-1/3-34	4	200	133	0.67	0.0201	0.0004	0.1460	0.0128	0.25	0.0528	0.0045	128.1	2.8	138.4	12.1	318.9	195.0	93
LYN-1/3-35	5	207	170	0.82	0.0203	0.0004	0.1461	0.0131	0.24	0.0522	0.0047	129.5	2.8	138.5	12.4	294.2	206.4	94
LYN-1/3-36	3	159	83	0.52	0.0199	0.0005	0.1396	0.0178	0.18	0.0508	0.0064	127.1	3.0	132.6	16.9	233.5	292.0	96

Table 5-3 LA-MC-ICPMS zircon U-Pb data of the Laiyuan dyke suites analyzed in this study.

Identifier	Elements Concentrations				Isotopic ratios ($\pm 2\sigma$)							Age (Ma) ($\pm 2\sigma$)						Concordance
	Pb*	²³⁸ U	²³² Th	Th/U	²⁰⁶ Pb/ ²³⁸ U	2 σ	²⁰⁷ Pb/ ²³⁵ U	2 σ	Rho	²⁰⁷ Pb/ ²⁰⁶ Pb	2 σ	²⁰⁶ Pb/ ²³⁸ U	2 σ	²⁰⁷ Pb/ ²³⁵ U	2 σ	²⁰⁷ Pb/ ²⁰⁶ Pb	2 σ	
	ppm	ppm	ppm		abs			abs			abs			abs			%	
LY-8/1																		
LY-8/1-02	4	205	195	0.95	0.0175	0.0004	0.1204	0.0151	0.17	0.0498	0.0062	112.0	2.0	115.0	14.0	186.0	290.0	97
LY-8/1-03	11	454	774	1.71	0.0175	0.0004	0.1236	0.0069	0.36	0.0513	0.0028	112.0	2.0	118.0	7.0	254.0	124.0	94
LY-8/1-04	3	161	153	0.95	0.0187	0.0004	0.1258	0.0189	0.14	0.0488	0.0074	119.0	3.0	120.0	18.0	137.0	356.0	99
LY-8/1-05	4	196	174	0.89	0.0191	0.0004	0.1260	0.0183	0.15	0.0479	0.0068	122.0	3.0	120.0	18.0	96.0	336.0	101
LY-8/1-07	4	206	166	0.81	0.0184	0.0004	0.1200	0.0280	0.10	0.0473	0.0110	118.0	3.0	115.0	27.0	63.0	553.0	102
LY-8/1-08	5	240	211	0.88	0.0184	0.0005	0.1280	0.0210	0.15	0.0504	0.0083	118.0	3.0	122.0	20.0	212.0	380.0	96
LY-8/1-09	3	123	111	0.90	0.0181	0.0005	0.1293	0.0338	0.11	0.0517	0.0136	116.0	3.0	123.0	32.0	274.0	602.0	94
LY-8/1-10	4	192	137	0.72	0.0176	0.0004	0.1172	0.0246	0.11	0.0484	0.0101	112.0	3.0	113.0	24.0	117.0	494.0	100
LY-8/1-12	8	342	631	1.84	0.0181	0.0004	0.1236	0.0096	0.28	0.0495	0.0040	116.0	2.0	118.0	9.0	174.0	186.0	98
LY-8/1-13	4	157	199	1.27	0.0185	0.0004	0.1288	0.0281	0.10	0.0505	0.0108	118.0	3.0	123.0	27.0	217.0	495.0	96
LY-8/1-14	2	105	167	1.59	0.0181	0.0004	0.1209	0.0269	0.11	0.0484	0.0110	116.0	3.0	116.0	26.0	116.0	539.0	100
LY-8/1-15	14	724	569	0.79	0.0185	0.0004	0.1184	0.0103	0.24	0.0464	0.0042	118.0	2.0	114.0	10.0	19.0	215.0	104
LY-8/1-17	7	393	36	0.09	0.0181	0.0004	0.1225	0.0089	0.29	0.0491	0.0035	116.0	2.0	117.0	9.0	154.0	165.0	98
LY-8/1-19	7	307	422	1.37	0.0176	0.0004	0.1229	0.0100	0.26	0.0506	0.0040	113.0	2.0	118.0	10.0	223.0	182.0	96
LY-8/1-20	3	163	227	1.39	0.0177	0.0004	0.1172	0.0162	0.16	0.0481	0.0066	113.0	2.0	113.0	16.0	103.0	324.0	100
LY-8/1-21	3	136	158	1.16	0.0183	0.0004	0.1256	0.0236	0.13	0.0497	0.0119	117.0	3.0	120.0	23.0	182.0	560.0	97
LY-8/1-23	10	568	139	0.24	0.0180	0.0004	0.1244	0.0070	0.39	0.0500	0.0028	115.0	3.0	119.0	7.0	197.0	128.0	97
LY-8/1-24	14	864	180	0.21	0.0174	0.0004	0.1208	0.0043	0.57	0.0503	0.0017	111.0	2.0	116.0	4.0	207.0	77.0	96
LY-8/1-25	7	314	435	1.39	0.0182	0.0004	0.1221	0.0104	0.24	0.0486	0.0040	116.0	2.0	117.0	10.0	131.0	195.0	99

LY-8/1-28	5	220	234	1.06	0.0176	0.0004	0.1182	0.0140	0.18	0.0487	0.0056	113.0	2.0	113.0	13.0	133.0	269.0	99	
LY-16/1																			
LY-16/1-01	1	43	55	1.28	0.0180	0.0006	0.1226	0.0491	0.0836	0.0494	0.0210	115.0	4.0	117.0	47.0	165.0	993.0	98	
LY-16/1-02	1	54	47	0.87	0.0176	0.0005	0.1219	0.0429	0.0856	0.0503	0.0188	112.0	3.0	117.0	41.0	210.0	864.0	96	
LY-16/1-03	2	101	78	0.77	0.0177	0.0004	0.1202	0.0218	0.1275	0.0492	0.0090	113.0	3.0	115.0	21.0	159.0	428.0	98	
LY-16/1-04	1	41	56	1.35	0.0174	0.0006	0.1280	0.0719	0.0659	0.0534	0.0332	111.0	4.0	122.0	69.0	345.0	1405.0	91	
LY-16/1-05	1	33	44	1.35	0.0169	0.0007	0.1183	0.0721	0.0680	0.0507	0.0302	108.0	4.0	114.0	69.0	226.0	1378.0	95	
LY-16/1-06	1	44	40	0.90	0.0170	0.0006	0.1172	0.0486	0.0835	0.0500	0.0225	109.0	4.0	113.0	47.0	196.0	1046.0	97	
LY-16/1-07	3	120	167	1.39	0.0179	0.0004	0.1256	0.0194	0.1469	0.0510	0.0081	114.0	3.0	120.0	19.0	241.0	364.0	95	
LY-16/1-08	1	55	33	0.59	0.0176	0.0005	0.1211	0.0433	0.0821	0.0499	0.0194	113.0	3.0	116.0	41.0	189.0	904.0	97	
LY-16/1-09	3	161	54	0.34	0.0190	0.0004	0.1311	0.0231	0.1300	0.0502	0.0086	121.0	3.0	125.0	22.0	203.0	398.0	97	
LY-16/1-10	1	36	53	1.45	0.0176	0.0007	0.1194	0.0662	0.0711	0.0492	0.0285	112.0	4.0	114.0	64.0	160.0	1353.0	98	
LY-16/1-11	2	107	106	0.99	0.0173	0.0004	0.1251	0.0253	0.1247	0.0526	0.0120	110.0	3.0	120.0	24.0	311.0	520.0	92	
LY-16/1-12	1	39	55	1.41	0.0181	0.0008	0.1345	0.0745	0.0783	0.0538	0.0354	116.0	5.0	128.0	71.0	362.0	1483.0	90	
LY-16/1-13	2	69	112	1.64	0.0175	0.0004	0.1212	0.0307	0.1007	0.0502	0.0130	112.0	3.0	116.0	29.0	206.0	599.0	96	
LY-16/1-14	1	52	78	1.50	0.0180	0.0005	0.1292	0.0400	0.0965	0.0520	0.0176	115.0	3.0	123.0	38.0	286.0	772.0	93	
LY-16/1-15	2	80	59	0.73	0.0173	0.0005	0.1247	0.0269	0.1231	0.0522	0.0120	111.0	3.0	119.0	26.0	293.0	527.0	93	
LY-16/1-16	2	103	54	0.53	0.0184	0.0005	0.1312	0.0442	0.0797	0.0518	0.0179	117.0	3.0	125.0	42.0	275.0	790.0	94	
LY-16/1-17	2	101	149	1.47	0.0180	0.0004	0.1291	0.0277	0.1095	0.0520	0.0111	115.0	3.0	123.0	26.0	286.0	490.0	93	
LY-16/1-18	1	64	62	0.96	0.0182	0.0008	0.1254	0.0795	0.0657	0.0500	0.0344	116.0	5.0	120.0	76.0	197.0	1595.0	97	
LY-16/1-19	1	56	72	1.29	0.0180	0.0005	0.1200	0.0474	0.0728	0.0484	0.0213	115.0	3.0	115.0	45.0	118.0	1039.0	100	
LY-16/1-20	1	45	33	0.73	0.0183	0.0006	0.1298	0.0537	0.0801	0.0515	0.0256	117.0	4.0	124.0	51.0	261.0	1141.0	94	
LY-16/1-21	1	31	31	1.01	0.0180	0.0007	0.1440	0.0729	0.0792	0.0580	0.0356	115.0	5.0	137.0	69.0	529.0	1345.0	84	
LY-16/1-22	1	60	73	1.22	0.0179	0.0005	0.1280	0.0383	0.0910	0.0518	0.0160	115.0	3.0	122.0	37.0	276.0	708.0	94	
LY-16/1-23	1	36	23	0.63	0.0184	0.0008	0.1282	0.0705	0.0768	0.0504	0.0295	118.0	5.0	123.0	67.0	214.0	1355.0	96	
LY-16/1-24	1	38	44	1.17	0.0182	0.0009	0.1351	0.0899	0.0714	0.0538	0.0424	116.0	6.0	129.0	86.0	363.0	1778.0	90	

LY-16/1-25	1	46	65	1.42	0.0176	0.0005	0.1385	0.0445	0.0967	0.0571	0.0190	112.0	3.0	132.0	42.0	495.0	734.0	85
LY-16/1-27	1	32	41	1.28	0.0183	0.0007	0.1307	0.0691	0.0769	0.0519	0.0308	117.0	5.0	125.0	66.0	283.0	1355.0	93
LY-16/1-29	1	52	58	1.12	0.0173	0.0005	0.1290	0.0396	0.0934	0.0539	0.0169	111.0	3.0	123.0	38.0	369.0	708.0	90
LY-16/1-30	1	41	56	1.35	0.0179	0.0006	0.1225	0.0543	0.0768	0.0497	0.0258	114.0	4.0	117.0	52.0	179.0	1210.0	97
LY-16/1-31	1	25	15	0.59	0.0177	0.0009	0.1261	0.0895	0.0716	0.0518	0.0480	113.0	6.0	121.0	86.0	278.0	2122.0	94
LY-16/1-32	1	59	78	1.33	0.0175	0.0005	0.1209	0.0396	0.0927	0.0501	0.0179	112.0	3.0	116.0	38.0	201.0	831.0	96
LY-16/1-33	1	45	50	1.11	0.0174	0.0005	0.1240	0.0405	0.0920	0.0517	0.0171	111.0	3.0	119.0	39.0	271.0	758.0	94
LY-16/1-34	1	58	64	1.12	0.0183	0.0005	0.1244	0.0405	0.0911	0.0492	0.0167	117.0	3.0	119.0	39.0	157.0	793.0	98
LY-16/1-35	1	38	41	1.09	0.0186	0.0008	0.1195	0.0672	0.0729	0.0466	0.0250	119.0	5.0	115.0	64.0	26.0	1290.0	104
LY-16/1-36	1	41	49	1.19	0.0182	0.0006	0.1357	0.0630	0.0714	0.0541	0.0273	116.0	4.0	129.0	60.0	377.0	1134.0	90
LY-16/1-37	2	95	182	1.92	0.0186	0.0005	0.1236	0.0259	0.1232	0.0483	0.0104	119.0	3.0	118.0	25.0	115.0	508.0	100
LY-16/1-38	1	49	60	1.23	0.0183	0.0005	0.1240	0.0432	0.0850	0.0491	0.0173	117.0	3.0	119.0	41.0	152.0	825.0	99
LY-16/1-39	1	61	70	1.14	0.0185	0.0005	0.1234	0.0362	0.0952	0.0482	0.0146	118.0	3.0	118.0	35.0	111.0	713.0	100
LY-16/1-40	1	66	79	1.19	0.0179	0.0006	0.1275	0.0438	0.0907	0.0517	0.0180	114.0	4.0	122.0	42.0	274.0	796.0	94
LY-16/1-41	9	460	321	0.70	0.0185	0.0005	0.1225	0.0145	0.2242	0.0481	0.0056	118.0	3.0	117.0	14.0	103.0	273.0	101
LY-16/1-42	3	159	108	0.68	0.0183	0.0005	0.1221	0.0173	0.1770	0.0484	0.0067	117.0	3.0	117.0	17.0	117.0	326.0	100

LYN-1/1

LYN-1/1-02	8	362	355	0.98	0.0211	0.0004	0.1448	0.0123	0.24	0.0498	0.0042	134.0	3.0	137.0	12.0	186.0	195.0	98
LYN-1/1-03	10	446	424	0.95	0.0197	0.0004	0.1456	0.0085	0.35	0.0536	0.0030	126.0	3.0	138.0	8.0	353.0	129.0	91
LYN-1/1-04	6	284	255	0.90	0.0201	0.0004	0.1473	0.0143	0.21	0.0531	0.0051	128.0	3.0	140.0	14.0	332.0	220.0	92
LYN-1/1-5A	3	156	216	1.39	0.0176	0.0004	0.1293	0.0345	0.09	0.0534	0.0142	112.0	3.0	123.0	33.0	346.0	604.0	91
LYN-1/1-06	5	229	220	0.96	0.0196	0.0004	0.1409	0.0206	0.14	0.0520	0.0073	125.0	3.0	134.0	20.0	286.0	323.0	94
LYN-1/1-08	17	701	968	1.38	0.0206	0.0004	0.1411	0.0064	0.46	0.0498	0.0022	131.0	3.0	134.0	6.0	184.0	104.0	98
LYN-1/1-09	2	79	75	0.95	0.0187	0.0006	0.1337	0.0441	0.10	0.0520	0.0205	119.0	4.0	127.0	42.0	285.0	901.0	94
LYN-1/1-10	6	267	202	0.75	0.0199	0.0005	0.1409	0.0147	0.22	0.0514	0.0054	127.0	3.0	134.0	14.0	258.0	243.0	95
LYN-1/1-11	6	278	223	0.80	0.0203	0.0004	0.1469	0.0125	0.25	0.0526	0.0045	129.0	3.0	139.0	12.0	312.0	197.0	93

LYN-1/1-13	8	369	384	1.04	0.0199	0.0004	0.1454	0.0127	0.24	0.0529	0.0047	127.0	3.0	138.0	12.0	326.0	200.0	92
LYN-1/1-14	18	809	821	1.01	0.0194	0.0005	0.1352	0.0153	0.22	0.0506	0.0058	124.0	3.0	129.0	15.0	222.0	265.0	96
LYN-1/1-17	6	279	241	0.87	0.0202	0.0004	0.1473	0.0136	0.23	0.0529	0.0048	129.0	3.0	139.0	13.0	322.0	207.0	92
LYN-1/1-18	7	339	240	0.71	0.0201	0.0004	0.1446	0.0133	0.23	0.0521	0.0047	129.0	3.0	137.0	13.0	288.0	205.0	94
LYN-1/1-19	9	471	390	0.83	0.0177	0.0004	0.1320	0.0097	0.28	0.0540	0.0038	113.0	2.0	126.0	9.0	372.0	158.0	90
LYN-1/1-20	5	265	288	1.09	0.0183	0.0004	0.1377	0.0141	0.21	0.0545	0.0056	117.0	3.0	131.0	13.0	393.0	232.0	89
LYN-1/1-21	5	217	266	1.23	0.0187	0.0004	0.1312	0.0280	0.11	0.0509	0.0109	119.0	3.0	125.0	27.0	237.0	492.0	95
LYN-1/1-23	9	397	368	0.93	0.0199	0.0004	0.1439	0.0191	0.16	0.0524	0.0070	127.0	3.0	136.0	18.0	304.0	303.0	93
LYN-1/1-24	6	283	282	1.00	0.0205	0.0005	0.1440	0.0221	0.16	0.0509	0.0075	131.0	3.0	137.0	21.0	235.0	340.0	96
LYN-1/1-25	4	190	303	1.59	0.0175	0.0005	0.1300	0.0324	0.11	0.0540	0.0137	112.0	3.0	124.0	31.0	370.0	570.0	90
LYN-1/1-26	3	154	176	1.14	0.0178	0.0004	0.1306	0.0212	0.13	0.0534	0.0086	113.0	2.0	125.0	20.0	344.0	366.0	91
LYN-1/1-27	5	248	158	0.64	0.0197	0.0004	0.1423	0.0178	0.17	0.0524	0.0066	126.0	3.0	135.0	17.0	302.0	286.0	93
LYN-1/1-29	6	286	196	0.69	0.0186	0.0004	0.1402	0.0149	0.19	0.0547	0.0058	119.0	2.0	133.0	14.0	399.0	238.0	89
LYN-1/1-30	9	434	361	0.83	0.0192	0.0005	0.1438	0.0185	0.20	0.0544	0.0067	122.0	3.0	136.0	18.0	388.0	276.0	90
LYN-1/1-31	1	70	42	0.61	0.0200	0.0006	0.1434	0.0434	0.09	0.0521	0.0167	127.0	4.0	136.0	41.0	288.0	731.0	94
LYN-1/1-32	11	520	553	1.06	0.0195	0.0004	0.1396	0.0093	0.30	0.0519	0.0034	124.0	3.0	133.0	9.0	282.0	148.0	94
LYN-1/1-33	174	9300	3217	0.35	0.0194	0.0004	0.1278	0.0033	0.78	0.0478	0.0011	124.0	2.0	122.0	3.0	89.0	53.0	101
LYN-1/1-34	7	343	475	1.39	0.0186	0.0004	0.1279	0.0116	0.23	0.0499	0.0045	119.0	2.0	122.0	11.0	189.0	209.0	97
LYN-1/1-36	2	96	102	1.06	0.0208	0.0006	0.1401	0.0394	0.10	0.0488	0.0141	133.0	4.0	133.0	37.0	140.0	676.0	100
LYN-1/1-37	17	902	277	0.31	0.0195	0.0004	0.1480	0.0055	0.55	0.0551	0.0020	124.0	3.0	140.0	5.0	415.0	80.0	89

LYN-2/1

LYN-2/1-01	3	168	99	0.59	0.0199	0.0004	0.1860	0.0191	0.21	0.0678	0.0069	127.0	3.0	173.0	18.0	862.0	211.0	73
LYN-2/1-02	3	158	193	1.22	0.0174	0.0004	0.1233	0.0265	0.11	0.0513	0.0125	111.0	3.0	118.0	25.0	254.0	560.0	94
LYN-2/1-03	3	169	148	0.87	0.0196	0.0004	0.1549	0.0135	0.25	0.0573	0.0049	125.0	3.0	146.0	13.0	504.0	190.0	86
LYN-2/1-04A	2	107	156	1.45	0.0173	0.0004	0.1272	0.0244	0.12	0.0534	0.0101	110.0	3.0	122.0	23.0	345.0	427.0	91
LYN-2/1-04B	1	59	77	1.31	0.0172	0.0005	0.1790	0.0448	0.11	0.0754	0.0187	110.0	3.0	167.0	42.0	1080.0	497.0	66

LYN-2/1-07	3	170	83	0.49	0.0204	0.0004	0.1513	0.0160	0.20	0.0538	0.0058	130.0	3.0	143.0	15.0	362.0	243.0	91
LYN-2/1-08	5	247	198	0.80	0.0204	0.0004	0.1378	0.0114	0.24	0.0489	0.0040	130.0	3.0	131.0	11.0	145.0	190.0	99
LYN-2/1-09	9	405	483	1.19	0.0207	0.0004	0.1341	0.0070	0.39	0.0470	0.0024	132.0	3.0	128.0	7.0	49.0	124.0	103
LYN-2/1-10	16	957	323	0.34	0.0176	0.0004	0.1129	0.0039	0.58	0.0466	0.0015	112.0	2.0	109.0	4.0	29.0	76.0	103
LYN-2/1-12	3	139	172	1.24	0.0179	0.0004	0.1560	0.0165	0.20	0.0631	0.0068	115.0	2.0	147.0	16.0	712.0	228.0	78
LYN-2/1-13	2	120	184	1.53	0.0174	0.0004	0.1122	0.0180	0.14	0.0468	0.0075	111.0	3.0	108.0	17.0	39.0	383.0	103
LYN-2/1-14	14	696	204	0.29	0.0204	0.0004	0.1346	0.0049	0.58	0.0477	0.0017	130.0	3.0	128.0	5.0	86.0	82.0	102
LYN-2/1-15	4	199	231	1.16	0.0202	0.0004	0.1377	0.0124	0.24	0.0494	0.0045	129.0	3.0	131.0	12.0	168.0	212.0	98
LYN-2/1-16	1	52	43	0.82	0.0182	0.0005	0.1612	0.0431	0.11	0.0642	0.0179	116.0	3.0	152.0	41.0	750.0	589.0	77
LYN-2/1-17	2	107	53	0.49	0.0197	0.0005	0.1529	0.0240	0.15	0.0564	0.0092	126.0	3.0	144.0	23.0	468.0	360.0	87
LYN-2/1-18	4	152	187	1.23	0.0205	0.0005	0.1333	0.0166	0.18	0.0471	0.0059	131.0	3.0	127.0	16.0	52.0	301.0	103
LYN-2/1-19	1	78	76	0.97	0.0168	0.0004	0.1444	0.0328	0.12	0.0625	0.0147	107.0	3.0	137.0	31.0	692.0	500.0	78
LYN-2/1-22	1	69	57	0.82	0.0174	0.0005	0.0953	0.0397	0.08	0.0398	0.0190	111.0	4.0	92.0	38.0	-367.0	1241.0	120
LYN-2/1-23	2	106	151	1.43	0.0171	0.0004	0.1330	0.0261	0.13	0.0563	0.0126	110.0	3.0	127.0	25.0	463.0	495.0	86
LYN-2/1-25	2	90	93	1.04	0.0172	0.0004	0.1544	0.0269	0.14	0.0651	0.0115	110.0	3.0	146.0	25.0	779.0	373.0	75
LYN-2/1-26	2	112	74	0.66	0.0198	0.0004	0.1768	0.0235	0.17	0.0649	0.0090	126.0	3.0	165.0	22.0	771.0	291.0	76
LYN-2/1-28	1	68	57	0.84	0.0177	0.0005	0.1968	0.0345	0.15	0.0808	0.0143	113.0	3.0	182.0	32.0	1217.0	348.0	62
LYN-2/1-29	4	186	86	0.46	0.0198	0.0004	0.1284	0.0125	0.22	0.0470	0.0046	126.0	3.0	123.0	12.0	51.0	233.0	103
LYN-2/1-30	4	197	82	0.42	0.0206	0.0004	0.1524	0.0136	0.24	0.0537	0.0047	131.0	3.0	144.0	13.0	359.0	198.0	91
LYN-2/1-31	1	42	48	1.14	0.0177	0.0006	0.1805	0.0571	0.11	0.0738	0.0259	113.0	4.0	168.0	53.0	1035.0	710.0	67
LYN-2/1-34	2	92	83	0.91	0.0169	0.0004	0.1604	0.0251	0.15	0.0687	0.0108	108.0	3.0	151.0	24.0	890.0	326.0	72
LYN-2/1-35	5	252	164	0.65	0.0201	0.0004	0.1561	0.0098	0.33	0.0562	0.0035	129.0	3.0	147.0	9.0	461.0	137.0	87
LYN-2/1-36	5	292	108	0.37	0.0176	0.0004	0.1443	0.0090	0.33	0.0594	0.0036	113.0	2.0	137.0	8.0	580.0	133.0	82
LYN-2/1-37	2	103	98	0.95	0.0167	0.0004	0.0974	0.0219	0.11	0.0423	0.0095	107.0	3.0	94.0	21.0	-209.0	566.0	113
LYN-2/1-39	2	67	76	1.14	0.0170	0.0007	0.1711	0.0626	0.12	0.0730	0.0335	109.0	5.0	160.0	59.0	1014.0	930.0	68
LYN-2/1-40	2	74	77	1.05	0.0174	0.0005	0.1406	0.0288	0.13	0.0585	0.0123	111.0	3.0	134.0	27.0	548.0	461.0	83

LYN-2/1-41	5	232	138	0.60	0.0200	0.0004	0.1609	0.0115	0.29	0.0585	0.0040	127.0	3.0	152.0	11.0	548.0	150.0	84	
LY-15/1																			
LY-15/1-01	9	413	300	0.73	0.0191	0.0004	0.1312	0.0073	0.38	0.0498	0.0027	122.0	3.0	125.0	7.0	186.0	125.0	97	
LY-15/1-02	5	237	286	1.21	0.0192	0.0004	0.1329	0.0105	0.26	0.0503	0.0038	122.0	3.0	127.0	10.0	207.0	177.0	97	
LY-15/1-03	6	267	180	0.68	0.0196	0.0004	0.1327	0.0117	0.25	0.0491	0.0042	125.0	3.0	127.0	11.0	153.0	200.0	99	
LY-15/1-04	9	427	400	0.94	0.0193	0.0004	0.1353	0.0081	0.33	0.0509	0.0030	123.0	2.0	129.0	8.0	235.0	138.0	96	
LY-15/1-06	8	333	361	1.09	0.0190	0.0004	0.1296	0.0070	0.39	0.0496	0.0026	121.0	3.0	124.0	7.0	175.0	122.0	98	
LY-15/1-07	18	728	988	1.36	0.0195	0.0004	0.1318	0.0093	0.31	0.0490	0.0029	125.0	3.0	126.0	9.0	147.0	140.0	99	
LY-15/1-08	7	323	285	0.88	0.0199	0.0004	0.1318	0.0145	0.20	0.0481	0.0051	127.0	3.0	126.0	14.0	102.0	253.0	101	
LY-15/1-09	2	104	76	0.73	0.0193	0.0005	0.1326	0.0212	0.15	0.0498	0.0081	123.0	3.0	126.0	20.0	184.0	381.0	98	
LY-15/1-10	10	477	342	0.72	0.0193	0.0004	0.1319	0.0056	0.50	0.0495	0.0020	123.0	3.0	126.0	5.0	174.0	96.0	98	
LY-15/1-11	15	632	808	1.28	0.0191	0.0004	0.1303	0.0052	0.49	0.0494	0.0018	122.0	2.0	124.0	5.0	169.0	87.0	98	
LY-15/1-13	38	67	68	1.02	0.4712	0.0096	11.0568	0.2920	0.77	0.1702	0.0038	2489.0	51.0	2528.0	67.0	2560.0	38.0	97	
LY-15/1-14	7	263	247	0.94	0.0195	0.0004	0.1310	0.0062	0.48	0.0488	0.0024	124.0	3.0	125.0	6.0	139.0	114.0	99	
LY-15/1-15	10	423	387	0.91	0.0205	0.0004	0.1317	0.0093	0.29	0.0465	0.0033	131.0	3.0	126.0	9.0	23.0	170.0	104	
LY-15/1-16	17	628	1275	2.03	0.0192	0.0004	0.1359	0.0061	0.44	0.0513	0.0022	123.0	2.0	129.0	6.0	255.0	98.0	95	
LY-15/1-17	8	360	262	0.73	0.0195	0.0004	0.1373	0.0079	0.35	0.0512	0.0029	124.0	3.0	131.0	7.0	249.0	129.0	95	
LY-15/1-18	2	118	74	0.63	0.0198	0.0005	0.1362	0.0279	0.12	0.0499	0.0102	126.0	3.0	130.0	27.0	193.0	475.0	97	
LY-15/1-19	4	187	103	0.55	0.0200	0.0005	0.1311	0.0203	0.15	0.0475	0.0071	128.0	3.0	125.0	19.0	72.0	358.0	102	
LY-15/1-20	4	168	98	0.59	0.0204	0.0005	0.1361	0.0164	0.21	0.0484	0.0057	130.0	3.0	130.0	16.0	118.0	277.0	100	
LY-15/1-21	5	224	176	0.79	0.0202	0.0004	0.1373	0.0121	0.23	0.0492	0.0042	129.0	3.0	131.0	11.0	159.0	201.0	99	
LY-15/1-22	9	398	249	0.62	0.0201	0.0004	0.1340	0.0079	0.37	0.0483	0.0025	128.0	3.0	128.0	8.0	115.0	120.0	101	
LY-15/1-23	8	336	468	1.39	0.0201	0.0004	0.1328	0.0075	0.38	0.0480	0.0026	128.0	3.0	127.0	7.0	100.0	128.0	101	
LY-15/1-24	9	375	392	1.04	0.0196	0.0005	0.1344	0.0108	0.29	0.0497	0.0040	125.0	3.0	128.0	10.0	179.0	187.0	98	
LY-15/1-25	6	292	284	0.98	0.0195	0.0004	0.1337	0.0111	0.24	0.0497	0.0041	125.0	2.0	127.0	11.0	179.0	191.0	98	
LY-15/1-26	4	171	198	1.16	0.0198	0.0005	0.1360	0.0163	0.20	0.0499	0.0060	126.0	3.0	130.0	16.0	190.0	281.0	97	

LY-15/1-27	18	744	1125	1.51	0.0197	0.0004	0.1379	0.0057	0.47	0.0507	0.0020	126.0	2.0	131.0	5.0	226.0	91.0	96
LY-15/1-28	6	279	174	0.62	0.0196	0.0004	0.1390	0.0101	0.30	0.0514	0.0037	125.0	3.0	132.0	10.0	259.0	165.0	95
LY-15/1-29	16	646	1051	1.63	0.0195	0.0005	0.1347	0.0056	0.67	0.0502	0.0019	124.0	3.0	128.0	5.0	204.0	89.0	97
LY-15/1-30	11	436	634	1.45	0.0201	0.0004	0.1360	0.0060	0.46	0.0491	0.0021	128.0	3.0	129.0	6.0	151.0	101.0	99

LY-16/2

LY-16/2-01	12	619	411	0.66	0.0181	0.0004	0.1284	0.0055	0.48	0.0515	0.0022	116.0	2.0	123.0	5.0	262.0	96.0	94
LY-16/2-02	2	97	60	0.62	0.0184	0.0006	0.1305	0.0490	0.08	0.0514	0.0236	118.0	4.0	125.0	47.0	261.0	1051.0	94
LY-16/2-04	5	282	153	0.54	0.0178	0.0004	0.1258	0.0140	0.19	0.0512	0.0057	114.0	2.0	120.0	13.0	251.0	256.0	95
LY-16/2-05	2	105	155	1.49	0.0187	0.0005	0.1285	0.0259	0.12	0.0499	0.0104	119.0	3.0	123.0	25.0	190.0	483.0	97
LY-16/2-06	7	344	283	0.82	0.0182	0.0004	0.1277	0.0089	0.30	0.0509	0.0034	116.0	2.0	122.0	8.0	238.0	154.0	95
LY-16/2-07	15	841	345	0.41	0.0181	0.0004	0.1211	0.0044	0.56	0.0485	0.0016	116.0	2.0	116.0	4.0	125.0	80.0	100
LY-16/2-08	6	320	112	0.35	0.0183	0.0004	0.1232	0.0102	0.25	0.0489	0.0040	117.0	2.0	118.0	10.0	143.0	190.0	99
LY-16/2-09	13	693	540	0.78	0.0181	0.0004	0.1205	0.0050	0.55	0.0482	0.0018	116.0	3.0	116.0	5.0	111.0	88.0	100
LY-16/2-10	5	260	218	0.84	0.0184	0.0004	0.1236	0.0125	0.21	0.0488	0.0048	117.0	2.0	118.0	12.0	136.0	231.0	99
LY-16/2-11	13	701	225	0.32	0.0184	0.0004	0.1229	0.0162	0.16	0.0483	0.0063	118.0	2.0	118.0	15.0	114.0	306.0	100
LY-16/2-12	11	606	272	0.45	0.0182	0.0004	0.1244	0.0077	0.33	0.0495	0.0030	116.0	2.0	119.0	7.0	174.0	139.0	98
LY-16/2-13	6	332	150	0.45	0.0181	0.0004	0.1261	0.0097	0.27	0.0504	0.0039	116.0	2.0	121.0	9.0	215.0	181.0	96
LY-16/2-15	22	225	127	0.56	0.0976	0.0031	0.8084	0.0333	0.76	0.0601	0.0016	600.0	19.0	602.0	25.0	606.0	58.0	100
LY-16/2-16	14	764	470	0.62	0.0183	0.0004	0.1322	0.0074	0.38	0.0523	0.0028	117.0	3.0	126.0	7.0	299.0	122.0	93
LY-16/2-17	3	162	98	0.60	0.0179	0.0004	0.1208	0.0175	0.16	0.0490	0.0070	114.0	3.0	116.0	17.0	149.0	336.0	99
LY-16/2-18	10	562	246	0.44	0.0180	0.0004	0.1210	0.0056	0.46	0.0488	0.0021	115.0	2.0	116.0	5.0	136.0	102.0	99
LY-16/2-19	19	848	1465	1.73	0.0177	0.0004	0.1244	0.0044	0.58	0.0511	0.0017	113.0	2.0	119.0	4.0	243.0	75.0	95
LY-16/2-20	2	87	85	0.97	0.0181	0.0005	0.1293	0.0341	0.10	0.0517	0.0139	116.0	3.0	123.0	33.0	273.0	615.0	94
LY-16/2-21	7	361	161	0.45	0.0180	0.0004	0.1285	0.0101	0.27	0.0519	0.0042	115.0	2.0	123.0	10.0	282.0	186.0	93
LY-16/2-22	7	391	158	0.40	0.0185	0.0004	0.1328	0.0069	0.43	0.0520	0.0026	118.0	3.0	127.0	7.0	287.0	114.0	93
LY-16/2-23	3	146	211	1.45	0.0179	0.0004	0.1292	0.0190	0.15	0.0525	0.0079	114.0	3.0	123.0	18.0	306.0	341.0	92

LY-16/2-24	1	47	76	1.61	0.0186	0.0006	0.1329	0.0541	0.08	0.0518	0.0206	119.0	4.0	127.0	52.0	278.0	911.0	94
LY-16/2-25	2	118	71	0.60	0.0189	0.0005	0.1344	0.0443	0.08	0.0516	0.0181	121.0	3.0	128.0	42.0	266.0	805.0	94
LY-16/2-26	4	183	116	0.63	0.0189	0.0004	0.1284	0.0163	0.18	0.0492	0.0064	121.0	3.0	123.0	16.0	159.0	306.0	98
LY-16/2-27	17	864	654	0.76	0.0184	0.0004	0.1330	0.0050	0.59	0.0526	0.0019	117.0	3.0	127.0	5.0	310.0	83.0	92
LY-16/2-28	4	195	134	0.69	0.0179	0.0004	0.1319	0.0320	0.10	0.0535	0.0140	114.0	3.0	126.0	30.0	349.0	591.0	91
LY-16/2-29	2	115	106	0.92	0.0184	0.0004	0.1265	0.0244	0.12	0.0500	0.0099	117.0	3.0	121.0	23.0	195.0	458.0	97
LY-16/2-30	2	111	96	0.86	0.0178	0.0004	0.1261	0.0247	0.12	0.0515	0.0102	114.0	3.0	121.0	24.0	263.0	455.0	94
LY-16/2-31	14	734	526	0.72	0.0186	0.0004	0.1280	0.0056	0.46	0.0499	0.0021	119.0	2.0	122.0	5.0	192.0	99.0	97
LY-16/2-32	17	923	328	0.36	0.0183	0.0004	0.1316	0.0054	0.59	0.0520	0.0019	117.0	3.0	126.0	5.0	287.0	83.0	93
LY-16/2-34	5	244	171	0.70	0.0190	0.0004	0.1314	0.0170	0.17	0.0502	0.0065	121.0	3.0	125.0	16.0	204.0	302.0	97
LY-16/2-35	3	127	81	0.64	0.0186	0.0004	0.1252	0.0252	0.11	0.0487	0.0099	119.0	3.0	120.0	24.0	135.0	477.0	99
LY-16/2-36	11	589	296	0.50	0.0184	0.0004	0.1282	0.0062	0.43	0.0506	0.0023	117.0	2.0	123.0	6.0	223.0	107.0	96

LY-18/1

LY-18/1-01	6	249	287	1.15	0.0194	0.0004	0.1296	0.0102	0.27	0.0484	0.0038	124.0	3.0	124.0	10.0	121.0	187.0	100
LY-18/1-02	3	128	109	0.85	0.0193	0.0004	0.1288	0.0182	0.16	0.0483	0.0069	123.0	3.0	123.0	17.0	114.0	337.0	100
LY-18/1-03	3	141	117	0.83	0.0196	0.0004	0.1334	0.0161	0.18	0.0493	0.0061	125.0	3.0	127.0	15.0	162.0	288.0	99
LY-18/1-06	9	28	16	0.58	0.3109	0.0064	4.6960	0.1619	0.60	0.1096	0.0034	1745.0	36.0	1767.0	61.0	1792.0	57.0	97
LY-18/1-12	6	294	378	1.28	0.0188	0.0004	0.1309	0.0152	0.17	0.0506	0.0057	120.0	2.0	125.0	15.0	223.0	261.0	96
LY-18/1-13	7	313	245	0.78	0.0193	0.0004	0.1298	0.0121	0.24	0.0488	0.0043	123.0	3.0	124.0	12.0	140.0	205.0	99
LY-18/1-14	8	60	60	1.01	0.1211	0.0027	1.0721	0.0466	0.51	0.0642	0.0026	737.0	16.0	740.0	32.0	749.0	87.0	100
LY-18/1-15	11	479	603	1.26	0.0191	0.0004	0.1292	0.0057	0.46	0.0491	0.0021	122.0	3.0	123.0	5.0	151.0	99.0	99
LY-18/1-16	3	164	121	0.74	0.0191	0.0004	0.1296	0.0182	0.16	0.0492	0.0069	122.0	3.0	124.0	17.0	160.0	329.0	99
LY-18/1-17	2	89	61	0.69	0.0192	0.0005	0.1403	0.0551	0.07	0.0529	0.0217	123.0	3.0	133.0	52.0	325.0	932.0	92
LY-18/1-18	5	242	288	1.19	0.0190	0.0004	0.1275	0.0117	0.23	0.0487	0.0043	121.0	3.0	122.0	11.0	134.0	205.0	99
LY-18/1-23	21	972	1060	1.09	0.0191	0.0011	0.1416	0.0534	0.15	0.0538	0.0061	122.0	7.0	134.0	51.0	361.0	255.0	91

LY-26/1

LY-26/1-03	14	626	816	1.30	0.0186	0.0004	0.1293	0.0062	0.44	0.0506	0.0022	119.0	2.0	123.0	6.0	221.0	101.0	96
LY-26/1-04	9	390	523	1.34	0.0187	0.0004	0.1278	0.0090	0.31	0.0495	0.0036	120.0	3.0	122.0	9.0	172.0	170.0	98
LY-26/1-05	10	527	221	0.42	0.0187	0.0004	0.1231	0.0073	0.38	0.0478	0.0028	119.0	3.0	118.0	7.0	87.0	139.0	101
LY-26/1-06	2	76	80	1.05	0.0192	0.0006	0.1264	0.0359	0.11	0.0479	0.0164	122.0	4.0	121.0	34.0	93.0	811.0	101
LY-26/1-07	5	283	116	0.41	0.0186	0.0005	0.1316	0.0107	0.31	0.0513	0.0041	119.0	3.0	126.0	10.0	256.0	183.0	95
LY-26/1-08	4	163	270	1.65	0.0189	0.0004	0.1331	0.0153	0.21	0.0510	0.0057	121.0	3.0	127.0	15.0	240.0	259.0	95
LY-26/1-09	3	171	110	0.64	0.0193	0.0005	0.1294	0.0148	0.21	0.0486	0.0054	123.0	3.0	124.0	14.0	130.0	259.0	100
LY-26/1-10	5	245	77	0.31	0.0192	0.0005	0.1271	0.0151	0.24	0.0479	0.0056	123.0	3.0	121.0	14.0	97.0	279.0	101
LY-26/1-11	4	197	110	0.56	0.0186	0.0005	0.1294	0.0224	0.15	0.0505	0.0079	119.0	3.0	124.0	21.0	218.0	362.0	96
LY-26/1-12	10	491	424	0.86	0.0190	0.0004	0.1318	0.0064	0.42	0.0502	0.0024	122.0	2.0	126.0	6.0	205.0	109.0	97
LY-26/1-13	4	189	154	0.82	0.0194	0.0005	0.1311	0.0127	0.24	0.0490	0.0049	124.0	3.0	125.0	12.0	147.0	234.0	99
LY-26/1-14	2	79	79	1.00	0.0193	0.0005	0.1306	0.0335	0.10	0.0490	0.0125	123.0	3.0	125.0	32.0	147.0	597.0	99
LY-26/1-15	21	887	1297	1.46	0.0185	0.0004	0.1276	0.0044	0.58	0.0499	0.0016	118.0	2.0	122.0	4.0	193.0	76.0	97
LY-26/1-16	17	894	344	0.38	0.0186	0.0004	0.1228	0.0050	0.48	0.0479	0.0018	119.0	2.0	118.0	5.0	97.0	91.0	101
LY-26/1-17	16	806	506	0.63	0.0183	0.0004	0.1274	0.0042	0.63	0.0505	0.0015	117.0	2.0	122.0	4.0	219.0	70.0	96
LY-26/1-18	5	241	130	0.54	0.0189	0.0004	0.1272	0.0132	0.21	0.0487	0.0048	121.0	3.0	122.0	13.0	133.0	233.0	100
LY-26/1-19	4	206	94	0.46	0.0190	0.0005	0.1352	0.0147	0.25	0.0516	0.0055	121.0	3.0	129.0	14.0	269.0	246.0	94
LY-26/1-20	1	33	46	1.39	0.0191	0.0007	0.1345	0.0759	0.06	0.0512	0.0333	122.0	4.0	128.0	72.0	249.0	1498.0	95
LY-26/1-21	1	63	93	1.47	0.0185	0.0007	0.1284	0.0421	0.11	0.0503	0.0168	118.0	4.0	123.0	40.0	211.0	775.0	96
LY-26/1-22	4	208	186	0.89	0.0184	0.0004	0.1298	0.0130	0.22	0.0511	0.0051	118.0	3.0	124.0	12.0	245.0	229.0	95
LY-26/1-23	3	134	174	1.30	0.0191	0.0004	0.1281	0.0180	0.17	0.0487	0.0067	122.0	3.0	122.0	17.0	132.0	326.0	100
LY-26/1-24	10	421	639	1.52	0.0186	0.0004	0.1271	0.0068	0.37	0.0497	0.0026	119.0	2.0	122.0	7.0	181.0	123.0	98
LY-26/1-25	5	269	149	0.56	0.0191	0.0004	0.1304	0.0090	0.31	0.0494	0.0034	122.0	3.0	124.0	9.0	169.0	160.0	98
LY-26/1-26	2	81	169	2.08	0.0194	0.0005	0.1307	0.0291	0.11	0.0489	0.0109	124.0	3.0	125.0	28.0	142.0	523.0	99
LY-26/1-27	13	651	339	0.52	0.0193	0.0005	0.1313	0.0055	0.60	0.0495	0.0019	123.0	3.0	125.0	5.0	170.0	91.0	98
LY-26/1-28	10	484	323	0.67	0.0193	0.0005	0.1320	0.0072	0.44	0.0497	0.0025	123.0	3.0	126.0	7.0	180.0	119.0	98

LY-26/1-29	4	208	94	0.45	0.0182	0.0005	0.1314	0.0176	0.20	0.0524	0.0065	116.0	3.0	125.0	17.0	305.0	283.0	93
LY-26/1-33	23	896	1476	1.65	0.0191	0.0004	0.1308	0.0053	0.54	0.0497	0.0017	122.0	3.0	125.0	5.0	180.0	81.0	98
LY-26/1-34	7	340	234	0.69	0.0184	0.0004	0.1311	0.0086	0.36	0.0518	0.0034	117.0	3.0	125.0	8.0	276.0	149.0	94
LY-26/1-35	5	232	174	0.75	0.0189	0.0004	0.1332	0.0153	0.19	0.0511	0.0060	121.0	3.0	127.0	15.0	247.0	270.0	95
LY-26/1-36	8	391	198	0.51	0.0186	0.0004	0.1292	0.0076	0.38	0.0504	0.0028	119.0	3.0	123.0	7.0	214.0	127.0	96
LY-26/1-37	16	708	805	1.14	0.0187	0.0004	0.1280	0.0048	0.55	0.0497	0.0017	119.0	2.0	122.0	5.0	180.0	82.0	98

LYN-4/1

LYN-4/1-01	133	385	51	0.13	0.3473	0.0080	5.6525	0.1590	0.82	0.1180	0.0026	1922.0	44.0	1924.0	54.0	1927.0	40.0	100
LYN-4/1-04	6	265	298	1.12	0.0195	0.0004	0.1351	0.0135	0.21	0.0503	0.0050	124.0	3.0	129.0	13.0	207.0	230.0	97
LYN-4/1-05	9	439	296	0.67	0.0191	0.0004	0.1312	0.0112	0.25	0.0499	0.0042	122.0	3.0	125.0	11.0	189.0	198.0	97
LYN-4/1-07	6	316	132	0.42	0.0195	0.0004	0.1391	0.0113	0.26	0.0517	0.0041	125.0	3.0	132.0	11.0	273.0	180.0	94
LYN-4/1-08	17	851	740	0.87	0.0189	0.0004	0.1298	0.0054	0.47	0.0497	0.0019	121.0	2.0	124.0	5.0	183.0	91.0	98
LYN-4/1-09	10	524	338	0.65	0.0191	0.0004	0.1388	0.0077	0.37	0.0526	0.0029	122.0	3.0	132.0	7.0	311.0	126.0	93
LYN-4/1-10	4	199	150	0.75	0.0195	0.0004	0.1358	0.0172	0.18	0.0506	0.0062	124.0	3.0	129.0	16.0	221.0	284.0	96
LYN-4/1-11	5	222	224	1.01	0.0197	0.0004	0.1390	0.0134	0.22	0.0511	0.0049	126.0	3.0	132.0	13.0	243.0	221.0	95
LYN-4/1-12	8	384	233	0.61	0.0197	0.0004	0.1337	0.0084	0.34	0.0493	0.0031	126.0	3.0	127.0	8.0	162.0	147.0	99
LYN-4/1-14	87	128	140	1.09	0.5751	0.0129	17.6643	0.4908	0.81	0.2228	0.0050	2929.0	66.0	2972.0	83.0	3001.0	36.0	98
LYN-4/1-15	19	995	513	0.52	0.0195	0.0004	0.1360	0.0050	0.54	0.0505	0.0018	125.0	2.0	130.0	5.0	218.0	83.0	96
LYN-4/1-16	11	560	399	0.71	0.0193	0.0004	0.1358	0.0085	0.32	0.0510	0.0031	123.0	2.0	129.0	8.0	240.0	140.0	95
LYN-4/1-17	9	438	413	0.94	0.0196	0.0004	0.1353	0.0078	0.36	0.0501	0.0028	125.0	3.0	129.0	7.0	197.0	129.0	97
LYN-4/1-18	9	424	365	0.86	0.0194	0.0004	0.1332	0.0095	0.29	0.0498	0.0035	124.0	3.0	127.0	9.0	186.0	162.0	98
LYN-4/1-19	9	438	350	0.80	0.0190	0.0004	0.1342	0.0133	0.21	0.0513	0.0050	121.0	3.0	128.0	13.0	255.0	223.0	95
LYN-4/1-20	7	343	302	0.88	0.0195	0.0004	0.1359	0.0145	0.20	0.0504	0.0053	125.0	3.0	129.0	14.0	215.0	245.0	96
LYN-4/1-22	6	302	218	0.72	0.0191	0.0004	0.1324	0.0126	0.21	0.0503	0.0047	122.0	2.0	126.0	12.0	209.0	217.0	97
LYN-4/1-23	11	563	363	0.65	0.0192	0.0004	0.1388	0.0064	0.45	0.0525	0.0024	123.0	3.0	132.0	6.0	305.0	102.0	93

LY-34-1

LY-34-1-01	2	78	78	1.01	0.0204	0.0009	0.1624	0.0348	0.22	0.0577	0.0127	130.0	6.0	153.0	30.0	520.0	450.0	85
LY-34-1-02	3	94	60	0.64	0.0210	0.0011	0.1412	0.0350	0.21	0.0488	0.0124	134.0	7.0	134.0	31.0	140.0	548.0	100
LY-34-1-03	4	161	126	0.78	0.0200	0.0008	0.1262	0.0215	0.23	0.0459	0.0081	127.0	5.0	121.0	19.0	0.0	380.0	106
LY-34-1-04	4	135	119	0.88	0.0204	0.0008	0.1442	0.0231	0.24	0.0513	0.0085	130.0	5.0	137.0	21.0	254.0	361.0	95
LY-34-1-06	3	130	97	0.75	0.0201	0.0008	0.1771	0.0244	0.28	0.0639	0.0092	128.0	5.0	166.0	21.0	738.0	292.0	78
LY-34-1-07	5	143	141	0.98	0.0204	0.0008	0.1720	0.0251	0.27	0.0613	0.0094	130.0	5.0	161.0	22.0	648.0	313.0	81
LY-34-1-08	3	103	94	0.91	0.0203	0.0015	0.1637	0.0557	0.21	0.0585	0.0203	130.0	9.0	154.0	49.0	548.0	681.0	84
LY-34-1-09	286	516	258	0.50	0.4377	0.0105	9.3387	0.2496	0.90	0.1547	0.0066	2340.0	47.0	2372.0	25.0	2399.0	72.0	98
LY-34-1-10	4	121	119	0.99	0.0215	0.0009	0.1476	0.0285	0.21	0.0499	0.0099	137.0	6.0	140.0	25.0	190.0	432.0	98
LY-34-1-11	2	97	67	0.69	0.0204	0.0009	0.1261	0.0291	0.19	0.0448	0.0106	130.0	6.0	121.0	26.0	0.0	393.0	108
LY-34-1-13	7	249	228	0.92	0.0204	0.0007	0.1385	0.0162	0.28	0.0493	0.0061	130.0	4.0	132.0	14.0	162.0	277.0	99
LY-34-1-14	4	140	115	0.82	0.0201	0.0009	0.1544	0.0264	0.26	0.0557	0.0099	128.0	6.0	146.0	23.0	441.0	374.0	88
LY-34-1-15	9	302	335	1.11	0.0211	0.0007	0.1437	0.0171	0.28	0.0494	0.0062	135.0	4.0	136.0	15.0	167.0	282.0	99
LY-34-1-16	1	51	38	0.75	0.0206	0.0014	0.1389	0.0560	0.17	0.0490	0.0201	131.0	9.0	132.0	50.0	149.0	840.0	99
LY-34-1-17	2	95	67	0.70	0.0208	0.0009	0.1402	0.0320	0.20	0.0489	0.0114	133.0	6.0	133.0	29.0	143.0	507.0	100
LY-34-1-18	9	297	380	1.28	0.0207	0.0007	0.1407	0.0156	0.29	0.0493	0.0058	132.0	4.0	134.0	14.0	161.0	265.0	99
LY-34-1-19	5	109	75	0.69	0.0204	0.0011	0.1396	0.0330	0.22	0.0496	0.0121	130.0	7.0	133.0	29.0	178.0	521.0	98
LY-34-1-20	3	117	125	1.07	0.0206	0.0011	0.1395	0.0329	0.22	0.0492	0.0119	131.0	7.0	133.0	29.0	155.0	523.0	99
LY-34-1-22	20	572	1279	2.23	0.0201	0.0006	0.1345	0.0121	0.33	0.0486	0.0048	128.0	4.0	128.0	11.0	129.0	223.0	100
LY-34-1-23	2	92	89	0.97	0.0192	0.0008	0.1293	0.0234	0.22	0.0488	0.0091	123.0	5.0	124.0	21.0	140.0	411.0	99
LY-34-1-24	3	88	95	1.08	0.0210	0.0010	0.1330	0.0343	0.18	0.0460	0.0121	134.0	6.0	127.0	31.0	0.0	575.0	106
LY-34-1-25	3	121	87	0.72	0.0209	0.0008	0.1423	0.0239	0.23	0.0494	0.0086	133.0	5.0	135.0	21.0	168.0	382.0	99
LY-34-1-26	78	189	50	0.26	0.3516	0.0090	5.8717	0.1983	0.76	0.1212	0.0058	1942.0	43.0	1957.0	29.0	1973.0	84.0	98
LY-34-1-27	3	113	86	0.76	0.0205	0.0010	0.1442	0.0307	0.22	0.0510	0.0112	131.0	6.0	137.0	27.0	240.0	468.0	96
LY-34-1-28	1	53	46	0.87	0.0209	0.0012	0.1729	0.0464	0.21	0.0601	0.0165	133.0	8.0	162.0	40.0	608.0	545.0	82
LY-34-1-29	3	81	89	1.10	0.0210	0.0012	0.1423	0.0390	0.21	0.0492	0.0138	134.0	8.0	135.0	35.0	155.0	598.0	99

LY-34-1-30	3	127	102	0.81	0.0208	0.0008	0.1346	0.0258	0.21	0.0470	0.0093	133.0	5.0	128.0	23.0	48.0	441.0	103
LY-34-1-31	1	36	53	1.47	0.0205	0.0016	0.1389	0.0631	0.18	0.0491	0.0226	131.0	10.0	132.0	56.0	151.0	932.0	99
LY-34-1-32	3	110	109	0.99	0.0201	0.0010	0.1453	0.0330	0.22	0.0525	0.0123	128.0	6.0	138.0	29.0	305.0	493.0	93
LY-34-1-33	1	119	83	0.70	0.0204	0.0008	0.1470	0.0255	0.23	0.0524	0.0094	130.0	5.0	139.0	23.0	302.0	385.0	93

LYN-1/4

LYN-1/4-01	9	370	367	0.99	0.0200	0.0004	0.1519	0.0104	0.31	0.0550	0.0035	128.0	3.0	144.0	10.0	412.0	143.0	89
LYN-1/4-02	7	317	228	0.72	0.0201	0.0004	0.1387	0.0082	0.37	0.0501	0.0029	128.0	3.0	132.0	8.0	199.0	135.0	97
LYN-1/4-04	3	117	92	0.78	0.0199	0.0005	0.1478	0.0198	0.18	0.0538	0.0072	127.0	3.0	140.0	19.0	362.0	303.0	91
LYN-1/4-06	8	328	304	0.93	0.0203	0.0005	0.1361	0.0093	0.35	0.0486	0.0033	130.0	3.0	130.0	9.0	129.0	161.0	100
LYN-1/4-07	8	381	352	0.92	0.0195	0.0004	0.1375	0.0070	0.42	0.0511	0.0025	125.0	3.0	131.0	7.0	247.0	111.0	95
LYN-1/4-08	4	168	137	0.82	0.0204	0.0005	0.1393	0.0182	0.17	0.0496	0.0061	130.0	3.0	132.0	17.0	177.0	286.0	98
LYN-1/4-09	3	149	139	0.93	0.0193	0.0004	0.1349	0.0149	0.21	0.0506	0.0055	123.0	3.0	129.0	14.0	223.0	252.0	96
LYN-1/4-10	4	159	258	1.62	0.0202	0.0005	0.1412	0.0163	0.23	0.0506	0.0057	129.0	3.0	134.0	16.0	223.0	259.0	96
LYN-1/4-11	3	122	105	0.86	0.0196	0.0004	0.1462	0.0182	0.18	0.0541	0.0068	125.0	3.0	139.0	17.0	377.0	281.0	90
LYN-1/4-12	4	210	169	0.81	0.0198	0.0005	0.1392	0.0122	0.26	0.0510	0.0047	126.0	3.0	132.0	12.0	242.0	212.0	95
LYN-1/4-13	5	251	227	0.90	0.0195	0.0004	0.1337	0.0091	0.33	0.0497	0.0034	124.0	3.0	127.0	9.0	183.0	158.0	98
LYN-1/4-14	3	159	137	0.86	0.0200	0.0004	0.1374	0.0171	0.17	0.0499	0.0063	127.0	3.0	131.0	16.0	190.0	294.0	98
LYN-1/4-15	6	302	225	0.75	0.0200	0.0004	0.1369	0.0088	0.34	0.0496	0.0031	128.0	3.0	130.0	8.0	177.0	146.0	98
LYN-1/4-17	7	306	330	1.08	0.0205	0.0004	0.1476	0.0085	0.35	0.0522	0.0029	131.0	3.0	140.0	8.0	296.0	128.0	94
LYN-1/4-18	8	346	440	1.27	0.0199	0.0004	0.1478	0.0093	0.34	0.0538	0.0034	127.0	3.0	140.0	9.0	361.0	142.0	91
LYN-1/4-19	13	597	717	1.20	0.0200	0.0004	0.1304	0.0055	0.48	0.0473	0.0019	128.0	3.0	124.0	5.0	66.0	95.0	102
LYN-1/4-20	3	154	116	0.76	0.0192	0.0004	0.1370	0.0159	0.18	0.0517	0.0060	123.0	3.0	130.0	15.0	271.0	267.0	94
LYN-1/4-21	3	145	113	0.78	0.0201	0.0005	0.1394	0.0164	0.21	0.0502	0.0059	129.0	3.0	132.0	16.0	203.0	273.0	97
LYN-1/4-22	16	738	768	1.04	0.0200	0.0004	0.1468	0.0051	0.60	0.0531	0.0018	128.0	3.0	139.0	5.0	334.0	76.0	92
LYN-1/4-23	3	133	114	0.86	0.0199	0.0005	0.1408	0.0207	0.16	0.0514	0.0072	127.0	3.0	134.0	20.0	258.0	322.0	95
LYN-1/4-25	5	245	204	0.83	0.0200	0.0004	0.1460	0.0142	0.22	0.0529	0.0051	128.0	3.0	138.0	13.0	324.0	221.0	92

LYN-1/4-26	3	129	101	0.78	0.0193	0.0004	0.1446	0.0210	0.15	0.0543	0.0077	123.0	3.0	137.0	20.0	384.0	320.0	90
LYN-1/4-27	6	278	256	0.92	0.0203	0.0004	0.1487	0.0090	0.35	0.0530	0.0030	130.0	3.0	141.0	8.0	329.0	130.0	92
LYN-1/4-28	3	143	143	1.00	0.0196	0.0004	0.1399	0.0149	0.20	0.0518	0.0055	125.0	3.0	133.0	14.0	279.0	242.0	94
LYN-1/4-29	4	202	162	0.80	0.0199	0.0004	0.1387	0.0104	0.29	0.0505	0.0038	127.0	3.0	132.0	10.0	217.0	173.0	96
LYN-1/4-30	2	98	79	0.81	0.0198	0.0005	0.1351	0.0266	0.12	0.0496	0.0097	126.0	3.0	129.0	25.0	174.0	456.0	98
LYN-1/4-31	10	477	646	1.36	0.0203	0.0005	0.1352	0.0053	0.60	0.0482	0.0019	130.0	3.0	129.0	5.0	109.0	94.0	101
LYN-1/4-32	3	167	161	0.96	0.0191	0.0004	0.1319	0.0142	0.20	0.0500	0.0055	122.0	3.0	126.0	14.0	196.0	254.0	97
LYN-1/4-33	3	147	96	0.65	0.0199	0.0004	0.1452	0.0148	0.22	0.0528	0.0053	127.0	3.0	138.0	14.0	320.0	227.0	92
LYN-1/4-34	9	430	532	1.24	0.0194	0.0004	0.1316	0.0063	0.43	0.0492	0.0023	124.0	3.0	126.0	6.0	159.0	108.0	99
LYN-1/4-36	3	134	88	0.66	0.0199	0.0004	0.1339	0.0154	0.19	0.0489	0.0057	127.0	3.0	128.0	15.0	143.0	272.0	99
LYN-1/4-37	5	217	212	0.98	0.0203	0.0004	0.1353	0.0117	0.23	0.0483	0.0041	130.0	3.0	129.0	11.0	112.0	203.0	101
LYN-1/4-38	7	337	325	0.96	0.0204	0.0004	0.1454	0.0130	0.24	0.0518	0.0047	130.0	3.0	138.0	12.0	277.0	208.0	94
LYN-1/4-39	9	413	531	1.28	0.0198	0.0004	0.1364	0.0063	0.44	0.0501	0.0023	126.0	3.0	130.0	6.0	199.0	105.0	97
LYN-1/4-40	6	282	248	0.88	0.0202	0.0004	0.1450	0.0147	0.21	0.0520	0.0052	129.0	3.0	137.0	14.0	286.0	228.0	94

Table 6-1 Zircon in-situ Lu-Hf isotopic analytical results of the Laiyuan magmatic rocks in this study.

Identifier	Age (Ma)	$^{176}\text{Yb}/^{177}\text{Hf}$	$^{176}\text{Lu}/^{177}\text{Hf}$	$^{176}\text{Hf}/^{177}\text{Hf}$	2σ	$^{176}\text{Hf}/^{177}\text{Hf}_i$	$\epsilon_{\text{Hf}}(0)$	$\epsilon_{\text{Hf}}(t)$	T_{DM}^{C} (Ma)	$f_{\text{Lu/Hf}}$
LYN-3/2 (Trachydacite)										
LYN-3/2-06	128.9	0.0188	0.0006	0.282093	0.000013	0.282092	-24.0	-21.2	2532	-0.98
LYN-3/2-12	129.8	0.0369	0.0009	0.282091	0.000020	0.282089	-24.1	-21.3	2537	-0.97
LYN-3/2-14	129.1	0.0226	0.0006	0.282146	0.000020	0.282144	-22.1	-19.4	2414	-0.98
LYN-3/2-15	128.6	0.0285	0.0007	0.282095	0.000015	0.282093	-23.9	-21.2	2529	-0.98
LYN-3/2-19	129.6	0.0301	0.0008	0.282116	0.000018	0.282114	-23.2	-20.4	2481	-0.98
LYN-3/2-20	130.4	0.0187	0.0006	0.282068	0.000018	0.282067	-24.9	-22.1	2586	-0.98
LY-40/1 (Trachyandesite)										
LY-40/1-9	132.0	0.0143	0.0004	0.282027	0.000022	0.282026	-26.4	-23.5	2676	-0.99
LY-40/1-10	134.7	0.0289	0.0007	0.282113	0.000023	0.282112	-23.3	-20.4	2484	-0.98
LY-40/1-12	130.9	0.0128	0.0003	0.282122	0.000015	0.282121	-23.0	-20.2	2465	-0.99
LY-40/1-33	131.8	0.0348	0.0008	0.282096	0.000016	0.282094	-23.9	-21.1	2524	-0.98
LY-40/1-37	129.4	0.0375	0.0009	0.282031	0.000026	0.282029	-26.2	-23.4	2671	-0.97
LY-40/1-38	131.6	0.0231	0.0005	0.282096	0.000026	0.282094	-23.9	-21.1	2524	-0.98
LY-21/1 (Quartz Monzonite)										
LY-21/1-02	126.9	0.0343	0.0011	0.282133	0.000035	0.282130	-22.6	-19.9	2447	-0.97

LY-21/1-10	129.5	0.0218	0.0007	0.282149	0.000031	0.282147	-22.0	-19.3	2407	-0.98
LY-21/1-11	129.1	0.0279	0.0008	0.282113	0.000030	0.282111	-23.3	-20.5	2488	-0.98
LY-21/1-14	128.7	0.0306	0.0008	0.282135	0.000039	0.282133	-22.5	-19.8	2440	-0.97
LY-21/1-17	128.0	0.0394	0.0011	0.282180	0.000040	0.282177	-20.9	-18.2	2341	-0.97
LY-21/1-20	127.1	0.0245	0.0009	0.282139	0.000035	0.282137	-22.4	-19.7	2432	-0.97
LY-21/1-24	127.2	0.0335	0.0010	0.282153	0.000032	0.282151	-21.9	-19.2	2402	-0.97
LY-21/1-25	126.0	0.0147	0.0005	0.282143	0.000028	0.282142	-22.2	-19.5	2422	-0.99
LY-21/1-28	128.8	0.0178	0.0005	0.282126	0.000031	0.282125	-22.8	-20.1	2458	-0.98
LY-21/1-30	128.3	0.0174	0.0005	0.282132	0.000031	0.282131	-22.6	-19.9	2445	-0.98

LY-33/1 (Syenogranite)

LY-33/1-01	133.1	0.0414	0.0011	0.282170	0.000052	0.282167	-21.3	-18.5	2360	-0.97
LY-33/1-02	133.9	0.0556	0.0015	0.282103	0.000046	0.282099	-23.7	-20.9	2511	-0.96
LY-33/1-07	133.8	0.0685	0.0018	0.282117	0.000056	0.282112	-23.2	-20.4	2481	-0.95
LY-33/1-10	133.3	0.0419	0.0011	0.282126	0.000043	0.282123	-22.8	-20.0	2458	-0.97
LY-33/1-11	132.2	0.0647	0.0018	0.282136	0.000050	0.282132	-22.5	-19.8	2440	-0.95
LY-33/1-12	133.5	0.0670	0.0018	0.282140	0.000047	0.282136	-22.4	-19.6	2430	-0.95
LY-33/1-18	133.5	0.0515	0.0014	0.282154	0.000043	0.282151	-21.9	-19.1	2397	-0.96
LY-33/1-21	133.8	0.0467	0.0013	0.282117	0.000044	0.282114	-23.2	-20.3	2479	-0.96
LY-33/1-22	131.7	0.0486	0.0013	0.282145	0.000045	0.282142	-22.2	-19.4	2418	-0.96

LY-33/1-23	131.6	0.0486	0.0013	0.282127	0.000038	0.282124	-22.8	-20.0	2458	-0.96
LY-36/1 (Syenogranite)										
LY-36/1-02	130.8	0.0309	0.0008	0.282115	0.000040	0.282113	-23.2	-20.4	2483	-0.98
LY-36/1-04	129.3	0.0327	0.0009	0.282079	0.000034	0.282077	-24.5	-21.8	2564	-0.97
LY-36/1-07	127.0	0.0591	0.0015	0.282106	0.000050	0.282102	-23.6	-20.9	2508	-0.95
LY-36/1-09	126.4	0.0568	0.0015	0.282087	0.000046	0.282084	-24.2	-21.6	2551	-0.96
LY-36/1-11	132.7	0.0362	0.0010	0.282135	0.000037	0.282133	-22.5	-19.7	2438	-0.97
LY-36/1-16	132.2	0.0347	0.0009	0.282121	0.000039	0.282119	-23.0	-20.2	2469	-0.97
LY-36/1-23	132.8	0.0454	0.0012	0.282095	0.000039	0.282092	-23.9	-21.1	2528	-0.96
LY-36/1-24	129.5	0.0517	0.0013	0.282131	0.000049	0.282128	-22.7	-19.9	2451	-0.96
LY-36/1-26	127.6	0.0550	0.0014	0.282140	0.000041	0.282137	-22.4	-19.7	2432	-0.96
LY-36/1-29	132.8	0.0726	0.0019	0.282137	0.000050	0.282132	-22.5	-19.7	2438	-0.94
LY-42/1 (Monzonite)										
LY-42/1-02	138.2	0.0223	0.0006	0.282144	0.000037	0.282142	-22.2	-19.2	2413	-0.98
LY-42/1-05	138.8	0.0561	0.0013	0.282152	0.000047	0.282149	-21.9	-19.0	2398	-0.96
LY-42/1-06	136.9	0.1149	0.0028	0.282220	0.000082	0.282213	-19.5	-16.8	2255	-0.92
LY-42/1-08	132.5	0.0193	0.0005	0.282164	0.000037	0.282163	-21.5	-18.6	2372	-0.98
LY-42/1-10	136.9	0.0417	0.0010	0.282157	0.000046	0.282154	-21.7	-18.8	2387	-0.97
LY-42/1-11	137.9	0.0391	0.0010	0.282174	0.000046	0.282171	-21.1	-18.2	2348	-0.97

LY-42/1-12	137.0	0.0283	0.0007	0.282136	0.000034	0.282134	-22.5	-19.6	2432	-0.98
LY-42/1-18	130.1	0.0187	0.0005	0.282147	0.000038	0.282146	-22.1	-19.3	2411	-0.99
LY-42/1-20	133.6	0.0476	0.0011	0.282147	0.000045	0.282144	-22.1	-19.3	2412	-0.97
LY-42/1-24	131.5	0.0501	0.0012	0.282142	0.000047	0.282139	-22.3	-19.5	2424	-0.96
LY-42/1-30	135.9	0.0522	0.0013	0.282115	0.000052	0.282112	-23.2	-20.4	2482	-0.96
LY-42/1-31	135.8	0.0160	0.0004	0.282123	0.000026	0.282122	-23.0	-20.0	2460	-0.99
LY-42/1-33	131.7	0.0402	0.0010	0.282151	0.000042	0.282149	-22.0	-19.2	2403	-0.97
LY-42/1-34	137.0	0.0459	0.0011	0.282151	0.000037	0.282148	-22.0	-19.1	2401	-0.97

LYN-1/3 (Monzogranite)

LYN-1/3-11	128.0	0.0262	0.0007	0.282123	0.000016	0.282121	-23.0	-20.2	2466	-0.98
LYN-1/3-20	129.0	0.0317	0.0008	0.282126	0.000016	0.282124	-22.9	-20.1	2460	-0.98
LYN-1/3-21	127.6	0.0157	0.0004	0.282104	0.000012	0.282103	-23.6	-20.9	2507	-0.99
LYN-1/3-27	129.1	0.0231	0.0006	0.282125	0.000017	0.282123	-22.9	-20.1	2461	-0.98
LYN-1/3-32	129.5	0.0252	0.0007	0.282091	0.000016	0.282090	-24.1	-21.3	2536	-0.98

LY-8/1 (Lamprophyre)

LY-8/1-7	117.6	0.0258	0.0006	0.282128	0.000018	0.282126	-22.8	-20.3	2462	-0.98
LY-8/1-10	112.4	0.0350	0.0009	0.282234	0.000025	0.282232	-19.0	-16.6	2229	-0.97
LY-8/1-12	115.6	0.0350	0.0009	0.282134	0.000017	0.282132	-22.6	-20.1	2450	-0.97
LY-8/1-13	118.2	0.0430	0.0014	0.282139	0.000026	0.282136	-22.4	-19.9	2439	-0.96

LY-8/1-19	112.6	0.1193	0.0038	0.282605	0.000063	0.282597	-5.9	-3.7	1412	-0.89
LY-8/1-20	113.0	0.0871	0.0019	0.282224	0.000022	0.282219	-19.4	-17.1	2256	-0.94
LY-8/1-25	116.3	0.1513	0.0040	0.282653	0.000037	0.282644	-4.2	-2.0	1301	-0.88
LY-16/1 (Lamprophyre)										
LY-16/1-7	114.1	0.0616	0.0015	0.282366	0.000028	0.282363	-14.4	-12.0	1936	-0.95
LY-16/1-17	115.0	0.0476	0.0011	0.282431	0.000020	0.282428	-12.1	-9.6	1789	-0.97
LY-16/1-1	115.0	0.0339	0.0008	0.282551	0.000030	0.282549	-7.8	-5.4	1517	-0.98
LY-16/1-14	115.1	0.0477	0.0012	0.282497	0.000019	0.282494	-9.7	-7.3	1641	-0.96
LY-16/1-42	117.0	0.0423	0.0011	0.282343	0.000016	0.282340	-15.2	-12.7	1984	-0.97
LYN-1/1 (Lamprophyre)										
LYN-1/1-2	134.4	0.0703	0.0017	0.282141	0.000022	0.282137	-22.3	-19.5	2427	-0.95
LYN-1/1-3	125.8	0.0201	0.0006	0.282147	0.000013	0.282146	-22.1	-19.4	2414	-0.98
LYN-1/1-5	112.0	0.0452	0.0010	0.282235	0.000023	0.282233	-19.0	-16.6	2228	-0.97
LYN-1/1-25	111.6	0.0453	0.0011	0.282224	0.000019	0.282221	-19.4	-17.0	2254	-0.97
LYN-1/1-27	125.7	0.0258	0.0007	0.282093	0.000016	0.282092	-24.0	-21.3	2534	-0.98
LYN-1/1-34	118.8	0.0391	0.0009	0.282232	0.000015	0.282230	-19.1	-16.6	2231	-0.97
LYN-2/1 (Lamprophyre)										
LYN-2/1-1	127.0	0.0195	0.0005	0.282106	0.000014	0.282105	-23.6	-20.8	2504	-0.98
LYN-2/1-2	111.5	0.0534	0.0013	0.282245	0.000017	0.282243	-18.6	-16.3	2206	-0.96

LYN-2/1-4	110.5	0.0431	0.0010	0.282223	0.000022	0.282221	-19.4	-17.1	2256	-0.97
LYN-2/1-8	130.3	0.0242	0.0006	0.282110	0.000016	0.282109	-23.4	-20.6	2493	-0.98
LYN-2/1-9	132.0	0.0619	0.0015	0.282116	0.000021	0.282113	-23.2	-20.4	2483	-0.96
LYN-2/1-19	107.1	0.0649	0.0016	0.282230	0.000021	0.282226	-19.2	-17.0	2245	-0.95
LYN-2/1-28	112.9	0.0296	0.0007	0.282216	0.000018	0.282215	-19.7	-17.2	2268	-0.98
LYN-2/1-29	126.4	0.0441	0.0010	0.282526	0.000019	0.282523	-8.7	-6.0	1569	-0.97
LY-15/1 (Dolerite)										
LY-15/1-1	122.0	0.0433	0.0011	0.282222	0.000016	0.282220	-19.4	-16.9	2250	-0.97
LY-15/1-4	123.2	0.0425	0.0010	0.282232	0.000018	0.282229	-19.1	-16.5	2229	-0.97
LY-15/1-9	123.4	0.0326	0.0008	0.282255	0.000015	0.282253	-18.3	-15.6	2175	-0.98
LY-15/1-25	124.7	0.0434	0.0010	0.282064	0.000013	0.282062	-25.0	-22.4	2600	-0.97
LY-15/1-26	126.2	0.0275	0.0007	0.282062	0.000013	0.282061	-25.1	-22.4	2602	-0.98
LY-16/2 (Dolerite)										
LY-16/2-1	115.6	0.0406	0.0009	0.282085	0.000028	0.282083	-24.3	-21.8	2559	-0.97
LY-16/2-7	115.6	0.0357	0.0012	0.282085	0.000020	0.282082	-24.3	-21.9	2561	-0.96
LY-16/2-13	115.9	0.0345	0.0008	0.282300	0.000015	0.282298	-16.7	-14.2	2080	-0.97
LY-16/2-20	115.9	0.0460	0.0010	0.282169	0.000019	0.282167	-21.3	-18.9	2372	-0.97
LY-16/2-29	117.2	0.0376	0.0010	0.282163	0.000018	0.282160	-21.6	-19.1	2386	-0.97
LY-16/2-35	119.0	0.0288	0.0007	0.282154	0.000019	0.282153	-21.8	-19.3	2402	-0.98

LY-18/1 (Dolerite)

LY.18.1	123.9	0.0113	0.0003	0.282143	0.000022	0.282142	-22.3	-19.6	2424	-0.99
LY-18/1-2	123.5	0.0347	0.0008	0.282252	0.000033	0.282250	-18.4	-15.7	2181	-0.97
LY-18/1-13	123.1	0.0614	0.0015	0.282229	0.000028	0.282226	-19.2	-16.6	2236	-0.96
LY-18/1-15	121.9	0.0226	0.0007	0.282143	0.000021	0.282141	-22.2	-19.6	2426	-0.98
LY-18/1-16	121.9	0.0431	0.0010	0.282223	0.000022	0.282221	-19.4	-16.8	2249	-0.97

LY-26/1 (Dolerite)

LY-26/1-11	118.7	0.0235	0.0005	0.282054	0.000018	0.282053	-25.4	-22.8	2625	-0.98
LY-26/1-14	123.5	0.0203	0.0005	0.282109	0.000020	0.282108	-23.4	-20.8	2498	-0.98
LY-26/1-16	118.7	0.0369	0.0009	0.282091	0.000020	0.282089	-24.1	-21.6	2544	-0.97
LY-26/1-18	121.0	0.0235	0.0006	0.282039	0.000011	0.282038	-25.9	-23.3	2656	-0.98
LY-26/1-22	117.7	0.0271	0.0006	0.282089	0.000017	0.282088	-24.2	-21.6	2548	-0.98
LY-26/1-37	119.4	0.0413	0.0009	0.282059	0.000011	0.282057	-25.2	-22.7	2614	-0.97

LYN-4/1 (Dolerite)

LYN-4/1-4	124.5	0.0142	0.0004	0.282134	0.000018	0.282133	-22.6	-19.9	2442	-0.99
LYN-4/1-10	124.3	0.0247	0.0005	0.282140	0.000013	0.282139	-22.4	-19.7	2430	-0.98
LYN-4/1-12	125.6	0.0370	0.0009	0.282218	0.000014	0.282216	-19.6	-16.9	2256	-0.97
LYN-4/1-18	123.8	0.0220	0.0006	0.282136	0.000015	0.282135	-22.5	-19.8	2439	-0.98

LY-34/1 (Diorite)

LY-34/1-4	130.1	0.0377	0.0009	0.282132	0.000014	0.282129	-22.6	-19.9	2447	-0.97
LY-34/1-17	132.7	0.0305	0.0008	0.282146	0.000013	0.282144	-22.2	-19.3	2413	-0.98
LY-34/1-20	131.4	0.0275	0.0007	0.282093	0.000016	0.282091	-24.0	-21.2	2532	-0.98
LY-34/1-30	132.6	0.0323	0.0008	0.282163	0.000016	0.282161	-21.5	-18.7	2375	-0.98
LY-34/1-31	131.0	0.0525	0.0012	0.282066	0.000019	0.282063	-25.0	-22.2	2594	-0.96
LYN-1/4 (Granodiorite)										
LYN-1/4-2	128.1	0.0196	0.0005	0.282088	0.000016	0.282087	-24.2	-21.4	2544	-0.98
LYN-1/4-14	127.5	0.0301	0.0008	0.282117	0.000015	0.282115	-23.2	-20.4	2480	-0.98
LYN-1/4-21	128.6	0.0602	0.0014	0.282208	0.000016	0.282205	-19.9	-17.2	2279	-0.96
LYN-1/4-33	127.3	0.0204	0.0005	0.282081	0.000015	0.282080	-24.4	-21.7	2559	-0.98
LYN-1/4-36	126.8	0.0232	0.0006	0.282063	0.000017	0.282062	-25.1	-22.3	2599	-0.98
Reference data: ($^{176}\text{Hf}/^{177}\text{Hf}$) _{DM} =0.28325 (Griffin et al., 2000), ($^{176}\text{Lu}/^{177}\text{Hf}$) _{DM} =0.0384 (Griffin et al., 2000), ($^{176}\text{Lu}/^{177}\text{Hf}$) _{crust} =0.015 (Griffin et al., 2002)										

Table 7-1 Major and trace elemental data of the Laiyuan volcanic rocks analyzed in this study.

Sample	LY-39/1	LY-39/2	LY-39/3	LY-40/1	LY-40/2	LYN-3/1	LYN-3/2
Major elements (wt. %)							
SiO ₂	66.21	62.81	63.16	60.68	60.44	59.13	66.46
TiO ₂	0.53	0.75	0.68	0.89	0.82	0.88	0.49
Al ₂ O ₃	14.56	15.89	15.68	15.99	15.91	17.73	15.22
FeO	2.50	2.60	1.35	2.32	1.13	2.50	0.52
Fe ₂ O ₃	1.65	2.15	4.36	3.34	5.10	3.39	0.41
MnO	0.10	0.08	0.12	0.08	0.08	0.10	0.05
MgO	2.58	2.29	1.82	2.78	2.93	1.74	1.34
CaO	3.43	5.15	3.80	4.62	3.27	5.06	3.06
Na ₂ O	3.56	3.49	3.80	4.17	4.54	4.66	6.31
K ₂ O	3.77	2.99	2.99	3.41	3.86	2.73	3.25
P ₂ O ₅	0.22	0.30	0.26	0.42	0.28	0.36	0.21
CO ₂	0.26	0.26	0.17	0.17	0.26	0.17	2.06
H ₂ O ⁺	0.94	0.95	1.10	1.04	1.28	1.08	0.77
Total	100.31	99.71	99.29	99.91	99.90	99.53	100.15
LOI	0.70	0.69	1.35	1.00	1.43	0.85	2.58
TFeO	3.98	4.53	5.27	5.33	5.72	5.55	0.89
TFe ₂ O ₃	4.43	5.04	5.86	5.92	6.36	6.17	0.99
Mg [#]	53.58	47.38	38.09	48.20	47.73	35.85	72.88
Na ₂ O+K ₂ O	7.33	6.48	6.79	7.58	8.40	7.39	9.56
Trace elements (ppm)							
Li	8.74	3.73	10.90	10.30	9.68	10.10	10.50
Be	2.08	1.79	1.59	1.60	1.49	1.37	2.11
Mn	776.00	670.00	992.00	593.00	613.00	790.00	395.00
Co	13.40	13.00	16.00	15.90	19.60	13.50	2.27
Ni	21.70	22.80	21.20	21.00	37.30	5.43	7.77
Cu	27.90	56.80	8.95	20.50	4.99	17.90	5.17
Zn	134.00	100.00	108.00	87.60	198.00	83.80	59.00
Ga	19.40	20.80	20.30	21.30	21.10	21.50	20.00
Rb	78.30	46.20	51.90	63.80	66.60	59.20	76.70
Sr	748.00	1493.00	1026.00	1186.00	1060.00	1072.00	204.00
Mo	1.46	0.56	1.01	1.26	0.62	1.09	0.21
Cs	1.42	0.72	0.55	0.73	0.60	1.94	0.92
Ba	1484.00	2025.00	1548.00	1654.00	1828.00	1527.00	942.00
Tl	0.63	0.30	0.16	0.20	0.46	0.53	0.35
Pb	43.10	15.70	18.10	15.10	62.70	8.56	31.70
Th	9.49	6.79	6.53	6.23	5.04	4.54	7.88
U	2.33	1.58	1.58	1.37	1.14	0.96	1.73
Nb	9.19	8.65	8.25	9.62	8.51	8.38	9.91

Ta	0.65	0.58	0.57	0.57	0.53	0.47	0.62
Zr	145.00	172.00	176.00	207.00	181.00	205.00	137.00
Hf	4.22	4.67	4.93	5.34	4.77	5.29	3.92
W	1.54	0.80	0.99	0.61	0.81	0.57	2.69
As	0.80	1.00	1.44	1.20	4.34	0.99	0.74
V	88.20	101.00	105.00	113.00	118.00	116.00	67.90
La	61.10	52.50	50.80	59.20	43.70	42.30	18.90
Ce	92.90	98.10	94.40	113.00	92.10	95.50	53.10
Pr	8.91	10.60	10.10	12.30	10.50	10.70	6.96
Nd	29.90	37.00	34.90	44.10	36.90	39.70	29.50
Sm	4.97	5.83	5.62	7.04	6.05	6.73	5.05
Eu	1.34	1.69	1.52	1.85	1.55	1.76	1.14
Gd	3.49	3.60	3.57	4.40	4.06	4.59	3.58
Tb	0.48	0.47	0.46	0.57	0.56	0.65	0.41
Dy	2.32	2.07	2.10	2.59	2.67	3.29	1.91
Ho	0.41	0.34	0.36	0.44	0.47	0.62	0.29
Er	1.07	0.92	0.99	1.17	1.26	1.75	0.78
Tm	0.15	0.13	0.14	0.15	0.17	0.24	0.10
Yb	0.95	0.80	0.89	0.97	1.11	1.56	0.68
Lu	0.15	0.12	0.14	0.14	0.17	0.23	0.10
Sc	11.50	9.60	9.23	10.30	13.90	12.70	5.65
Y	11.50	9.52	9.53	12.10	13.70	16.70	8.29
ΣREE	208.14	214.17	205.99	247.92	201.27	209.62	122.50
LREE/HREE	22.08	24.35	22.81	22.77	18.22	15.21	14.61
(La/Yb)_N	46.13	47.07	40.94	43.78	28.24	19.45	19.94
δEu	0.93	1.05	0.97	0.95	0.90	0.92	0.78
δCe	0.86	0.96	0.96	0.97	1.02	1.07	1.13
Nb/U	3.94	5.47	5.22	7.02	7.46	8.73	5.73
Lu/Yb	0.16	0.15	0.16	0.14	0.15	0.15	0.15
Sr/Y	65.04	156.83	107.66	98.02	77.37	64.19	24.61
La/Yb	64.32	65.63	57.08	61.03	39.37	27.12	27.79

$Mg^{\#} = 100 \times \text{molar Mg}/(\text{Mg} + \text{Fe})$.

Table 8-1 Major and trace elemental data of the Laiyuan granitoids analyzed in this study.

Sample	Syenogranite			Monzogranite					Quartz monzonite				Monzonite				
	LY-33/1	LY-36/1	LY-37/1 -1	LY-19/1	LY-21/2	LY-22/3	LY-22/4 -1	LYN-1/ 3	LY-21/1	LY-22/4 -2	LY-37/1 -2	LYN-1/ 2	LY-20/1	LY-22/1	LY-22/2	LY-42/1	LY-42/2
Major elements (wt. %)																	
SiO₂	75.20	74.93	75.95	69.17	70.39	69.58	69.77	71.34	61.99	60.85	65.23	60.98	58.84	58.99	58.02	59.23	55.01
TiO₂	0.11	0.23	0.13	0.57	0.35	0.39	0.50	0.36	0.74	1.01	0.49	0.95	0.91	0.84	0.86	0.98	1.08
Al₂O₃	13.21	13.17	13.03	14.50	14.68	14.90	14.37	14.07	16.77	16.42	16.80	16.44	16.76	16.29	16.55	15.69	16.86
Fe₂O₃	0.73	0.77	0.86	1.42	1.05	1.17	1.46	1.34	2.21	2.73	1.61	3.49	2.41	3.45	3.23	3.65	5.06
FeO	0.30	0.30	0.09	1.55	0.99	1.11	1.31	1.13	2.58	2.82	1.56	2.07	3.64	3.54	3.75	2.68	2.78
MnO	0.01	0.05	0.02	0.05	0.04	0.05	0.04	0.06	0.08	0.05	0.13	0.05	0.10	0.13	0.14	0.12	0.12
MgO	0.13	0.21	0.11	1.17	0.78	0.84	1.07	1.03	1.99	2.67	1.36	1.91	2.74	3.34	3.46	3.76	3.74
CaO	0.34	0.67	0.36	2.27	1.75	2.24	2.37	2.01	4.00	3.33	3.07	2.00	5.07	5.02	5.69	3.95	5.03
Na₂O	4.47	4.45	4.33	3.89	4.25	4.83	4.59	3.91	4.92	5.70	6.94	4.30	4.13	4.45	4.19	4.73	4.64
K₂O	4.81	4.58	4.43	4.74	4.86	3.62	3.57	4.14	3.17	2.37	2.05	4.01	3.47	2.46	2.70	1.90	2.98
P₂O₅	0.02	0.02	0.01	0.16	0.13	0.14	0.17	0.16	0.36	0.43	0.18	0.86	0.33	0.39	0.40	0.32	0.35
H₂O⁺	0.46	0.14	0.48	0.70	0.34	0.40	0.32	0.66	0.74	0.90	0.56	2.38	1.08	0.94	0.87	2.01	1.93
CO₂	0.11	0.09	0.06	0.12	0.07	0.04	0.07	0.17	0.05	0.07	0.20	0.51	0.06	0.17	0.17	0.17	0.17

LOI	0.63	0.58	0.69	0.88	0.62	0.95	0.59	0.48	0.88	1.32	1.12	2.88	1.14	0.58	0.42	2.06	1.87
TFe2O3	1.07	1.11	0.96	3.14	2.14	2.40	2.91	2.60	5.07	5.87	3.35	5.79	6.46	7.38	7.40	6.63	8.15
A/CNK	1.00	0.98	1.04	0.93	0.95	0.94	0.91	0.97	0.89	0.91	0.87	1.09	0.85	0.85	0.82	0.92	0.84
K₂O/Na₂O	1.08	1.03	1.02	1.22	1.14	0.75	0.78	1.06	0.64	0.42	0.30	0.93	0.84	0.55	0.64	0.40	0.64
Mg[#]	20	27	19	43	42	41	42	44	44	47	45	40	46	47	48	53	48
T_{Zr} (°C)	774	781	775	841	801	810	815	773	859	847	820	885	816	785	782	769	773

Trace elements (ppm)

Rb	113.90	87.18	101.20	162.90	102.80	100.20	87.36	95.30	80.30	145.10	40.57	128.00	88.34	136.00	129.00	34.50	53.30
Sr	46.43	100.60	73.14	517.40	608.40	695.90	642.60	547.00	1251.00	836.10	783.10	730.00	919.30	889.00	936.00	785.00	879.00
Ba	265.48	354.42	310.13	1101.31	1760.41	990.49	811.95	1243.00	1545.28	561.95	585.08	2347.00	1332.95	871.00	1147.00	1019.00	1724.00
Th	10.43	7.51	9.45	12.54	8.11	8.62	11.67	9.82	5.74	16.87	6.32	6.86	4.23	4.94	5.09	2.33	2.58
U	2.45	1.23	1.08	2.02	3.11	2.22	1.50	2.57	1.87	3.05	1.53	1.59	0.62	1.36	1.37	0.86	0.99
Nb	17.02	15.74	14.55	25.11	14.69	13.33	18.60	12.30	14.44	32.94	22.59	37.60	10.90	9.93	9.98	6.51	7.19
Ta	0.93	1.44	1.89	1.81	1.79	1.49	2.37	0.74	1.11	1.53	2.04	1.84	0.85	0.58	0.63	0.40	0.44
Zr	141.64	153.19	143.42	295.79	192.55	209.91	223.24	138.00	353.99	312.19	234.50	458.00	225.47	160.00	153.00	132.00	139.00
Hf	3.91	4.98	4.76	8.57	5.33	6.56	6.02	4.01	8.52	8.09	7.41	8.91	6.27	4.07	4.18	3.50	3.89
Co	1.75	1.05	0.64	6.80	4.40	4.40	6.23	4.94	10.10	12.55	7.49	11.80	17.78	20.00	18.30	24.80	22.60

Ni	1.23	1.31	1.29	6.21	4.91	5.44	6.71	5.77	8.88	17.26	7.74	11.40	11.16	12.30	12.80	38.10	35.40
Cr	4.74	5.33	5.07	14.82	10.93	10.15	14.59	14.50	20.32	40.31	13.56	23.60	21.02	16.30	16.70	70.70	85.30
V	8.69	13.71	1.78	59.32	37.53	28.09	62.20	44.00	76.49	105.11	58.29	94.40	133.66	139.00	141.00	168.00	179.00
Sc	1.15	1.08	0.91	4.54	2.08	2.55	3.10	4.44	5.07	7.24	4.17	7.16	10.33	17.20	17.50	16.40	16.90
Li	5.15	12.88	16.54	33.52	13.78	15.41	13.15	9.09	23.84	35.63	22.38	44.80	15.34	24.40	22.10	24.80	16.10
Cs	0.79	1.25	1.42	4.76	1.13	1.61	0.96	1.55	1.50	5.05	1.03	4.76	2.48	5.89	5.36	0.44	0.58
Be	2.29	1.58	2.11	2.59	1.90	2.32	2.19	2.54	2.08	3.78	2.17	3.20	1.67	1.83	1.70	0.95	1.02
Ga	18.96	16.63	17.57	18.72	18.85	19.12	20.02	17.70	23.09	27.90	21.02	22.40	20.53	20.30	20.50	20.80	20.10
In	0.01	0.01	0.01	0.03	0.01	0.02	0.01	<0.05	0.04	0.02	0.03	0.05	0.03	0.06	0.05	0.05	0.06
Tl	0.37	0.36	0.40	0.78	0.45	0.71	0.33	0.55	0.44	0.61	0.13	0.67	0.50	0.92	1.03	0.27	0.43
Cu	23.93	2.52	2.75	9.87	3.15	4.08	18.13	4.44	8.41	7.26	8.66	6.85	17.88	1.04	<0.05	1.70	17.70
Pb	11.68	17.55	12.19	20.60	22.66	24.15	12.79	20.10	16.19	13.96	15.57	14.40	13.05	23.80	30.00	18.50	21.50
Zn	14.17	27.17	14.79	52.39	39.95	54.70	30.85	47.60	82.05	44.23	68.98	111.00	76.10	130.00	141.00	147.00	117.00
As	0.88	0.90	1.14	1.65	0.87	0.97	1.09	0.28	1.12	0.97	1.43	0.44	1.21	0.83	0.76	8.51	8.09
Sb	0.76	0.13	0.11	0.38	0.08	0.19	0.14	<0.05	1.43	0.08	0.21	<0.05	0.13	0.15	0.15	0.54	0.61
Bi	0.19	0.04	0.29	0.17	0.04	0.06	0.06	<0.05	0.09	0.09	0.07	0.48	0.07	0.12	<0.05	0.17	0.16
W	0.77	0.64	1.61	1.38	0.51	2.26	0.92	0.48	1.00	4.62	0.30	8.14	0.63	2.83	1.77	0.48	0.43

Sn	1.08	1.17	1.18	1.63	0.97	0.95	1.04	0.89	1.13	1.74	1.69	1.35	1.08	0.97	0.88	0.99	0.76
Mo	0.53	0.36	0.27	1.22	0.39	0.48	0.65	0.44	0.65	1.11	0.31	0.57	0.26	0.36	0.36	1.02	1.08
Cd	0.04	0.02	0.02	0.03	0.02	0.02	0.03	<0.05	0.04	0.07	0.04	0.09	0.09	<0.05	<0.05	0.10	0.07
La	228.17	30.35	19.02	33.19	9.52	22.60	29.92	50.30	20.81	53.70	29.47	124.00	19.28	35.80	35.40	28.60	33.70
Ce	321.47	50.91	33.88	65.82	23.62	37.58	51.83	77.70	44.02	83.81	53.75	225.00	39.04	80.30	82.10	67.00	76.00
Pr	26.92	4.48	2.56	6.22	2.74	3.37	4.70	7.48	4.56	6.86	5.24	25.50	4.04	9.34	9.35	7.92	9.21
Nd	109.82	20.55	10.91	30.48	15.04	16.13	23.08	24.20	24.61	33.29	26.77	120.00	22.64	35.60	35.10	31.90	36.10
Sm	16.10	3.29	1.66	4.72	2.43	2.38	3.45	3.49	4.08	5.21	5.07	12.20	4.19	6.51	6.53	5.67	6.58
Eu	1.43	0.40	0.27	0.95	0.70	0.72	0.95	0.97	1.23	1.29	0.90	3.16	1.33	1.78	1.89	1.66	1.95
Gd	12.04	2.61	1.38	3.81	1.82	1.93	2.77	2.43	2.95	4.25	4.05	7.57	3.60	5.10	5.14	4.09	4.74
Tb	1.31	0.35	0.19	0.52	0.23	0.24	0.31	0.29	0.37	0.47	0.61	0.84	0.54	0.72	0.73	0.59	0.67
Dy	5.49	1.73	1.14	2.60	1.04	1.10	1.38	1.35	1.74	2.01	3.30	3.74	2.81	3.73	3.85	2.92	3.27
Ho	1.01	0.36	0.24	0.54	0.19	0.22	0.27	0.21	0.34	0.39	0.71	0.58	0.60	0.69	0.72	0.53	0.58
Er	2.61	1.01	0.76	1.49	0.50	0.62	0.73	0.60	0.88	1.07	1.93	1.40	1.56	1.99	2.05	1.39	1.60
Tm	0.35	0.16	0.13	0.23	0.07	0.09	0.11	0.08	0.13	0.15	0.29	0.19	0.23	0.28	0.28	0.19	0.21
Yb	1.92	0.99	0.84	1.41	0.43	0.53	0.61	0.57	0.76	0.88	1.66	1.16	1.30	1.82	1.92	1.23	1.33
Lu	0.30	0.16	0.13	0.23	0.07	0.09	0.10	0.09	0.12	0.16	0.24	0.17	0.22	0.27	0.29	0.18	0.20

Y	28.99	8.19	5.32	11.73	4.31	4.82	5.84	6.51	6.96	8.65	15.50	16.70	11.76	19.90	19.50	14.50	15.40
ΣREE	728.95	117.33	73.10	152.21	58.42	87.62	120.21	169.76	106.60	193.56	133.99	525.51	101.36	183.93	185.35	153.87	176.14
LREE/HREE	28.12	14.95	14.18	13.06	12.36	17.14	18.14	29.21	13.63	19.60	9.48	32.58	8.35	11.60	11.37	12.84	12.98
(La/Yb)_N	85.10	21.99	16.22	16.90	15.70	30.47	35.06	63.30	19.67	43.82	12.70	76.68	10.63	14.11	13.23	16.68	18.18
δEu	0.30	0.40	0.52	0.67	0.97	1.00	0.91	0.97	1.04	0.82	0.59	0.93	1.03	0.91	0.96	1.00	1.02
δCe	0.84	0.95	1.03	1.05	1.12	0.94	0.96	0.87	1.06	0.92	0.98	0.93	1.03	1.05	1.08	1.07	1.04
Sr/Y	1.60	12.28	13.76	44.13	141.02	144.36	110.09	84.02	179.70	96.70	50.51	43.71	78.14	44.67	48.00	54.14	57.08
Th/Yb	5.42	7.59	11.23	8.90	18.65	16.21	19.07	17.23	7.57	19.19	3.79	5.91	3.25	2.71	2.65	1.89	1.94
Nb/Yb	8.85	15.90	17.29	17.83	33.79	25.05	30.39	21.58	19.03	37.47	13.57	32.41	8.38	5.46	5.20	5.29	5.41

Table 9-1 EPMA data of clinopyroxene.

No.	1	2	3	4	5	6	7	8	9	10	11	12	1	2	3
Sample No.	LY-13/2												LY-16/1		
No. oxygen	6														
SiO₂	48.05	49.46	51.00	50.87	49.99	51.08	50.17	50.56	49.85	47.41	46.99	50.83	49.35	47.70	47.63
Al₂O₃	5.52	4.67	3.50	3.59	3.25	3.48	3.77	3.56	3.90	6.31	6.59	3.02	6.20	8.53	8.44
TiO₂	2.16	1.62	1.17	1.09	1.11	1.22	1.12	1.00	1.29	1.80	2.37	1.05	0.78	1.37	1.18
Cr₂O₃	0.00	0.00	0.06	0.11	0.02	0.06	0.21	0.12	0.10	0.26	0.11	0.00	0.21	0.08	0.12
FeO	8.81	8.36	8.03	7.44	7.58	8.05	7.41	7.70	9.08	9.11	9.11	7.86	5.45	5.61	5.39
MnO	0.19	0.21	0.22	0.14	0.18	0.16	0.16	0.11	0.22	0.20	0.22	0.17	0.12	0.10	0.12
MgO	13.68	14.43	15.16	15.06	14.85	14.96	15.14	15.42	15.58	13.60	13.30	15.34	14.67	13.89	13.75
CaO	20.96	21.17	20.47	20.98	21.98	21.13	20.96	20.77	19.21	20.38	20.88	20.61	21.48	21.47	21.59
Na₂O	0.57	0.51	0.46	0.48	0.50	0.50	0.43	0.53	0.39	0.62	0.54	0.50	0.71	0.76	0.83
Total	100.02	100.43	100.06	99.79	99.55	100.64	99.39	99.78	99.65	99.69	100.09	99.40	98.97	99.53	99.08
Si	1.80	1.84	1.89	1.89	1.87	1.89	1.87	1.88	1.86	1.78	1.76	1.90	1.84	1.77	1.77
Al	0.24	0.20	0.15	0.16	0.14	0.15	0.17	0.16	0.17	0.28	0.29	0.13	0.27	0.37	0.37
Ti	0.06	0.05	0.03	0.03	0.03	0.03	0.03	0.03	0.04	0.05	0.07	0.03	0.02	0.04	0.03
Fe²⁺	0.28	0.26	0.25	0.23	0.24	0.25	0.23	0.24	0.28	0.29	0.29	0.25	0.17	0.17	0.17
Mn	0.01	0.01	0.01	0.00	0.01	0.00	0.01	0.00	0.01	0.01	0.01	0.01	0.00	0.00	0.00
Mg	0.76	0.80	0.84	0.83	0.83	0.82	0.84	0.85	0.87	0.76	0.74	0.85	0.81	0.77	0.76
Ca	0.84	0.84	0.81	0.83	0.88	0.84	0.84	0.83	0.77	0.82	0.84	0.82	0.86	0.85	0.86
Na	0.04	0.04	0.03	0.03	0.04	0.04	0.03	0.04	0.03	0.05	0.04	0.04	0.05	0.05	0.06
Total	4.04	4.03	4.02	4.02	4.04	4.02	4.03	4.03	4.03	4.04	4.04	4.02	4.03	4.03	4.04

Mg/(Fe+Mg)	0.73	0.75	0.77	0.78	0.78	0.77	0.78	0.78	0.75	0.73	0.72	0.78	0.83	0.82	0.82
En (Mg)	0.41	0.42	0.44	0.44	0.43	0.43	0.44	0.44	0.45	0.41	0.40	0.44	0.44	0.43	0.43
Wo (Ca)	0.45	0.44	0.43	0.44	0.45	0.44	0.44	0.43	0.40	0.44	0.45	0.43	0.47	0.48	0.48
Fs (Fe)	0.15	0.14	0.13	0.12	0.12	0.13	0.12	0.12	0.15	0.15	0.15	0.13	0.09	0.10	0.09

Continued Table 9-1

No.	4	5	6	7	8	9	10	11	12	13	14	15	16	17	18
Sample No.	LY-16/1														
SiO₂	48.64	48.73	44.37	45.00	46.14	45.98	37.57	47.49	47.14	48.76	49.31	49.61	47.97	48.49	48.25
Al₂O₃	7.49	7.62	9.50	9.04	7.98	8.74	14.18	6.18	6.31	7.01	7.34	6.84	5.28	5.69	5.72
TiO₂	1.22	1.19	3.11	2.92	1.75	2.17	5.22	2.20	2.30	1.06	1.00	1.15	1.72	1.86	1.92
Cr₂O₃	0.04	0.06	0.02	0.08	0.08	0.03	0.01	0.02	0.02	0.28	0.36	0.19	0.07	0.05	0.00
FeO	5.70	5.60	8.02	7.90	7.40	6.99	10.95	7.88	8.12	5.58	7.32	5.38	7.11	7.25	7.09
MnO	0.15	0.08	0.12	0.15	0.24	0.11	0.19	0.08	0.14	0.10	0.23	0.14	0.14	0.16	0.15
MgO	14.28	14.12	11.49	11.69	13.02	12.36	12.27	13.10	13.05	14.53	13.34	14.56	13.87	13.33	13.47
CaO	21.57	21.60	22.62	22.60	21.78	22.86	12.04	23.03	22.95	20.93	19.85	21.20	22.60	22.59	22.67
Na₂O	0.78	0.77	0.60	0.54	0.54	0.45	2.16	0.42	0.36	0.68	1.12	0.80	0.33	0.47	0.45
K₂O	0.00	0.01	0.04	0.01	0.25	0.00	1.59	0.02	0.01	0.01	0.00	0.00	0.01	0.00	0.01
Total	99.90	99.81	99.87	99.92	99.22	99.66	96.20	100.42	100.39	98.96	99.86	99.93	99.09	99.89	99.73
Si	1.80	1.80	1.67	1.69	1.74	1.72	5.70	1.78	1.77	1.81	1.83	1.82	1.81	1.81	1.81
Al	0.33	0.33	0.42	0.40	0.35	0.39	2.53	0.27	0.28	0.31	0.32	0.30	0.23	0.25	0.25
Ti	0.03	0.03	0.09	0.08	0.05	0.06	0.60	0.06	0.06	0.03	0.03	0.03	0.05	0.05	0.05
Fe²⁺	0.18	0.17	0.25	0.25	0.23	0.22	1.39	0.25	0.25	0.17	0.23	0.17	0.22	0.23	0.22
Mn	0.00	0.00	0.00	0.00	0.01	0.00	0.02	0.00	0.00	0.00	0.01	0.00	0.00	0.00	0.00
Mg	0.79	0.78	0.65	0.66	0.73	0.69	2.77	0.73	0.73	0.80	0.74	0.80	0.78	0.74	0.75
Ca	0.85	0.85	0.91	0.91	0.88	0.92	1.96	0.92	0.92	0.83	0.79	0.84	0.91	0.90	0.91

Na	0.06	0.06	0.04	0.04	0.04	0.03	0.63	0.03	0.03	0.05	0.08	0.06	0.02	0.03	0.03
Total	4.03	4.03	4.05	4.04	4.06	4.04	15.91	4.04	4.04	4.02	4.02	4.02	4.04	4.03	4.03
Mg/(Fe+Mg)	0.82	0.82	0.72	0.73	0.76	0.76	0.67	0.75	0.74	0.82	0.76	0.83	0.78	0.77	0.77
En (Mg)	0.43	0.43	0.36	0.36	0.40	0.38	0.45	0.38	0.38	0.44	0.42	0.44	0.41	0.40	0.40
Wo (Ca)	0.47	0.47	0.50	0.50	0.48	0.50	0.32	0.49	0.48	0.46	0.45	0.46	0.48	0.48	0.48
Fs (Fe)	0.10	0.10	0.14	0.14	0.13	0.12	0.23	0.13	0.13	0.10	0.13	0.09	0.12	0.12	0.12

Table 9-2 EPMA data of feldspar.

No.	1	2	1	2	3	4	5	6	1	2	3
Sample No.	LY-13/2		LY-16/1						LYN-1/4		
No. oxygen	8										
SiO ₂	67.09	66.69	57.33	55.58	57.98	56.94	65.70	65.90	63.45	63.51	64.77
Al ₂ O ₃	20.23	19.92	25.36	27.13	24.99	25.20	18.52	18.79	22.28	22.31	21.91
TiO ₂	0.00	0.01	0.14	0.10	0.07	0.09	0.02	0.00	0.00	0.00	0.00
Cr ₂ O ₃	0.02	0.01	0.00	0.06	0.00	0.00	0.00	0.06	0.00	0.00	0.03
FeO	0.02	0.00	0.32	0.47	0.32	0.54	0.23	0.19	0.21	0.18	0.19
MnO	0.00	0.04	0.02	0.00	0.00	0.00	0.00	0.01	0.00	0.02	0.00
NiO	0.00	0.04	0.07	0.00	0.00	0.02	0.01	0.00	0.00	0.00	0.07
MgO	0.01	0.01	0.03	0.09	0.01	0.11	0.00	0.00	0.00	0.00	0.02
CaO	0.99	0.92	6.97	8.58	6.41	7.16	0.38	0.47	4.04	4.03	3.29
Na ₂ O	11.61	11.70	5.67	5.53	5.91	6.12	3.91	4.04	9.21	9.00	9.66
K ₂ O	0.08	0.12	1.98	1.29	2.18	1.59	11.05	10.94	0.41	0.63	0.33
Total	100.05	99.46	97.87	98.82	97.86	97.77	99.81	100.40	99.60	99.67	100.26
Si	2.9432	2.9460	2.6316	2.5374	2.6582	2.6209	2.9933	2.9844	2.8206	2.8220	2.8530
Al	1.0457	1.0371	1.3715	1.4596	1.3502	1.3669	0.9940	1.0028	1.1669	1.1679	1.1370
Ti	0.0000	0.0003	0.0047	0.0033	0.0022	0.0031	0.0007	0.0000	0.0000	0.0000	0.0000
Cr	0.0008	0.0005	0.0000	0.0021	0.0000	0.0000	0.0000	0.0022	0.0000	0.0000	0.0011
Fe ²⁺	0.0006	0.0000	0.0122	0.0181	0.0124	0.0209	0.0086	0.0072	0.0078	0.0066	0.0070
Mn	0.0000	0.0015	0.0008	0.0000	0.0000	0.0000	0.0000	0.0004	0.0002	0.0007	0.0000
Ni	0.0000	0.0012	0.0025	0.0000	0.0000	0.0008	0.0002	0.0000	0.0000	0.0000	0.0025
Mg	0.0008	0.0005	0.0022	0.0063	0.0005	0.0077	0.0000	0.0000	0.0000	0.0000	0.0010
Ca	0.0464	0.0435	0.3425	0.4195	0.3149	0.3528	0.0185	0.0229	0.1922	0.1917	0.1550

Na	0.9871	1.0014	0.5045	0.4890	0.5247	0.5455	0.3452	0.3544	0.7932	0.7748	0.8244
K	0.0047	0.0069	0.1158	0.0750	0.1273	0.0936	0.6422	0.6319	0.0232	0.0356	0.0183
Total	5.0294	5.0390	4.9881	5.0104	4.9904	5.0121	5.0027	5.0062	5.0041	4.9993	4.9993
Mg/(Fe+Mg)	0.59	1.00	0.15	0.26	0.04	0.27	0.00	0.00	0.00	0.00	0.13
Ca/(Ca+Na+K)	0.04	0.04	0.36	0.43	0.33	0.36	0.02	0.02	0.19	0.19	0.16
Mg/(Fe+Mg+Ca+Mn)	0.02	0.01	0.01	0.01	0.00	0.02	0.00	0.00	0.00	0.00	0.01
An%	4.47	4.13	35.58	42.66	32.56	35.57	1.84	2.27	19.06	19.13	15.53
Ab%	95.08	95.21	52.40	49.72	54.27	55.00	34.32	35.11	78.64	77.32	82.64
Or%	0.45	0.65	12.03	7.62	13.16	9.43	63.84	62.61	2.30	3.56	1.83

Continued Table 9-2

No.	4	5	6	7	8	9	10	11	12	13	14
Sample No.	LYN1-4										
No. oxygen	8										
SiO₂	64.63	63.02	62.93	66.58	66.67	58.27	60.67	59.60	67.07	63.47	64.00
Al₂O₃	21.37	23.04	22.55	20.28	20.28	25.41	23.94	24.09	20.21	17.99	18.19
TiO₂	0.00	0.00	0.00	0.03	0.00	0.00	0.04	0.00	0.00	0.02	0.03
Cr₂O₃	0.00	0.02	0.01	0.00	0.00	0.00	0.00	0.02	0.00	0.03	0.00
FeO	0.16	0.17	0.11	0.09	0.05	0.31	0.30	0.26	0.08	0.03	0.11
MnO	0.01	0.00	0.02	0.02	0.00	0.00	0.01	0.05	0.00	0.03	0.00
NiO	0.02	0.00	0.02	0.01	0.01	0.00	0.00	0.01	0.02	0.01	0.02
MgO	0.00	0.00	0.02	0.00	0.00	0.01	0.00	0.02	0.01	0.01	0.04
CaO	3.19	3.28	3.99	1.52	1.49	7.74	6.20	6.31	1.66	0.01	0.06
Na₂O	9.81	8.79	9.11	11.00	11.10	6.83	7.46	7.49	11.06	0.17	0.20
K₂O	0.28	1.02	0.29	0.10	0.08	0.54	0.73	0.71	0.18	16.01	16.02
Total	99.48	99.35	99.04	99.63	99.70	99.11	99.34	98.57	100.30	97.78	98.67

Si	2.8677	2.8068	2.8101	2.9346	2.9361	2.6342	2.7222	2.7001	2.9387	2.9999	2.9968
Al	1.1174	1.2094	1.1866	1.0535	1.0525	1.3535	1.2656	1.2861	1.0434	1.0017	1.0039
Ti	0.0000	0.0000	0.0000	0.0010	0.0000	0.0000	0.0012	0.0001	0.0000	0.0007	0.0012
Cr	0.0000	0.0007	0.0002	0.0000	0.0000	0.0000	0.0000	0.0008	0.0001	0.0010	0.0000
Fe²⁺	0.0060	0.0063	0.0041	0.0032	0.0020	0.0117	0.0114	0.0097	0.0030	0.0013	0.0043
Mn	0.0003	0.0000	0.0006	0.0007	0.0001	0.0000	0.0005	0.0019	0.0000	0.0012	0.0000
Ni	0.0009	0.0000	0.0006	0.0004	0.0005	0.0000	0.0000	0.0005	0.0008	0.0004	0.0008
Mg	0.0001	0.0001	0.0013	0.0000	0.0000	0.0003	0.0000	0.0014	0.0005	0.0006	0.0027
Ca	0.1515	0.1566	0.1906	0.0718	0.0704	0.3745	0.2980	0.3063	0.0781	0.0007	0.0028
Na	0.8438	0.7589	0.7885	0.9391	0.9475	0.5983	0.6484	0.6579	0.9394	0.0158	0.0185
K	0.0158	0.0578	0.0162	0.0057	0.0047	0.0313	0.0415	0.0410	0.0101	0.9652	0.9567
Total	5.0034	4.9965	4.9989	5.0100	5.0138	5.0039	4.9888	5.0058	5.0143	4.9885	4.9877
Mg/(Fe+Mg)	0.02	0.01	0.24	0.00	0.00	0.03	0.00	0.13	0.15	0.07	0.28
Ca/(Ca+Na+K)	0.15	0.16	0.19	0.07	0.07	0.37	0.30	0.30	0.08	1.60	1.89
Mg/(Fe+Mg+Ca+Mn)	0.00	0.00	0.01	0.00	0.00	0.00	0.00	0.00	0.01	98.32	97.83
An%	14.98	16.09	19.15	7.07	6.89	37.30	30.17	30.47	7.60	0.07	0.28
Ab%	83.46	77.97	79.22	92.37	92.65	59.59	65.63	65.45	91.42	1.60	1.89
Or%	1.56	5.94	1.63	0.56	0.46	3.12	4.20	4.08	0.98	98.32	97.83

Table 9-3 EPMA data of amphibole.

No.	1	2	1	2	3	4	5	6	1	2	3	4	5	6
Sample No.	LY-13/2		LY16-1						LYN1-4					
No. oxygen	23													
Comment	matrix	matrix	core	mantle	rim	core	core	rim	core	core	mantle	mantle	rim	rim
SiO ₂	40.71	39.78	37.57	38.17	38.89	37.57	37.78	38.69	45.76	48.44	47.91	47.92	44.10	45.70
Al ₂ O ₃	11.55	11.30	14.18	14.30	13.78	14.42	14.58	13.81	7.76	6.19	6.25	6.17	8.20	8.04
TiO ₂	5.12	5.32	5.22	4.87	3.31	5.88	5.88	3.61	1.82	1.31	1.16	1.09	1.96	1.73
Cr ₂ O ₃	0.00	0.00	0.01	0.00	0.06	0.05	0.00	0.00	0.00	0.02	0.00	0.00	0.02	0.01
FeO	10.85	11.27	10.95	11.46	14.62	10.92	10.88	14.11	14.03	12.80	13.60	13.57	14.95	13.84
MnO	0.21	0.15	0.19	0.14	0.22	0.18	0.14	0.28	0.43	0.45	0.45	0.47	0.47	0.41
NiO	0.0250	0.0000	0.0190	0.0000	0.0680	0.0000	0.0140	0.0040	0.0100	0.0000	0.0000	0.0280	0.0040	0.0360
MgO	12.46	12.86	12.27	12.37	10.93	12.02	12.16	10.51	13.27	14.54	14.05	13.94	13.51	13.45
CaO	10.89	11.42	12.04	12.03	11.55	11.90	12.09	11.31	11.51	11.52	11.47	11.32	11.25	11.31
Na ₂ O	2.60	2.55	2.16	2.24	2.33	1.99	2.15	2.36	1.73	1.46	1.42	1.42	1.92	1.91
K ₂ O	1.81	1.47	1.59	1.57	1.81	1.59	1.61	1.70	0.88	0.66	0.65	0.64	0.87	0.87
Total	93.70	93.49	96.20	97.14	97.56	96.53	97.28	96.37	97.19	97.39	96.96	96.58	97.23	97.30
Si	6.13	6.03	5.70	5.73	5.90	5.67	5.66	5.92	6.82	7.11	7.09	7.12	6.62	6.79
Al	2.05	2.02	2.53	2.53	2.46	2.56	2.57	2.49	1.36	1.07	1.09	1.08	1.45	1.41
Ti	0.58	0.61	0.60	0.55	0.38	0.67	0.66	0.41	0.20	0.14	0.13	0.12	0.22	0.19
Cr	0.00	0.00	0.00	0.00	0.01	0.01	0.00	0.00	0.00	0.00	0.00	0.00	0.00	0.00
Fe ²⁺	1.37	1.43	1.39	1.44	1.85	1.38	1.36	1.80	1.75	1.57	1.68	1.69	1.88	1.72
Mn	0.03	0.02	0.02	0.02	0.03	0.02	0.02	0.04	0.05	0.06	0.06	0.06	0.06	0.05
Ni	0.0030	0.0000	0.0023	0.0000	0.0083	0.0000	0.0017	0.0005	0.0012	0.0000	0.0000	0.0033	0.0005	0.0043

Mg	2.80	2.90	2.77	2.77	2.47	2.70	2.71	2.39	2.94	3.18	3.10	3.09	3.02	2.98
Ca	1.76	1.85	1.96	1.93	1.88	1.92	1.94	1.85	1.84	1.81	1.82	1.80	1.81	1.80
Na	0.76	0.75	0.63	0.65	0.68	0.58	0.62	0.70	0.50	0.42	0.41	0.41	0.56	0.55
K	0.35	0.28	0.31	0.30	0.35	0.31	0.31	0.33	0.17	0.12	0.12	0.12	0.17	0.16
Total	15.82	15.88	15.91	15.93	16.01	15.82	15.86	15.94	15.63	15.48	15.50	15.48	15.79	15.66
Mg/(Fe+Mg)	0.67	0.67	0.67	0.66	0.57	0.66	0.67	0.57	0.63	0.67	0.65	0.65	0.62	0.63

Table 9-4 EPMA data of biotite

No.	1	2	3	4	5	6
Sample No.	LYN1-4					
No. oxygen	22					
SiO₂	38.06	37.94	37.39	37.23	36.64	36.98
Al₂O₃	13.79	13.97	13.21	13.22	13.85	13.88
TiO₂	2.33	2.45	3.73	3.87	2.83	2.60
Cr₂O₃	0.043	0.017	0.017	0.000	0.033	0.027
FeO	16.00	16.27	16.19	16.84	17.69	17.43
MnO	0.30	0.38	0.92	1.00	0.92	0.91
NiO	0.000	0.000	0.022	0.000	0.048	0.000
MgO	13.92	13.74	13.39	13.19	12.48	12.67
CaO	0.15	0.10	0.06	0.03	0.14	0.10
Na₂O	0.07	0.07	0.11	0.12	0.14	0.16
K₂O	8.95	9.18	9.31	9.53	9.10	9.16
Total	93.62	94.12	94.34	95.03	93.87	93.90
Si	5.80	5.77	5.71	5.67	5.66	5.70
Al	2.48	2.50	2.38	2.37	2.52	2.52
Ti	0.27	0.28	0.43	0.44	0.33	0.30
Cr	0.0052	0.0020	0.0021	0.0000	0.0040	0.0033
Fe²⁺	2.04	2.07	2.07	2.14	2.29	2.25
Mn	0.04	0.05	0.12	0.13	0.12	0.12
Mg	3.16	3.11	3.04	2.99	2.87	2.91
Ca	0.02	0.02	0.01	0.00	0.02	0.02
Na	0.02	0.02	0.03	0.03	0.04	0.05
K	1.74	1.78	1.81	1.85	1.79	1.80
Total	15.57	15.60	15.60	15.64	15.66	15.66
Mg/(Fe+Mg)	0.61	0.60	0.60	0.58	0.56	0.56
Ca/(Ca+Na+K)	0.01	0.01	0.01	0.00	0.01	0.01
Mg/(Fe+Mg+Ca+Mn)	0.60	0.59	0.58	0.57	0.54	0.55
ΣAl	2.48	2.50	2.38	2.37	2.52	2.52
Fe/(Mg+Fe)	0.39	0.40	0.40	0.42	0.44	0.44

Table 9-5 Major and trace elemental data of the Laiyuan dyke suites analyzed in this study.

Lamprophyre Dykes					Dolerite Dykes										Felsic Dykes		
Sample	LYN-1/1	LYN-2/1	LY-8/1	LY-16/1	LY-18/1	LY-13/1	LY-13/2	LY-15/1	LY-15/2	LYN-4/1	LY-16/2	LY-26/1	LY-26/2	LY-7/1	LY-34/1	LYN-1/4	LYN-1/5
Major elements (wt. %)																	
SiO₂	46.97	46.65	44.57	44.51	48.32	50.25	50.16	51.77	50.44	55.05	55.60	56.50	56.82	47.98	58.02	68.65	73.27
Al₂O₃	15.72	16.01	16.63	14.44	15.26	15.66	15.51	15.82	15.44	16.01	15.23	15.90	15.98	14.39	16.80	15.32	14.23
Fe₂O₃	4.51	3.34	4.30	3.99	4.38	4.63	4.02	3.28	3.44	4.37	1.97	3.32	3.26	4.88	3.23	1.63	1.24
FeO	3.83	4.58	5.44	5.44	4.83	4.58	5.05	4.36	4.04	3.32	3.65	3.00	3.07	3.75	2.89	1.17	0.31
MgO	4.65	4.47	4.96	8.37	4.57	4.52	5.22	4.82	4.36	4.40	2.50	2.68	2.71	5.01	3.28	1.07	0.37
CaO	6.75	7.06	7.85	9.20	6.07	5.29	5.56	4.75	5.51	3.81	5.20	3.65	3.48	6.03	3.97	2.02	0.76
Na₂O	3.48	4.22	3.47	2.65	3.17	3.70	3.70	3.36	4.51	3.96	5.22	4.21	4.63	2.84	4.74	4.01	4.02
K₂O	3.79	3.70	3.67	3.41	4.36	4.50	4.17	4.25	3.04	4.05	2.84	4.51	4.12	3.76	3.23	4.07	4.77
TiO₂	1.44	1.45	2.01	1.71	2.08	1.95	1.91	1.60	1.59	1.57	1.09	1.14	1.15	1.62	0.95	0.38	0.23
P₂O₅	0.99	0.98	1.14	1.01	1.14	1.03	0.95	1.00	1.02	0.95	0.86	0.98	0.97	0.93	0.41	0.18	0.06
MnO	0.12	0.13	0.14	0.15	0.11	0.11	0.12	0.09	0.09	0.09	0.09	0.07	0.08	0.12	0.05	0.06	0.03
CO₂	3.94	4.20	2.40	0.86	2.49	0.69	0.51	1.29	3.26	0.17	3.17	1.80	1.46	4.97	0.77	0.26	0.26
H₂O⁺	3.05	2.46	2.73	3.42	2.66	2.66	2.60	3.18	2.85	2.13	1.74	1.64	1.79	3.10	1.22	1.51	0.68

Total	99.24	99.25	99.31	99.16	99.44	99.57	99.48	99.57	99.59	99.88	99.16	99.40	99.52	99.38	99.56	100.33	100.23
LOI	6.88	6.39	4.62	3.65	4.42	2.71	2.38	4.23	5.65	2.08	4.52	3.04	2.91	7.39	1.69	1.32	0.90
TFe₂O₃	8.77	8.43	10.34	10.03	9.75	9.72	9.63	8.12	7.93	8.06	6.03	6.65	6.67	9.05	6.44	2.93	1.58
Mg[#]	51.2	51.2	48.7	62.3	48.2	48.0	51.8	54.0	52.1	52.0	45.1	44.4	44.6	52.3	50.2	42.0	31.7

Trace elements (ppm)

Rb	110.00	81.40	114.00	113.00	127.00	123.00	130.00	98.50	74.30	72.50	70.60	172.00	105.00	98.50	105.00	96.10	129.00
Ba	2839.00	3910.00	3159.00	2434.00	1910.00	2792.00	1970.00	2832.00	2091.00	2618.00	2633.00	3127.00	2998.00	1672.0	1954.00	1381.00	1358.00
Pb	17.80	13.30	6.79	6.73	4.95	6.95	7.42	11.00	10.90	19.60	8.38	17.70	15.90	10.70	7.99	22.70	77.50
Sr	999.00	1798.00	1431.00	1949.00	916.00	972.00	924.00	1124.00	779.00	1381.00	941.00	1228.00	1141.00	754.00	1262.00	549.00	277.00
Cs	5.09	4.56	55.50	61.40	1.58	1.27	1.51	1.23	0.79	0.98	0.53	1.73	0.94	4.35	3.02	1.43	1.37
Th	9.89	9.93	7.24	7.83	2.43	2.55	2.57	3.18	3.34	4.41	7.12	7.91	7.68	2.85	4.54	8.78	10.40
U	2.32	2.44	1.53	1.58	0.66	0.73	0.80	0.79	0.84	1.23	1.79	2.07	1.95	0.84	1.82	2.26	2.81
Ta	3.14	3.15	3.84	4.38	2.83	2.44	2.27	1.60	1.69	1.81	2.09	2.11	2.07	1.87	0.50	0.73	0.82
Nb	64.90	64.50	65.80	76.40	44.30	39.60	36.90	27.40	29.20	32.70	35.30	35.90	34.70	30.30	8.76	11.20	12.20
Zr	370.00	362.00	241.00	245.00	303.00	305.00	300.00	328.00	331.00	358.00	336.00	354.00	351.00	265.00	192.00	185.00	176.00
Hf	6.93	6.97	6.44	6.19	7.97	7.98	7.62	8.38	8.51	7.28	8.65	8.94	8.64	6.75	4.95	5.22	5.01
Cr	75.80	68.60	28.30	279.00	77.60	90.60	103.00	110.00	104.00	80.10	33.80	33.10	31.10	117.00	102.00	11.30	3.51

Ni	37.70	38.70	30.70	119.00	45.00	43.20	58.30	52.40	54.70	40.40	17.80	18.90	18.90	60.60	32.00	4.63	1.43
Co	28.60	27.60	30.10	38.00	26.90	26.50	28.30	23.60	23.20	25.60	14.40	15.70	15.90	26.80	12.70	4.35	2.34
V	167.00	161.00	200.00	197.00	154.00	139.00	158.00	147.00	146.00	155.00	81.90	104.00	105.00	161.00	137.00	43.00	15.60
W	3.21	1.75	1.03	1.27	0.78	0.76	0.87	1.52	7.52	4.02	6.26	1.92	1.26	0.69	2.46	1.36	6.83
Li	73.50	54.70	39.60	39.40	33.60	29.60	33.10	39.90	49.80	23.90	41.40	27.00	22.00	85.10	42.70	7.83	6.31
Be	3.33	2.85	1.98	1.93	2.11	2.00	2.03	2.47	2.50	3.06	2.34	2.91	2.87	2.22	2.30	2.60	2.38
Mn	1003.00	1048.00	1090.00	1184.00	813.00	842.00	946.00	730.00	723.00	717.00	737.00	586.00	607.00	912.00	408.00	461.00	206.00
Mo	0.55	0.50	2.35	1.75	1.60	1.37	1.36	0.96	0.35	0.24	2.53	0.69	0.53	0.99	1.16	0.25	0.25
La	113.00	116.00	103.00	106.00	59.20	61.60	59.60	85.60	81.10	83.30	111.00	124.00	120.00	65.90	55.00	44.60	42.10
Ce	220.00	221.00	194.00	196.00	130.00	132.00	127.00	170.00	171.00	168.00	212.00	233.00	228.00	141.00	103.00	74.10	60.90
Pr	24.30	24.60	21.00	20.70	16.20	16.00	15.60	20.00	20.00	20.40	22.60	25.40	24.60	16.80	11.40	7.97	6.32
Nd	118.00	118.00	94.60	87.50	64.80	64.00	61.30	94.60	91.80	103.00	100.00	111.00	111.00	65.10	42.00	27.40	18.70
Sm	12.80	12.60	10.90	10.80	11.20	10.50	10.30	11.80	11.90	12.30	11.20	12.80	12.50	10.30	6.98	4.22	2.66
Eu	3.44	3.58	3.03	2.86	3.13	2.82	2.81	2.90	2.94	3.29	2.74	3.07	3.01	2.66	1.87	1.17	0.73
Gd	7.77	8.04	7.00	7.13	7.63	7.14	6.94	6.68	6.73	8.35	6.02	7.00	6.57	6.66	4.32	3.20	1.95
Tb	0.90	0.91	0.98	1.01	1.03	0.97	0.97	0.89	0.86	0.91	0.76	0.84	0.81	0.88	0.56	0.38	0.24
Dy	4.32	4.62	4.88	5.22	4.76	4.40	4.68	4.03	4.02	4.59	3.37	3.60	3.56	4.25	2.48	1.88	1.17

Ho	0.73	0.75	0.88	0.94	0.80	0.74	0.80	0.67	0.66	0.75	0.56	0.60	0.58	0.73	0.41	0.32	0.20
Er	1.98	2.07	2.25	2.47	1.95	1.88	2.03	1.58	1.58	1.97	1.30	1.36	1.36	1.92	1.06	0.97	0.68
Tm	0.27	0.28	0.30	0.34	0.25	0.24	0.26	0.21	0.21	0.27	0.18	0.19	0.19	0.26	0.14	0.14	0.10
Yb	1.71	1.77	1.84	2.13	1.52	1.44	1.60	1.28	1.27	1.62	1.08	1.12	1.12	1.60	0.88	0.87	0.76
Lu	0.26	0.26	0.28	0.31	0.22	0.21	0.24	0.18	0.18	0.24	0.15	0.17	0.16	0.23	0.13	0.14	0.13
Sc	16.20	15.10	15.70	25.30	13.80	13.50	15.30	13.30	13.60	15.40	8.55	8.98	9.07	15.40	12.50	4.97	2.04
Y	20.40	19.90	22.30	25.10	19.90	19.00	20.70	17.40	17.30	20.10	15.40	16.20	16.30	19.20	11.40	8.95	6.21
(La/Yb)_N	47.40	47.01	40.15	35.70	27.94	30.68	26.72	47.97	45.81	36.88	73.72	79.42	76.85	29.54	44.83	36.77	39.73
δEu	0.98	1.02	0.99	0.94	0.98	0.94	0.96	0.91	0.92	0.94	0.92	0.90	0.91	0.92	0.97	0.93	0.94
δGd	1.49	1.48	1.39	1.30	1.14	1.16	1.13	1.41	1.36	1.50	1.38	1.35	1.40	1.14	1.09	1.05	0.95
Nb/U	27.97	26.43	43.01	48.35	67.12	54.25	46.13	34.68	34.76	26.59	19.72	17.34	17.79	36.07	4.81	4.96	4.34
Sr/Y	48.97	90.35	64.17	77.65	46.03	51.16	44.64	64.60	45.03	68.71	61.10	75.80	70.00	39.27	110.70	61.34	44.61

Appendix II: Curriculum Vitae

Name: Fei Xue

Gender: Male

Date of Birth: 1992/09/21

Nationality: Chinese

Place of Birth: Jiangsu, China

Affiliation: School of Earth Sciences and Engineering, Hohai University, Nanjing, China



Education Background

- October 2018—September 2021
Ph.D. in Geology (Petrology)
University of Tsukuba, Japan
- September 2017—June 2020
Ph.D. in Geology (Mineralogy, Petrology and Mineral Deposit)
China University of Geosciences Beijing, China
- September 2014—June 2017
Master of Science in Geology (Mineral Resource Prospecting and Exploration)
China University of Geosciences Beijing, China
- September 2010—June 2014
Bachelor of Science in Geology (Geological Engineering)
China University of Mining and Technology, China

Publications

1. Xue, F., Santosh, M*, Kim, S. W., Tsunogae, T., and Yang, F., 2021. Thermo-mechanical destruction of Archean cratonic roots: Insights from the Mesozoic Laiyuan granitoid complex, North China Craton. *Lithos* 400-401: 106394.

2. **Xue, F.**, Santosh, M*, Tsunogae, T., Zhou, H.Y. and Yang, F., 2020. The genesis of high Ba-Sr adakitic rocks: Insights from an Early Cretaceous volcanic suite in the central North China Craton. *Geological Journal* 55: 5398-5416.
3. **Xue, F.**, Santosh, M*, Tsunogae, T. and Yang, F., 2019. Geochemical and isotopic imprints of early cretaceous mafic and felsic dyke suites track lithosphere-asthenosphere interaction and craton destruction in the North China Craton. *Lithos* 326-327: 174-199.
4. **Xue, F.**, Santosh, M*, Li, S., Zhang, J. and Tsunogae, T., 2019. Early Cretaceous cryptoexplosive breccia-related gold mineralization in the North China Craton: Evidence from the Puziwan gold deposit. *Ore Geology Reviews* 111: 102986.
5. **Xue, F.**, Wang, G*, Santosh, M., Yang, F., Shen, Z., Kong, L., Guo, N., Zhang, X. and Jia, W., 2018. Geochemistry and geochronology of ore-bearing and barren intrusions in the Luanchuan ore fields of East Qinling metallogenic belt, China: diverse tectonic evolution and implications for mineral exploration. *Journal of Asian Earth Sciences* 157: 57-77.
6. Yang, F., **Xue, F***, Santosh, M., Qian, Z., Zhang, C. and Tu, J., 2021. Petrogenesis and tectonic evolution of the Palaeozoic to Mesozoic Niuxinshan granitoids in the North Qilian orogen, NW China. *Geological Journal*. <https://doi.org/10.1002/gj.4093>.
7. Yang, F*, **Xue, F.**, Santosh, M., Wang, G.W., Kim, S.W., Shen, Z.W., Jia, W.J. and Zhang, X.H., 2019. Late Mesozoic magmatism in the East Qinling Orogen, China and its tectonic implications. *Geoscience Frontiers* 10(5): 1803-1821.
8. Yang F*, Santosh M., Glorie S., **Xue F.**, Zhang S. and Zhang X., 2020. Apatite geochronology and chemistry of Luanchuan granitoids in the East Qinling Orogen, China: Implications for petrogenesis, metallogenesis and exploration. *Lithos* 378: 105797.
9. Yang, F*, Santosh, M., Kim, S.W., Zhou, H.Y. and **Xue, F.**, 2018. Early Cretaceous adakitic granitoids from the Zhijiazhuang skarn iron deposit, North Taihang Mountain, China: Implications for petrogenesis and metallogenesis associated with craton destruction. *Geological Journal* 54(6): 3189-3211.

10. Yang, F., Wang, G*, Cao, H., Li, R., Tang, L., Huang, Y., Zhang, H., **Xue, F.**, Jia, W. and Guo, N., 2017. Timing of formation of the Hongdonggou Pb-Zn polymetallic ore deposit, Henan Province, China: Evidence from Rb-Sr isotopic dating of sphalerites. *Geoscience Frontiers* 8(3): 605-616.

11. Guo, X. G., Li, J. W*., Zhang, D. H., **Xue, F.**, Xian, H. B., Wang, S. J., and Jiao, T. L., 2020. Petrogenesis and tectonic setting of igneous rocks from the Dongbulage porphyry Mo deposit, Great Hinggan Range, NE China: Constraints from geology, geochronology, and isotope geochemistry. *Ore Geology Reviews*: 103326.

Research Gate page:

https://www.researchgate.net/profile/Fei_Xue47